



**HAL**  
open science

# Influence of the porous structure of different tio<sub>x</sub> electrodes on the effectiveness of the anodic oxidation process for water treatment

Jing Ma

► **To cite this version:**

Jing Ma. Influence of the porous structure of different tio<sub>x</sub> electrodes on the effectiveness of the anodic oxidation process for water treatment. Environmental Engineering. Université Gustave Eiffel, 2022. English. NNT : 2022UEFL2061 . tel-04348093

**HAL Id: tel-04348093**

**<https://theses.hal.science/tel-04348093v1>**

Submitted on 16 Dec 2023

**HAL** is a multi-disciplinary open access archive for the deposit and dissemination of scientific research documents, whether they are published or not. The documents may come from teaching and research institutions in France or abroad, or from public or private research centers.

L'archive ouverte pluridisciplinaire **HAL**, est destinée au dépôt et à la diffusion de documents scientifiques de niveau recherche, publiés ou non, émanant des établissements d'enseignement et de recherche français ou étrangers, des laboratoires publics ou privés.

**Université Paris-Est**

**Université Gustave Eiffel**

**École Doctorale SIE - Sciences, Ingénierie et Environnement**

**Thèse de doctorat - PhD Thesis**

**Spécialité: Sciences et Techniques de l'Environnement**

**Jing MA**

**Influence of the Porous Structure of Different  $\text{TiO}_x$   
Electrodes on the Effectiveness of the Anodic Oxidation  
Process for Water Treatment**

Defended on December 15<sup>th</sup>, 2022

Thesis defense committee:

Prof. Karine GROENEN SERRANO	Reviewer
Dr. Jelena RADJENOVIC	Reviewer
Prof. Marc CRETIN	Examiner (President)
Dr. Emmanuel MOUSSET	Examiner
Eng. Stéphane RAFFY	Examiner
Prof. Mehmet A. OTURAN	Thesis supervisor
Dr. Clément TRELLU	Thesis co-supervisor



## Acknowledgements

I would like to take this opportunity to express my genuine gratitude to everyone who has helped me during my pursuit of PhD degree in Université Gustave Eiffel. The guidance, help and great support from all these people are indispensable for me to accomplish my PhD work. First of all, I would like to express my sincere acknowledgement to Prof. Mehmet A. Oturan. Thanks to Prof. Oturan, I could have this precious chance to work in Laboratoire Géomatériaux et Environnement (LGE). Over the past three years, Prof. Oturan has been very supportive and has given me valuable advices for my study as well as pursuing an academic career. Prof. Oturan has not only profound knowledge of electrochemistry, but also admirable research attitude. I've learned a lot from his good qualities and guidance. It is a great pleasure for me to work with a researcher like Prof. Oturan.

I would like to express my great gratitude to Dr. Clément Trelu. Dr. Trelu has been an invaluable guide during my thesis work. I really appreciate the discussions with him. These discussions have been extremely important to keep my project moving forward efficiently. He has also greatly encouraged and supported me to participate in international conferences and accomplish a mobility in Spain. With his guidance, I have improved my knowledge in electrochemistry as well as my research, writing and presentation skills. More importantly, he has set me an example of how to be an excellent researcher. It is a great honor to have him as my guide.

I would like to thank Dr. Nihal Oturan. She has given me valuable advices to refine my study as well as great technical support in the lab. I also appreciate very much her kindness and care.

I am also grateful to the members of my thesis committee, Prof. Christine Cachet-Vivier, Prof. Marc Cretin and Dr. Yoan Pechaud. They gave me very helpful feedbacks and advices to improve my study.

I would also like to express my appreciation to my colleagues in LGE for their professional help and tremendous support. I would like to thank Chloé Fourdrin for Raman spectroscopy. I would like to thank Julie Jonfal for her help with digital microscope and ICP analyses. I



would like to thank Camille Muller and Chloé Boutillez for digital microscope as well. I am also thankful to Théo Isigkeit, who has provided lots of assistance for my lab work and kept things moving in the lab. I want to thank Prof. Stéphanie Rossano for her help with administrative processes. I would like to thank all my colleagues for their help and kindness. They have made my journey of PhD memorable and precious. I would also like to thank Thibault Dubois for the Python program I used in my first study. Except for the professional help, I want to especially thank Julie Jonfal, Camille Muller, Chloé Boutillez, Sule Camcioglu, Baran Özyurt and Màxim Gibert-Vilas for bringing me laugh and joy, giving me advices and cheering me up during bad times. The wonderful time and experiences I had with them comprised a very important part of my PhD life.

I would like to thank Prof. Jelena Radjenovic for welcoming me to do a mobility in Institut Català de Recerca de l'Aigua (ICRA). Thanks to this chance, I could do AOX analysis and finish my study on chloride oxidation.

I would like to thank Dr. Semyon Mareev and Ekaterina Skolotneva. The collaboration with them on the modeling of  $TiO_x$  and BDD electrodes' reactivity during anodic oxidation of organic pollutants allowed me to have a better understanding of near electrode surface phenomena and mechanisms during the AO process. This understanding has been very important for the subsequent study.

I would like to acknowledge China scholarship council (CSC) for the financial support for my PhD work (201906970041). I would also like to acknowledge Saint-Gobain Research Provence for providing all the  $TiO_x$  electrodes.

Finally, I would like to express my sincere appreciation to my family and friends. The unconditional love from my parents and sister has always kept me supported and helped me get through tough times. Everything I have accomplished so far is thanks to them. My friends Lulu, Jinghua and Manli also deserve my appreciation. Their accompany, encouragement and comfort have been priceless for me to come all this far.

**Table of contents**

Acknowledgements .....	I
Abstract .....	III
Résumé.....	V
List of Figures .....	VII
List of Tables.....	XIII
List of abbreviations.....	XIV
Chapter I Introduction .....	1
1. Anodic oxidation process. Main advantages and challenges.....	2
1.1 Formation of oxidant species .....	3
1.2 Anode material development.....	5
1.3 Chlorine evolution and potential risks associated to the formation of other chlorinated compounds .....	7
1.4 Development of porous materials and influence of electrochemical cell configuration.....	9
2. Research objectives of the thesis.....	12
References.....	14
Chapter II Literature Review.....	21
1. Focus on the state of the art related to TiO <sub>x</sub> materials for the anodic oxidation process.....	22
1.1 Synthesis of TiO <sub>x</sub> electrodes.....	22
1.2 Application of TiO <sub>x</sub> electrodes in AO.....	26
2. Active chlorine-mediated oxidation and formation of toxic chlorinated by-products.....	35
2.1 Active chlorine-mediated oxidation .....	35
2.2 Formation of undesired by-products during active chlorine-mediated oxidation of organic pollutants .....	36
2.3 Application of TiO <sub>x</sub> electrodes for active chlorine-mediated oxidation .....	38
3. Conclusions .....	38
References.....	40
Chapter III Development of Ti/TiO <sub>x</sub> Foams for Removal of Organic Pollutants from Water: Influence of Porous Structure of Ti Substrate.....	47
Abstract .....	48
1. Introduction .....	49
2. Materials and Methods.....	51
2.1 Chemicals and instruments.....	51
2.2 Synthesis of electrode materials .....	51
2.3 Material characterization.....	52
2.4 Electrochemical setup.....	53
2.5 Electrochemical characterization.....	53

## Table of contents

---

2.6 Determination of the effective roughness factor (ERF).....	54
2.7 Probe molecules, model pollutant and quenching experiments.....	55
2.8 Electrode stability.....	57
2.9 Analytical methods.....	57
3. Results and Discussion.....	58
3.1 Characterization of Ti/TiO <sub>x</sub> materials: how the substrate influences the coating?.....	58
3.2 Electrochemical reactivity of Ti/TiO <sub>x</sub> materials.....	66
3.3 Degradation and mineralization of a model pollutant: effectiveness and reaction mechanisms.....	71
3.4 Application of foam 1 in flow-through configuration.....	82
3.5 Electrode stability.....	83
4. Conclusions.....	84
Acknowledgements.....	84
References.....	86
Chapter IV Porous Magnéli Phase Obtained from 3D Printing for Efficient Anodic Oxidation Process ..	93
Abstract.....	94
1. Introduction.....	95
2. Materials and methods.....	96
2.1 Chemicals.....	96
2.2 Electrode synthesis.....	97
2.3 Physico-chemical characterization.....	97
2.4 Electrochemical characterization.....	98
2.5 Experimental.....	98
2.6 Analytical methods.....	99
2.7 Calculation of mineralization current efficiency (MCE).....	99
3. Results and discussion.....	100
3.1 Physicochemical characterization of 3D TiO <sub>x</sub> electrode.....	100
3.2 Electrochemical characterization of 3D TiO <sub>x</sub> electrode.....	102
3.3 Electrochemical reactivity assessment.....	103
3.4 Degradation of paracetamol in the absence and presence of quenchers.....	105
3.5 Fate of degradation by-products.....	106
4. Conclusions.....	109
Acknowledgement.....	110
References.....	111
Chapter V Development of 100% TiO <sub>x</sub> Electrodes for Removal of Organic Compounds in Flow-Through Configuration: The Key Role of Material Pore Size.....	117
Abstract.....	118
1. Introduction.....	119
2. Materials and methods.....	121
2.1 Chemicals.....	121
2.2 Material synthesis.....	121
2.3 Material characterization.....	122
2.4 Electrochemical characterization.....	122
2.5 Experimental configurations for stirred-tank and flow-through reactors.....	123

2.6 Electrode reactivity assessment using probe molecules .....	123
2.7 Analytical methods .....	124
2.8 Calculation of mineralization current efficiency (MCE).....	124
3. Results and discussions .....	124
3.1 Material characterization .....	124
3.2 Reactivity of TiO <sub>x</sub> electrodes in stirred-tank reactor .....	129
3.3 Reactivity of electrodes in flow-through reactor .....	132
4. Conclusions .....	136
References .....	138
Chapter VI Chloride Oxidation on TiO <sub>x</sub> Electrodes: Influence of Porous Structure and Reactor Configuration .....	143
Abstract .....	144
1. Introduction .....	145
2. Materials and methods .....	147
2.1 Chemicals .....	147
2.2 Electrode materials .....	148
2.3 Treatment of synthetic solutions in stirred-tank and flow-through reactors .....	149
2.4 Treatment of a real effluent in stirred-tank and flow-through reactors.....	150
2.5 Analytical methods .....	151
2.6 Calculation of accumulation rate of different chlorine species .....	152
3. Results and discussions .....	153
3.1 Chloride oxidation in synthetic solution.....	153
3.2 Application of 100% TiO <sub>x</sub> electrodes for a complex effluent treatment and the role of organic pollutants .....	164
4. Conclusions .....	169
References .....	171
Chapter VII Conclusions and Perspectives .....	175
1. General conclusions .....	176
2. Perspectives and future work .....	179
2.1 How is the stability of TiO <sub>x</sub> electrodes? .....	179
2.2 How the increase of the anodic potential allows for prediction of the lifetime of TiO <sub>x</sub> electrodes?.....	180
2.3 Is the increase of anodic potential suitable for representing the real reactivity loss of TiO <sub>x</sub> electrodes for removal of organic compounds?.....	182
2.4 What is the cause for the reactivity loss of TiO <sub>x</sub> electrodes?.....	184
References .....	189
Curriculum Vitae .....	191



## Abstract

This thesis focused on the application of new sub-stoichiometric titanium oxide ( $\text{TiO}_x$ ) electrodes for water treatment by anodic oxidation process:

- $\text{Ti}/\text{TiO}_x$  electrodes, fabricated by coating  $\text{TiO}_x$  particles on different Ti substrates by plasma spraying ( $\text{Ti}/\text{TiO}_x$  plate and foams);
- 100%  $\text{TiO}_x$  electrodes fabricated by 3D printing, foaming process or carbothermal reduction of  $\text{TiO}_2$  (3D  $\text{TiO}_x$ ,  $\text{TiO}_x$  foam and reactive electrochemical membrane (REM)).

The objectives of this thesis were to: (i) characterize the composition of these electrodes and their porous structure, (ii) study their electrochemical characteristics, (iii) identify the electro-oxidation mechanisms for degradation of organic pollutants and evolution of chlorine species, (iv) understand the influence of porous structure and reactor configuration (stirred-tank vs flow-through) on mass transfer condition and reactivity of the electrodes.

The electrodes were characterized by (i) scanning electron microscopy and optical microscopy, (ii) Hg porosimetry, (iii) X-ray diffraction, (iv) Raman microscopy and (v) X-ray photoelectron spectroscopy. Oxygen evolution reaction as well as electrochemical active surface area were studied by voltammetry. Reactivity of the electrodes were assessed based on (i) the use of probe molecules, (ii) degradation of paracetamol as a model pollutant, (iii) the use of ethanol as quencher to study the role of hydroxyl radicals and (iv) the use of synthetic NaCl solution as well as a real effluent from the textile industry to study the evolution of chlorine species.

This work firstly made it possible to identify that Ti substrate presenting the most appropriate porous structure could achieve (i) homogeneous  $\text{TiO}_x$  coating leading to more favorable condition for hydroxyl radical generation and, (ii) suitable coarse roughness for improving mass transfer condition and thus promote efficient degradation of organic pollutants in stirred-tank reactor.

An even better behavior in stirred-tank reactor was obtained by using 3D TiO<sub>x</sub> electrode, whose synthesis technique allows to control the pore size. In comparison, 100% TiO<sub>x</sub> REM was proved to be less efficient in stirred-tank reactor due to its small pore size which gives the coarse roughness that can be averaged into the diffusion field at surface of electrode.

In flow-through reactor, the efficiency of all porous electrodes has been improved. Diffusion is indeed accelerated inside small pores. The mass transport of the pollutants could be therefore improved by increasing convection through the electrode. Thus, 100% TiO<sub>x</sub> REM electrode (small pore size) was proved to be the most efficient for terephthalic acid degradation (in g h<sup>-1</sup> m<sup>-2</sup>) (48 times higher than the degradation rate in stirred-tank reactor at an optimal flow of 1600 L h<sup>-1</sup> m<sup>-2</sup>).

With regard to the evolution of chlorine species, the application of 100% TiO<sub>x</sub> foam in stirred-tank reactor and various porous electrodes at high flux in flow-through reactor have enabled the maximization of active chlorine generation with minimized formation of chlorate / perchlorate. The underlying mechanisms seem mainly related to the promotion or the contact between the different chlorine species and hydroxyl radicals formed at electrode/solution interface.

However, the formation of toxic by-products and halogenated-organic compounds remains a problem to be taken into consideration within the framework of a complete treatment chain. Particular attention should also be paid to the evaluation and optimization of electrode lifetime for industrial application.

## Résumé

Cette thèse a porté sur l'application de nouvelles électrodes en oxyde de titane sous-stœchiométriques ( $\text{TiO}_x$ ) pour le traitement de l'eau par oxydation anodique :

- Les électrodes  $\text{Ti/TiO}_x$ , fabriquées par revêtement de particules de  $\text{TiO}_x$  sur différents substrats de Ti par projection plasma (plaques et mousses  $\text{Ti/TiO}_x$ ) ;
- Les électrodes 100%  $\text{TiO}_x$  fabriquées par impression 3D, procédé de moussage ou réduction carbothermique de  $\text{TiO}_2$  ( $\text{TiO}_x$  3D, mousse  $\text{TiO}_x$  et membrane électro-active (MEA)).

Les objectifs de cette thèse ont été de : (i) caractériser la composition de ces électrodes et leur structure poreuse, (ii) étudier leurs caractéristiques électrochimiques, (iii) identifier les mécanismes d'électro-oxydation pour l'élimination des polluants organiques et l'évolution des chlorures, (iv) comprendre l'influence de la structure poreuse et de la configuration du réacteur (parfaitement agité vs cellule sous flux) sur le transport de matière et la réactivité des électrodes.

Les matériaux ont été caractérisés par les techniques suivantes : (i) microscopie électronique à balayage et microscopie optique, (ii) porosimétrie Hg, (iii) diffraction des rayons X, (iv) microscopie Raman et (v) spectroscopie photoélectronique X. La voltamétrie a permis d'étudier la réaction d'évolution de l'oxygène ainsi qu'estimer les surfaces électro-actives. L'aspect réactif des électrodes a reposé sur (i) l'utilisation de molécules sondes, (ii) l'étude du paracétamol comme polluant modèle, (iii) l'utilisation de l'éthanol comme agent masquant de l'effet des radicaux hydroxyles, (iv) l'utilisation de solutions synthétiques de NaCl ainsi que d'un effluent réel issue de l'industrie textile pour étudier l'évolution des chlorures.

Ce travail a tout d'abord permis d'identifier le substrat Ti présentant la structure poreuse la plus appropriée pour aboutir (i) à un revêtement de  $\text{TiO}_x$  homogène permettant de promouvoir la formation de radicaux hydroxyles et (ii) à une rugosité de surface pertinente pour améliorer les conditions de transfert de masse et promouvoir ainsi l'élimination des polluants organiques en réacteur parfaitement agité.



Un comportement encore meilleur en réacteur parfaitement agité a ensuite été obtenu grâce à l'utilisation des électrodes  $\text{TiO}_x$  3D, dont la technique de synthèse permet de contrôler la taille des pores. En comparaison, l'électrode 100%  $\text{TiO}_x$  en tant que MEA ne s'est pas avérée pertinente pour ce type de réacteur en raison de la faible taille de ses pores qui lui confère une surface électro-active moyennée dans le champ de diffusion à la surface de l'électrode.

Dans une cellule sous flux, l'efficacité de toutes les électrodes poreuses a été améliorée. La diffusion est en effet accélérée à l'intérieur des pores de petites tailles. Le transport de matière des polluants a pu alors être amélioré en augmentant la convection au travers de l'électrode. Ainsi, c'est l'électrode 100%  $\text{TiO}_x$  MEA qui s'est avérée la plus pertinente (faible taille de pore) avec un taux de dégradation de l'acide téréphtalique (en  $\text{g h}^{-1} \text{m}^{-2}$ ) multiplié par 48 par rapport à l'application en réacteur parfaitement agité pour un flux optimal de  $1600 \text{ L h}^{-1} \text{m}^{-2}$ .

En ce qui concerne l'évolution des chlorures, ce sont l'utilisation des mousses 100% en réacteur parfaitement agité et l'utilisation des différentes électrodes poreuses sous flux élevé qui ont permis la maximisation de la formation de chlore actif et la minimisation des chlorates / perchlorates. Les mécanismes sous-jacents semblent principalement liés à la promotion ou non du contact entre les différentes espèces chlorées et les radicaux hydroxyles formés à l'interface électrode/solution.

Cependant, la formation de ces composés et celle de composés organiques halogénés restent une problématique à prendre en compte dans le cadre d'une filière complète de traitement. Une attention particulière doit aussi être portée sur l'évaluation et l'optimisation de la durée de vie de ces matériaux afin d'envisager un développement industriel.

## List of Figures

Fig. 1-1 - Demonstration of different configurations: (a) stirred-tank reactor, (b) flow-by reactor, (c) flow-through reactor and corresponding mass transfer conditions.....	11
Fig. 3-1 - Plot of incremental pore volume as a function of pore diameter for foam 1 from Hg porosimetry (a) and pore size of foam 2 observed from optical microscopy (b).....	58
Fig. 3-2 - SEM images of (a): Ti/TiO <sub>x</sub> plate, (b), (c): foam 1 and (d), (e) and (f): foam 2.....	60
Fig. 3-3 - XRD pattern for TiO <sub>x</sub> coating of Ti/TiO <sub>x</sub> materials (using database PDF2-2004).....	61
Fig. 3-4 - Raman spectra obtained for Ti/TiO <sub>x</sub> plate surface. Laser energy was tuned with 5% and 50% filter irradiation .....	61
Fig. 3-5 - Surface roughness of different materials observed from optical microscopy.....	62
Fig. 3-6 - Measurement of double layer capacitance for Ti/TiO <sub>x</sub> foam 2 (reference electrode: Ag/AgCl/3 M KCl, supporting electrolyte: 100 mM NaClO <sub>4</sub> , scan rate: 0.006-0.01 V s <sup>-1</sup> ).....	63
Fig. 3-7 - Cyclic voltammogram for Fe(CN) <sub>6</sub> <sup>4-</sup> /Fe(CN) <sub>6</sub> <sup>3-</sup> system using BDD electrode for determination of mass transfer coefficient (reference electrode: Ag/AgCl/3 M KCl, supporting electrolyte: 100 mM NaClO <sub>4</sub> , scan rate: 0.01 V s <sup>-1</sup> ) .....	65
Fig. 3-8 - Observation of electrode surface (foam 1) and influence of diffusion layer thickness .....	66
Fig. 3-9 - Correction of LSV data of Ti/TiO <sub>x</sub> plate by ohmic drop. (a) Determination of the uncompensated resistance, (b) LSV curves before and after ohmic drop correction.....	67
Fig. 3-10 - Calculation of OEP from corrected LSV curve (Ti/TiO <sub>x</sub> plate).....	67
Fig. 3-11 - LSV curves of different materials used in this study (reference electrode: Ag/AgCl/3 M KCl, supporting electrolyte: 100 mM NaClO <sub>4</sub> , scan rate: 0.01 V s <sup>-1</sup> ).....	69
Fig. 3-12 - TA degradation kinetic (a) and pseudo first order rate constant values (b) obtained during electro-oxidation of TA with different Ti/TiO <sub>x</sub> materials and BDD anodes (initial C <sub>TA</sub> = 0.1 mM, effective surface area = 23.6 cm <sup>2</sup> , S <sub>electrode</sub> /V <sub>solution</sub> = 7.9 m <sup>-1</sup> , current density = 5 mA cm <sup>-2</sup> ) .....	70
Fig. 3-13 - Generation of HTA during degradation of TA on different electrode surface (initial C <sub>TA</sub> = 0.1 mM, effective surface area = 23.6 cm <sup>2</sup> , S <sub>electrode</sub> /V <sub>solution</sub> = 7.9 m <sup>-1</sup> , current density = 5 mA cm <sup>-2</sup> ).....	70
Fig. 3-14 - Oxidative degradation kinetic (a) and pseudo first order rate constant (b) obtained during electro-oxidation of PCT using different Ti/TiO <sub>x</sub> materials and BDD as anode (initial C <sub>PCT</sub> = 0.1 mM,	

effective surface area = 23.6 cm <sup>2</sup> , $S_{\text{electrode}}/V_{\text{solution}} = 7.9$ , current density = 5 mA cm <sup>-2</sup> ).....	72
Fig. 3-15 - Degradation kinetic (a) and values of pseudo first order rate constants (b) obtained during anodic oxidation of oxalic acid (OA) with Ti/TiO <sub>x</sub> material (foam 2) and BDD anodes (initial C <sub>OA</sub> = 0.4 mM, effective surface area = 23.6 cm <sup>2</sup> , $S_{\text{electrode}}/V_{\text{solution}} = 7.9$ m <sup>-1</sup> , current density = 5 mA cm <sup>-2</sup> )..	73
Fig. 3-16 - Mineralization yield of PCT after 2 h (a) and 8 h (b) of electrolysis using different Ti/TiO <sub>x</sub> materials and BDD as anode under following operating conditions: initial C <sub>PCT</sub> = 0.1 mM, initial TOC = 9.6 mg L <sup>-1</sup> , effective surface area = 23.6 cm <sup>2</sup> , $S_{\text{electrode}}/V_{\text{solution}} = 7.9$ m <sup>-1</sup> , current density = 5 mA cm <sup>-2</sup> .....	74
Fig. 3-17 - PCT degradation during anodic oxidation process using different anode materials in the presence and absence of EtOH and TBA: (a) foam 1, (b) foam 2, (c) Ti/TiO <sub>x</sub> plate and (d) BDD (initial C <sub>PCT</sub> = 0.1 mM, effective surface area = 23.6 cm <sup>2</sup> , $S_{\text{electrode}}/V_{\text{solution}} = 7.9$ m <sup>-1</sup> , current density = 5 mA cm <sup>-2</sup> , mol <sub>EtOH/TBA</sub> /mol <sub>PCT</sub> = 1000).....	78
Fig. 3-18 - Paracetamol degradation mechanism proposed by Sirés et al. (Sirés et al., 2006).....	79
Fig. 3-19 - Evolution of by-products during PCT degradation by different materials in the absence and presence of EtOH: (a) foam 1, (b) foam 2, (c) Ti/TiO <sub>x</sub> plate and (d) BDD and (e) evolution of total concentration of (HQ + BQ) (initial C <sub>PCT</sub> = 0.1 mM, effective surface area = 23.6 cm <sup>2</sup> , $S_{\text{electrode}}/V_{\text{solution}} = 7.9$ m <sup>-1</sup> , current density = 5 mA cm <sup>-2</sup> , mol <sub>EtOH/TBA</sub> /mol <sub>PCT</sub> = 1000) .....	81
Fig. 3-20 - PCT concentration kinetic during anodic oxidation with foam 1 in batch and flow-through mode with continuous recirculation of the solution flowing through the electrode ([PCT] <sub>0</sub> = 0.1 mM, effective surface area = 9.6 cm <sup>2</sup> , $S_{\text{electrode}}/V_{\text{solution}} = 7.9$ m <sup>-1</sup> , current density = 5 mA cm <sup>-2</sup> , flux = 1200 L h <sup>-1</sup> m <sup>-2</sup> ).....	82
Fig. 3-21 - Evolution of the concentration of paracetamol (C/C <sub>0</sub> ) using Ti/TiO <sub>x</sub> plate electrode at 5 mA cm <sup>-2</sup> . The same electrode was used for several repetitive cycles (initial C <sub>PCT</sub> = 0.1 mM, effective surface area = 23.6 cm <sup>2</sup> , $S_{\text{electrode}}/V_{\text{solution}} = 7.9$ m <sup>-1</sup> , current density = 5 mA cm <sup>-2</sup> ).....	83
Fig. 4-1 - XRD pattern for 3D TiO <sub>x</sub> electrode.....	100
Fig. 4-2 - Porous structure and pore size of 3D TiO <sub>x</sub> observed by microscopy (a), SEM image of 3D TiO <sub>x</sub> (b) .....	101
Fig. 4-3 - Measurement of double layer capacitance for 3D TiO <sub>x</sub> (reference electrode: Ag/AgCl/3 M KCl, supporting electrolyte: 100 mM NaClO <sub>4</sub> , scan rate: 0.006-0.01 V s <sup>-1</sup> ) .....	102

- Fig. 4-4 - LSV curves obtained with 3D TiO<sub>x</sub> anode compared to BDD and Ti/TiO<sub>x</sub> plate anodes (reference electrode: Ag/AgCl/3 M KCl), supporting electrolyte: 100 mM NaClO<sub>4</sub>, scan rate: 0.01 V s<sup>-1</sup>) ..... 103
- Fig. 4-5 - Degradation kinetic of OA by AO using 3D TiO<sub>x</sub> anode compared to BDD and Ti/TiO<sub>x</sub> plate anodes (a) and corresponding pseudo first order rate constants (b); degradation kinetic of TA by AO using 3D TiO<sub>x</sub> compared to BDD and Ti/TiO<sub>x</sub> plate anodes (c) and corresponding pseudo first order rate constants (d); generation of HTA during degradation of TA by 3D TiO<sub>x</sub>, BDD and Ti/TiO<sub>x</sub> plates anodes (e). Experimental conditions: initial C<sub>TA</sub> = 0.1 mM, initial C<sub>OA</sub> = 0.4 mM, effective surface area = 23.6 cm<sup>2</sup>, S<sub>electrode</sub>/V<sub>solution</sub> = 7.9 m<sup>-1</sup>, current density = 5 mA cm<sup>-2</sup> ..... 105
- Fig. 4-6 - Degradation kinetic of PCT by 3D TiO<sub>x</sub> in comparison with BDD and Ti/TiO<sub>x</sub> plate electrodes with and without using EtOH as quencher (a) and corresponding pseudo first order rate constants (b). Experimental conditions: initial C<sub>PCT</sub> = 0.1 mM, C<sub>EtOH</sub>/C<sub>PCT</sub> = 1000, effective surface area = 23.6 cm<sup>2</sup>, S<sub>electrode</sub>/V<sub>solution</sub> = 7.9 m<sup>-1</sup>, current density = 5 mA cm<sup>-2</sup> ..... 106
- Fig. 4-7 - Evolution of HQ and BQ (a) and total amount of HQ and BQ during the PCT degradation by AO using 3D TiO<sub>x</sub> anode in comparison with BDD and Ti/TiO<sub>x</sub> plate anodes (b) in absence and presence of EtOH. Experimental conditions: initial C<sub>PCT</sub> = 0.1 mM, C<sub>EtOH</sub>/C<sub>PCT</sub> = 1000, effective surface area = 23.6 cm<sup>2</sup>, S<sub>electrode</sub>/V<sub>solution</sub> = 7.9 m<sup>-1</sup>, current density = 5 mA cm<sup>-2</sup> ..... 108
- Fig. 4-8 - PCT mineralization yield after 2 h electrolysis by 3D TiO<sub>x</sub>, Ti/TiO<sub>x</sub> plate and BDD plate anodes. Experimental conditions: initial C<sub>PCT</sub> = 0.1 mM, effective surface area = 23.6 cm<sup>2</sup>, S<sub>electrode</sub>/V<sub>solution</sub> = 7.9 m<sup>-1</sup>, current density = 5 mA cm<sup>-2</sup> ..... 109
- Fig. 5-1 - Incremental intrusion volume of Hg according to pore diameter: 100% TiO<sub>x</sub> foam (a) and 100% TiO<sub>x</sub> REM (b) ..... 125
- Fig. 5-2 - Porous structure observed by a field emission electron probe microanalyzer for 100% TiO<sub>x</sub> foam (a) and REM (b) and by a digital microscope for 100% TiO<sub>x</sub> foam (c) and REM (d) ..... 126
- Fig. 5-3 - XRD patterns for 100% TiO<sub>x</sub> foam (a) and REM (b) electrodes (database: PDF2-2004) ..... 127
- Fig. 5-4 - Raman spectra of 100% TiO<sub>x</sub> foam and REM ..... 127
- Fig. 5-5 - LSV curves of 100% TiO<sub>x</sub> foam and REM (reference electrode: Ag/AgCl/3 M KCl, supporting electrolyte: 100 mM NaClO<sub>4</sub>, scan rate: 0.01 V s<sup>-1</sup>) ..... 128
- Fig. 5-6 - Degradation kinetics of OA (a) with the pseudo first order rate constants (b) and degradation kinetics of TA (c) with the pseudo first order rate constants (d) by anodic oxidation with 100% TiO<sub>x</sub>

anodes in the stirred-tank reactor (compared with Ti/TiO<sub>x</sub> foam) (initial C<sub>TA</sub> = 0.1 mM, initial C<sub>OA</sub> = 0.4 mM, S<sub>electrode</sub>/V<sub>solution</sub> = 7.9 m<sup>-1</sup>, current density = 5 mA cm<sup>-2</sup>)..... 131

Fig. 5-7 - Mineralization yield of 0.1 mM TA solution by anodic oxidation with 100% TiO<sub>x</sub> anodes after 2 h of electrolysis in the stirred-tank reactor (compared with Ti/TiO<sub>x</sub> foam) (S<sub>electrode</sub>/V<sub>solution</sub> = 7.9 m<sup>-1</sup>, current density = 5 mA cm<sup>-2</sup>)..... 132

Fig. 5-8 - OA mineralization yield by 100% TiO<sub>x</sub> foam, REM and Ti/TiO<sub>x</sub> foam in flow-through configuration and the comparison with the mineralization yield (dash lines) obtained in stirred-tank reactor (with same electric charge passed) (initial C<sub>OA</sub> = 0.4 mM, effective surface area = 12.56 cm<sup>2</sup>, current density = 5 mA cm<sup>-2</sup>)..... 135

Fig. 5-9 - TA degradation efficiency by 100% TiO<sub>x</sub> foam, REM and Ti/TiO<sub>x</sub> foam during anodic oxidation in flow-through configuration comparing to the efficiency (dash lines) in stirred-tank reactor with same electric charge (initial C<sub>TA</sub> = 0.1 mM, effective surface area = 12.56 cm<sup>2</sup>, current density = 5 mA cm<sup>-2</sup>) ..... 136

Fig. 6-1 - Mass balance of chloride and different oxidation species (anode: 100% TiO<sub>x</sub> foam, cathode: CF, initial [NaCl]<sub>0</sub> = 12 mM, pH<sub>0h</sub>: 5.7-5.9, pH<sub>2h</sub>: 7.1-7.8, S<sub>electrode</sub>/V<sub>solution</sub> = 7.9 m<sup>-1</sup>, current density = 5 mA cm<sup>-2</sup>)..... 153

Fig. 6-2 - Generation of active chlorine (a) and accumulation rate evolution of active chlorine (b) by different anodes in stirred-tank reactor (initial [NaCl]<sub>0</sub> = 12 mM, pH<sub>0h</sub>: 5.6-6.5, pH<sub>2h</sub>: 6.0-7.8, cathode: CF, S<sub>electrode</sub>/V<sub>solution</sub> = 7.9 m<sup>-1</sup>, current density = 5 mA cm<sup>-2</sup>). Results of active chlorine generation are presented as a molar ratio between active chlorine (AC) and initial concentration of chloride ions .. 154

Fig. 6-3 - Evolution of chlorate (a), perchlorate (c) and accumulation rate of chlorate (b), perchlorate (d) during 2 h electrolysis by different anodes in stirred-tank reactor; ([NaCl]<sub>0</sub> = 12 mM, cathode: CF, S<sub>electrode</sub>/V<sub>solution</sub> = 7.9 m<sup>-1</sup>, current density = 5 mA cm<sup>-2</sup>). Evolution of chlorate and perchlorate formation are presented as a molar ratio between the target oxychlorinated compound and the initial concentration of chloride ions ..... 157

Fig. 6-4 - Calculation of current efficiency for chloride oxidation during 2 h electrolysis by different anodes in stirred-tank reactor ([NaCl]<sub>0</sub> = 12 mM, cathode: CF, S<sub>electrode</sub>/V<sub>solution</sub> = 7.9 m<sup>-1</sup>, current density = 5 mA cm<sup>-2</sup>)..... 158

Fig. 6-5 - Generation of active chlorine (a) and its accumulation rate (b) by 100% TiO<sub>x</sub> and Ti/TiO<sub>x</sub> foams

using different cathodes ( $[\text{NaCl}]_0 = 12 \text{ mM}$ ,  $S_{\text{electrode}}/V_{\text{solution}} = 7.9 \text{ m}^{-1}$ , current density =  $5 \text{ mA cm}^{-2}$ ). Active chlorine generation are presented as a molar ratio between active chlorine (AC) and the initial concentration of chloride ions ..... 159

Fig. 6-6 - Generation of active chlorine (a) and its accumulation rate (b) by 100%  $\text{TiO}_x$ ,  $\text{Ti}/\text{TiO}_x$  foams and DSA with/without using TBA as  $\cdot\text{OH}$  quencher (stirred-tank reactor, initial  $[\text{NaCl}]_0 = 12 \text{ mM}$ , cathode: SS,  $S_{\text{electrode}}/V_{\text{solution}} = 7.9 \text{ m}^{-1}$ , current density =  $5 \text{ mA cm}^{-2}$ ). Generation of active chlorine are presented as a molar ratio between active chlorine (AC) and the initial concentration of chloride ions ..... 160

Fig. 6-7 - Evolution of active chlorine (a) and chlorate (b) by 100%  $\text{TiO}_x$  foam, REM and  $\text{Ti}/\text{TiO}_x$  foam regarding flux in flow-through configuration with 0% recirculation of the solution (initial  $[\text{NaCl}]_0 = 12 \text{ mM}$ , current density =  $5 \text{ mA cm}^{-2}$ , BDD grid as cathode)..... 163

Fig. 6-8 - Evolution of active chlorine (a), chlorate (c) and their accumulation rates ((b) for active chlorine and (d) for chlorate) during 4.4 h electrolysis by 100%  $\text{TiO}_x$  foam and REM in flow-through reactor with continuous recirculation of the solution (batch mode) ( $[\text{NaCl}]_0 = 12 \text{ mM}$ ,  $S_{\text{electrode}}/V_{\text{solution}} = 3.6 \text{ m}^{-1}$ , current density =  $5 \text{ mA cm}^{-2}$ , BDD grid as cathode,  $J = 1590 \text{ L h}^{-1} \text{ m}^{-2}$ ) ..... 163

Fig. 6-9 - Discoloration (a) and TOC removal (b) during 4.4 h treatment of the dye effluent by 100%  $\text{TiO}_x$  foam in both stirred-tank and flow-through reactors (batch mode) and compared with BDD and DSA in stirred-tank reactor ( $[\text{NaCl}]_0 = 12 \text{ mM}$ , initial TOC =  $9.6 \text{ mg L}^{-1}$ , cathode: BDD grid,  $S_{\text{electrode}}/V_{\text{solution}} = 3.6 \text{ m}^{-1}$ , current density =  $5 \text{ mA cm}^{-2}$ ,  $J = 1590 \text{ L h}^{-1} \text{ m}^{-2}$ ) ..... 165

Fig. 6-10 - Evolution and accumulation rates of active chlorine ((a) and (b)), chlorate ((c) and (d)) and perchlorate ((e) and (f)) during 4.4 h treatment by anodic oxidation using 100%  $\text{TiO}_x$  foam as anode in stirred-tank and flow-through reactors ( $J = 1590 \text{ L h}^{-1} \text{ m}^{-2}$ ; batch mode with 100% recirculation). Results are compared with BDD and DSA plates applied in stirred-tank reactor ( $[\text{NaCl}]_0 = 12 \text{ mM}$ , initial TOC =  $9.6 \text{ mg L}^{-1}$ ,  $S_{\text{electrode}}/V_{\text{solution}} = 3.6 \text{ m}^{-1}$ , current density =  $5 \text{ mA cm}^{-2}$ )..... 167

Fig. 6-11 - Evolution of AOX during anodic oxidation with different anodes in stirred-tank and flow-through reactors (batch mode with 100% recirculation) ( $J = 1590 \text{ L h}^{-1} \text{ m}^{-2}$ ; initial TOC =  $9.6 \text{ mg L}^{-1}$ ,  $S_{\text{electrode}}/V_{\text{solution}} = 3.6 \text{ m}^{-1}$ , current density =  $5 \text{ mA cm}^{-2}$ )..... 169

Fig. 7-1 - Effectiveness of  $\text{Ti}/\text{TiO}_x$  foam anode during seven consecutive experiments for degradation of paracetamol ( $C/C_0$ ) under same experimental conditions (cathode: carbon felt, initial  $C_{\text{PCT}} = 0.1 \text{ mM}$ ,

effective surface area = 23.6 cm <sup>2</sup> , S <sub>electrode</sub> /V <sub>solution</sub> = 7.9 m <sup>-1</sup> , current density = 5 mA cm <sup>-2</sup> , electrolyte: 50 mM Na <sub>2</sub> SO <sub>4</sub> ) .....	180
Fig. 7-2 - Evolution of anodic potential during the accelerated lifetime test of Ti/TiO <sub>x</sub> plate electrode (30°C, current density = 75 mA cm <sup>-2</sup> , electrolyte: 1 M Na <sub>2</sub> SO <sub>4</sub> ).....	182
Fig. 7-3 - Evolution of apparent rate constant for terephthalic acid degradation by Ti/TiO <sub>x</sub> plate during the accelerated lifetime tests under following operating conditions: current density = 50 mA cm <sup>-2</sup> , electrolyte: 50 mM Na <sub>2</sub> SO <sub>4</sub> , cathode: stainless steel; terephthalic acid degradation conditions: cathode: carbon felt, initial C <sub>TA</sub> = 0.1 mM, effective surface area = 23.6 cm <sup>2</sup> , S <sub>electrode</sub> /V <sub>solution</sub> = 7.9 m <sup>-1</sup> , current density = 5 mA cm <sup>-2</sup> , electrolyte: 50 mM Na <sub>2</sub> SO <sub>4</sub> .....	183
Fig. 7-4 - XPS spectra for 100% TiO <sub>x</sub> foam before ageing.....	185
Fig. 7-5 - Elemental mapping of Ti for 100% TiO <sub>x</sub> foam before ageing (a) and 100% TiO <sub>x</sub> foam after ageing (b) and of O for 100% TiO <sub>x</sub> foam before ageing (c) and 100% TiO <sub>x</sub> foam after ageing (d). Accelerated lifetime test conditions: current density = 50 mA cm <sup>-2</sup> , electrolyte: 50 mM Na <sub>2</sub> SO <sub>4</sub> , cathode: stainless steel; microprobe analysis: using a field emission electron probe microanalyzer (JEOL FEG JXA-8530F microscope coupled with wavelength dispersive spectrometer (WDS) and energy dispersive spectrometer (EDS) at 12 kV with current 34 nA .....	186
Fig. 7-6 - XRD patterns for 100% TiO <sub>x</sub> foam before and after accelerated lifetime test (using database PDF2-2004). Accelerated lifetime test conditions: current density = 50 mA cm <sup>-2</sup> , electrolyte: 50 mM Na <sub>2</sub> SO <sub>4</sub> , cathode: stainless steel; XRD analysis conditions: Bruker D8 ENDEAVOR, Cu K $\alpha$ radiation ( $\lambda=1.5418 \text{ \AA}$ ), at 40 kV and 40 mA.....	187

## List of Tables

Table 2-1 Summary of characteristics and application of TiO <sub>x</sub> electrodes in anodic oxidation .....	29
Table 3-1 Calculated values of effective roughness factor according to electrode material and thickness of the diffusion layer ( $\delta$ ).....	64
Table 3-2 Comparison of Ti/TiO <sub>x</sub> foam 1 performance in terms of model pollutant degradation with published studies .....	76
Table 4-1 Pore size distribution of 3D TiO <sub>x</sub> electrode.....	102
Table 5-1 Hg porosimetry analysis of different TiO <sub>x</sub> electrodes .....	125
Table 5-2 Electrochemical characteristics of TiO <sub>x</sub> electrodes .....	129
Table 5-3 Chemical composition of TiO <sub>x</sub> electrodes.....	130
Table 6-1 Summary of characteristics of TiO <sub>x</sub> electrodes .....	149
Table 6-2 Main characteristics of the effluent used for experiments.....	151
Table 7-1 Prediction of TiO <sub>x</sub> electrode failure time at different current density .....	182
Table 7-2 Ti (III) and Ti (IV) contents of 100% TiO <sub>x</sub> foam before and after ageing .....	185



## List of abbreviations

<b>3D:</b> three-dimensional	<b>HQ:</b> hydroquinone
<b>AO:</b> anodic oxidation	<b>HTA:</b> 2-hydroxyterephthalic acid
<b>AOPs:</b> advanced oxidation processes	<b>LSV:</b> linear sweep voltammetry
<b>AOX:</b> adsorbable organic halides	<b>MCE:</b> mineralization current efficiency
<b>BDD:</b> boron-doped diamond	<b>NTA:</b> nanotube arrays
<b>BNTA:</b> blue TiO <sub>2</sub> nanotube arrays	<b>OA:</b> oxalic acid
<b>BQ:</b> benzoquinone	<b>OCP:</b> open circuit potential
<b>CF:</b> carbon felt	<b>OEP:</b> oxygen evolution potential
<b>COD:</b> chemical oxygen demand	<b>OER:</b> oxygen evolution reaction
<b>CV:</b> cyclic voltammetry	<b>•OH:</b> hydroxyl radical
<b>DET:</b> direct electron transfer	<b>PCT:</b> paracetamol
<b>DFT:</b> density functional theory	<b>PFOA:</b> perfluorooctanoate
<b>DSA:</b> dimensionally stable anodes	<b>PFOS:</b> perfluorooctanesulfonate
<b>EAOPs:</b> electrochemical advanced oxidation processes	<b>RCS:</b> reactive chlorine species
<b>EASA:</b> electroactive surface area	<b>RF:</b> roughness factor
<b>ERF:</b> effective roughness factor	<b>SEM:</b> scanning electron microscopy
<b>EtOH:</b> ethanol	<b>SS:</b> stainless steel
<b>GON:</b> graphene oxide nanoparticles	<b>TA:</b> terephthalic acid
<b>HER:</b> hydrogen evolution reaction	<b>TBA:</b> tert-Butyl alcohol
<b>HOCs:</b> halogenated organic compounds	<b>TOC:</b> total organic carbon
	<b>XRD:</b> X-Ray diffraction

# **Chapter I**

## **Introduction**

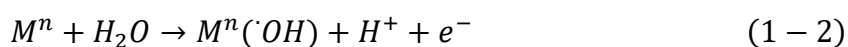
The growing water consumption and contamination of surface and groundwater put human under serious ‘water stress’ (WHO, 2014). The problem is further complexed by the emergence of anthropogenic products, such as heavy metals and persistent organic pollutants (Wang et al., 2020). Conventional water treatment technologies such as biological process, physical processes (e.g., adsorption, filtration and coagulation) and chemical oxidation have been applied for long time but they all face one or more problems, e.g., not effective for removal of pollutants (physical process), requirement for sludge disposal (physical process), not effective for the removal of biorefractory and toxic pollutants (biological process) and transport and storage of harmful chemicals (chemical oxidation) (Bousher et al., 1997; Panizza and Cerisola, 2009; Martínez-Huitle et al., 2015) et al. Therefore, more efficient, cost-effective and chemical-free technologies are demanded (Shannon et al., 2008).

In this context, advanced oxidation processes (AOPs) have been developed to overcome the disadvantages of conventional treatment methods (Oturán and Aaron, 2014). Among these processes, the electrochemical AOPs (EAOPs) have been emerged in beginning of 2000s as clean and effective water treatment techniques (Sirés et al., 2014). One of the most popular EAOPs is the anodic oxidation (or electrooxidation) process.

## **1. Anodic oxidation process. Main advantages and challenges**

Anodic oxidation (AO), also known as electrochemical oxidation (EO), is one of the most efficient and widely-studied EAOPs for decontamination of water (Martínez-Huitle and Ferro, 2006; Guinea et al., 2009; Panizza and Cerisola, 2009; Rodrigo et al., 2010; Sirés et al., 2014; Martínez-Huitle et al., 2015). Combination of the following two electrocatalytic pathways allows AO process to oxidize a large range of recalcitrant organics: (i) direct electron transfer (DET) from target molecule to anode (Eq. 1-1) and (ii) indirect oxidation mediated by oxidants generated during electrolysis, mainly hydroxyl radicals ( $\cdot\text{OH}$ ) formed from water oxidation on the anode surface according to Eq. 1-2. Indirect oxidation can also be facilitated by other oxidants such as  $\text{H}_2\text{O}_2$ ,  $\text{SO}_4^{\cdot-}$ ,  $\text{S}_2\text{O}_8^{2-}$  and active chlorine, depending on the inorganic matrix of the treated water (presence of  $\text{SO}_4^{2-}$  or  $\text{Cl}^-$ ). The great effectiveness of AO process is mainly related to  $\cdot\text{OH}$ -mediated oxidation because of its high reactivity for non-selective

oxidation of numerous recalcitrant organics.  $\cdot\text{OH}$  can react with organic compounds through four possible pathways: (i) abstraction of hydrogen atom ( $10^6$ - $10^8 \text{ M}^{-1} \text{ s}^{-1}$ ), (ii) addition to an unsaturated bond ( $10^8$ - $10^{10} \text{ M}^{-1} \text{ s}^{-1}$ ), (iii) electron transfer (redox) reaction and (iv) ipso substitution of halogen atoms (Brillas et al., 2009; Mousset et al., 2018). Moreover, DET can also participate to oxidize organics which are recalcitrant to  $\cdot\text{OH}$ -mediated oxidation such as short-chain carboxylic acids or perfluoroalkyl substances (Carter and Farrell, 2008; Zhuo et al., 2011).



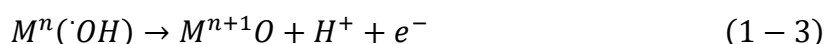
Based on advantages for non-selective oxidation of organics and low requirements in chemicals, AO has been widely studied for wastewater treatment, including landfill leachate, wastewaters containing a large range of concentrations of phenolic compounds, dyes, disinfection by-products, per- and poly-fluoroalkyl substances (PFAS), pharmaceuticals, etc. (Anglada et al., 2010; Chaplin et al., 2010; Enache and Oliveira-Brett, 2011; Zhuo et al., 2011; Feng et al., 2013; Chaplin, 2014; Brillas and Martínez-Huitle et al., 2015; Garcia-Segura et al., 2015; Radjenovic et al., 2020). AO has also been combined with other process to achieve different objectives, e.g., AO was integrated in other advanced oxidation processes (electro Fenton, ozonation) to enhance process effectiveness, or applied as pre-treatment to increase the biodegradability of wastewater (pretreatment step for biologic process), or combined with electrocoagulation for step by step removal of the organic load (Zhu et al., 2009; Oturan, 2021). In addition to massive and successful application in water treatment, AO has also been applied in other environmental fields, such as soil remediation and gas effluents purification (Trellu et al., 2016; Muñoz-Morales et al., 2019; Barbosa Ferreira et al., 2020; Brillas, 2021; Hu et al., 2021).

### 1.1 Formation of oxidant species

The indirect oxidation mediated by oxidant species is an essential pathway for AO process,

especially  $\cdot\text{OH}$ -mediated oxidation, which is able to degrade organic compounds in a non-selective way (Chaplin, 2014; Sirés et al., 2014).  $\cdot\text{OH}$  are formed from water oxidation as expressed in Eq. 1-2. These  $\cdot\text{OH}$  are then accumulated at the electrode/solution interface as chemisorbed or physisorbed to the anode surface depending on the nature of the anode material. Accordingly, the anode material is categorized as “active” (producing chemisorbed  $\cdot\text{OH}$ ) and “non-active” (producing physisorbed  $\cdot\text{OH}$  which promotes the reaction of  $\cdot\text{OH}$  with dissolved species in the solution) electrode. Most of times, non-active electrodes are characterized by higher overpotentials for oxygen evolution reaction (OER).

On the surface of an active electrode, chemisorbed  $\cdot\text{OH}$  interact with electrode surface and form higher oxide (Eq. 1-3):

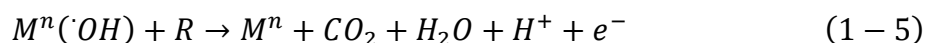


The redox couple  $M^n(\cdot\text{OH})/M^{n+1}\text{O}$  plays a role in mediating oxidation of target pollutant to recover the oxidation site (Eq. 1-4):



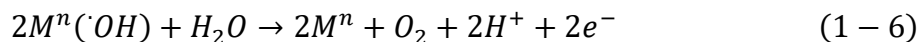
Active electrodes can achieve only partial and selective oxidation of organics due to the low availability of  $\cdot\text{OH}$  (because of their chemisorption) for reaction at the anode surface with dissolved compounds in the treated water (Comninellis, 1994).

In contrast, physisorbed  $\cdot\text{OH}$  at “non-active” electrodes are available for non-selective and complete mineralization of target pollutants (Eq. 1-5) owing to the presence of their high local concentrations and availability (physisorption) of  $\cdot\text{OH}$  at the anode surface:

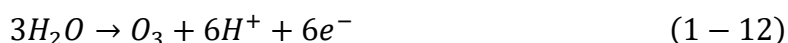
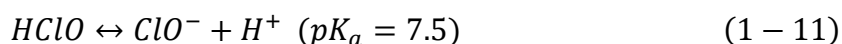
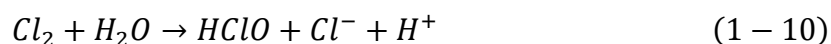
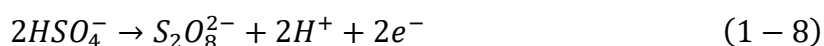


At potentials in the region of water stability, target pollutants can potentially be oxidized via DET. However, this electrocatalytic pathway is strongly selective and leads to low oxidation process effectiveness. Therefore, AO systems are always operated in the anodic potential region of water oxidation in order to promote the generation of  $\cdot\text{OH}$ . Moreover, oxidation through DET might also be enhanced in this region. However, using higher anodic potential can promote a simultaneous waste reaction related to further evolution of  $\cdot\text{OH}$  to  $\text{O}_2$  (Eq. 1-6).

In this context, mass transport of organic compounds from the bulk solution to the electrode surface is a crucial phenomenon for achieving high Faraday efficiency for oxidation of organic compounds.



Depending on the anode material and inorganic matrix, other oxidants can also be formed and further contribute to the AO process, e.g., hydrogen peroxide, peroxodisulfate (and further activation to sulfate radical), active chlorine and ozone (Martínez-Huitle and Ferro, 2006; Panizza and Cerisola, 2009; Comninellis and Chen, 2010; Martínez-Huitle et al., 2015) (Eq. 1-7 – 1-13). These chemical species usually have lower oxidation power. However, they often have longer lifetime than  $\cdot OH$ , allowing the oxidation of organic compounds in a homogeneous way in the bulk solution.



## 1.2 Anode material development

Nature of the anode material is a crucial factor for all EAOPs, particularly for AO process (Du et al., 2021; Oturan et al., 2021). Electrode conductivity and reactivity for  $\cdot OH$ -mediated oxidation are for example two key parameters. As introduced in 1.1.1, anodes producing chemisorbed  $\cdot OH$  are defined as active electrodes, while anodes producing physisorbed  $\cdot OH$

are defined as non-active electrodes.

Most of dimensionally stable anodes (DSA), carbon-based materials and platinum (Pt) are active electrodes. As active electrodes, these anodes have low overpotential values and therefore are less efficient for  $\cdot\text{OH}$ -mediated oxidation of organic compounds. DSA electrodes usually use Ti as substrate with a coating of pure or mixed metal (e.g., Ru, Ir, Ta and Ti) oxide. DSA electrodes are good electrocatalysts for OER (Panizza and Cerisola, 2009), due to their low oxygen evolution potential (OEP). They were found to be efficient for promoting active chlorine generation (particularly  $\text{RuO}_2/\text{IrO}_2$ ), that might result in active chlorine-mediated oxidation of organics or disinfection of the treated water (Panizza and Cerisola, 2009; Martínez-Huitle and Panizza, 2018). Although studies showed that DSA can participate in reaction with aromatic compounds to open aromatic rings, it is usually not able to further oxidize the intermediates, which lead to partial mineralization of the organics (Stucki et al., 1991; Martínez-Huitle and Brillas, 2009; Sopaj et al., 2015). Carbon-based electrodes (e.g., graphite and carbon fibers) have been widely used in three-dimensional electrochemical reactor, due to their low cost, large specific surface area, high adsorption capacity and good conductivity (Panizza and Cerisola, 2009). However, these materials commonly suffer from short service time because of (i) a rapid surface passivation with polymeric products generated at the electrode at low potential and (ii) a rapid material corrosion at high potential (Panizza and Cerisola, 2009). However, promising results have also been recently obtained using reduced graphene oxide (Cuervo Lumbaque et al., 2022; Duinslaeger and Radjenovic, 2022). Pt has been used for oxidation of diverse organic compounds thanks to its great chemical resistance (Martínez-Huitle and Ferro, 2006; Martínez-Huitle and Brillas, 2009; Panizza and Cerisola, 2009). Nevertheless, it also suffers from the same limitations as other active materials. Moreover, it is a costly material, which is mainly used for research purposes as ideal active material (Stucki et al., 1991; Martínez-Huitle and Brillas, 2009).

In comparison, non-active electrodes, (e.g.,  $\text{PbO}_2$ ,  $\text{SnO}_2$ , boron-doped diamond (BDD) and Magnéli phases) are more suitable for removing organic compounds from water during AO process. For example,  $\text{PbO}_2$  electrode has been studied widely because of its low cost, good

conductivity and high overpotential for oxygen evolution. PbO<sub>2</sub> electrodes showed efficient oxidation and complete mineralization of various organic compounds (Rodgers et al., 1999; Panizza and Cerisola, 2008; Zhao et al., 2010). Some studies achieved further enhancement of electrocatalytic reactivity of PbO<sub>2</sub> electrode by adding doping agents (e.g., Bi, Co, F, Fe) to reduce crystal particle size and increase electroactive surface area (Liu et al., 2008; Chaplin, 2014; Bian et al., 2019). Despite its high electrochemical reactivity and low cost, application of PbO<sub>2</sub> electrodes is limited by the possibility of Pb<sup>2+</sup> leaching (Martínez-Huitle and Ferro, 2006; Chaplin, 2014), which can pose serious risk to environment and human health. SnO<sub>2</sub> electrodes have also been applied in AO process, with the assistance of doping agents (e.g., Ar, B, Bi, F, Cl, P) to enhance their poor conductivity (Chaplin, 2014). The electrochemical reactivity and service lifetime of doped-SnO<sub>2</sub> electrodes vary according to the type and quantity of dopant (Chaplin, 2014). BDD electrodes have been studied for decades and appeared as the most efficient electrode for non-selective oxidation of various organic pollutants and for application to the treatment of real wastewater. BDD electrode has high OEP and allows for the generation of large amount of •OH, which are loosely adsorbed to the inert BDD surface, providing high reactivity towards oxidation of organics (Martínez-Huitle and Brillas, 2009; Panizza and Cerisola, 2009; Oturan, 2021). Moreover, BDD electrodes possess other interesting properties such as excellent resistance to corrosion and low double layer capacitance. All these properties allow the successful application of BDD electrodes in decontamination of wastewaters. It is considered as a gold-standard material for such application. One important challenge for BDD is related to the selection of a suitable substrate for reducing cost and improving service time (Martínez-Huitle and Brillas, 2009). It is also important to notice that high OEP leads to higher energy consumption.

### **1.3 Chlorine evolution and potential risks associated to the formation of other chlorinated compounds**

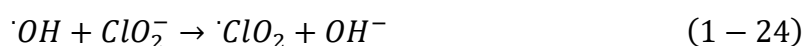
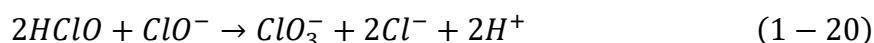
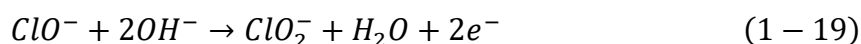
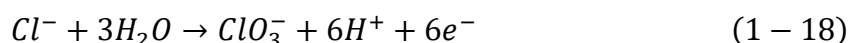
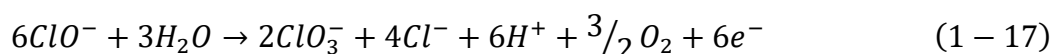
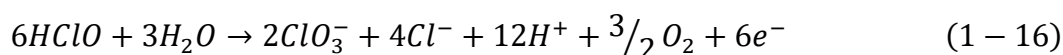
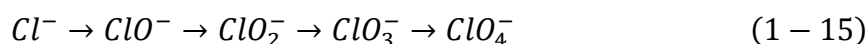
The formation of toxic organic and inorganic chlorinated by-products during the AO process is currently one of the main challenges for further development of this technology for water

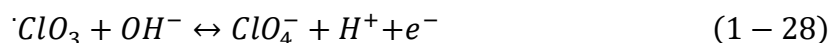


treatment since most of wastewaters contain significant concentrations of chloride ions.

The first step of oxidation of chloride ions can lead to the formation of active chlorine ( $\text{Cl}_2$ ,  $\text{ClO}^-/\text{HClO}$ ). Active chlorine represents a potentially effective oxidant. The interest is related to its oxidation power, its convenience for application in  $\text{Cl}^-$ -containing real effluent treatment, the possibility to promote homogenous oxidation of organic compounds in the bulk and its disinfectant power (Martínez-Huitle and Ferro, 2006; Martínez-Huitle and Brillas, 2009, 2021; Panizza and Cerisola, 2009). The formation of active chlorine can be expressed as described in Eq. 1-9 - 1-11 (Trasatti, 1987; Jung et al., 2010; Brito et al., 2015).

Active chlorine-mediated oxidation has been applied in many studies; however, several problems emerged at the same time. The most worrying problem is related to the formation of toxic chlorinated by-products, i.e.,  $\text{ClO}_3^-$ ,  $\text{ClO}_4^-$  and halogenated organic compounds (HOCs). Formation of chlorate and perchlorate is ascribed to further oxidation of active chlorine to the oxychlorinated compounds (Eq. 1-15). Various reactions can also be taken into consideration for the complex oxidation of chloride to perchlorate (Eq. 1-15 – 1-20, 1-22 – 1-28) (Trasatti, 1987; Jung et al., 2010; Brito et al., 2015). For example, very strict regulation of the concentration of perchlorate in drinking water has been set in US (USEPA, 2008).





HOCs are generated from the reaction between organics and active chlorine or chlorine radicals as a reactive chlorine species (RCS). Formation of HOCs highly depends on the nature of anode material and the operating condition (electrolyte, type of organic pollutants, pH, current density and initial chloride concentration) (Anglada et al., 2010; Li and Ni, 2012; Bagastyo et al., 2013). There is a large range of HOCs, which are generally toxic and persistent (Xu et al., 2021; Dorner et al., 2022). Formation of HOCs has been observed for example during application of AO for treatment of landfill leachates, reverse osmosis concentrates and synthetic solutions containing different organics (Bagastyo et al., 2013; Ganzenko et al., 2021; Norra and Radjenovic, 2021; İskurt et al., 2022).

#### 1.4 Development of porous materials and influence of electrochemical cell configuration

The configuration of the electrochemical cell is also crucial for the effectiveness of the EAOPs. Different reactors have been developed to offer better mass transfer conditions of organics from the bulk to the electrode surface. Stirred-tank reactors and flow-by cells are most commonly used in lab-scale experiments.

Fig. 1-1 (a) shows a typical setup for a stirred-tank reactor. Anode and cathode are placed in an undivided cell in parallel and connected to a power supply. Stirred-tank reactors have been mostly used for lab-scale studies since it is easy to build, to operate and to follow degradation kinetics of target compounds. In such stirred-tank reactor, convection comes from mechanical (or magnetic) stirring and is controlled by the stirring rate. Since reaction occurs at the electrode surface, a gradient of target molecule concentration rapidly appears from bulk solution to electrode surface (so-called diffusion boundary layer). Due to the short lifetime of  $\cdot OH$  and the fact that anodic oxidation takes place only in the vicinity of the electrode surface,

mass transfer of molecules from the bulk to the electrode surface becomes the crucial factor that limits the oxidation rate of organic compounds. When a current density smaller than the limiting current density ( $I_{lim}$ , calculated as Eq. 1-29) is applied to the AO system, the process is operated under current limitation (Panizza and Cerisola, 2009). In this case, the low current density does not allow for generation of enough  $\cdot\text{OH}$  for degradation of target organic compounds that reach the anode surface. When the applied current exceeds  $I_{lim}$ , the anode is able to generate enough  $\cdot\text{OH}$  to degrade target molecules, and the mass transfer of target molecules from the bulk to the anode surface becomes the limiting factor. In this case, waste reactions (e.g., oxidation of water to  $\text{O}_2$ ) are also promoted. Application of the process under current limitation reduces the productivity of the process, while energy efficiency of the process is strongly affected under mass transport limitation. Therefore, improving mass transfer conditions is crucial for AO efficiency.

$$I_{lim} = 4Fk_mCOD \quad (1 - 29)$$

where  $I_{lim}$  is the limiting current density ( $\text{A m}^{-2}$ ),  $F$  is the Faraday constant,  $k_m$  is the mass transfer coefficient and  $COD$  is the chemical oxygen demand ( $\text{mol m}^{-3}$ ) of the solution.

Conventional flow-by cells are composed of flat plate electrodes put in parallel (Fig. 1-1 (b)). In this configuration, mass transport is also limited by the diffusion boundary layer and Taylor dispersion (Zaky and Chaplin, 2014; Xu et al., 2021). The thickness of the diffusion layer depends on the flow rate between the two flat plates. Flow-by reactors are generally operated with high recirculation rate in order to achieve sufficient effectiveness.

In the stirred-tank or flow-by reactor, the thickness of the diffusion layer can be up to hundreds of micrometers. Due to such mass transport limitations existing in these reactors, flow-through reactors were developed for increasing the current efficiency of AO process for the treatment of effluents with low pollutant concentrations (Fig. 1-1 (c)).

By applying porous electrodes in flow-through reactor, diffusion of pollutants is strongly enhanced owing to fast radial diffusion within sufficiently small pores that present sufficiently small size. Therefore, it is possible to achieve a convection-enhanced mass transport of pollutants by simply increasing the flow rate through the electrode. Such configuration allows

for achieving much higher current efficiency for the treatment of low or medium concentration of pollutants (Trellu et al., 2018). However, the use of porous electrodes in flow-through configuration also rises other issues related to pressure drop through the electrode and electrode fouling because of small pore size.

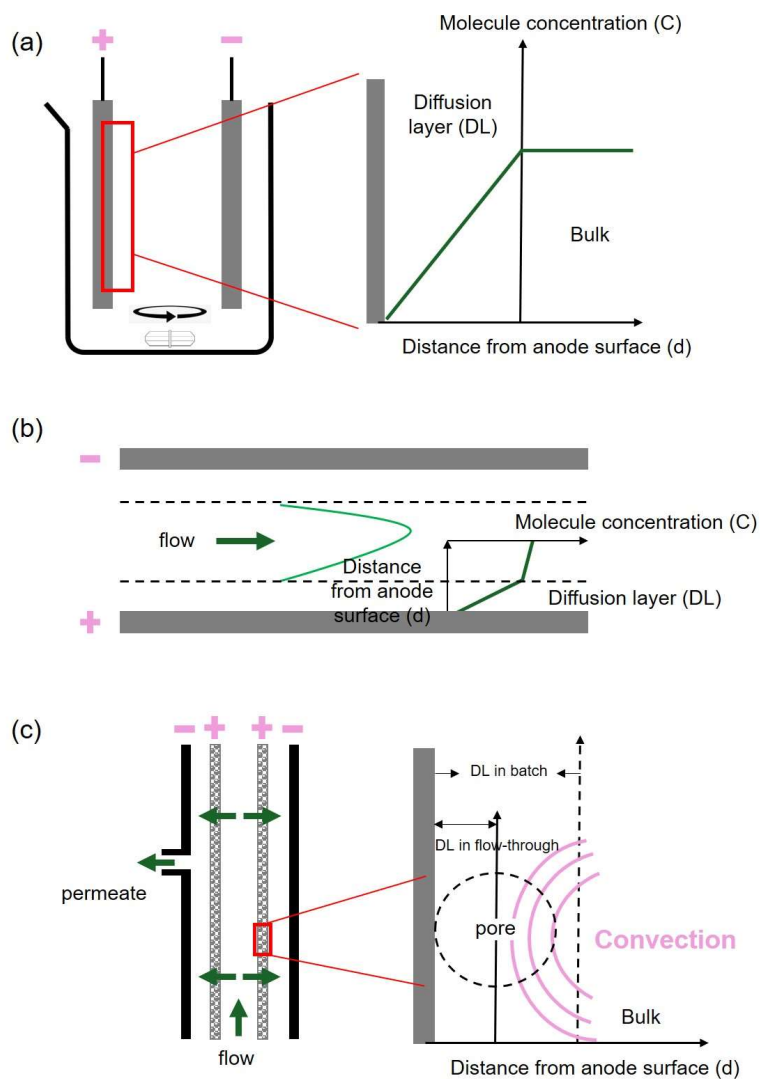


Fig. 1-1 - Demonstration of different configurations: (a) stirred-tank reactor, (b) flow-by reactor, (c) flow-through reactor and corresponding mass transfer conditions

## 2. Research objectives of the thesis

The research goal of this thesis was the identification of advantages and drawbacks of different porous  $\text{TiO}_x$  electrodes for application in water treatment, with a particular emphasis on the influence of the porous structure and reactor configuration. This study was carried out in collaboration with Saint Gobain Research Provence, who synthesized all the  $\text{TiO}_x$  electrodes used in this thesis. Two types of  $\text{TiO}_x$  electrodes were synthesized and studied: (i)  $\text{Ti}/\text{TiO}_x$  foams obtained from plasma spraying and (ii) 100%  $\text{TiO}_x$  electrodes, including electrodes obtained from three-dimensional (3D) printing, foaming process (100%  $\text{TiO}_x$  foam) and carbothermal reduction (100%  $\text{TiO}_x$  REM), respectively.

More specifically, the research work has been divided in different sub-objectives, corresponding to the different chapters of this thesis:

### *1) Application of different $\text{Ti}/\text{TiO}_x$ foams in stirred-tank reactor*

Ti substrates with different structures were used for fabrication of  $\text{Ti}/\text{TiO}_x$  foams. The objective was to identify the role of the Ti substrate structure on performances of electrodes for the removal of organic compounds.

### *2) Using 3D printing for synthesis of 100% $\text{TiO}_x$ electrode and the application in stirred-tank reactor*

A new technique based on 3D printing was used for synthesis of a 100%  $\text{TiO}_x$  electrode. The porous structure fitted with conclusions raised from the previous study on  $\text{Ti}/\text{TiO}_x$  electrodes. The reactivity of 3D-printed  $\text{TiO}_x$  electrode and its capacity to remove a model pollutant was assessed.

### *3) Comparative study of application of different $\text{TiO}_x$ electrodes in stirred-tank and flow-through configurations*

Ti/TiO<sub>x</sub> foam, 100% TiO<sub>x</sub> foam and 100% TiO<sub>x</sub> REM were applied in stirred-tank and flow-through configurations for the removal of organic compounds. The objective was to further understand how the flow-through configuration enhances the performances of these electrodes depending on material pore size.

*4) Behavior of TiO<sub>x</sub> electrodes for chlorine evolution and formation of toxic chlorinated compounds*

TiO<sub>x</sub> electrodes were applied in both stirred-tank and flow-through configurations in order to study their behavior for chlorine evolution and formation of toxic chlorinated by-products. Different electrodes were compared in order to understand the influence of porous structure and reactor configuration. The most suitable electrode was then further applied for the treatment of a chloride containing effluent from textile industry to investigate the process effectiveness and formation of chlorinated organic compounds.

*5) Assessment of TiO<sub>x</sub> electrodes' lifetime*

Lifetime of such electrodes is one of the crucial factors for further development and potential application at industrial scale. Investigations were focused on the identification of a suitable protocol for assessment of electrode ageing. Future perspectives of this thesis are mainly related to this crucial phenomenon.

## References

- Anglada, A., Ortiz, D., Urriaga, A.M., Ortiz, I., 2010. Electrochemical oxidation of landfill leachates at pilot scale: evaluation of energy needs. *Water Sci. Technol.* 61, 2211–2217. <https://doi.org/10.2166/wst.2010.130>
- Bagastyo, A.Y., Batstone, D.J., Rabaey, K., Radjenovic, J., 2013. Electrochemical oxidation of electrodyalysed reverse osmosis concentrate on Ti/Pt–IrO<sub>2</sub>, Ti/SnO<sub>2</sub>–Sb and boron-doped diamond electrodes. *Water Res.* 47, 242–250. <https://doi.org/10.1016/j.watres.2012.10.001>
- Barbosa Ferreira, M., Sales Solano, A.M., Vieira dos Santos, E., Martínez-Huitle, C.A., Ganiyu, S.O., 2020. Coupling of Anodic Oxidation and Soil Remediation Processes: A Review. *Materials* 13, 4309. <https://doi.org/10.3390/ma13194309>
- Bian, X., Xia, Y., Zhan, T., Wang, L., Zhou, W., Dai, Q., Chen, J., 2019. Electrochemical removal of amoxicillin using a Cu doped PbO<sub>2</sub> electrode: Electrode characterization, operational parameters optimization and degradation mechanism. *Chemosphere* 233, 762–770. <https://doi.org/10.1016/j.chemosphere.2019.05.226>
- Bousher, A., Shen, X., Edyvean, R.G.J., 1997. Removal of coloured organic matter by adsorption onto low-cost waste materials. *Water Res.* 31, 2084–2092. [https://doi.org/10.1016/S0043-1354\(97\)00037-7](https://doi.org/10.1016/S0043-1354(97)00037-7)
- Brillas, E., 2021. Recent development of electrochemical advanced oxidation of herbicides. A review on its application to wastewater treatment and soil remediation. *J. Clean. Prod.* 290, 125841. <https://doi.org/10.1016/j.jclepro.2021.125841>
- Brillas, E., Martínez-Huitle, C.A., 2015. Decontamination of wastewaters containing synthetic organic dyes by electrochemical methods. An updated review. *Appl. Catal. B Environ.* 166–167, 603–643. <https://doi.org/10.1016/j.apcatb.2014.11.016>
- Brillas, E., Sirés, I., Oturan, M.A., 2009. Electro-Fenton Process and Related Electrochemical Technologies Based on Fenton's Reaction Chemistry. *Chem. Rev.* 109, 6570–6631. <https://doi.org/10.1021/cr900136g>
- Brito, C. do N., de Araújo, D.M., Martínez-Huitle, C.A., Rodrigo, M.A., 2015. Understanding active chlorine species production using boron doped diamond films with lower and higher sp<sup>3</sup>/sp<sup>2</sup> ratio. *Electrochem. Commun.* 55, 34–38. <https://doi.org/10.1016/j.elecom.2015.03.013>

- Carter, K.E., Farrell, J., 2008. Oxidative Destruction of Perfluorooctane Sulfonate Using Boron-Doped Diamond Film Electrodes. *Environ. Sci. Technol.* 42, 6111–6115. <https://doi.org/10.1021/es703273s>
- Chaplin, B.P., 2014. Critical review of electrochemical advanced oxidation processes for water treatment applications. *Env. Sci Process. Impacts* 16, 1182–1203. <https://doi.org/10.1039/C3EM00679D>
- Chaplin, B.P., Schrader, G., Farrell, J., 2010. Electrochemical Destruction of *N*-Nitrosodimethylamine in Reverse Osmosis Concentrates using Boron-doped Diamond Film Electrodes. *Environ. Sci. Technol.* 44, 4264–4269. <https://doi.org/10.1021/es903872p>
- Comninellis, C., 1994. Electrocatalysis in the electrochemical conversion/combustion of organic pollutants for waste water treatment. *Electrochim. Acta* 39, 1857–1862. [https://doi.org/10.1016/0013-4686\(94\)85175-1](https://doi.org/10.1016/0013-4686(94)85175-1)
- Comninellis, C., Chen, G. (Eds.), 2010. *Electrochemistry for the Environment*. Springer New York, New York, NY. <https://doi.org/10.1007/978-0-387-68318-8>
- Cuervo Lumbaque, E., Baptista-Pires, L., Radjenovic, J., 2022. Functionalization of graphene sponge electrodes with two-dimensional materials for tailored electrocatalytic activity towards specific contaminants of emerging concern. *Chem. Eng. J.* 446, 137057. <https://doi.org/10.1016/j.cej.2022.137057>
- Dorner, M., Lokesh, S., Yang, Y., Behrens, S., 2022. Biochar-mediated abiotic and biotic degradation of halogenated organic contaminants – A review. *Sci. Total Environ.* 852, 158381. <https://doi.org/10.1016/j.scitotenv.2022.158381>
- Du, X., Oturan, M.A., Zhou, M., Belkessa, N., Su, P., Cai, J., Trelu, C., Mousset, E., 2021. Nanostructured electrodes for electrocatalytic advanced oxidation processes: From materials preparation to mechanisms understanding and wastewater treatment applications. *Appl. Catal. B Environ.* 296, 120332. <https://doi.org/10.1016/j.apcatb.2021.120332>
- Duinslaeger, N., Radjenovic, J., 2022. Electrochemical degradation of per- and polyfluoroalkyl substances (PFAS) using low-cost graphene sponge electrodes. *Water Res.* 213, 118148. <https://doi.org/10.1016/j.watres.2022.118148>
- Enache, T.A., Oliveira-Brett, A.M., 2011. Phenol and para-substituted phenols electrochemical oxidation pathways. *J. Electroanal. Chem.* 655, 9–16. <https://doi.org/10.1016/j.jelechem.2011.02.022>



- Feng, L., van Hullebusch, E.D., Rodrigo, M.A., Esposito, G., Oturan, M.A., 2013. Removal of residual anti-inflammatory and analgesic pharmaceuticals from aqueous systems by electrochemical advanced oxidation processes. A review. *Chem. Eng. J.* 228, 944–964. <https://doi.org/10.1016/j.cej.2013.05.061>
- Ganzenko, O., Sístat, P., Trelu, C., Bonniol, V., Rivallin, M., Cretin, M., 2021. Reactive electrochemical membrane for the elimination of carbamazepine in secondary effluent from wastewater treatment plant. *Chem. Eng. J.* 419, 129467. <https://doi.org/10.1016/j.cej.2021.129467>
- García-Segura, S., Keller, J., Brillas, E., Radjenovic, J., 2015. Removal of organic contaminants from secondary effluent by anodic oxidation with a boron-doped diamond anode as tertiary treatment. *J. Hazard. Mater.* 283, 551–557. <https://doi.org/10.1016/j.jhazmat.2014.10.003>
- Guinea, E., Brillas, E., Centellas, F., Cañizares, P., Rodrigo, M.A., Sáez, C., 2009. Oxidation of enrofloxacin with conductive-diamond electrochemical oxidation, ozonation and Fenton oxidation. A comparison. *Water Res.* 43, 2131–2138. <https://doi.org/10.1016/j.watres.2009.02.025>
- Hu, Z., Cai, J., Song, G., Tian, Y., Zhou, M., 2021. Anodic oxidation of organic pollutants: Anode fabrication, process hybrid and environmental applications. *Curr. Opin. Electrochem.* 26, 100659. <https://doi.org/10.1016/j.coelec.2020.100659>
- İskurt, Ç., Aliyev, E., Gengec, E., Kobya, M., Khataee, A., 2022. Electrochemical oxidation of pretreated landfill leachate nanofiltration concentrate in terms of pollutants removal and formation of by-products. *Chemosphere* 307, 135954. <https://doi.org/10.1016/j.chemosphere.2022.135954>
- Jung, Y.J., Baek, K.W., Oh, B.S., Kang, J.-W., 2010. An investigation of the formation of chlorate and perchlorate during electrolysis using Pt/Ti electrodes: The effects of pH and reactive oxygen species and the results of kinetic studies. *Water Res.* 44, 5345–5355. <https://doi.org/10.1016/j.watres.2010.06.029>
- Li, H., Ni, J., 2012. Electrogenation of disinfection byproducts at a boron-doped diamond anode with resorcinol as a model substance. *Electrochim. Acta* 69, 268–274. <https://doi.org/10.1016/j.electacta.2012.02.098>
- Liu, H., Liu, Y., Zhang, C., Shen, R., 2008. Electrocatalytic oxidation of nitrophenols in aqueous solution using modified PbO<sub>2</sub> electrodes. *J. Appl. Electrochem.* 38, 101–108. <https://doi.org/10.1007/s10800-007-9406-1>

- Martínez-Huitle, C.A., Brillas, E., 2021. A critical review over the electrochemical disinfection of bacteria in synthetic and real wastewaters using a boron-doped diamond anode. *Curr. Opin. Solid State Mater. Sci.* 25, 100926. <https://doi.org/10.1016/j.cossms.2021.100926>
- Martínez-Huitle, C.A., Brillas, E., 2009. Decontamination of wastewaters containing synthetic organic dyes by electrochemical methods: A general review. *Appl. Catal. B Environ.* 87, 105–145. <https://doi.org/10.1016/j.apcatb.2008.09.017>
- Martínez-Huitle, C.A., Ferro, S., 2006. Electrochemical oxidation of organic pollutants for the wastewater treatment: direct and indirect processes. *Chem. Soc. Rev.* 35, 1324–1340. <https://doi.org/10.1039/B517632H>
- Martínez-Huitle, C.A., Panizza, M., 2018. Electrochemical oxidation of organic pollutants for wastewater treatment. *Curr. Opin. Electrochem.* 11, 62–71. <https://doi.org/10.1016/j.coelec.2018.07.010>
- Martínez-Huitle, C.A., Rodrigo, M.A., Sirés, I., Scialdone, O., 2015. Single and Coupled Electrochemical Processes and Reactors for the Abatement of Organic Water Pollutants: A Critical Review. *Chem. Rev.* 115, 13362–13407. <https://doi.org/10.1021/acs.chemrev.5b00361>
- Mousset, E., Oturan, N., Oturan, M.A., 2018. An unprecedented route of  $\cdot\text{OH}$  radical reactivity evidenced by an electrocatalytical process: Ipso-substitution with perhalogenocarbon compounds. *Appl. Catal. B Environ.* 226, 135–146. <https://doi.org/10.1016/j.apcatb.2017.12.028>
- Muñoz-Morales, M., Sáez, C., Cañizares, P., Rodrigo, M.A., 2019. A new electrochemically-based process for the removal of perchloroethylene from gaseous effluents. *Chem. Eng. J.* 361, 609–614. <https://doi.org/10.1016/j.cej.2018.12.119>
- Norra, G.-F., Radjenovic, J., 2021. Removal of persistent organic contaminants from wastewater using a hybrid electrochemical-granular activated carbon (GAC) system. *J. Hazard. Mater.* 415, 125557. <https://doi.org/10.1016/j.jhazmat.2021.125557>
- Oturan, M.A., 2021. Outstanding performances of the BDD film anode in electro-Fenton process: Applications and comparative performance. *Curr. Opin. Solid State Mater. Sci.* 25, 100925. <https://doi.org/10.1016/j.cossms.2021.100925>
- Oturan, M.A., Aaron, J.-J., 2014. Advanced Oxidation Processes in Water/Wastewater Treatment: Principles and Applications. A Review. *Crit. Rev. Environ. Sci. Technol.* 44, 2577–2641. <https://doi.org/10.1080/10643389.2013.829765>

- Oturan, N., Bo, J., Trelu, C., Oturan, M.A., 2021. Comparative Performance of Ten Electrodes in Electro-Fenton Process for Removal of Organic Pollutants from Water. *Chem. Electro. Chem.* 8, 3294–3303. <https://doi.org/10.1002/celec.202100588>
- Panizza, M., Cerisola, G., 2009. Direct And Mediated Anodic Oxidation of Organic Pollutants. *Chem. Rev.* 109, 6541–6569. <https://doi.org/10.1021/cr9001319>
- Panizza, M., Cerisola, G., 2008. Electrochemical Degradation of Methyl Red Using BDD and PbO<sub>2</sub> Anodes. *Ind. Eng. Chem. Res.* 47, 6816–6820. <https://doi.org/10.1021/ie8001292>
- Radjenovic, J., Duinslaeger, N., Avval, S.S., Chaplin, B.P., 2020. Facing the Challenge of Poly- and Perfluoroalkyl Substances in Water: Is Electrochemical Oxidation the Answer? *Environ. Sci. Technol.* 54, 14815–14829. <https://doi.org/10.1021/acs.est.0c06212>
- Rodgers, J.D., Jedral, W., Bunce, N.J., 1999. Electrochemical Oxidation of Chlorinated Phenols. *Environ. Sci. Technol.* 33, 1453–1457. <https://doi.org/10.1021/es9808189>
- Rodrigo, M.A., Cañizares, P., Sánchez-Carretero, A., Sáez, C., 2010. Use of conductive-diamond electrochemical oxidation for wastewater treatment. *Catal. Today* 151, 173–177. <https://doi.org/10.1016/j.cattod.2010.01.058>
- Shannon, M.A., Bohn, P.W., Elimelech, M., Georgiadis, J.G., Mariñas, B.J., Mayes, A.M., 2008. Science and technology for water purification in the coming decades. *Nature* 452, 301–310. <https://doi.org/10.1038/nature06599>
- Sirés, I., Brillas, E., Oturan, M.A., Rodrigo, M.A., Panizza, M., 2014. Electrochemical advanced oxidation processes: today and tomorrow. A review. *Environ. Sci. Pollut. Res.* 21, 8336–8367. <https://doi.org/10.1007/s11356-014-2783-1>
- Sopaj, F., Rodrigo, M.A., Oturan, N., Podvorica, F.I., Pinson, J., Oturan, M.A., 2015. Influence of the anode materials on the electrochemical oxidation efficiency. Application to oxidative degradation of the pharmaceutical amoxicillin. *Chem. Eng. J.* 262, 286–294. <https://doi.org/10.1016/j.cej.2014.09.100>
- Stucki, S., Kötz, R., Carcer, B., Suter, W., 1991. Electrochemical waste water treatment using high overvoltage anodes Part II: Anode performance and applications. *J. Appl. Electrochem.* 21, 99–104. <https://doi.org/10.1007/BF01464288>
- Trasatti, S., 1987. Progress in the understanding of the mechanism of chlorine evolution at oxide electrodes.

- Electrochim. Acta 32, 369–382. [https://doi.org/10.1016/0013-4686\(87\)85001-6](https://doi.org/10.1016/0013-4686(87)85001-6)
- Trellu, C., Chaplin, B.P., Coetsier, C., Esmilaire, R., Cerneaux, S., Causserand, C., Cretin, M., 2018. Electro-oxidation of organic pollutants by reactive electrochemical membranes. *Chemosphere* 208, 159–175. <https://doi.org/10.1016/j.chemosphere.2018.05.026>
- Trellu, C., Ganzenko, O., Papirio, S., Pechaud, Y., Oturan, N., Huguenot, D., van Hullebusch, E.D., Esposito, G., Oturan, M.A., 2016. Combination of anodic oxidation and biological treatment for the removal of phenanthrene and Tween 80 from soil washing solution. *Chem. Eng. J.* 306, 588–596. <https://doi.org/10.1016/j.cej.2016.07.108>
- U.S. EPA, 2008. Interim Drinking Water Health Advisory for perchlorate EPA 822-R-08-025, Washington, DC.
- Wang, H., Mi, X., Li, Y., Zhan, S., 2020. 3D Graphene-Based Macrostructures for Water Treatment. *Adv. Mater.* 32, 1806843. <https://doi.org/10.1002/adma.201806843>
- WHO., 2014. Progress on drinking water and sanitation: 2014 Update. World Health Organization, Geneva, Switzerland.
- Xu, L., Niu, J., Xie, H., Ma, X., Zhu, Y., Crittenden, J., 2021. Effective degradation of aqueous carbamazepine on a novel blue-colored TiO<sub>2</sub> nanotube arrays membrane filter anode. *J. Hazard. Mater.* 402, 123530. <https://doi.org/10.1016/j.jhazmat.2020.123530>
- Xu, R., Xie, Y., Tian, J., Chen, L., 2021. Adsorbable organic halogens in contaminated water environment: A review of sources and removal technologies. *J. Clean. Prod.* 283, 124645. <https://doi.org/10.1016/j.jclepro.2020.124645>
- Zaky, A.M., Chaplin, B.P., 2014. Mechanism of p-Substituted Phenol Oxidation at a Ti<sub>4</sub>O<sub>7</sub> Reactive Electrochemical Membrane. *Environ. Sci. Technol.* 48, 5857–5867. <https://doi.org/10.1021/es5010472>
- Zhao, G., Zhang, Y., Lei, Y., Lv, B., Gao, J., Zhang, Y., Li, D., 2010. Fabrication and Electrochemical Treatment Application of A Novel Lead Dioxide Anode with Superhydrophobic Surfaces, High Oxygen Evolution Potential, and Oxidation Capability. *Environ. Sci. Technol.* 44, 1754–1759. <https://doi.org/10.1021/es902336d>
- Zhu, X., Ni, J., Lai, P., 2009. Advanced treatment of biologically pretreated coking wastewater by electrochemical oxidation using boron-doped diamond electrodes. *Water Res.* 43, 4347–4355.

<https://doi.org/10.1016/j.watres.2009.06.030>

Zhuo, Q., Deng, S., Yang, B., Huang, J., Yu, G., 2011. Efficient Electrochemical Oxidation of Perfluorooctanoate Using a Ti/SnO<sub>2</sub>-Sb-Bi Anode. *Environ. Sci. Technol.* 45, 2973–2979.

<https://doi.org/10.1021/es1024542>

## **Chapter II**

### **Literature Review**

## 1. Focus on the state of the art related to $TiO_x$ materials for the anodic oxidation process

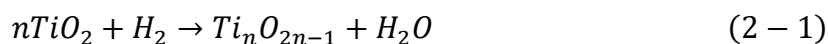
Sub-stoichiometric  $TiO_2$ , indicated as  $TiO_x$  with formula of  $Ti_nO_{2n-1}$  ( $4 \leq n \leq 6$ ), also called Magnéli phase, has been a popular research topic due to the wide availability of Ti on Earth, material's high conductivity, high resistance to corrosion and chemical inertness. The application of  $TiO_x$  materials have been studied widely in environmental remediation, especially as anode material in anodic oxidation (AO) process. Different methods have been developed to obtain  $TiO_x$  electrodes with higher stability, preferable chemical composition and suitable structure (e.g., powders, rods, porous and dense electrodes) to adapt to different reactors and applications.

### 1.1 Synthesis of $TiO_x$ electrodes

#### 1.1.1 Reduction of $TiO_2$

Reduction of  $TiO_2$  is the most common  $TiO_x$  synthesis method. Rutile and anatase  $TiO_2$  is generally used as precursor and their reduction can be accomplished by hydrogen reduction, carbothermal reduction or metallothermic reduction.

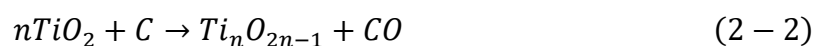
The mechanism of  $TiO_2$  reduction using hydrogen gas as reducing agent can be expressed as:



Lin et al. (2018) reported the synthesis of microporous  $Ti_4O_7$  electrodes by hydrogen reduction (Lin et al., 2018). Nano  $TiO_2$  powders were reduced under hydrogen atmosphere at 950 °C, then the obtained  $Ti_4O_7$  nano powders were mixed with a binder, spray-dried and then pressed into a ceramic preform and sintered at 1350 °C under vacuum for 11 h. The reduction temperature and time are critical factors determining the chemical composition of  $TiO_x$ , and they can be controlled to obtain a certain phase or a mixture of different phases (Geng et al., 2015). Guo et al. (2016) showed that with a reduction temperature of 1050 °C, longer reduction time led to higher portion of more reduced Magnéli phase (Guo et al., 2016).

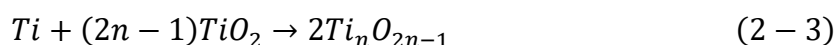
The study of Geng et al. (2015) also showed that temperature control is crucial for reduction from  $TiO_2$  to  $Ti_4O_7$ . By controlling reduction time, pure Magnéli  $Ti_4O_7$ , a mixture of Magnéli phases (shorter reduction time) or a mixture of Magnéli/non-Magnéli phases (longer reduction time) was obtained (Geng et al., 2015).

The mechanism of carbothermal reduction of  $TiO_2$  is summarized in Eq. 2-2:



In the carbothermal reduction process, organic polymer and carbon black are most commonly used as reducing agents. The reduction temperature and ratio between carbon and  $TiO_2$  have a great impact on  $TiO_x$  phases and properties. Under optimized conditions, pure  $Ti_4O_7$  phase can be obtained (Zhu et al., 2013). Wang et al. (2017) fabricated electrodes with high purity of  $Ti_4O_7$  by carbothermal reduction from molten salt and solid-state resources (Wang et al., 2017). Both resources were a mixture of  $TiO_2$  and carbon (NaCl was also added in molten salt). The resources were milled, dried and heated under argon atmosphere for 120 min at 850 - 1000 °C for molten salt and 900 - 1200 °C for solid-state resource.

Metals like metallic titanium, sodium, calcium, aluminum and silicon can also be used as reducing agents for  $TiO_2$  (Xu et al., 2016):



By controlling the ratio of metal/ $TiO_2$ , ideal phase of  $TiO_x$  can also be obtained. For example, He et al. (2015) synthesized  $Ti_8O_{15}$  nanowire on a Ti foil (He et al., 2015).  $TiO_2$  powders were put in a boat and placed in a tube of a conventional furnace while the polished Ti substrate was placed 6 cm away. The system was flushed by  $N_2$  for several times to remove oxygen and moisture and then was heated by increasing the temperature from 8 °C to 1050 °C and kept for 2 h under a hydrogen flow.  $Ti_8O_{15}$  nanowires were then observed on the surface of Ti substrate.

It is important to notice that this section does not provide an exhaustive overview of all synthesis methods. Many other studies have developed alternative methods for  $TiO_2$  reduction.



### 1.1.2 Oxidation of organotitanium and inorganotitanium chemicals

Other sources of Ti other than  $\text{TiO}_2$  (e.g., metallic titanium and  $\text{Ti}(\text{OC}_4\text{H}_9)_4$ ) were also used as precursor for  $\text{TiO}_x$  synthesis.

Qing et al. (2021) successfully synthesized  $\text{Ti}_4\text{O}_7$  nanoparticles from a mixture of  $\text{TiCl}_3/\text{TiF}_4$  by a hydrothermal and calcination processes (Qing et al., 2021).  $\text{TiCl}_3$  and  $\text{TiF}_4$  were mixed in anhydrous alcohol, stirred and kept in a Teflon autoclave at  $180\text{ }^\circ\text{C}$  for 12 h. Then the precipitates were washed and dried in a vacuum oven to obtain powders and these powders were annealed under hydrogen atmosphere at  $850\text{ }^\circ\text{C}$  for 2 h to obtain  $\text{Ti}_4\text{O}_7$  nanoparticles.

Yao and co-workers (2017) also used  $\text{Ti}(\text{OC}_4\text{H}_9)_4$  as titania precursor for synthesis of  $\text{Ti}_4\text{O}_7$  (Yao et al., 2017).  $\text{Ti}(\text{OC}_4\text{H}_9)_4$  was dissolved and mixed with  $\text{HNO}_3$  to produce  $\text{TiO}(\text{NO}_3)_2$ . The  $\text{TiO}(\text{NO}_3)_2$  precursor was washed, dried and annealed in a hydrogen atmosphere at  $1000\text{ }^\circ\text{C}$  for 6 h.

### 1.1.3 Fabrication of blue $\text{TiO}_2$

Blue  $\text{TiO}_2$  nanotube arrays (BNTA) have also attracted much attention due to their low cost, easy preparation and excellent performances. Xu et al. (2021) reported successfully BNTA synthesis by the following method: a porous Ti plate was first cleaned and then anodized at a constant voltage of 40 V for 8 h using an ethylene glycol electrolyte consisting of 0.3%  $\text{NH}_4\text{F}$  and 5% ultrapure water. Two Ti plates were used as cathodes. The anodizing process was followed by annealing at  $450\text{ }^\circ\text{C}$  for 2 h and then the reducing process was conducted at constant current density of  $3\text{ mA cm}^{-2}$  in 0.1 M  $(\text{NH}_4)_2\text{SO}_4$  for 10 min (Xu et al., 2021).

### 1.1.4 Synthesis of porous $\text{TiO}_x$ for application in flow-through configurations

Porous  $\text{TiO}_x$  materials applied in flow-through configuration have been often named as reactive electrochemical membrane (REM) when pore size is sufficiently low to consider that

the material may act as a membrane. The synthesis of  $\text{TiO}_x$  REM reported in the literature generally included 3 steps: (i)  $\text{TiO}_2$  reduction, (ii) shaping and (iii) sintering. Based on these three steps, two synthesis processes have been reported.

Firstly,  $\text{TiO}_2$  slurry was mixed with organic binders (e.g., polyvinyl alcohol, polyacrylamide and polyvinylidene fluoride), followed by shape forming using an extrusion die with mechanical press to form  $\text{TiO}_2$  pellets, and then the  $\text{TiO}_2$  pellets were sintered to form porous structure and remove the binders (You et al., 2016).

Secondly,  $\text{TiO}_2$  powders were first reduced to  $\text{TiO}_x$  powders by hydrogen reduction. Then, the obtained  $\text{TiO}_x$  powders were mixed with organic binders and shaped using an extrusion die and followed by sintering under hydrogen atmosphere (Liang et al., 2018; Nayak and Chaplin, 2018; Almassi et al., 2019; Lin et al., 2020).

Another synthesis method is also based on the use of commercial tubular  $\text{TiO}_2$  membranes, which are used for hydrogen reduction to obtain directly tubular  $\text{TiO}_x$  electrodes (Hua et al., 2020). Some studies also reported REM synthesis from carbothermal reduction of  $\text{TiO}_2$  pellets (Trellu et al., 2018).

### **1.1.5 Addition of doping agents in $\text{TiO}_x$ electrodes**

The objective is to synthesize electrode materials able to maximize hydroxyl radicals ( $\cdot\text{OH}$ ) generation rate and reaction sites and decrease charge transfer resistance. Many studies have used dopants to solve these problems and improve the performance of  $\text{TiO}_x$  electrodes (Almassi et al., 2019; Martinez-Oviedo et al., 2019; Lin et al., 2021; Liu et al., 2021; Feng et al., 2022; Li et al., 2022a).

Carbonaceous materials, metals and nonmetal elements (e.g., fluorine) have been demonstrated to be effective dopants. Generally, the dopant was mixed with  $\text{TiO}_x$  powders in polyvinyl alcohol (PVA)/acetone/ethanol, well dispersed and stirred to obtain a slurry. Then the slurry was dried in vacuum and subsequently sintered to obtain doped  $\text{TiO}_x$  electrode (Lin et al., 2021; Feng et al., 2022; Li et al., 2022b).

## 1.2 Application of TiO<sub>x</sub> electrodes in AO

TiO<sub>x</sub> materials have been widely studied in AO for wastewater treatment applications, e.g., decontamination of pesticides, phenolic compounds, perfluorooctanoate (PFOA)/perfluorooctanesulfonate (PFOS), organic dyes, landfill leachates and so on. Different factors can have a significant impact on process efficiency, including the nature of the anode material (chemical composition and physical structure), operating conditions (reactor configuration, current density) and nature of the treated water. An overview of the existing studies is provided in [Table 2-1](#).

Ti<sub>4</sub>O<sub>7</sub> is the preferred Magnéli phase because it has the greatest conductivity and was reported as the most efficient phase for <sup>•</sup>OH generation (Guo et al., 2016; Zhao et al., 2022). The presence of other phases might weaken the conductivity and electrochemical reactivity of TiO<sub>x</sub> electrodes. For example, REM with pure Ti<sub>4</sub>O<sub>7</sub> phase showed higher conductivity (1132 S m<sup>-1</sup>) than the mixture of Ti<sub>4</sub>O<sub>7</sub> and Ti<sub>6</sub>O<sub>11</sub> (221 S m<sup>-1</sup>) or the pure Ti<sub>6</sub>O<sub>11</sub> phase (56.6 S m<sup>-1</sup>). REM with pure Ti<sub>4</sub>O<sub>7</sub> phase also achieved 62.4% removal of coumarin (probe molecule for <sup>•</sup>OH-mediated oxidation), while no coumarin removal was observed with Ti<sub>6</sub>O<sub>11</sub> or Ti<sub>4</sub>O<sub>7</sub>/Ti<sub>6</sub>O<sub>11</sub>, indicating the lower reactivity of these phases for <sup>•</sup>OH generation (Guo et al., 2016). The study of Geng et al. (2015) also showed that pure Ti<sub>4</sub>O<sub>7</sub> nanotube arrays (NTA) exhibited faster degradation kinetic of phenol than Ti<sub>3</sub>O<sub>5</sub>/Ti<sub>4</sub>O<sub>7</sub> NTA or Ti<sub>4</sub>O<sub>7</sub>/Ti<sub>5</sub>O<sub>9</sub>/Ti<sub>6</sub>O<sub>11</sub> NTA (Geng et al., 2015). The use of doping agents might also be an efficient mean to enhance the reactivity of TiO<sub>x</sub> anodes. Li et al. (2022) used graphene oxide nanoparticles (GON) as dopant and observed that Ti<sub>4</sub>O<sub>7</sub> membrane with 1 wt% GON doping decreased electrode's impedance, enhanced electrode's stability and reactivity for both direct electron transfer (DET) and <sup>•</sup>OH-mediated oxidation and obtained faster degradation rate constant of 1,4-dioxane (Li et al., 2022b). Ti<sub>4</sub>O<sub>7</sub> electrode doped by Ce<sup>3+</sup> led to the formation of extra superficial oxygen vacancies and resulted in more efficient charge transfer and further production of <sup>•</sup>OH (Lin et al., 2021). Feng et al. (2022) revealed that doping with V also enhanced electron transfer as well as improved oxygen evolution potential (OEP). Moreover, the presence of redox couple V<sup>3+</sup>/V<sup>4+</sup> and V<sup>4+</sup>/V<sup>5+</sup> increased the amount of active sites for

peroxydisulfate activation (Feng et al., 2022). Almassi et al. (2020) also doped  $Ti_4O_7$  electrode with carbonaceous materials and observed a higher electroactive surface area (EASA) as well as an enhanced reaction rate (Almassi et al., 2020).

Reactor configuration and operating conditions are other critical factors for the efficiency of the AO process using  $TiO_x$  electrodes. Due to the existence of a thick diffusion boundary layer at the anode surface, mass transfer of molecules from bulk to anode surface is strongly limited in stirred-tank and flow-by configurations. Thus, for the treatment of low molecule concentrations, the limiting current density is very low (Eq. 1-29). In conventional stirred-tank reactors, mass transfer conditions can be improved by increasing the stirring rate but the improvement is limited because of the nature of the reactor that avoid to control hydrodynamic conditions in the vicinity of the electrode. Conventional flow-by reactors also suffer from the diffusion boundary layer and Taylor dispersion, as well as low residence time requiring high recirculation rate. The application of porous electrodes in flow-through reactors has offered a more efficient way to improve mass transfer conditions. Porous electrodes usually present pore size that is smaller than the thickness of the diffusion layer in stirred-tank / flow-by reactors. Thus, fast radial diffusion within pores strongly improved mass transport conditions (Trellu et al., 2020). Moreover, convection through the electrodes can be simply enhanced by increasing the filtration flow rate. It results in much higher mass transfer rate (higher  $k_m$ ) and limiting current density (Eq. 1-29). Shi and co-workers (2019) implemented a tubular Ebonex electrode (with a median pore diameter of  $1.12 \mu m$  (as regards to pore volume)) in both stirred-tank and flow-through reactors. The EASA of the electrode measured in flow-through reactor was 4.4 times higher than in stirred-tank reactor (using the method of voltammetric charge measurement). The mass transfer rate constant (measured by limiting current technique) of PFOS was also observed to be improved from  $2.56 \times 10^{-6} m s^{-1}$  in stirred-tank reactor to  $6.21 \times 10^{-6} m s^{-1}$  in flow-through reactor. The cross-flow filtration mode achieved 98.3% of PFOS removal with one single pass (at  $J = 45.6 L h^{-1} m^{-2}$ ), while the batch mode required 100 min to achieve 99.1% of PFOS removal (Shi et al., 2019). Xu et al. (2021) also compared the effectiveness of carbamazepine removal by blue  $TiO_2$  NTA in flow-by and flow-through reactors. Results showed that with the same recirculation condition,

flow-through reactor achieved 99% of removal efficiency in 15 min (with rate constant of  $0.345 \text{ min}^{-1}$ ) and flow-by mode achieved only 16% of removal efficiency with rate constant of only  $0.009 \text{ min}^{-1}$  (Xu et al., 2021). Application in flow-through configuration is the key strategy to really take advantage of the higher EASA of porous materials, owing to improved mass transfer conditions.

In addition, operating parameters like current density and filtration flow rate in flow-through mode can also affect the efficiency of the process. High current density promotes faster degradation kinetic and removal rate of pollutants but leads to the decrease of current efficiency when it exceeds the limiting current density. Increasing the filtration flow rate promotes convection-enhanced mass transfer in flow-through mode and improve the effectiveness of the process. However, high flow rate also leads to a decrease of efficiency because of shorter residence time and enhanced OER by continuously sweeping away  $\text{O}_2$  bubbles generated at the electrode surface (Guo et al., 2016).

Table 2-1 Summary of characteristics and application of TiO<sub>x</sub> electrodes in anodic oxidation

Anode	Fabrication method	Anode composition	Pore size	Specific surface area (m <sup>2</sup> g <sup>-1</sup> )	OEP	Conductivity (resistance)	$\frac{S_{anod}}{V_{sol}}$ (m <sup>-1</sup> )	cathode	Configuration (working mode)	Flow rate	j (mA cm <sup>-2</sup> )	electrolyte	pollutant	Degradation rate	Degradation rate constant	TOC (or COD) removal	ref
Tubular TiO <sub>x</sub>	Obtained commercially	Ti <sub>4</sub> O <sub>7</sub> , Ti <sub>5</sub> O <sub>9</sub> , Ti <sub>9</sub> O <sub>17</sub>	0.2-2 μm		2.6 V/SHE	900-1050 S cm <sup>-1</sup>		Stainless steel	Tubular electrode assembly reactor (continuous flow)	90 min (residence time)	9	0.5 M Na <sub>2</sub> SO <sub>4</sub>	Methylene blue (50 mg L <sup>-1</sup> )	98.35% (3 h) (discoloration)		35.51% (3 h)	(Liang et al., 2021)
Ti/Ti <sub>4</sub> O <sub>7</sub> plate	Ti/Ti <sub>4</sub> O <sub>7</sub> was obtained from plasma spraying	High purity Ti <sub>4</sub> O <sub>7</sub>					83.3	Ti plate	Stirred-tank (batch)		10	50 mM Na <sub>2</sub> SO <sub>4</sub>	PFOA (0.12 mM)		0.41 ± 0.02 h <sup>-1</sup>		(Huang et al., 2020)
Amorphous Pd-Ti/Ti <sub>4</sub> O <sub>7</sub> plate															2.02 ± 0.02 h <sup>-1</sup>		
Crystalline Pd-Ti/Ti <sub>4</sub> O <sub>7</sub>															0.6 ± 0.02 h <sup>-1</sup>		
Ti <sub>4</sub> O <sub>7</sub>	Hydrogen reduction from TiO <sub>2</sub>	Pure TiO <sub>2</sub>		6.1901 (BET)	2.14 V/SCE			Ti	Undivided cylindrical reactor (batch)		10	20 mM Na <sub>2</sub> SO <sub>4</sub>	Ciprofloxacin (10 mg L <sup>-1</sup> )	44.47% (1 h)		(Feng et al., 2022)	
V@Ti <sub>4</sub> O <sub>7</sub>				11.7593 (BET)	2.28 V/SCE									67.19% (with persulfate)			58.29% (1 h)

Chapter II Literature Review

Anode	Fabrication method	Anode composition	Pore size	Specific surface area (m <sup>2</sup> g <sup>-1</sup> )	OEP	Conductivity (resistance)	$S_{anod}$ $e/V_{sol}$ ution (m <sup>-1</sup> )	cathode	Configurati on (working mode)	Flow rate	j (mA cm <sup>-2</sup> )	electrolyte	pollutant	Degradation rate	Degradation rate constant	TOC (or COD) removal	ref			
Ti/Ti <sub>4</sub> O <sub>7</sub>	Plasma spraying	Ti <sub>4</sub> O <sub>7</sub> , TiO <sub>2</sub>			2.30 V/SCE		66.6 7	Ti plate	Undivided acrylic reactor (batch)		10	0.1 M NaClO <sub>4</sub>	Coal chemical concentrated brine			~56% (1 h)	(Wang et al., 2021)			
Ti/Ti <sub>4</sub> O <sub>7</sub> NTA	Anodizing-annealing-ca thodizing	Ti <sub>4</sub> O <sub>7</sub> , TiO <sub>2</sub> , Ti			2.44 V/SCE															
Ti/Ti <sub>4</sub> O <sub>7</sub>	Plasma spraying	Ti <sub>4</sub> O <sub>7</sub> , TiO <sub>2</sub>			2.30 V/SCE								4			p-nitrophenol (50 mg L <sup>-1</sup> )		~88% (0.5 h)	0.0762 min <sup>-1</sup>	~70% (1 h)
Ti/Ti <sub>4</sub> O <sub>7</sub> NTA	Anodizing-annealing-ca thodizing	Ti <sub>4</sub> O <sub>7</sub> , TiO <sub>2</sub> , Ti			2.44 V/SCE													~90% (0.5 h)	0.091 min <sup>-1</sup>	~72% (1 h)
Ti <sub>4</sub> O <sub>7</sub>	Sparking plasma sintering	High purity Ti <sub>4</sub> O <sub>7</sub>	28.8 μm (medium)	11.9 (raw Ti <sub>4</sub> O <sub>7</sub> powders)	2.2 V/SCE			Stainless steel	Flow-by (recirculatio n)	80 mL min <sup>-1</sup>	20	0.1 M NaClO <sub>4</sub>	PFOS (20 μM)	86.2% (2 h)	0.015 ± 0.001 min <sup>-1</sup>		(Lin et al., 2021)			
Ce <sup>3+</sup> doped Ti <sub>4</sub> O <sub>7</sub>				(raw Ti <sub>4</sub> O <sub>7</sub> powders)	(BET)															
Ebonex		Ti <sub>9</sub> O <sub>17</sub> , Ti <sub>6</sub> O <sub>11</sub> , TiO <sub>2</sub>	1.12 μm (median)	0.193 (Hg porosimetry)		43.3 ± 4.2 S m <sup>-1</sup>		Stainless steel	Flow-throug h reactor (cross flow filtration)	40 mL min <sup>-1</sup> (permeate flow rate: 0.079 cm min <sup>-1</sup> )	4	100 mM Na <sub>2</sub> SO <sub>4</sub>	PFOS (2 μM)	98.3%			(Shi et al., 2019)			

Anode	Fabrication method	Anode composition	Pore size	Specific surface area (m <sup>2</sup> g <sup>-1</sup> )	OEP	Conductivity (resistance)	$S_{anod}$ $e/V_{sol}$ ution (m <sup>-1</sup> )	cathode	Configurati on (working mode)	Flow rate	j (mA cm <sup>-2</sup> )	electrolyte	pollutant	Degradation rate	Degradation rate constant	TOC (or COD) removal	ref
Ti <sub>4</sub> O <sub>7</sub>	Hydrogen reduction from TiO <sub>2</sub>	Pure Ti <sub>4</sub> O <sub>7</sub>	2.99 μm (median)	0.658 (Hg porosimetry)		1132 S m <sup>-1</sup>		Stainless steel	Flow-throug h (cross flow filtration)	793 LMH	2.94 V/Ag/ AgCl	100 mM NaClO <sub>4</sub>	Oxalic acid (1 mM)	401.5 ± 18.1 mmol h <sup>-1</sup> m <sup>-2</sup>			(Guo et al., 2016)
										116 LMH	2.64 V/Ag/ AgCl		Terephthalic acid (0.1 mM)	57.8%			
Ti <sub>4</sub> O <sub>7</sub>	Hydrogen reduction from TiO <sub>2</sub>	High purity Ti <sub>4</sub> O <sub>7</sub>	3.6 μm (median)	0.12 (Hg porosimetry)		2.4×10 <sup>-3</sup> Ω cm		Stainless steel	Stirred-tank reactor (batch)		5	20 mM NaClO <sub>4</sub>	PFOA (0.5 mM)	>99.9% (3 h)	(3.4 ± 0.11) × 10 <sup>-2</sup>		(Lin et al., 2018)
														PFOS (0.1 mM)	93.1% (3 h)	(1.3 ± 0.055) × 10 <sup>-2</sup>	
Blue TiO <sub>2</sub> NTA	Anodizing-annealing-ca thodizing	anatase TiO <sub>2</sub> , Ti <sub>4</sub> O <sub>7</sub> , Ti <sub>5</sub> O <sub>9</sub>	45.4 μm (median)	2.01 (BET)				blue TiO <sub>2</sub> NTA	Flow-throug h (recirculatio n)	240 mL min <sup>-1</sup>	2	10 mM Na <sub>2</sub> SO <sub>4</sub>	carbamazepine (10 mg L <sup>-1</sup> )	99% (15 min)	0.345 min <sup>-1</sup>		(Xu et al., 2021)
									Flow-by (recirculatio n)							16% (20 min)	
Ti <sub>4</sub> O <sub>7</sub>	hydrogen reduction of TiO <sub>2</sub>	high purity Ti <sub>4</sub> O <sub>7</sub>	3.6 μm (median)					39	stainless steel	undivided stirred-tank (batch)		10	100 mM Na <sub>2</sub> SO <sub>4</sub>	PFOS (2 uM)	~98.6% (20 min)		(Wang et al., 2020)



Chapter II Literature Review

Anode	Fabrication method	Anode composition	Pore size	Specific surface area (m <sup>2</sup> g <sup>-1</sup> )	OEP	Conductivity (resistance)	$S_{anod}$ $e/V_{sol}$ ution (m <sup>-1</sup> )	cathode	Configurati on (working mode)	Flow rate	j (mA cm <sup>-2</sup> )	electrolyte	pollutant	Degradation rate	Degradation rate constant	TOC (or COD) removal	ref
Ti <sub>4</sub> O <sub>7</sub>							10.4	Carbon felt	Undivided stirred-tank (batch)		5	0.05 M Na <sub>2</sub> SO <sub>4</sub>	Paracetamol (0.2 mM)	~100% (2 h)		81% (8 h)	(Ganiyu et al., 2019)
Ti <sub>4</sub> O <sub>7</sub>	Hydrogen reduction from TiO <sub>2</sub>	High purity Ti <sub>4</sub> O <sub>7</sub>	2.6 (average)		2.3 V/SCE		40	Stainless steel	Stirred-tank (batch)		0.5	100 mM Na <sub>2</sub> SO <sub>4</sub>	tetracycline (10 ppm)	75.2% (2 h)	1.05 * 10 <sup>-2</sup> min <sup>-1</sup>	27.5% (2 h)	(Liang et al., 2018)
Ti <sub>4</sub> O <sub>7</sub>	spark plasma sintering from Ti <sub>4</sub> O <sub>7</sub> powders	Ti <sub>4</sub> O <sub>7</sub> , Ti <sub>5</sub> O <sub>9</sub>				833.3 S cm <sup>-1</sup> (1.2 mΩ cm)	10.9	Ti mesh	Stirred-tank (batch)		9.86	0.1 M NaCl	methyl orange (100 mg L <sup>-1</sup> )	97.7% (2 h) (discoloration)		35.9% (2 h) (COD)	(He et al., 2018)
Ti <sub>4</sub> O <sub>7</sub>	carbothermal reduction +spark plasma sintering	Ti <sub>4</sub> O <sub>7</sub> , Ti <sub>5</sub> O <sub>9</sub>			2.2 V/SCE	961.5 S cm <sup>-1</sup>		Ti mesh	undivided stirred-tank (batch)		10	0.01 M NaCl	methyl orange (150 mg L <sup>-1</sup> )	98.2% (0.5 h) (discoloration)	4.2 * 10 <sup>-3</sup> min <sup>-1</sup> (COD)	74% (5 h) (COD)	(Wang et al., 2020)
Ti <sub>4</sub> O <sub>7</sub>		high purity Ti <sub>4</sub> O <sub>7</sub>	3.6 um (median)				37.5	stainless steel	undivided stirred-tank (batch)		10	100 mM Na <sub>2</sub> SO <sub>4</sub>	PFOS (2 μM)	75% (0.5 h)	0.0471 min <sup>-1</sup>		(Yang et al., 2020)
Ti <sub>4</sub> O <sub>7</sub>	Hydrogen reduction from TiO <sub>2</sub>	Ti <sub>4</sub> O <sub>7</sub> , Ti <sub>5</sub> O <sub>9</sub>		0.19 (BET)	1.56 V/SHE		11.6	Stainless steel	Flow-through (recirculation)	0 mL cm <sup>-2</sup> s <sup>-1</sup> 0.023 mL cm <sup>-2</sup> s <sup>-1</sup>	5	0.04 M Na <sub>2</sub> SO <sub>4</sub>	4-chlorophenol (20 mg L <sup>-1</sup> ) industrial wastewater (4-chlorophenol of 20-30 mg L <sup>-1</sup> )	40.4% (2 h)		63.10% (TOC), 67.40% (COD)	(Zhao et al., 2022)

Chapter II Literature Review

Anode	Fabrication method	Anode composition	Pore size	Specific surface area (m <sup>2</sup> g <sup>-1</sup> )	OEP	Conductivity (resistance)	$S_{anod}$ $e/V_{sol}$ ution (m <sup>-1</sup> )	cathode	Configurati on (working mode)	Flow rate	j (mA cm <sup>-2</sup> )	electrolyte	pollutant	Degradation rate	Degradation rate constant	TOC (or COD) removal	ref
Ti/Ti <sub>4</sub> O <sub>7</sub>	Plasma spraying							Ti	Undivided stirred-tank (batch)		8	30 mM Na <sub>2</sub> SO <sub>4</sub>	4-chlorophenol (20 mg L <sup>-1</sup> )	100% (2 h)		50.3% (1 h) (TOC), 78.7% (1 h) (COD)	(Zhi et al., 2020)
													coal gasification wastewater		54.8% (1 h) (TOC), 85.8% (1 h) (COD)		
Ti <sub>4</sub> O <sub>7</sub>		High purity Ti <sub>4</sub> O <sub>7</sub>	0.54 μm (average)	4.4 (Hg porosimetry)		737 S m <sup>-1</sup>		Stainless steel	Flow-throug h	720 LMH	2.9 V/SHE	100 mM K <sub>2</sub> HPO <sub>4</sub>	PFOA (10 μM)	3415 ±203 μmol m <sup>-2</sup> h <sup>-1</sup>	607 h <sup>-1</sup>		(Le et al., 2019)
													PFOS (10 μM)	2436±106 μmol m <sup>-2</sup> h <sup>-1</sup>	210 h <sup>-1</sup>		
Blue TiO <sub>2</sub> NTA	Electrochemical reduction	Anatase TiO <sub>2</sub>						Stainless steel	Undivided stirred-tank (batch)		2.5	30 mM persulfate	2,4-dichloropheno xyacetic (20 mg L <sup>-1</sup> )	100% (1 h)	4.17 h <sup>-1</sup>		(Cai et al., 2021)

Chapter II Literature Review

Anode	Fabrication method	Anode composition	Pore size	Specific surface area (m <sup>2</sup> g <sup>-1</sup> )	OEP	Conductivity (resistance)	S <sub>anod</sub> / V <sub>sol</sub> / ution (m <sup>-1</sup> )	cathode	Configurati on (working mode)	Flow rate	j (mA cm <sup>-2</sup> )	electrolyte	pollutant	Degradation rate	Degradation rate constant	TOC (or COD) removal	ref
Ti <sub>4</sub> O <sub>7</sub>	Hydrogen reduction+plasma spraying	Ti <sub>4</sub> O <sub>7</sub>			2.6 V/SCE			Ti	Undivided stirred-tank (batch)		15	30 mM Na <sub>2</sub> SO <sub>4</sub>	tetracycline (5 mg L <sup>-1</sup> )	95.8% (40 min)	(8.2 ± 0.3) * 10 <sup>-2</sup> min <sup>-1</sup>		(Wang et al., 2018)
Blue TiO <sub>2</sub> NTA	two-step anodization-annealing-reduction	TiO <sub>2</sub>						Stainless steel	Undivided stirred-tank (batch)		2.5	0.1 M Na <sub>2</sub> SO <sub>4</sub>	phenol (100 mg L <sup>-1</sup> )	87% (4 h)	0.0071 min <sup>-1</sup>	5 h: 44% (TOC), 59% (COD)	(Cai et al., 2019)
Ti <sub>4</sub> O <sub>7</sub>	Hydrogen reduction+mechanical pressing	High purity Ti <sub>4</sub> O <sub>7</sub>	0.89 μm (median)	4.4 (Hg porosimetry)		737 S m <sup>-1</sup>		Stainless steel	Flow-throug h	454 LMH	3.16 V/SHE	100 mM NaClO <sub>4</sub>	OA (1 mM)	88.3%		(Nayak and Chaplin, 2018)	
											2.86 V/SHE		TA (0.1 mM)	40.3%			
	Gel casting+sintering+hydrogen reduction		1.4 μm (median)	2.7 (Hg porosimetry)		1349 S m <sup>-1</sup>			656 LMH	3.16 V/SHE		OA (1 mM)	98.10%				
										2.86 V/SHE		TA (0.1 mM)	48.7%				
Ti <sub>4</sub> O <sub>7</sub> NTA		Pure Ti <sub>4</sub> O <sub>7</sub>	80 nm (average)	11.7 (BET)	2.4 V/Ag/Ag Cl		24	Pt	Stirred-tank (batch)		2.5	0.1 M Na <sub>2</sub> SO <sub>4</sub>	phenol (100 mg L <sup>-1</sup> )	>95% (3 h)	0.0148 min <sup>-1</sup>	95.3% (3 h) (COD)	(Geng et al., 2015)

## **2. Active chlorine-mediated oxidation and formation of toxic chlorinated by-products**

Research has shown that many electrodes (dimensionally stable anodes (DSA), Pt, graphite and boron-doped diamond (BDD)) are able to promote generation of active chlorine (Zhang et al., 2018). By promoting effective active chlorine-mediated oxidation, these electrodes can be applied for water disinfection, oxidation of organic pollutants, removal of ammonia and real wastewater treatment (Zhang et al., 2018; Ferreira de Melo et al., 2020; K. Liu et al., 2021). However, active chlorine-mediated oxidation also brings the concern of toxic by-products formation. The generation of organochlorinated compounds was observed and raised concerns because these organic by-products can be even more toxic than the initial organic pollutants (Panizza and Cerisola, 2003; Martínez-Huitle et al., 2015). Another issue is related to further oxidation of active chlorine to chlorate and perchlorate. Therefore, an important challenge is also related to the evolution and control of the formation of such toxic by-products during the process. In this sub-section, effectiveness of active chlorine-mediated oxidation and the evolution of the formation of toxic chlorinated byproducts during electrolysis are summarized and results obtained with  $\text{TiO}_x$  materials are compared with those obtained with conventional anodes like BDD and DSA electrodes.

### **2.1 Active chlorine-mediated oxidation**

As highlighted in previous sections, the effectiveness of active chlorine-mediated oxidation is highly dependent on the anode material (Tomcsányi et al., 1999; Rahmani et al., 2019). Along with active chlorine generation, side reactions take place during the electrolysis, such as oxygen evolution reaction (OER). Therefore, an anode material with high current efficiency for active chlorine formation should limit the other side reactions. In literatures, metal oxides, especially active anodes, have been proved to achieve active chlorine formation with higher current efficiency (Sirés et al., 2014; Martínez-Huitle et al., 2015).

The evolution of the pH in the bulk and at the electrode surface has an influence on active chlorine-mediated oxidation. This is an important phenomenon to take into consideration since local pH conditions near the anode surface evolves due to the oxygen evolution reaction. It is generally considered that low pH favors active chlorine-mediated oxidation. Moreover, the proportion of the different active chlorine species depends on pH since the predominant compounds are  $\text{Cl}_2$ ,  $\text{HClO}$  and  $\text{ClO}^-$  within the pH range of  $<3$ ,  $3-8$  and  $>8$ , respectively (Ferreira de Melo et al., 2020). Among these three species,  $\text{Cl}_2$  and  $\text{HClO}$  have higher standard potential (1.36 and 1.49 V/SHE for  $\text{Cl}_2$  and  $\text{HClO}$ , respectively) compared to  $\text{ClO}^-$  (0.89 V/SHE) (Martínez-Huitle and Brillas, 2009). Besides,  $\text{HClO}$  and  $\text{ClO}^-$  tend to be further oxidized to form undesired by-products (e.g.,  $\text{ClO}_3^-$  and  $\text{ClO}_4^-$ ).

Other operating conditions such as pH, concentration of chloride, current density and flow rate also have impact on the effectiveness of active chlorine-mediated oxidation (Ferreira de Melo et al., 2020). As described previously, the efficiency of active-chlorine mediated oxidation (in terms of current efficiency) also depends on the comparison of the applied current with the limiting current density. Finally, it is also important to notice that though active chlorine can achieve high oxidation efficiency of organic compounds (de Moura et al., 2014; Martínez-Huitle et al., 2015; Brito et al., 2016), the mineralization rate is generally unsatisfactory (Ferreira de Melo et al., 2020). Active chlorine presents a lower oxidant power compared to  $\cdot\text{OH}$ , which results in more selective oxidation of organic compounds and formation of by-products.

## **2.2 Formation of undesired by-products during active chlorine-mediated oxidation of organic pollutants**

During active chlorine-mediated oxidation of organic pollutants, a complex reaction scheme occurs due to the following reactions that take place simultaneously: (i) OER, (ii) formation of active chlorine; (iii) further oxidation of active chlorine to toxic by-products such as chlorate and perchlorate, (iv) active chlorine-mediated degradation of target pollutants, (v)

reaction of active chlorine with other compounds such as ammonium and (v) reduction of active chlorine at the cathode. Particularly, a competition might occur between reaction of active chloride with organic compounds and further evolution to chlorate and perchlorate. It means that the oxidation of target pollutants might reduce the formation of chlorate/perchlorate (Zhang et al., 2018). The presence of other competitive species (e.g., ammonium) able to react with chlorine and might also reduce the formation of chlorate and perchlorate (Bergmann and Rollin, 2007; Bergmann et al., 2009; Comninellis and Chen, 2010; Jung et al., 2010). Low current density and acidic pH might also participate in lower formation of these compounds.

Without sufficient concentration of competitive species, formation of chlorate/perchlorate might become very important. Chlorate and perchlorate are formed by a chain of oxidation reaction starting from chloride (Eq. 1-15). The oxidation from chlorate to perchlorate is the rate-determining step (Bergmann and Rollin, 2007; Jung et al., 2010). Formation of chlorate and perchlorate constitutes a major drawback for process efficiency since (i) they are considered as toxic compounds and (ii) it consumes electrical energy for oxidation of active chlorine to undesired products.

Some DSA electrodes, which are well-known as efficient electrode for active chlorine generation, also leads to the formation of significant amount of chlorate. However, low perchlorate formation is usually reported (Sánchez-Carretero et al., 2011; Zhang et al., 2018). More significant perchlorate formation was observed at BDD anode by several studies (Bergmann et al., 2009; Sánchez-Carretero et al., 2011). This might be ascribed to the fact that BDD is able to generate large amounts of physisorbed  $\cdot\text{OH}$ , which might be involved in the formation of perchlorate according to Eq. 1-27. For example, complete transformation of 0.1 M NaCl to perchlorate at BDD anode was even observed using high electric charge (200 Ah dm<sup>-3</sup>) (Sánchez-Carretero et al., 2011). Brito et al. (2015) found that  $\text{sp}^3/\text{sp}^2$  ratio of BDD can be a key factor for the formation of  $\text{ClO}_3^-$  and  $\text{ClO}_4^-$ . Higher  $\text{sp}^3$  content would effectively reduce the formation of  $\text{ClO}_3^-$  and  $\text{ClO}_4^-$  (Brilo et al., 2015). These results indicate that surface characteristics might strongly influence these reactions.

Besides, it is also important to take into consideration that reaction of active chlorine with

organic compounds might lead to the formation of toxic chlorinated organic compounds. Formation of halogenated organic compounds (HOCs) has been observed during the treatment of real effluents using both DSA and BDD anodes. In the case of BDD, prolonging the electrolysis time might reduce the accumulation of these compounds due to complete mineralization of the organic load.

### **2.3 Application of TiO<sub>x</sub> electrodes for active chlorine-mediated oxidation**

TiO<sub>x</sub> electrodes have also been studied for active chlorine-mediated oxidation of pollutants. Cai et al. (2021) applied blue TiO<sub>2</sub> NTA anode for degradation of 2,4-dichlorophenoxyacetic acid and observed an enhanced degradation kinetic (from 1.02 to 2.82 h<sup>-1</sup>) with the presence of 5 mM Cl<sup>-</sup> (Cai et al., 2021). The degradation kinetic was further enhanced with higher Cl<sup>-</sup> concentration, indicating that the presence of Cl<sup>-</sup> facilitated the degradation of pollutant by generating active chlorine. Wang and co-workers studied how the presence of Cl<sup>-</sup> impacted the degradation of PFOS by Ti<sub>4</sub>O<sub>7</sub> and BDD anodes (Wang et al., 2020). The results showed that the presence of Cl<sup>-</sup> inhibited the degradation of PFOS on Ti<sub>4</sub>O<sub>7</sub> anode while positive effect was observed on BDD anode. In fact, Cl<sup>•</sup> formation from oxidation of Cl<sup>-</sup> via DET at BDD anode enhanced PFOS degradation, while the oxidation of Cl<sup>-</sup> on Ti<sub>4</sub>O<sub>7</sub> and was in competition with the formation of <sup>•</sup>OH. Meanwhile, less chlorate and perchlorate were formed on Ti<sub>4</sub>O<sub>7</sub>. Lin et al. (2020) also observed less chlorate/perchlorate formation on Ti<sub>4</sub>O<sub>7</sub> than on BDD (Lin et al., 2020). Moreover, less perchlorate formation was observed when resorcinol was added as model pollutant, owing to this competition phenomenon.

## **3. Conclusions**

The AO process is currently a widely studied process owing to its high effectiveness for non-selective oxidation of organic compounds and disinfection. However, further development requires facing several challenges related to the formation of toxic chlorinated

compounds and implementation of suitable reactor configurations for mass transport enhancement during the treatment of low concentration of pollutants. It is the reason why current researches are focused on the development of suitable porous electrode materials as well as optimizing operating conditions of the process. With the merits of high conductivity, low cost, and suitable reactivity,  $\text{TiO}_x$  electrodes have been widely studied during the last decade. These electrodes are most commonly fabricated from reduction of  $\text{TiO}_2$ . By controlling the fabrication parameters (reduction temperature and time), different composition of Magnéli phase can be obtained. Dopants have also been used to enhance the performance of  $\text{TiO}_x$  electrode. Applying porous  $\text{TiO}_x$  electrode in flow-through reactors can greatly enhance process effectiveness, owing to fast radial diffusion with small pores and convection-enhanced mass transport through the electrode. Moreover,  $\text{TiO}_x$  might also participate in active chlorine formation. Therefore, the objective of this thesis is to offer new insights on the influence of the porous structure of different  $\text{TiO}_x$  materials on (i) mass transport conditions in different reactor configurations, (ii) process effectiveness and reaction mechanisms for oxidation of organic compounds, and (iii) active chlorine formation leading to the formation of toxic chlorinated compounds.



## References

- Almassi, S., Li, Z., Xu, W., Pu, C., Zeng, T., Chaplin, B.P., 2019. Simultaneous Adsorption and Electrochemical Reduction of N-Nitrosodimethylamine Using Carbon-Ti<sub>4</sub>O<sub>7</sub> Composite Reactive Electrochemical Membranes. *Environ. Sci. Technol.* 53, 928–937. <https://doi.org/10.1021/acs.est.8b05933>
- Almassi, S., Samonte, P.R.V., Li, Z., Xu, W., Chaplin, B.P., 2020. Mechanistic Investigation of Haloacetic Acid Reduction Using Carbon-Ti<sub>4</sub>O<sub>7</sub> Composite Reactive Electrochemical Membranes. *Environ. Sci. Technol.* 54, 1982–1991. <https://doi.org/10.1021/acs.est.9b06744>
- Bergmann, M.E.H., Rollin, J., 2007. Product and by-product formation in laboratory studies on disinfection electrolysis of water using boron-doped diamond anodes. *Catal. Today* 124, 198–203. <https://doi.org/10.1016/j.cattod.2007.03.038>
- Bergmann, M.E.H., Rollin, J., Iourtchouk, T., 2009. The occurrence of perchlorate during drinking water electrolysis using BDD anodes. *Electrochim. Acta* 54, 2102–2107. <https://doi.org/10.1016/j.electacta.2008.09.040>
- Brito, C. do N., da Silva, D.R., Garcia-Segura, S., de Moura, D.C., Martínez-Huitle, C.A., 2016. Indirect Electrochemical Oxidation of Reactive Blue 19 Dye as a Model Organic Substrate: Role of Anode Material and Oxidants Electrochemically Generated. *J. Electrochem. Soc.* 163, E62–E69. <https://doi.org/10.1149/2.0191603jes>
- Brito, C. do N., de Araújo, D.M., Martínez-Huitle, C.A., Rodrigo, M.A., 2015. Understanding active chlorine species production using boron doped diamond films with lower and higher sp<sup>3</sup>/sp<sup>2</sup> ratio. *Electrochem. Commun.* 55, 34–38. <https://doi.org/10.1016/j.elecom.2015.03.013>
- Cai, J., Zhou, M., Du, X., Xu, X., 2021. Enhanced mechanism of 2,4-dichlorophenoxyacetic acid degradation by electrochemical activation of persulfate on Blue-TiO<sub>2</sub> nanotubes anode. *Sep. Purif. Technol.* 254, 117560. <https://doi.org/10.1016/j.seppur.2020.117560>
- Cai, J., Zhou, M., Pan, Y., Du, X., Lu, X., 2019. Extremely efficient electrochemical degradation of organic pollutants with co-generation of hydroxyl and sulfate radicals on Blue-TiO<sub>2</sub> nanotubes anode. *Appl. Catal. B Environ.* 257, 117902. <https://doi.org/10.1016/j.apcatb.2019.117902>
- Comninellis, C., Chen, G. (Eds.), 2010. *Electrochemistry for the Environment*. Springer New York, New York, NY. <https://doi.org/10.1007/978-0-387-68318-8>

- de Moura, D.C., de Araújo, C.K.C., Zanta, C.L.P.S., Salazar, R., Martínez-Huitle, C.A., 2014. Active chlorine species electrogenerated on  $\text{Ti/Ru}_{0.3}\text{Ti}_{0.7}\text{O}_2$  surface: Electrochemical behavior, concentration determination and their application. *J. Electroanal. Chem.* 731, 145–152. <https://doi.org/10.1016/j.jelechem.2014.08.008>
- Feng, W., Lin, H., Armutlulu, A., Chen, J., Liu, R., Xie, R., Lai, B., 2022. Anodic activation of persulfate by V-mediated  $\text{Ti}_4\text{O}_7$ : Improved stability and ROS generation. *Sep. Purif. Technol.* 299, 121794. <https://doi.org/10.1016/j.seppur.2022.121794>
- Ferreira de Melo, J., Medeiros de Araújo, D., Ribeiro da Silva, D., Martinez Huitle, C.A., Villegas-Guzman, P., 2020. Applicability of Electrochemical Technology for Treating a Real Petrochemical Effluent by Electro-generated Active Chlorine Species. *Int. J. Electrochem. Sci.* 10262–10275. <https://doi.org/10.20964/2020.10.66>
- Ganiyu, S.O., Oturan, N., Raffy, S., Cretin, M., Causserand, C., Oturan, M.A., 2019. Efficiency of plasma elaborated sub-stoichiometric titanium oxide ( $\text{Ti}_4\text{O}_7$ ) ceramic electrode for advanced electrochemical degradation of paracetamol in different electrolyte media. *Sep. Purif. Technol.* 208, 142–152. <https://doi.org/10.1016/j.seppur.2018.03.076>
- Geng, P., Su, J., Miles, C., Comninellis, C., Chen, G., 2015. Highly-Ordered Magnéli  $\text{Ti}_4\text{O}_7$  Nanotube Arrays as Effective Anodic Material for Electro-oxidation. *Electrochim. Acta* 153, 316–324. <https://doi.org/10.1016/j.electacta.2014.11.178>
- Guo, L., Jing, Y., Chaplin, B.P., 2016. Development and Characterization of Ultrafiltration  $\text{TiO}_2$  Magnéli Phase Reactive Electrochemical Membranes. *Environ. Sci. Technol.* 50, 1428–1436. <https://doi.org/10.1021/acs.est.5b04366>
- He, C., Chang, S., Huang, X., Wang, Q., Mei, A., Shen, P.K., 2015. Direct synthesis of pure single-crystalline Magnéli phase  $\text{Ti}_8\text{O}_{15}$  nanowires as conductive carbon-free materials for electrocatalysis. *Nanoscale* 7, 2856–2861. <https://doi.org/10.1039/C4NR05806B>
- He, W., Liu, Y., Ye, J., Wang, G., 2018. Electrochemical degradation of azo dye methyl orange by anodic oxidation on  $\text{Ti}_4\text{O}_7$  electrodes. *J. Mater. Sci. Mater. Electron.* 29, 14065–14072. <https://doi.org/10.1007/s10854-018-9538-6>
- Hua, L., Cao, H., Ma, Q., Shi, X., Zhang, X., Zhang, W., 2020. Microalgae Filtration Using an Electrochemically Reactive Ceramic Membrane: Filtration Performances, Fouling Kinetics, and

- Foulant Layer Characteristics. *Environ. Sci. Technol.* 54, 2012–2021. <https://doi.org/10.1021/acs.est.9b07022>
- Huang, D., Wang, K., Niu, J., Chu, C., Weon, S., Zhu, Q., Lu, J., Stavitski, E., Kim, J.-H., 2020. Amorphous Pd-Loaded  $\text{Ti}_4\text{O}_7$  Electrode for Direct Anodic Destruction of Perfluorooctanoic Acid. *Environ. Sci. Technol.* 54, 10954–10963. <https://doi.org/10.1021/acs.est.0c03800>
- Jung, Y.J., Baek, K.W., Oh, B.S., Kang, J.-W., 2010. An investigation of the formation of chlorate and perchlorate during electrolysis using Pt/Ti electrodes: The effects of pH and reactive oxygen species and the results of kinetic studies. *Water Res.* 44, 5345–5355. <https://doi.org/10.1016/j.watres.2010.06.029>
- Le, T.X.H., Haflich, H., Shah, A.D., Chaplin, B.P., 2019. Energy-Efficient Electrochemical Oxidation of Perfluoroalkyl Substances Using a  $\text{Ti}_4\text{O}_7$  Reactive Electrochemical Membrane Anode. *Environ. Sci. Technol. Lett.* 6, 504–510. <https://doi.org/10.1021/acs.estlett.9b00397>
- Li, W., Xiao, R., Lin, H., Yang, K., Li, W., He, K., Yang, L.-H., Pu, M., Li, M., Lv, S., 2022a. Electro-activation of peroxymonosulfate by a graphene oxide/iron oxide nanoparticle-doped  $\text{Ti}_4\text{O}_7$  ceramic membrane: mechanism of singlet oxygen generation in the removal of 1,4-dioxane. *J. Hazard. Mater.* 424, 127342. <https://doi.org/10.1016/j.jhazmat.2021.127342>
- Li, W., Xiao, R., Xu, J., Lin, H., Yang, K., Li, W., He, K., Tang, L., Chen, J., Wu, Y., Lv, S., 2022b. Interface engineering strategy of a  $\text{Ti}_4\text{O}_7$  ceramic membrane via graphene oxide nanoparticles toward efficient electrooxidation of 1,4-dioxane. *Water Res.* 216, 118287. <https://doi.org/10.1016/j.watres.2022.118287>
- Liang, J., You, S., Yuan, Y., Yuan, Y., 2021. A tubular electrode assembly reactor for enhanced electrochemical wastewater treatment with a Magnéli-phase titanium suboxide (M-TiSO) anode and *in situ* utilization. *RSC Adv.* 11, 24976–24984. <https://doi.org/10.1039/D1RA02236A>
- Liang, S., Lin, H., Yan, X., Huang, Q., 2018. Electro-oxidation of tetracycline by a Magnéli phase  $\text{Ti}_4\text{O}_7$  porous anode: Kinetics, products, and toxicity. *Chem. Eng. J.* 332, 628–636. <https://doi.org/10.1016/j.cej.2017.09.109>
- Lin, H., Niu, J., Liang, S., Wang, C., Wang, Y., Jin, F., Luo, Q., Huang, Q., 2018. Development of macroporous Magnéli phase  $\text{Ti}_4\text{O}_7$  ceramic materials: As an efficient anode for mineralization of poly- and perfluoroalkyl substances. *Chem. Eng. J.* 354, 1058–1067.

- <https://doi.org/10.1016/j.cej.2018.07.210>
- Lin, H., Xiao, R., Xie, R., Yang, L., Tang, C., Wang, R., Chen, J., Lv, S., Huang, Q., 2021. Defect Engineering on a  $\text{Ti}_4\text{O}_7$  Electrode by  $\text{Ce}^{3+}$  Doping for the Efficient Electrooxidation of Perfluorooctanesulfonate. *Environ. Sci. Technol.* 55, 2597–2607. <https://doi.org/10.1021/acs.est.0c06881>
- Lin, M.-H., Bulman, D.M., Remucal, C.K., Chaplin, B.P., 2020. Chlorinated Byproduct Formation during the Electrochemical Advanced Oxidation Process at Magnéli Phase  $\text{Ti}_4\text{O}_7$  Electrodes. *Environ. Sci. Technol.* 54, 12673–12683. <https://doi.org/10.1021/acs.est.0c03916>
- Liu, K., Yi, Y., Zhang, N., 2021. Anodic oxidation produces active chlorine to treat oilfield wastewater and prepare ferrate (VI). *J. Water Process Eng.* 41, 101998. <https://doi.org/10.1016/j.jwpe.2021.101998>
- Liu, X., Kepaptsoglou, D., Gao, Z., Thomas, A., Maji, K., Guilmeau, E., Azough, F., Ramasse, Q.M., Freer, R., 2021. Controlling the Thermoelectric Properties of Nb-Doped  $\text{TiO}_2$  Ceramics through Engineering Defect Structures. *ACS Appl. Mater. Interfaces* 13, 57326–57340. <https://doi.org/10.1021/acsami.1c18236>
- Martínez-Huitle, C.A., Brillas, E., 2009. Decontamination of wastewaters containing synthetic organic dyes by electrochemical methods: A general review. *Appl. Catal. B Environ.* 87, 105–145. <https://doi.org/10.1016/j.apcatb.2008.09.017>
- Martínez-Huitle, C.A., Rodrigo, M.A., Sirés, I., Scialdone, O., 2015. Single and Coupled Electrochemical Processes and Reactors for the Abatement of Organic Water Pollutants: A Critical Review. *Chem. Rev.* 115, 13362–13407. <https://doi.org/10.1021/acs.chemrev.5b00361>
- Martinez-Oviedo, A., Ray, S.K., Nguyen, H.P., Lee, S.W., 2019. Efficient photo-oxidation of  $\text{NO}_x$  by Sn doped blue  $\text{TiO}_2$  nanoparticles. *J. Photochem. Photobiol. Chem.* 370, 18–25. <https://doi.org/10.1016/j.jphotochem.2018.10.032>
- Nayak, S., Chaplin, B.P., 2018. Fabrication and characterization of porous, conductive, monolithic  $\text{Ti}_4\text{O}_7$  electrodes. *Electrochim. Acta* 263, 299–310. <https://doi.org/10.1016/j.electacta.2018.01.034>
- Panizza, M., Cerisola, G., 2003. Electrochemical oxidation of 2-naphthol with in situ electrogenerated active chlorine. *Electrochim. Acta* 48, 1515–1519. [https://doi.org/10.1016/S0013-4686\(03\)00028-8](https://doi.org/10.1016/S0013-4686(03)00028-8)
- Qing, Y., Li, Y., Li, W., Yao, H., 2021.  $\text{Ti}^{3+}$  self-doped dark  $\text{TiO}_2$  nanoparticles with tunable and unique dielectric properties for electromagnetic applications. *J. Mater. Chem. C* 9, 1205–1214.

- <https://doi.org/10.1039/D0TC05112H>
- Rahmani, A.R., Samarghandi, M.R., Nematollahi, D., Zamani, F., 2019. A comprehensive study of electrochemical disinfection of water using direct and indirect oxidation processes. *J. Environ. Chem. Eng.* 7, 102785. <https://doi.org/10.1016/j.jece.2018.11.030>
- Sánchez-Carretero, A., Sáez, C., Cañizares, P., Rodrigo, M.A., 2011. Electrochemical production of perchlorates using conductive diamond electrolyses. *Chem. Eng. J.* 166, 710–714. <https://doi.org/10.1016/j.cej.2010.11.037>
- Shi, H., Wang, Y., Li, C., Pierce, R., Gao, S., Huang, Q., 2019. Degradation of Perfluorooctanesulfonate by Reactive Electrochemical Membrane Composed of Magnéli Phase Titanium Suboxide. *Environ. Sci. Technol.* 53, 14528–14537. <https://doi.org/10.1021/acs.est.9b04148>
- Sirés, I., Brillas, E., Oturan, M.A., Rodrigo, M.A., Panizza, M., 2014. Electrochemical advanced oxidation processes: today and tomorrow. A review. *Environ. Sci. Pollut. Res.* 21, 8336–8367. <https://doi.org/10.1007/s11356-014-2783-1>
- Tomcsányi, L., De Battisti, A., Hirschberg, G., Varga, K., Liszi, J., 1999. The study of the electrooxidation of chloride at RuO<sub>2</sub>/TiO<sub>2</sub> electrode using CV and radiotracer techniques and evaluating by electrochemical kinetic simulation methods. *Electrochim. Acta* 44, 2463–2472. [https://doi.org/10.1016/S0013-4686\(98\)00381-8](https://doi.org/10.1016/S0013-4686(98)00381-8)
- Trellu, C., Coetsier, C., Rouch, J.-C., Esmilaire, R., Rivallin, M., Cretin, M., Causserand, C., 2018. Mineralization of organic pollutants by anodic oxidation using reactive electrochemical membrane synthesized from carbothermal reduction of TiO<sub>2</sub>. *Water Res.* 131, 310–319. <https://doi.org/10.1016/j.watres.2017.12.070>
- Trellu, C., Rivallin, M., Cerneaux, S., Coetsier, C., Causserand, C., Oturan, M.A., Cretin, M., 2020. Integration of sub-stoichiometric titanium oxide reactive electrochemical membrane as anode in the electro-Fenton process. *Chem. Eng. J.* 400, 125936. <https://doi.org/10.1016/j.cej.2020.125936>
- Wang, G., Liu, Y., Ye, J., Lin, Z., Yang, X., 2020. Electrochemical oxidation of methyl orange by a Magnéli phase Ti<sub>4</sub>O<sub>7</sub> anode. *Chemosphere* 241, 125084. <https://doi.org/10.1016/j.chemosphere.2019.125084>
- Wang, G., Liu, Y., Ye, J., Qiu, W., 2017. Synthesis, microstructural characterization, and electrochemical performance of novel rod-like Ti<sub>4</sub>O<sub>7</sub> powders. *J. Alloys Compd.* 704, 18–25.

- <https://doi.org/10.1016/j.jallcom.2017.02.022>
- Wang, H., Li, Z., Zhang, F., Wang, Y., Zhang, X., Wang, J., He, X., 2021. Comparison of Ti/Ti<sub>4</sub>O<sub>7</sub>, Ti/Ti<sub>4</sub>O<sub>7</sub>-PbO<sub>2</sub>-Ce, and Ti/Ti<sub>4</sub>O<sub>7</sub> nanotube array anodes for electro-oxidation of p-nitrophenol and real wastewater. *Sep. Purif. Technol.* 266, 118600. <https://doi.org/10.1016/j.seppur.2021.118600>
- Wang, J., Zhi, D., Zhou, H., He, X., Zhang, D., 2018. Evaluating tetracycline degradation pathway and intermediate toxicity during the electrochemical oxidation over a Ti/Ti<sub>4</sub>O<sub>7</sub> anode. *Water Res.* 137, 324–334. <https://doi.org/10.1016/j.watres.2018.03.030>
- Wang, L., Lu, J., Li, L., Wang, Y., Huang, Q., 2020. Effects of chloride on electrochemical degradation of perfluorooctanesulfonate by Magnéli phase Ti<sub>4</sub>O<sub>7</sub> and boron doped diamond anodes. *Water Res.* 170, 115254. <https://doi.org/10.1016/j.watres.2019.115254>
- Xu, B., Sohn, H.Y., Mohassab, Y., Lan, Y., 2016. Structures, preparation and applications of titanium suboxides. *RSC Adv.* 6, 79706–79722. <https://doi.org/10.1039/C6RA14507H>
- Xu, L., Niu, J., Xie, H., Ma, X., Zhu, Y., Crittenden, J., 2021. Effective degradation of aqueous carbamazepine on a novel blue-colored TiO<sub>2</sub> nanotube arrays membrane filter anode. *J. Hazard. Mater.* 402, 123530. <https://doi.org/10.1016/j.jhazmat.2020.123530>
- Yang, P., Wang, Y., Lu, J., Tishchenko, V., Huang, Q., 2020. Electrochemical Oxidation of Perfluorooctanesulfonate by Magnéli Phase Ti<sub>4</sub>O<sub>7</sub> Electrode in the Presence of Trichloroethylene. *Adv. Environ. Eng. Res.* 1(4). <https://doi.org/10.21926/aeer.2004006>
- Yao, S., Xue, S., Zhang, Y., Shen, X., Qian, X., Li, T., Xiao, K., Qin, S., Xiang, J., 2017. Synthesis, characterization, and electrochemical performance of spherical nanostructure of Magnéli phase Ti<sub>4</sub>O<sub>7</sub>. *J. Mater. Sci. Mater. Electron.* 28, 7264–7270. <https://doi.org/10.1007/s10854-017-6410-z>
- You, S., Liu, B., Gao, Y., Wang, Y., Tang, C.Y., Huang, Y., Ren, N., 2016. Monolithic Porous Magnéli-phase Ti<sub>4</sub>O<sub>7</sub> for Electro-oxidation Treatment of Industrial Wastewater. *Electrochim. Acta* 214, 326–335. <https://doi.org/10.1016/j.electacta.2016.08.037>
- Zhang, C., He, D., Ma, J., Waite, T.D., 2018. Active chlorine mediated ammonia oxidation revisited: Reaction mechanism, kinetic modelling and implications. *Water Res.* 145, 220–230. <https://doi.org/10.1016/j.watres.2018.08.025>
- Zhao, Z., Zhang, J., Yao, J., You, S., 2022. Electrochemical removal of 4-chlorophenol in water using a porous Magnéli-phase (Ti<sub>4</sub>O<sub>7</sub>) electrode. *Environ. Res.* 210, 113004.

<https://doi.org/10.1016/j.envres.2022.113004>

Zhi, D., Zhang, J., Wang, J., Luo, L., Zhou, Y., Zhou, Y., 2020. Electrochemical treatments of coking wastewater and coal gasification wastewater with Ti/Ti<sub>4</sub>O<sub>7</sub> and Ti/RuO<sub>2</sub>-IrO<sub>2</sub> anodes. *J. Environ. Manage.* 265, 110571. <https://doi.org/10.1016/j.jenvman.2020.110571>

Zhu, R., Liu, Y., Ye, J., Zhang, X., 2013. Magnéli phase Ti<sub>4</sub>O<sub>7</sub> powder from carbothermal reduction method: formation, conductivity and optical properties. *J. Mater. Sci. Mater. Electron.* 24, 4853–4856. <https://doi.org/10.1007/s10854-013-1487-5>

## **Chapter III**

### **Development of Ti/TiO<sub>x</sub> Foams for Removal of Organic Pollutants from Water: Influence of Porous Structure of Ti Substrate**



## Abstract

Ti/TiO<sub>x</sub> foams used as anode were obtained by plasma spraying technique using different Ti substrates. The reactivity of these anodes for removing organic pollutants from water was investigated using linear sweep voltammetry, probe molecules, quenchers and model pollutants, with a particular emphasis on the formation of <sup>•</sup>OH. Degradation and mineralization kinetics were assessed. Degradation by-products were monitored for better understanding of reaction mechanisms. Porous structure of the substrate strongly influenced mass transport conditions and reactivity. Substrate morphology should allow for homogeneous coating of the surface in order to promote non-selective <sup>•</sup>OH-mediated oxidation of recalcitrant organic pollutants. Coarse roughness with characteristic scale that is larger than the diffusion boundary layer improved mass transport conditions even in stirred-tank reactor. Flow-through application of the most suitable Ti/TiO<sub>x</sub> foam allowed for a 3.9- and 1.9-times enhancement of the degradation kinetic of paracetamol (as target pollutant) compared to Ti/TiO<sub>x</sub> and BDD plate, respectively.

**Keywords:** Anodic oxidation, Sub-stoichiometric titanium oxide, Porous electrode, Hydroxyl radical, Direct electron transfer, Organic pollutants

## 1. Introduction

In the past few decades, electrochemical advanced oxidation processes (EAOPs) have been considered as promising technologies for water treatment due to their capacity to remove a large number of organics from water, including persistent and recalcitrant organics and inorganics (Zaky and Chaplin, 2013; Sirés et al., 2014; Mousset et al., 2016; Nidheesh et al., 2018, 2019; Trellu et al., 2021;). The great potential of EAOPs comes from in situ generation of reactive radicals (especially hydroxyl radicals ( $\cdot\text{OH}$ ), which can fulfill effective degradation of pollutants and achieve high mineralization yields (Scialdone, 2009; Oturan and Aaron, 2014; Moreira et al., 2017; Jia et al., 2021). Anodic oxidation (AO) is a typical technology among EAOPs. The objective is to promote oxidation of target pollutants through two main pathways including direct electron transfer (DET) and radical-mediated oxidation (mainly  $\cdot\text{OH}$ ) (Panizza and Cerisola, 2009).  $\cdot\text{OH}$ -mediated oxidation is a key phenomenon for the removal of organic pollutants as  $\cdot\text{OH}$  reacts in a non-selective way with a large range of compounds. However,  $\cdot\text{OH}$  has short lifetime of microseconds and can therefore accumulate only within a thin layer (from nanometers to micrometers) in the vicinity of the electrode surface (Kapałka et al., 2009; Groenen-Serrano et al., 2013; Attri et al., 2015). For example, in mixed-tank reactor mode, the efficiency of anodic oxidation is limited by the existence of a thick diffusion layer (up to hundreds of micrometers). Through this diffusion layer, concentration of target molecule decreased greatly from bulk solution towards electrode surface. Therefore, the process is generally limited by mass transfer conditions. The main points for an efficient anodic oxidation process are to achieve (i) suitable electrochemical reactivity for oxidation of organic compounds and (ii) efficient mass transfer of target molecule towards a large electroactive surface area (EASA) of the anode. Proper anode materials must address these crucial aspects.

As regards to the reactivity, non-active electrodes with high oxygen evolution potential (OEP) generally have more suitable electrochemical reactivity for the removal of organics owing to the generation of physisorbed  $\cdot\text{OH}$  (Garcia-Segura et al., 2018; Cai et al., 2019; Ganiyu et al., 2021; Oturan, 2021). Among non-active electrodes, TiO<sub>x</sub> has gained much attention because of its lower cost compared to well-known boron-doped diamond (BDD) electrodes (Radjenovic and

Sedlak, 2015; You et al., 2016; Nayak and Chaplin, 2018; Trellu et al., 2018b; Xie et al., 2020).

As regards to mass transfer conditions, application of porous materials in flow-through configuration is able to enhance mass transfer and degradation kinetics of pollutants (Guo et al., 2016; Mousset, 2022). Low pore size allows for reducing the limitation related to the diffusion of organic compounds from the bulk to the electrode surface. Thus, it is possible to enhance mass transfer by increasing convection (i.e., permeate flux) through the electrode (Trellu et al., 2018a). However, one of the drawbacks of this configuration might come from electrode fouling during filtration of real effluents (Guo et al., 2012; Trellu et al., 2018a). Physical structure (porosity, electro-active surface area, pore size distribution) of the material is therefore crucial for the behavior of such porous electrodes.

One of the main objectives of porous materials is to promote mass transfer conditions for the removal of low concentrations of pollutants. Particularly, pharmaceuticals have become a notable group of micropollutants over the past few decades. Among these pharmaceuticals, paracetamol (PCT) is one of the top analgesics consumed every year in the world (Hinojosa Guerra et al., 2019; Przybyła et al., 2021). Concentrations in the range from ng L<sup>-1</sup> to µg L<sup>-1</sup> have been reported in the water bodies (Ghanbari et al., 2021). Many studies have been dedicated to the removal of PCT from aqueous effluents. Therefore, it was considered as a suitable model pollutant for comparison with other previous studies.

In this study, porous Ti/TiO<sub>x</sub> foams as anode material were obtained from plasma spraying. The objective was to synthesize porous electrode materials with the following features: (i) relevant synthesis method for scale-up and industrial development, (ii) suitable reactivity for removal of organic compounds from water, (iii) suitable physical structure for mass transport enhancement and (iv) suitable pore size for reducing fouling issues. Surface morphology and electrochemical characteristics of these new electrode materials were studied. Particularly, the influence of the nature of the Ti substrate was investigated. Terephthalic acid (TA) and oxalic acid (OA) were used as probe molecules to assess the reactivity of the electrodes for <sup>•</sup>OH generation and DET, respectively. As model pollutant, PCT degradation mechanisms were assessed using quenching experiments as well as through identification and quantification of by-products. Finally, mass transport enhancement in flow-through mode was investigated in order to assess the potential of

these electrodes for such application. Results were compared with the use of Ti/TiO<sub>x</sub> plate for highlighting the role of the porous structure of the substrate. They have also been compared with the effectiveness of a commercial BDD plate electrode considered as gold standard for such application.

## 2. Materials and Methods

### 2.1 Chemicals and instruments

Formic acid ( $\geq 96\%$ ), phosphoric acid (85-88%), paracetamol (98%), hydroquinone ( $\geq 99\%$ ), potassium hexacyanoferrate (III) (K<sub>3</sub>Fe(CN)<sub>6</sub>) (99%), potassium hexacyanoferrate (II) trihydrate (K<sub>4</sub>[Fe(CN)<sub>6</sub>] · 3H<sub>2</sub>O) and 2-hydroxyterephthalic acid (HTA) were purchased from Sigma-Aldrich. Sodium hydroxide ( $\geq 98\%$ ), sodium sulfate ( $\geq 99\%$ ) and oxalic acid ( $\geq 97\%$ ) were provided by Fluka. Terephthalic acid ( $\geq 99\%$ ) and tert-Butanol (99.5%) were purchased from Acros Organics. Ethanol ( $\geq 97\%$ ) was provided by Chimie-Plus Laboratoires. Methanol was purchased from Honeywell Riedel-de Haën (HPLC grade,  $\geq 99.9\%$ ). All chemicals were used without any further purification. All eluents for HPLC and UHPLC were prepared using ultrapure water ( $R > 18.2 \text{ M}\Omega$ ) obtained from a Smart2Pure device, provided by Thermo Scientific, France).

### 2.2 Synthesis of electrode materials

All TiO<sub>x</sub>-coated Ti materials (plate, foam 1 and foam 2) were provided by Saint-Gobain Research Provence, CREE. Different porous Ti substrates were used for foam 1 and foam 2. The substrate used for the Ti/TiO<sub>x</sub> plate electrode was a 2 mm thick TA6V plate sanded with alumina zirconia grains under pressure of 5 bars. Porous Ti substrates from American Elements and SELEE were used for foam 1 and foam 2, respectively. The substrate of foam 2 has larger pore size and more open porous structure than that of foam 1, as detailed in results and discussion section.

All Ti/TiO<sub>x</sub> materials were then obtained using the same coating procedure. A Saint-Gobain pro plasma torch supplied with mixed gas of Ar (45 L min<sup>-1</sup>) and H<sub>2</sub> (11 L min<sup>-1</sup>) at a voltage of 63-66 V (600 A) was employed for plasma generation. The electro-fused TiO<sub>x</sub> powder with an average particle size of 30 μm was injected (using argon gas as carrier at a flow rate of 4 L min<sup>-1</sup>) into the generated plasma. The spray distance was 110 mm and the TiO<sub>x</sub> particles were deposited on both sides of the substrates. An argon shield was used to prevent reoxidation of TiO<sub>x</sub> particles during the spraying process.

Results obtained with Ti/TiO<sub>x</sub> electrodes were compared with the use of a BDD anode (Diachem) obtained from Condias (Germany).

### 2.3 Material characterization

The chemical composition of the TiO<sub>x</sub> coating was analyzed by X-Ray diffraction (XRD) (Bruker D8 ENDEAVOR) with Cu K<sub>α</sub> radiation ( $\lambda=1.5418 \text{ \AA}$ ) at 40 kV and 40 mA. The coating was removed from electrodes by milling to obtain a free-standing sample. The phase composition was identified by referring to the standard card PDF2-2004 (ICDD). The surface of the coating was also characterized in-situ by Raman spectroscopy. The Raman spectra was obtained by a Renishaw inVia Raman microscope with solid-state green (Nd:YAG) laser of 532 nm (maximum laser power: 50 mW). The laser energy filter was set to 5% and 50%.

Porous structure, coating thickness and coating surface distribution were observed by scanning electron microscopy (SEM, TM3030 and TM-1000, HITACHI). Porosity and pore size distribution of foam 1 were analyzed by Hg porosimetry (Micrometrics AutoPore IV 9500 V1.06). Mercury intrusion was conducted with pressure in the range of 0.1 to 60000 psia. The contact angle of mercury was 140.9 degrees and the mercury surface tension was 485 dynes cm<sup>-1</sup>. A digital optical microscope (KEYENCE, VHX-7000) was used for measuring the size of the large pores of foam 2. The optical microscope also allowed for visualization of surface roughness of the different materials.

## 2.4 Electrochemical setup

AO was mainly performed in a stirred-tank reactor made of a cylindrical undivided glass cell containing 300 mL of solution. The reactor was operated in batch mode. Ti/TiO<sub>x</sub> electrodes were used as anode, while carbon felt with similar electrode surface was used as cathode. Electrodes were set face to face with an effective geometric surface area of 23.6 cm<sup>2</sup> ( $S_{\text{electrode}}/V_{\text{solution}}=7.9 \text{ m}^{-1}$ ) and an inter-electrode distance of 2.5 cm. Experiments were performed in galvanostatic mode with constant current density of 5 mA cm<sup>-2</sup>. The reactor was continuously stirred under magnetic agitation at 750 rpm. Samples were taken at different time intervals for analysis.

Electrooxidation of selected pollutants was also performed in flow-through configuration. The reactor was operated in batch mode since the solution was continuously recirculated. The flow rate was set at 1200 L h<sup>-1</sup> m<sup>-2</sup> using a peristaltic pump (FH100, Thermo Scientific) and the process was also operated at 5 mA cm<sup>-2</sup>. Perforated Ti was used as cathode. The ratio  $S_{\text{electrode}}/V_{\text{solution}}$  was the same as in stirred-tank experiments (7.9 m<sup>-1</sup>).

## 2.5 Electrochemical characterization

The same reactor setup was used for electrochemical characterization. Linear sweep voltammetry (LSV) and cyclic voltammetry (CV) data were recorded using 100 mM NaClO<sub>4</sub> as inert supporting electrolyte, stainless steel as counter electrode and Ag/AgCl/3 M KCl electrode as reference electrode. Experiments were performed on a Metrohm Autolab PGSTAT.

LSV was used to study oxygen evolution reaction (OER). LSV tests were performed at scan rate of 0.01 V s<sup>-1</sup>. Raw LSV data was corrected according to the uncompensated resistance of the system, based on the method reported previously (De Faria et al., 1996; Krstajic and Trasatti, 1998; Kapalka et al., 2008).

EASA of Ti/TiO<sub>x</sub> materials were determined by the method described by Nayak and Chaplin (Nayak and Chaplin, 2018). CV curves were recorded at various scanning rate in the range of 6-10 mV s<sup>-1</sup> in order to estimate the double layer capacitance. EASA was then obtained by using

the specific capacitance of such material reported in the literature (60 μF cm<sup>-2</sup>) (Bockris and Otagawa, 1984; Nayak and Chaplin, 2018). The roughness factor (RF) was obtained from the ratio between EASA and geometrical surface area ( $S_{geo}$ ).

Limiting current technique was used to determine the mass transfer coefficient with BDD in the stirred-tank reactor, as reported in a previous study (Nayak and Chaplin, 2018). The similar experiment setup was used. Stainless steel was used as counter electrode, an Ag/AgCl/3 M KCl electrode was used as reference electrode and 100 mM NaClO<sub>4</sub> was used as supporting electrolyte. The limiting current was obtained from a CV scan (from 0.28 to 2.2 V at scan rate of 0.01V s<sup>-1</sup>) with redox couple of Fe(CN)<sub>6</sub><sup>4-</sup> (5 mM)/ Fe(CN)<sub>6</sub><sup>3-</sup> (20 mM) and the mass transfer coefficient was calculated according to Eq. 3-1:

$$k_m = \frac{I_{lim}}{zFAC_b} \quad (3 - 1)$$

where  $I_{lim}$  is the limiting current,  $z$  is the number of electrons involved (1 in this case),  $F$  is Faraday constant,  $A$  is effective geometric surface area (m<sup>2</sup>) and  $C_b$  is the concentration of the redox species (mol m<sup>-3</sup>).

The thickness of the diffusion boundary layer was then estimated in PCT degradation system using Eq. 3-2:

$$\delta = \frac{D}{k_m} \quad (3 - 2)$$

Where  $D$  is the diffusion coefficient (7.26×10<sup>-10</sup> m<sup>2</sup> s<sup>-1</sup>) (Konopka and McDuffie, 1970),  $k_m$  is mass transfer coefficient determined by limiting current technique.

## 2.6 Determination of the effective roughness factor (ERF)

It has already been described in the literature that features of surface roughness are averaged into the diffusion field when the characteristic scale of this roughness is too small compared to the thickness of the diffusion layer ( $\delta$ ) (Trellu et al., 2018a). Therefore, one objective of this study was to assess whether it is possible to qualitatively correlate the effectiveness of electrodes with a parameter called ERF, obtained as follow. The 1-D profile of each electrode

surface was recorded (at  $\mu\text{m}$  scale) using optical microscopy. The surface roughness at sub- $\mu\text{m}$  scale was not taken into consideration since it is averaged into the diffusion field. Then, the 1-D profiles of the boundary diffusion layer according to different values of  $\delta$  (from 7.5 to 100  $\mu\text{m}$ ) were calculated using following method (taking  $\delta = 30 \mu\text{m}$  as an example):

- 1) according to the 1-D profile of the electrode surface obtained by optical microscopy, the diffusion layer was firstly generated by simply adding 30  $\mu\text{m}$  to the electrode surface
- 2) for each point of the diffusion layer, its distance to every point of electrode surface was calculated and compared to 30  $\mu\text{m}$ , if this distance was smaller than 30  $\mu\text{m}$ , this point on diffusion layer was moved 0.1  $\mu\text{m}$  above and the distance was checked again. This step was repeated until each point of the diffusion layer was at least 30  $\mu\text{m}$  away from every point of the electrode surface. This step was accomplished using a Python program.

Thus, it was possible to calculate the surface area formed by the diffusion layer ( $S_\delta$ ) and to determine this ERF from the ratio between  $S_\delta$  and  $S_{\text{geo}}$  using Eq. 3-3:

$$ERF = \frac{[\sum_{x=0}^{x_i} \sqrt{(\Delta x)^2 + (\Delta y)^2}]^2}{(x_i - 0)^2} \quad (3 - 3)$$

where (x,y) represents the coordinates of the 1-D profile of the diffusion layer and  $x_i$  represents the geometrical length of the studied profile.

These calculations are based on the assumption of a homogeneous diffusion layer thickness.

## 2.7 Probe molecules, model pollutant and quenching experiments

Preliminary tests were performed during 2 h without current supply in order to assess adsorption of target compounds on electrode materials. The adsorption rate was <3% for all configurations.

### 2.7.1 Probe molecules

Different probe molecules were used for assessment of the reactivity of the electrodes. OA was chosen as probe molecule for DET since it reacts slowly with  $\cdot\text{OH}$  (Shih et al., 2019). TA, likewise, was used as probe molecule for  $\cdot\text{OH}$ -mediated oxidation because it cannot be oxidized



via DET (Jing and Chaplin, 2017). Jing and Chaplin (2017) highlighted the suitability of TA as probe molecule from experimental results and density functional theory (DFT) calculations (Jing and Chaplin, 2017).

Similar concentration in term of total organic carbon (TOC) (9.6 mg L<sup>-1</sup>) was used for all experiments with probe molecules. The concentrations of OA and TA were therefore 0.4 and 0.1 mM, respectively. These experiments were performed under mass transport limitation ( $j > j_{lim}$ ) according to Eq. 3-4 (Panizza and Cerisola, 2009). All experiments were performed using 50 mM Na<sub>2</sub>SO<sub>4</sub> as supporting electrolyte.

$$j_{lim} = 4 F k_m COD \quad (3 - 4)$$

where  $j_{lim}$  is the limiting current density (A m<sup>-2</sup>);  $F$  is the Faraday constant (96 485 C mol<sup>-1</sup>);  $k_m$  is the mass transport coefficient (m s<sup>-1</sup>) and COD is the chemical oxygen demand (mol m<sup>-3</sup>) of the treated solution.

### 2.7.2 Model pollutant and quenching experiments

PCT was selected as model pollutant since it is able to react through both <sup>•</sup>OH -mediated oxidation and DET. Firstly, degradation kinetic and mineralization yield of 0.1 mM PCT (9.6 mg L<sup>-1</sup> TOC) in 50 mM Na<sub>2</sub>SO<sub>4</sub> was studied. Then, quenching experiments were conducted to study the potential contribution of <sup>•</sup>OH and DET to PCT degradation. As Na<sub>2</sub>SO<sub>4</sub> was used as electrolyte, quenching experiments were also performed in order to assess the role of sulfate radicals (SO<sub>4</sub><sup>•-</sup>). Ethanol (EtOH) was used as quencher of <sup>•</sup>OH and SO<sub>4</sub><sup>•-</sup> since EtOH can react with both <sup>•</sup>OH and SO<sub>4</sub><sup>•-</sup> with high rate constants ((1.2 - 2.8) × 10<sup>9</sup> M<sup>-1</sup> s<sup>-1</sup> for <sup>•</sup>OH and 1.6 - 7.7 × 10<sup>7</sup> M<sup>-1</sup> s<sup>-1</sup> for SO<sub>4</sub><sup>•-</sup>) (Hayon et al., 1972; Buxton et al., 1988; Neta et al., 1988; Wu et al., 2022). Tert-Butyl alcohol (TBA) was used as quencher of only <sup>•</sup>OH since it reacts with <sup>•</sup>OH much more rapidly than with SO<sub>4</sub><sup>•-</sup> (3.8 - 7.6 × 10<sup>8</sup> M<sup>-1</sup> s<sup>-1</sup> for <sup>•</sup>OH and 4 - 9.1 × 10<sup>5</sup> M<sup>-1</sup> s<sup>-1</sup> for SO<sub>4</sub><sup>•-</sup>) (Buxton et al., 1988; Neta et al., 1988; Anipsitakis and Dionysiou, 2004; Li et al., 2022;). For all quenchers, a molar ratio of 1000:1 (quencher: initial PCT) was used to ensure that excess quenchers were available in solution for consuming radicals. The influence of quenchers on the

formation of main degradation by-products of PCT was also investigated.

## 2.8 Electrode stability

Experiments were performed for preliminary assessment of electrode stability. First, Ti leaching into the solution was monitored using inductively coupled plasma - optical emission spectroscopy (ICP – OES). The solution was collected after electrolysis and the concentration of Ti in the solution was analyzed using a PerkinElmer Optima 8300 ICP-OES. The selected analytic emission lines were 337.3 nm and 368.5 nm. Then, evolution of the degradation kinetic of PCT was monitored during several successive cycles in order to assess the stability of electrode reactivity in the range of operating conditions tested in this study.

## 2.9 Analytical methods

The mineralization of OA and PCT was monitored using a TOC analyzer (TOC-L, SHIMADZU). Concentrations of TA and its byproduct, 2-hydroxyterephthalic acid (HTA) were detected by a HITACHI Elite LaChrom HPLC system equipped with a UV detector (L-2400, set at  $\lambda = 254$  nm), a fluorescence detector (L-2480, set at Ex/Em=315/435 nm), a pump (L-2130) set at constant flow rate of 0.8 mL min<sup>-1</sup> and a LiChroCART Purospher® STAR RP-18e (5  $\mu$ m) column (set in an oven at 40 °C). Eluent was a mixture of methanol (40%) and water with 0.1% formic acid (60%). Concentrations of PCT and its main aromatic byproducts, hydroquinone (HQ) and benzoquinone (BQ), were measured by a Dionex UltiMate 3000 UHPLC system, including an UltiMate 3000 RS pump set at constant flow of 0.1 mL min<sup>-1</sup>, an UltiMate 3000 Diode Array Detector ( $\lambda = 243$  nm) and a Hypersil GOLD™ (100×2.1 mm, 1.9  $\mu$ m) column set in an UltiMate 3000 column compartment at 40 °C. The eluent was a mixture of 5 mM Na<sub>2</sub>HPO<sub>4</sub> and 7.5 mM H<sub>3</sub>PO<sub>4</sub> in water (85%) and methanol (15%).

### 3. Results and Discussion

#### 3.1 Characterization of Ti/TiO<sub>x</sub> materials: how the substrate influences the coating?

##### 3.1.1 Porosity and pore size distribution

The porous structure of the electrodes was controlled by the nature of the substrate material. The median pore size of foam 1 was determined from Hg porosimetry as 15 μm as regards to surface area and 88 μm as regards to porous volume (Fig. 3-1 (a)). The porosity and the specific surface area were measured as 35% and 130 cm<sup>2</sup> g<sup>-1</sup>, respectively. As shown in Fig. 3-1 (b), pore size of foam 2 was in the range of 0.7 - 1.6 mm.

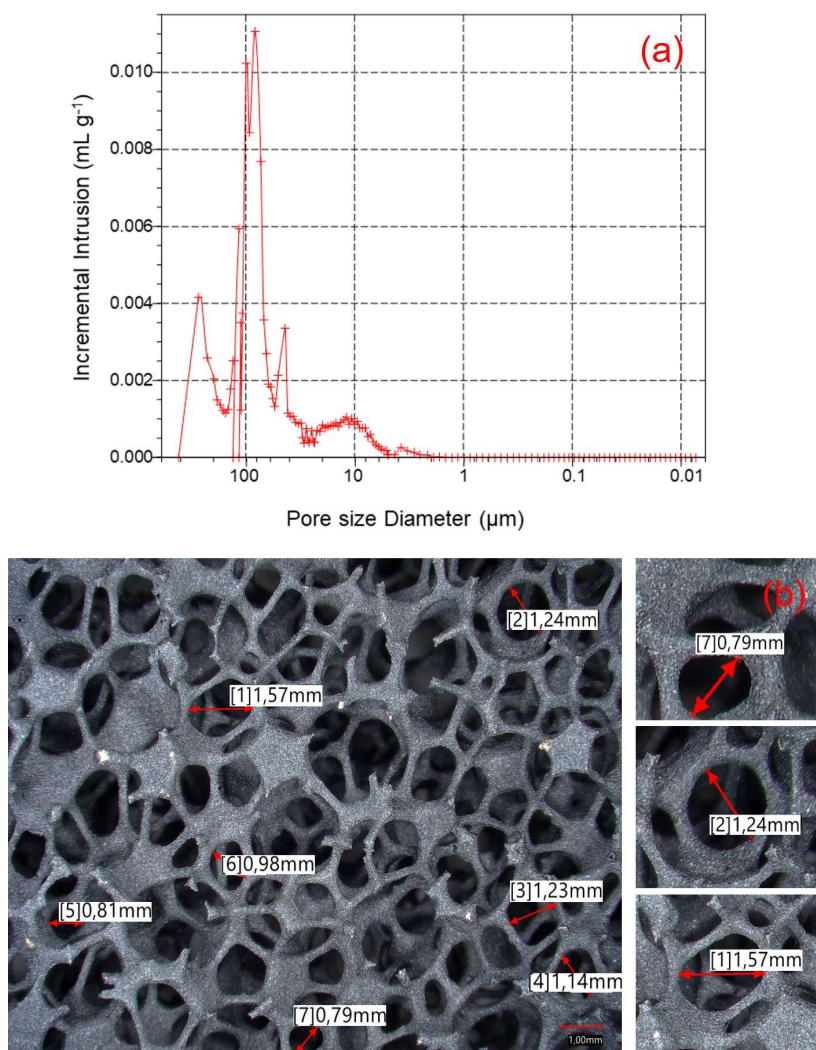


Fig. 3-1 - Plot of incremental pore volume as a function of pore diameter for foam 1 from Hg

porosimetry (a) and pore size of foam 2 observed from optical microscopy (b)

### 3.1.2 Scanning electron microscopy

Scanning electron microscope was utilized to observe porous structure as well as distribution of the TiO<sub>x</sub> coating on different substrates. Using Ti plate as substrate allowed to achieve a homogeneously distributed TiO<sub>x</sub> coating of approximately 300 μm (Fig. 3-2 (a)). The porous structure of foam 1 observed in Fig. 3-2 (b), showed that TiO<sub>x</sub> coating can be only deposited on its external surface. The coating was evenly distributed on the top of the substrate (Fig. 3-2 (c)). The average thickness of the coating was approximately 30 μm. The coating did not clog the surface porosity and the material was still water permeable.

Foam 2 presents a more open porous structure. Consequently, the coating was able to reach a portion of the inner surface of the substrate (Fig. 3-2 (d)). However, the coating was not distributed as evenly as for Ti/TiO<sub>x</sub> plate electrode or foam 1. It can be spotted clearly from cross sections that TiO<sub>x</sub> coating accumulated at the bottom of pores but not on the side walls (Figs. 3-2 (e) and 3-2 (f)) since this surface area was not accessible for the plasma spraying technique. The coating thickness of foam 2 ranged from 0 to approximately 60 μm.

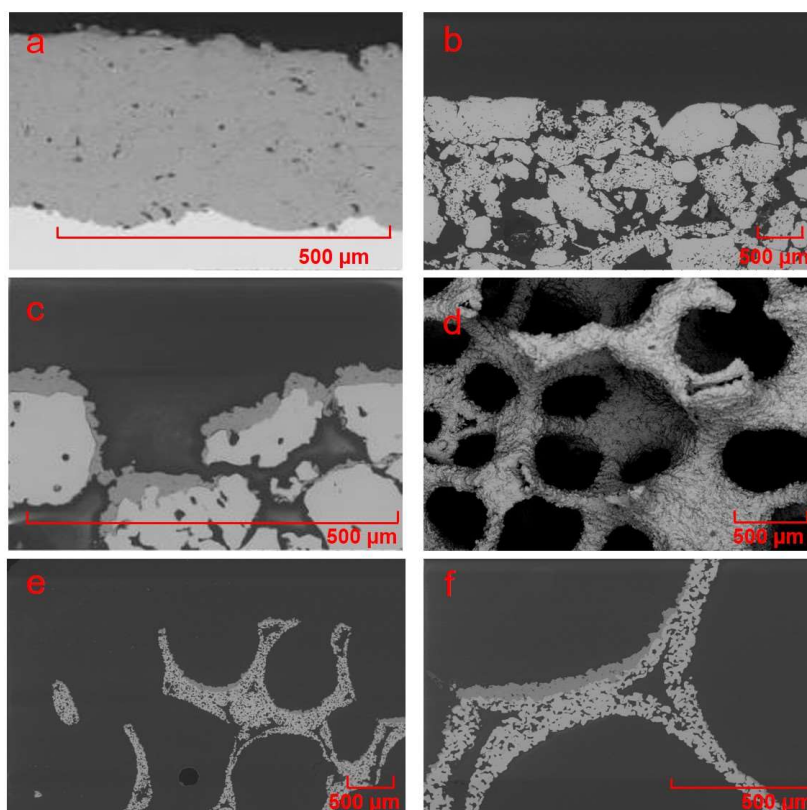


Fig. 3-2 - SEM images of (a): Ti/TiO<sub>x</sub> plate, (b), (c): foam 1 and (d), (e) and (f): foam 2

### 3.1.3 XRD and Raman spectroscopy

The chemical composition of the TiO<sub>x</sub> coating was studied by XRD. As a consequence of the similar coating procedure, different materials shared the same chemical structure. From XRD data, it was observed that the major phase of the coating was Ti<sub>4</sub>O<sub>7</sub> (Fig. 3-3), which has the highest conductivity among all phases of TiO<sub>x</sub> (Walsh and Wills, 2010). The coating also contained other minor phases of TiO<sub>x</sub> (e.g., Ti<sub>6</sub>O<sub>11</sub> and Ti<sub>8</sub>O<sub>15</sub>) (Fig. 3-3).

Raman spectra were also recorded at different laser intensity (Fig. 3-4) for further characterization of the electrode surface. A peak was observed at 144 cm<sup>-1</sup> with a laser filter irradiation set to 5% (Fig. 3-4). Such a peak is typical of Ti<sub>4</sub>O<sub>7</sub> phase (Watanabe, 2009; Li et al., 2010). When 50% laser filter irradiation was applied, three more peaks at 261, 408 and 611cm<sup>-1</sup> were appeared. These peaks correspond to rutile TiO<sub>2</sub> (Yao et al., 2017). The appearance of TiO<sub>2</sub> peaks suggested that high laser filter irradiation led to oxidation of Ti<sub>4</sub>O<sub>7</sub> to rutile TiO<sub>2</sub>. Yao et al. (Yao et al., 2017) already reported this behavior for the

characterization of Ti<sub>4</sub>O<sub>7</sub> phase.

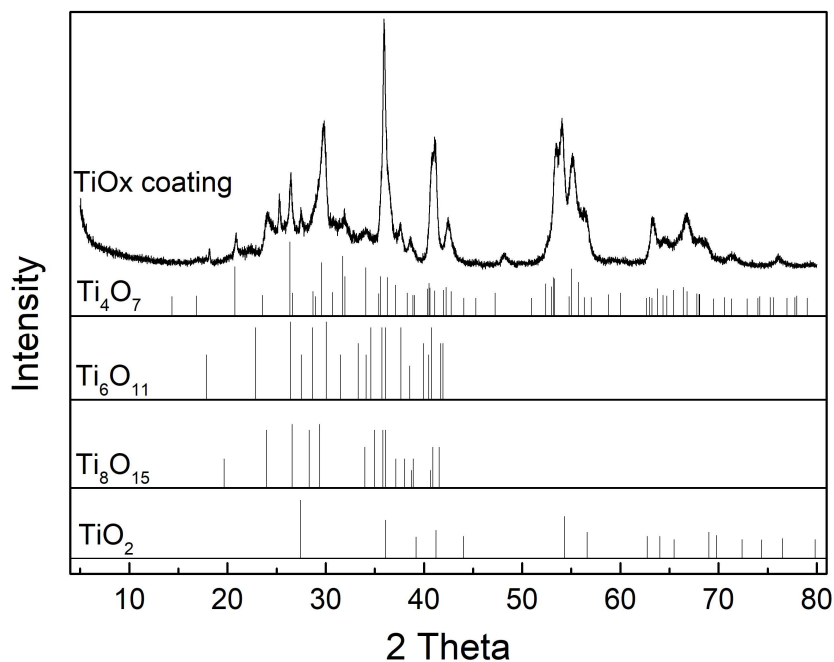


Fig. 3-3 - XRD pattern for TiO<sub>x</sub> coating of Ti/TiO<sub>x</sub> materials (using database PDF2-2004)

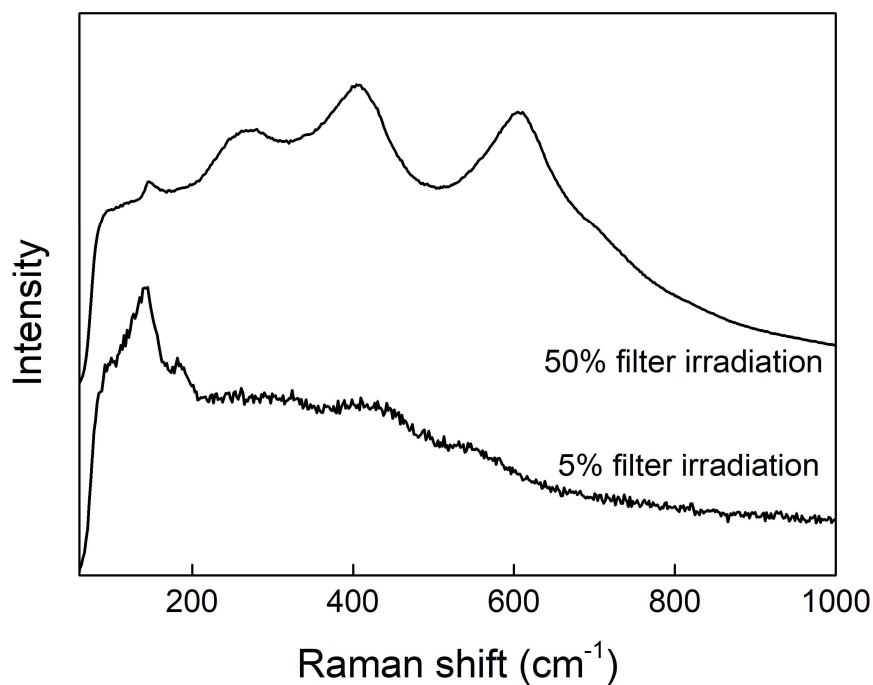


Fig. 3-4 - Raman spectra obtained for Ti/TiO<sub>x</sub> plate surface. Laser energy was tuned with 5% and 50% filter irradiation

### 3.1.4 Coarse surface roughness

The coarse surface roughness (at  $\mu\text{m}$  scale) was observed using optical microscopy (Fig. 3-5). There was not very significant coarse surface roughness for the Ti/TiO<sub>x</sub> plate electrode because of the homogenous deposition of the coating on the flat plate. The characteristic scale of coarse surface roughness of foam 1 was around 100  $\mu\text{m}$  because of pore characteristics of the substrate. This value further increased with foam 2 (1000  $\mu\text{m}$ ), which presented larger pores. For comparison, the characteristic scale of coarse surface roughness of conventional BDD plate was around 10  $\mu\text{m}$ .

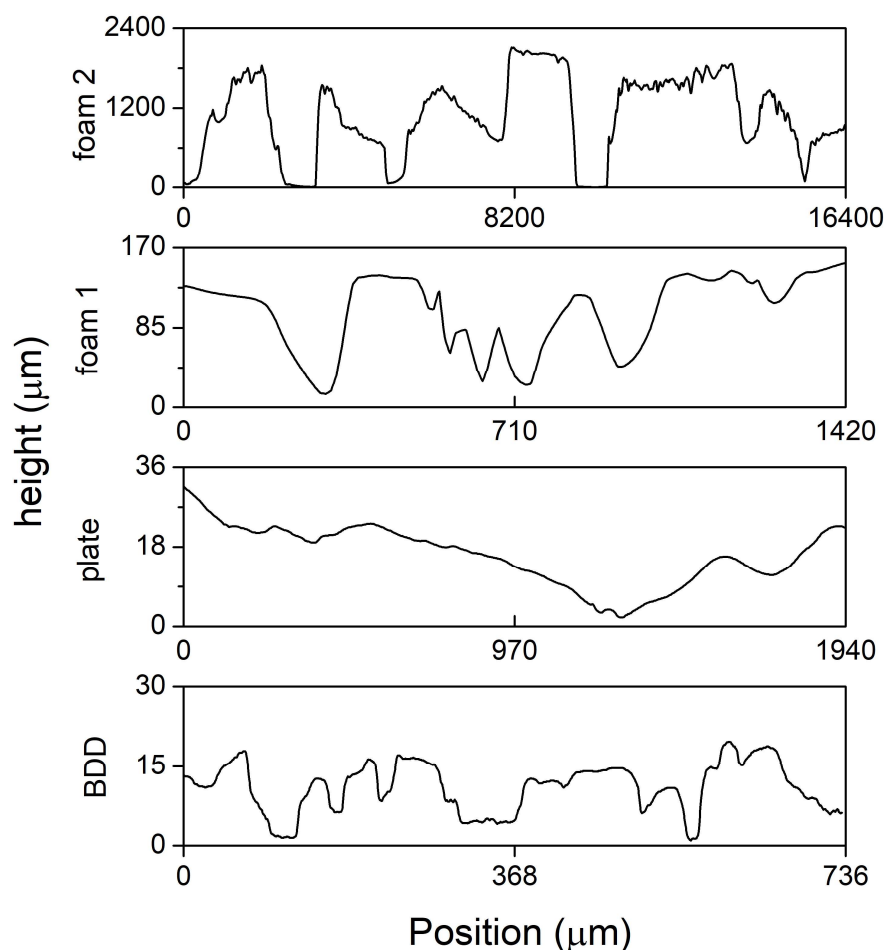


Fig. 3-5 - Surface roughness of different materials observed from optical microscopy



### 3.1.5 EASA and RF

EASA of Ti/TiO<sub>x</sub> materials was estimated based on the measurement of capacitance (Fig. 3-6) according to the method reported previously (Nayak and Chaplin, 2018) for porous TiO<sub>x</sub> materials. This method allows for taking into account only the EASA ascribed to the reactive TiO<sub>x</sub> layer since Ti substrate has negligible capacitance compared to TiO<sub>x</sub>. The EASA of Ti/TiO<sub>x</sub> plate was 2200 cm<sup>2</sup>, which corresponds to a RF of 93. This high EASA for a plate electrode might be ascribed to the roughness created by the plasma spraying technique at sub- $\mu$ m scale. The EASA of foam 1 and 2 was 1.36 and 1.83 times lower than Ti/TiO<sub>x</sub> plate (1620 cm<sup>2</sup> for foam 1 and 1200 cm<sup>2</sup> for foam 2), thus corresponding to a RF of 69 and 51, respectively. The lower EASA of foams compared to Ti/TiO<sub>x</sub> plate electrode might be mainly explained by a lack of interconnectivity between some pores. The EASA of foam 1 can also be compared to its total surface area (2186 cm<sup>2</sup>) calculated from the specific surface area obtained with Hg porosimetry. The total surface area takes into consideration both TiO<sub>x</sub>-coated and non-coated Ti surface, while the EASA takes into consideration only the TiO<sub>x</sub>-coated surface. There was only a small difference between both values, despite the fact that only the top of the foam was coated with TiO<sub>x</sub>. In fact, the specific surface area was mostly ascribed to surface roughness created by the TiO<sub>x</sub> coating at sub- $\mu$ m scale, compared to the surface area of the raw Ti foam.

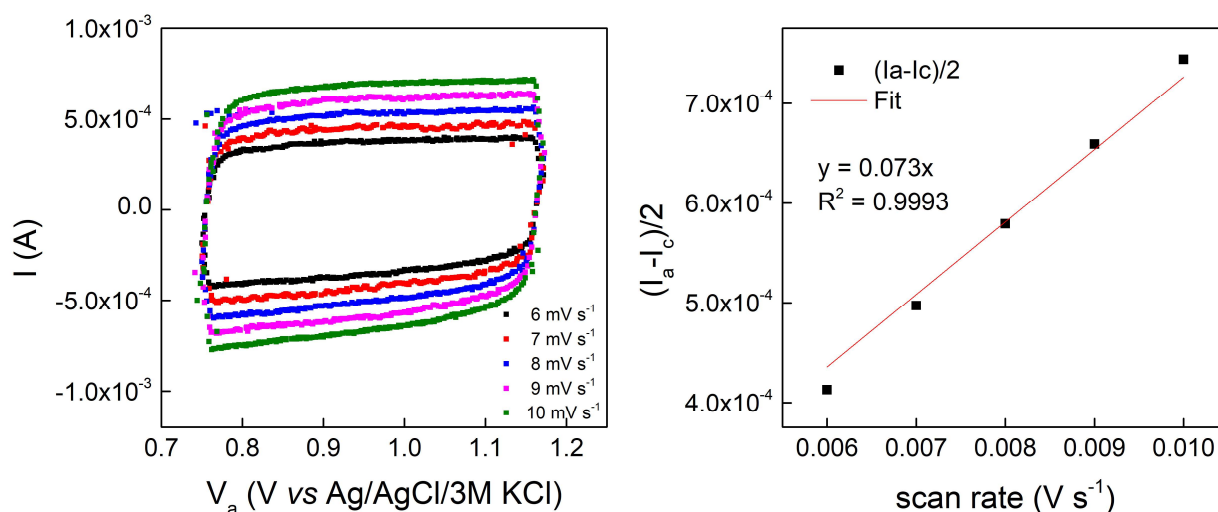


Fig. 3-6 - Measurement of double layer capacitance for Ti/TiO<sub>x</sub> foam 2 (reference electrode:



Ag/AgCl/3 M KCl, supporting electrolyte: 100 mM NaClO<sub>4</sub>, scan rate: 0.006-0.01 V s<sup>-1</sup>)

### 3.1.6 ERF

As explained previously, surface roughness at sub- $\mu\text{m}$  scale is averaged in the diffusion field when the electrodes are applied in stirred-tank (or flow-by) reactor. The ERF was calculated to estimate how the morphology of the material could potentially really enhance mass transport conditions in stirred-tank configuration. Results are depicted in [Table 3-1](#), according to different values of  $\delta$  (thickness of diffusion boundary layer).

[Table 3-1](#) Calculated values of effective roughness factor according to electrode material and thickness of the diffusion layer ( $\delta$ )

	$\delta = 7.5 \mu\text{m}$	$\delta = 30 \mu\text{m}$	$\delta = 100 \mu\text{m}$
foam 1	1.67	1.54	1.17
foam 2	4.59	4.18	3.45
Ti/TiO <sub>x</sub> plate	1.002	1.002	1.002
BDD	1.13	1.07	1.04

The mass transfer coefficient in stirred-tank reactor used in this study was determined using the limiting current technique in the ferro-ferricyanide system with BDD anode ([Fig. 3-7](#)). The value for  $\delta$  was thereby estimated to be 30  $\mu\text{m}$ . For this value of  $\delta$ , the ERF was 1.002 for Ti/TiO<sub>x</sub> plate. The surface roughness of Ti/TiO<sub>x</sub> plate at sub- $\mu\text{m}$  scale is fully averaged into the diffusion field. Thus, it could not contribute to reaching high ERF. The ERF calculated for BDD plate was also low (1.07). It was slightly higher than that of Ti/TiO<sub>x</sub> plate due to its coarser roughness observed at characteristic scale of 10  $\mu\text{m}$  ([Fig. 3-5](#)). Higher ERF (1.54) was obtained

for foam 1 thanks to the coarse surface roughness related to its porous structure. The ERF was further increased for foam 2 (4.18) because of its more open porous structure.

Besides, it is interesting to notice that the value of ERF decreases when increasing the value of  $\delta$ . The greater the diffusion layer thickness, the more the surface roughness is averaged into the diffusion field (Fig. 3-8).

As further investigated below, a high value of ERF is expected to enhance mass transport conditions. Therefore, degradation kinetics should be improved for experiments performed under mass transport limitation.

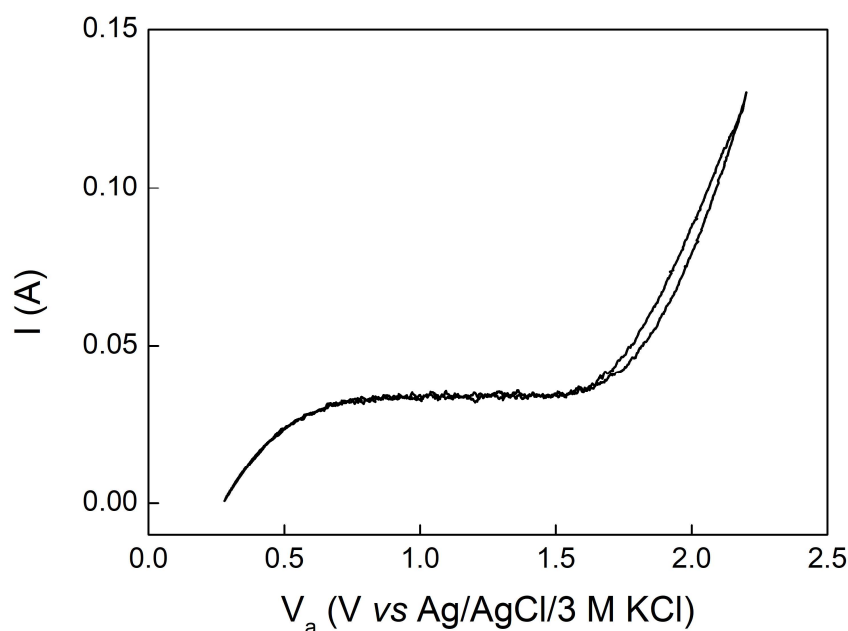


Fig. 3-7 - Cyclic voltammogram for Fe(CN)<sub>6</sub><sup>4-</sup>/Fe(CN)<sub>6</sub><sup>3-</sup> system using BDD electrode for determination of mass transfer coefficient (reference electrode: Ag/AgCl/3 M KCl, supporting electrolyte: 100 mM NaClO<sub>4</sub>, scan rate: 0.01 V s<sup>-1</sup>)

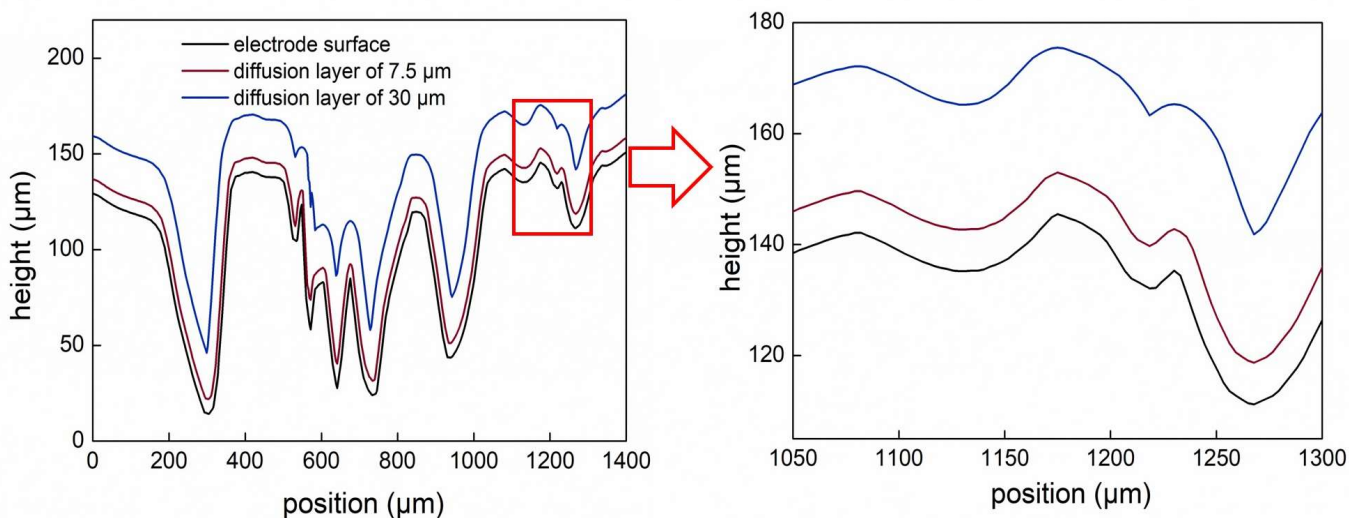


Fig. 3-8 - Observation of electrode surface (foam 1) and influence of diffusion layer thickness

## 3.2 Electrochemical reactivity of Ti/TiO<sub>x</sub> materials

### 3.2.1 OER

Electrode materials for the anodic oxidation process are usually classified in two different types, including active electrodes with low overpotential for OER (e.g., Pt) and non-active electrodes with high overpotential for OER (e.g., BDD). Non-active electrodes are usually considered as the most suitable electrodes for promoting the formation of  $\cdot\text{OH}$  from one electron oxidation of water (Eq. 3-5) instead of two-electron oxidation of water to O<sub>2</sub> (Eq. 3-6). BDD is the widely studied non-active and stable anode and represents a suitable reference for comparison of OEP measured for Ti/TiO<sub>x</sub> materials. Correction of raw LSV data and OEP calculation of Ti/TiO<sub>x</sub> plate was presented as an example (Fig. 3-9 and Fig. 3-10).

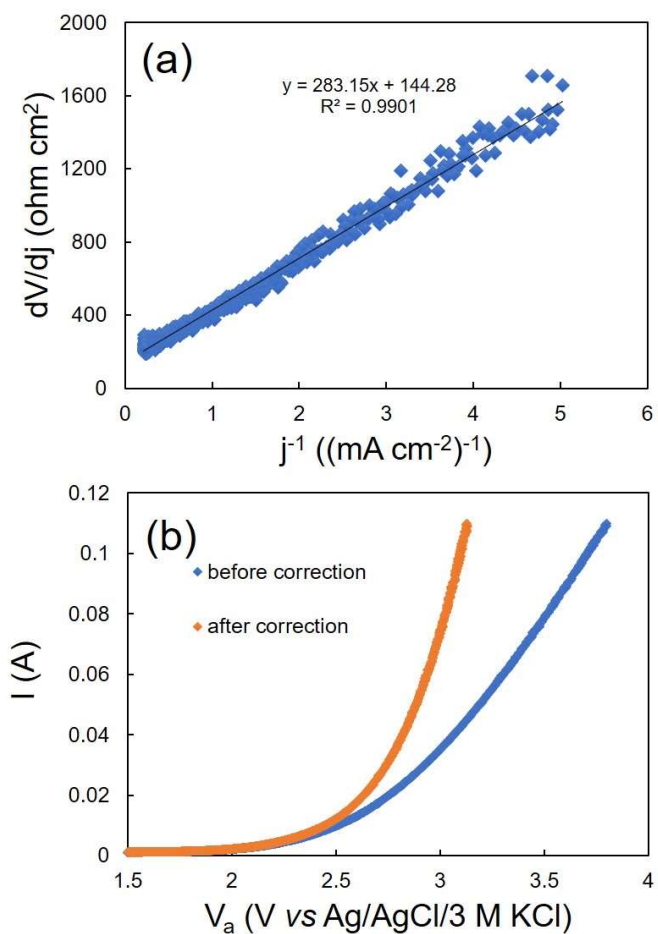


Fig. 3-9 - Correction of LSV data of Ti/TiO<sub>x</sub> plate by ohmic drop. (a) Determination of the uncompensated resistance, (b) LSV curves before and after ohmic drop correction

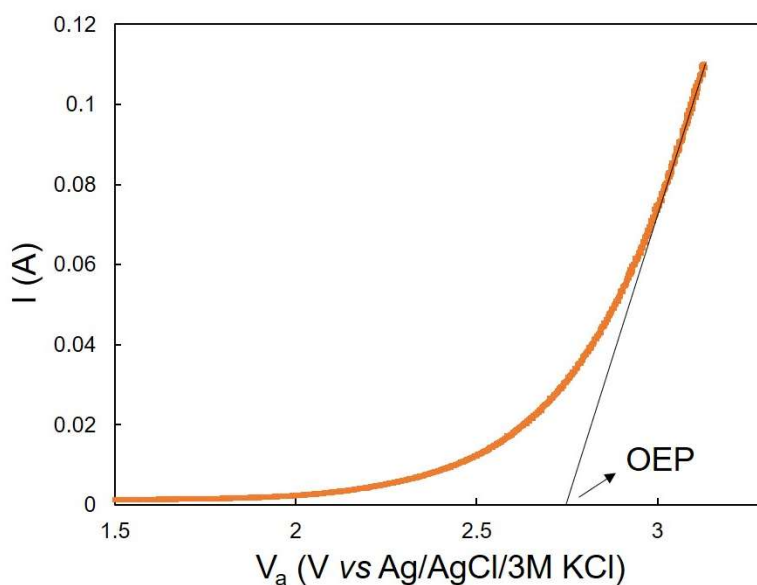
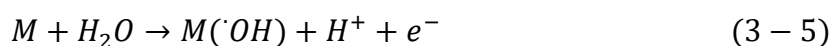


Fig. 3-10 - Calculation of OEP from corrected LSV curve (Ti/TiO<sub>x</sub> plate)

As shown in Fig. 3-11, BDD and Ti/TiO<sub>x</sub> plate have an OEP of 2.27 and 2.78 V *vs* Ag/AgCl/3 M KCl, respectively. Thus, both electrodes present high overpotential for OER since the thermodynamic potential for O<sub>2</sub> formation is 1.30 V *vs* Ag/AgCl/3 M KCl (Trellu et al., 2018a). The measured OEPs are higher than the thermodynamic potential for •OH generation, which is 2.17 V *vs* Ag/AgCl/3M KCl (Kapałka et al., 2009). Therefore, these electrodes have great potential for generation of physisorbed •OH. Similar results are usually obtained in the literature with these kinds of materials (Chen, 2004; Xie et al., 2020). Foam 1 has an OEP of 2.82 V *vs* Ag/AgCl/3 M KCl, which is similar to Ti/TiO<sub>x</sub> plate. This result indicated that the coating obtained on foam 1 might present similar reactivity than Ti/TiO<sub>x</sub> plate in terms of potential formation of •OH. On the contrary, foam 2 has a lower OEP of 2.26 V *vs* Ag/AgCl/3 M KCl. It indicated that the coating obtained on foam 2 was not sufficiently homogeneous for achieving similar reactivity than Ti/TiO<sub>x</sub> plate. The porous structure of foam 2 leads to the presence of some uncovered surface area (naked Ti surface) that is directly in contact with the electrolytic solution (Fig. 3-2). Thus, direct evolution of water to O<sub>2</sub> at naked Ti surface might be further promoted. This lower OEP might strongly enhance waste reaction of O<sub>2</sub> formation (Eq. 3-6) at the expense of •OH formation (Eq. 3-5).



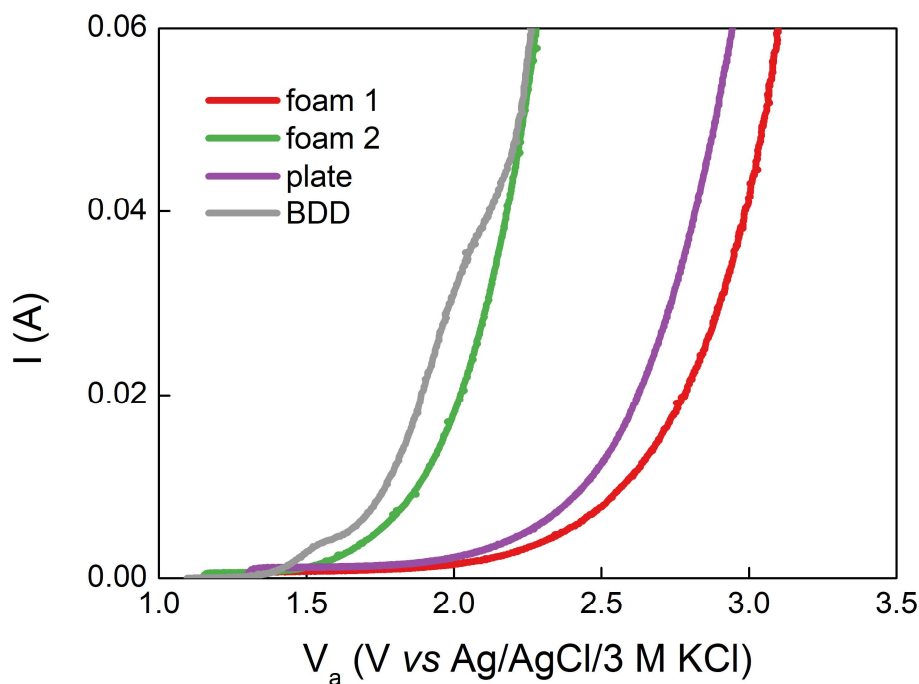


Fig. 3-11 - LSV curves of different materials used in this study (reference electrode: Ag/AgCl/3 M KCl, supporting electrolyte: 100 mM NaClO<sub>4</sub>, scan rate: 0.01 V s<sup>-1</sup>)

### 3.2.2 <sup>•</sup>OH-mediated oxidation

<sup>•</sup>OH-mediated oxidation is the most effective pathway for non-selective electro-oxidation of organic pollutants due to the high reactivity of this radical towards a large range of recalcitrant organic compounds. Fig. 3-12 depicts the reactivity of different materials for <sup>•</sup>OH generation using TA degradation as probe molecule. Besides, the generation of by-product, HTA, constituted second evidence of the presence of <sup>•</sup>OH formation (Fig. 3-13) (Jing and Chaplin, 2017). Very different degradation kinetics of TA were obtained with the different Ti/TiO<sub>x</sub> materials. BDD plate was also used for comparison as gold standard electrode for the generation of <sup>•</sup>OH. All degradation kinetics fitted well with pseudo-first order kinetics.

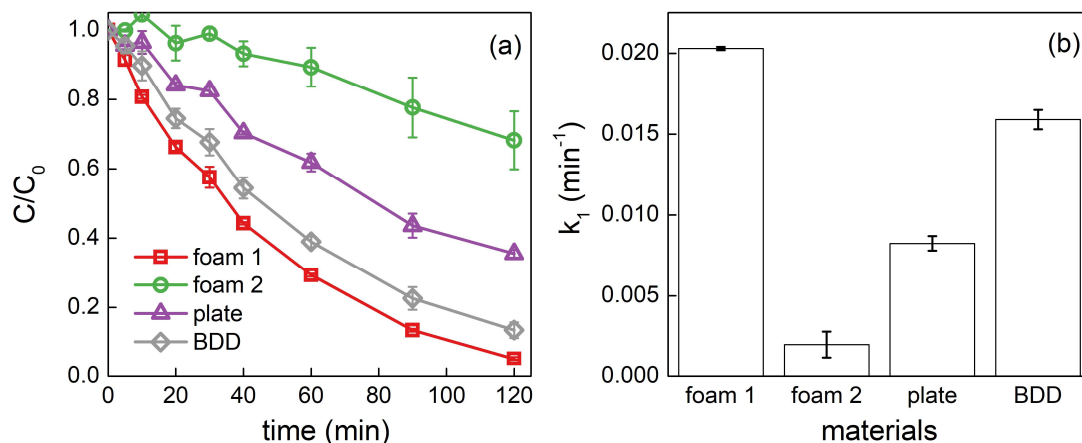


Fig. 3-12 - TA degradation kinetic (a) and pseudo first order rate constant values (b) obtained during electro-oxidation of TA with different Ti/TiO<sub>x</sub> materials and BDD anodes (initial  $C_{TA} = 0.1$  mM, effective surface area =  $23.6$  cm<sup>2</sup>,  $S_{\text{electrode}}/V_{\text{solution}} = 7.9$  m<sup>-1</sup>, current density =  $5$  mA cm<sup>-2</sup>)

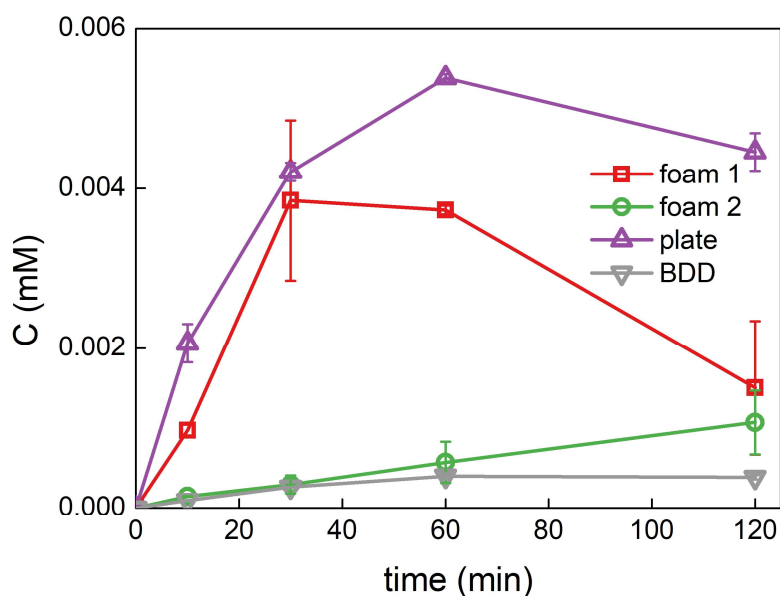


Fig. 3-13 - Generation of HTA during degradation of TA on different electrode surface (initial  $C_{TA} = 0.1$  mM, effective surface area =  $23.6$  cm<sup>2</sup>,  $S_{\text{electrode}}/V_{\text{solution}} = 7.9$  m<sup>-1</sup>, current density =  $5$  mA cm<sup>-2</sup>)

The apparent degradation kinetic rate ( $k_1$ ) of TA using BDD plate was  $(1.59 \pm 0.06) \times 10^{-2}$  min<sup>-1</sup>. By comparison, this value was divided by 1.9 using Ti/TiO<sub>x</sub> plate. Interestingly, the reactivity of

Ti/TiO<sub>x</sub> was strongly improved when using foam 1. The value of  $k_1$  was 2.4 times higher compared to Ti/TiO<sub>x</sub> plate, thus reaching a value higher than that obtained with BDD electrode. This result highlights that the porosity and coarse surface roughness of foam 1 strongly participated to enhance the degradation rate in this stirred-tank reactor. As similar coating was used for all Ti/TiO<sub>x</sub> electrodes, faster degradation rate can be ascribed to more favorable mass transport conditions, rather than different reactivity. The 2.4 times faster degradation rate obtained with foam 1 compared to Ti/TiO<sub>x</sub> plate can be correlated with the 1.5 times higher value of the ERF that promotes effective mass transport conditions. The high ERF increases the surface area availability to enhance the transport of TA from bulk to electrode surface.

Contrary to foam 1, the degradation kinetic of TA using foam 2 was much slower. This slow kinetics can be ascribed to a limitation coming from the different reactivity of foam 2. In fact, the poor reactivity of foam 2 for <sup>•</sup>OH-mediated oxidation of TA agrees with its lower OEP (Fig. 3-11). It is related to the heterogeneous distribution of the coating with uncovered surface areas. These uncovered areas are directly in contact with the electrolyte (Figs. 3-2 (e) and (f)) and promote the 2 e<sup>-</sup> oxidation of water to O<sub>2</sub>.

Overall, it appears that the porous structure of the substrate is critical for material's performance. The structure of the Ti substrate was the key parameter for (i) mass transport conditions, depending on surface roughness and morphology (ii) material reactivity, depending on the homogeneity of the TiO<sub>x</sub> coating.

### **3.3 Degradation and mineralization of a model pollutant: effectiveness and reaction mechanisms**

#### **3.3.1 Degradation kinetics of PCT**



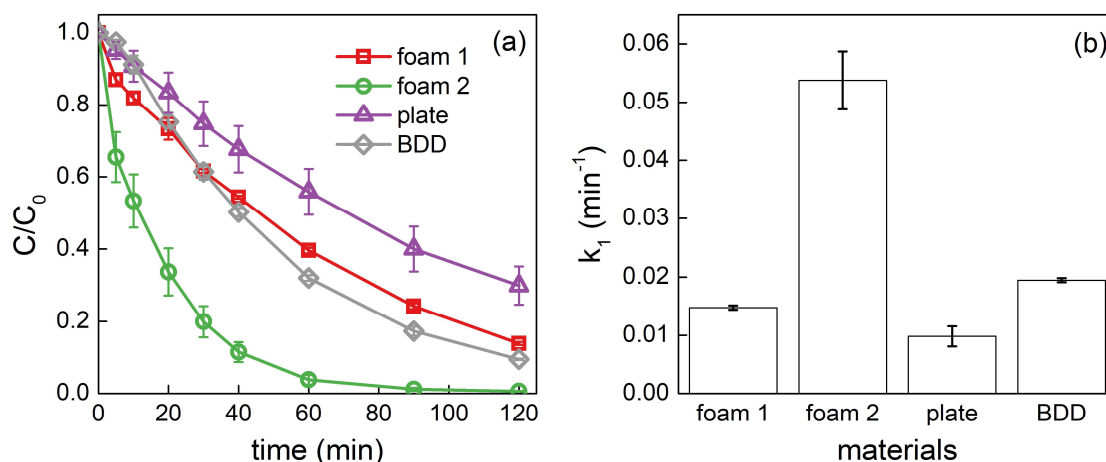


Fig. 3-14 - Oxidative degradation kinetic (a) and pseudo first order rate constant (b) obtained during electro-oxidation of PCT using different Ti/TiO<sub>x</sub> materials and BDD as anode (initial  $C_{PCT} = 0.1$  mM, effective surface area =  $23.6$  cm<sup>2</sup>,  $S_{\text{electrode}}/V_{\text{solution}} = 7.9$ , current density =  $5$  mA cm<sup>-2</sup>)

The results presented in Fig. 3-14 show different degradation kinetics behaviors for PCT degradation using different anode materials. Compared to TA degradation, similar trends were obtained. The apparent degradation kinetic was  $(0.98 \pm 0.17) \times 10^{-2}$  min<sup>-1</sup> for Ti/TiO<sub>x</sub> plate. It was multiplied by 1.5 with Ti/TiO<sub>x</sub> foam 1 (thus reaching a value close to that obtained with BDD). It can also be correlated to its more favorable surface roughness (higher ERF) that favors mass transport conditions, as previously discussed.

Interestingly, the faster degradation kinetic of PCT was obtained using foam 2. The apparent degradation kinetic was even 2.8 and 5.5 times higher compared to BDD and Ti/TiO<sub>x</sub> plate, respectively. It suggested that the degradation of PCT was not limited by generation of  $\cdot\text{OH}$ , on the contrary to the degradation of TA. Previous results highlighted the lower reactivity of foam 2 for  $\cdot\text{OH}$ -mediated oxidation because of heterogeneous TiO<sub>x</sub> coating. Therefore, these results indicated that PCT might also be degraded through DET (as further investigated below). This reaction mechanism would be more independent of the homogeneity of TiO<sub>x</sub> coating, compared to  $\cdot\text{OH}$ -mediated oxidation. With lower limitation from material reactivity (compared to degradation of TA), foam 2 was able to achieve very fast degradation kinetic of PCT because of

its favorable morphology for mass transport of PCT from the bulk to the electrode surface. In fact, its open porosity (Fig. 3-2 (d)) and suitable surface roughness (Fig. 3-5) allowed for reaching high value of ERF (4.2 and 2.7 times higher than that of Ti/TiO<sub>x</sub> plate and foam 1, respectively).

The suitability of foam 2 for removal of organic compounds able of reacting via DET was further confirmed by using OA as model compound since it reacts very slowly with hydroxyl radicals ( $k = 1.4 \times 10^6 \text{ M}^{-1} \text{ s}^{-1}$ ) (Shih et al., 2019). Results presented in Fig. 3-15 showed that foam 2 was able to strongly increase the degradation kinetic of OA compared to BDD electrode, thus confirming the suitability of this material for the removal of organic compounds through DET.

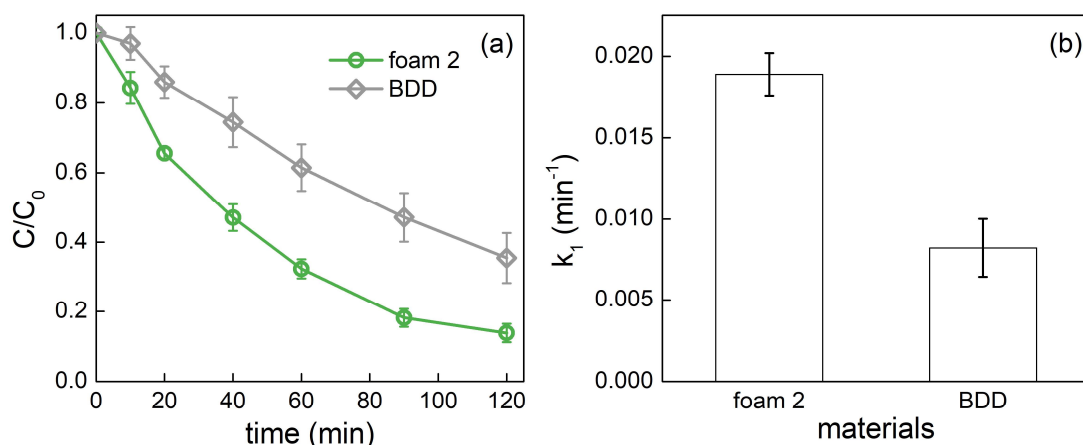


Fig. 3-15 - Degradation kinetic (a) and values of pseudo first order rate constants (b) obtained during anodic oxidation of oxalic acid (OA) with Ti/TiO<sub>x</sub> material (foam 2) and BDD anodes (initial  $C_{OA} = 0.4 \text{ mM}$ , effective surface area =  $23.6 \text{ cm}^2$ ,  $S_{\text{electrode}}/V_{\text{solution}} = 7.9 \text{ m}^{-1}$ , current density =  $5 \text{ mA cm}^{-2}$ )

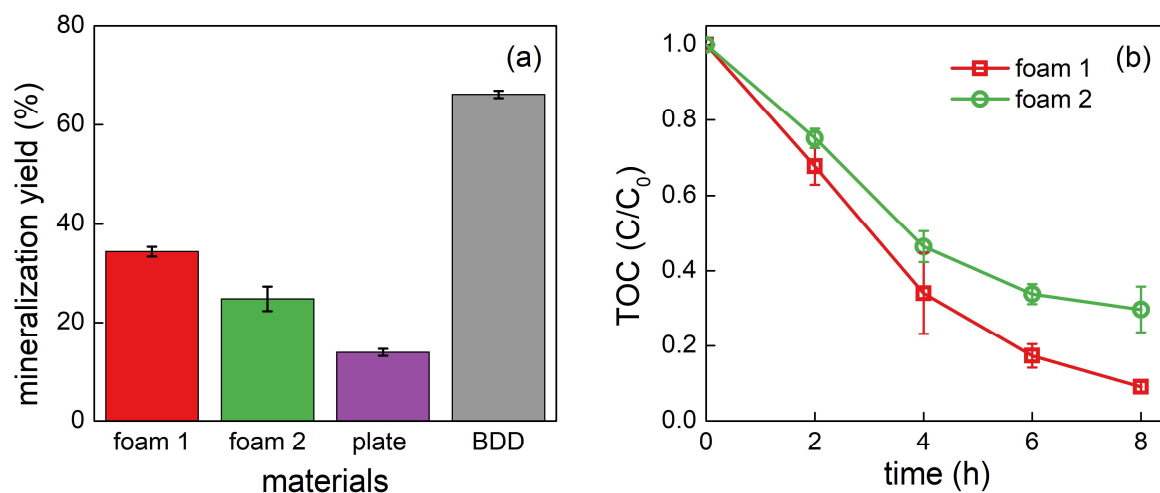


Fig. 3-16 - Mineralization yield of PCT after 2 h (a) and 8 h (b) of electrolysis using different Ti/TiO<sub>x</sub> materials and BDD as anode under following operating conditions: initial C<sub>PCT</sub> = 0.1 mM, initial TOC = 9.6 mg L<sup>-1</sup>, effective surface area = 23.6 cm<sup>2</sup>, S<sub>electrode</sub> c/V<sub>solution</sub> = 7.9 m<sup>-1</sup>, current density = 5 mA cm<sup>-2</sup>

### 3.3.2 Mineralization of PCT by foam 1 and foam 2

The degradation of the mother molecule might lead to the generation of toxic by-products. It might also be important to achieve complete mineralization of organic compounds. Therefore, the removal of PCT was also assessed as regards to the mineralization yield achieved after 2 h of treatment (Fig. 3-16 (a)). Much higher mineralization yield was obtained with BDD (66%) compared to Ti/TiO<sub>x</sub> plate (14%). Among different Ti/TiO<sub>x</sub> materials, the maximum mineralization yield was obtained with foam 1 (34%). The excellent performance of foam 1 comes from (i) its suitable porous structure for mass transport enhancement and (ii) its capacity to generate <sup>•</sup>OHs for non-selective degradation of recalcitrant by-products. The comparison of the behavior of foam 1 and foam 2 for mineralization of PCT was further investigated and mineralization kinetics have been represented in Fig. 3-16 (b). Slightly faster mineralization was obtained with foam 1 during the first hours of treatment, but the most significant difference was obtained on longer treatment times (4-8 h). The concentration of TOC in the solution reached almost a plateau with foam 2, indicating that strongly recalcitrant

organic compounds were remaining in the solution. These results confirmed that by-products that were not able to react through DET accumulated in the solution because of the poor reactivity of foam 2 for promoting <sup>•</sup>OH-mediated oxidation. As regards to foam 1, these recalcitrant by-products were more easily removed through <sup>•</sup>OH-mediated oxidation. The higher reactivity of foam 1 for <sup>•</sup>OH generation was crucial for achieving higher mineralization yield of PCT. [Table 3-2](#) is provided to compare these results with previous data obtained in the literature using TiO<sub>x</sub> materials.

Table 3-2 Comparison of Ti/TiO<sub>x</sub> foam 1 performance in terms of model pollutant degradation with published studies

Anode	Fabrication method	Composition	Structure	Model pollutant	Initial concentration	Selectrode/ V <sub>solution</sub>	Current density	Cathode	K <sub>1</sub> (min <sup>-1</sup> )	time (90% pollutant degradation)	TOC removal	COD removal	Reference
Ti/Ti <sub>4</sub> O <sub>7</sub>	plasma spraying	Ti <sub>4</sub> O <sub>7</sub>	plate electrode	Tetracycline	5 mg L <sup>-1</sup>		15mA cm <sup>-2</sup>	Ti plate	(8.2±0.3)×10 <sup>-2</sup>	25 min	75.7% (40 min)		(Wang et al., 2018)
Ti/TiO <sub>x</sub>	plasma deposition	Ti <sub>3</sub> O <sub>5</sub> /Ti <sub>4</sub> O <sub>7</sub> /Ti <sub>5</sub> O <sub>9</sub> /Ti <sub>6</sub> O <sub>11</sub>	plate electrode	amoxicillin	0.1 mM	10.4 m <sup>-1</sup>	5 mA cm <sup>-2</sup>	carbon-felt	0.1	25 min	69% (8 h)		(Ganiyu et al., 2016)
Ti <sub>4</sub> O <sub>7</sub>	Spark plasma sintering	Ti <sub>4</sub> O <sub>7</sub> /Ti <sub>5</sub> O <sub>9</sub>		methyl orange	150 mg L <sup>-1</sup>		6 mA cm <sup>-2</sup>	Ti mesh	0.0035	25 min		67% (5 h)	(Wang et al., 2020)
Ti <sub>4</sub> O <sub>7</sub>	high-temperature sintering	high purity Ti <sub>4</sub> O <sub>7</sub>	porous structure	PFOA/PFO S	0.5 mM/0.1 mM		5 mA cm <sup>-2</sup>	stainless steel sheets	(3.4±0.11)×10 <sup>-2</sup> / (1.3±0.055)×10 <sup>-2</sup>	75 min/165 min	>95%/90.3% (3 h)		(Lin et al., 2018)
Ti <sub>4</sub> O <sub>7</sub>	high temperature sintering	Ti <sub>4</sub> O <sub>7</sub> as major phase	porous structure	tetracycline	50 ppm		3 mA cm <sup>-2</sup>	304 stainless steel plate	2.46×10 <sup>-2</sup>	0.6 h			(Liang et al., 2018)
Ti/TiO <sub>x</sub>	plasma spraying	Ti <sub>4</sub> O <sub>7</sub> /Ti <sub>6</sub> O <sub>11</sub> /Ti <sub>8</sub> O <sub>15</sub>	porous structure	paracetamol	0.1 mM	7.9 m <sup>-1</sup>	5 mA cm <sup>-2</sup>	carbon felt	(1.48±0.04)×10 <sup>-2</sup>	120 min	82.7% (6 h)		This study (Ti/TiO <sub>x</sub> foam 1)

### 3.3.3 Degradation mechanism of PCT: quenching experiments

Fig. 3-17 shows the time-course for degradation of PCT in presence of EtOH and TBA as quenchers. The results were compared with PCT degradation without quencher. Results obtained with different electrode materials are compared. In the absence of any quencher,  $\cdot\text{OH}$  accumulated at the vicinity of the electrode surface. When PCT molecules are transported from bulk solution to electrode surface, they react quickly with  $\cdot\text{OH}$  as a result of both (i) high reaction rate constant with  $\cdot\text{OH}$  and (ii) mass transport-limited conditions resulting in generation of  $\cdot\text{OH}$  in excess compared to the amount of PCT to be oxidized. When excessive EtOH was added to the solution,  $\cdot\text{OH}$  reacted with this large amount of EtOH, thus avoiding their accumulation at the electrode surface. Therefore, PCT molecules were not able to react through  $\cdot\text{OH}$ -mediated oxidation. However, they could still reach the electrode surface for oxidation *via* DET. This large amount of EtOH was also able to react with  $\text{SO}_4^{\cdot-}$  so that possible reaction of PCT through  $\text{SO}_4^{\cdot-}$ -mediated oxidation could also be avoided. When excessive TBA was added to the PCT solution, similar phenomenon occurred for  $\cdot\text{OH}$  scavenging. However, the lower reaction rate constant of TBA with  $\text{SO}_4^{\cdot-}$  implied that  $\text{SO}_4^{\cdot-}$ -mediated oxidation might still occur in this case.

Similar degradation kinetics were obtained for both foam 1 and Ti/TiO<sub>x</sub> plate when using TBA or EtOH as quencher, indicating that  $\text{SO}_4^{\cdot-}$  were not significantly involved in the degradation of PCT.

When adding EtOH as quencher, a fraction of PCT was still degraded when using BDD (63% at  $t = 2$  h), Ti/TiO<sub>x</sub> plate (44% at  $t = 2$  h) and foam 1 (62% at  $t = 2$  h). These results confirmed that PCT was also able to react through DET. However, degradation kinetics were much slower than without EtOH, emphasizing the key role of  $\cdot\text{OH}$  during PCT oxidation. Foam 2 showed a very different trend compared to other electrodes. When adding EtOH as quencher, PCT degradation kinetic did not significantly change. Almost complete degradation was still obtained after 2 h. This result further confirmed that DET was actually the key mechanism for explaining PCT

degradation at foam 2.

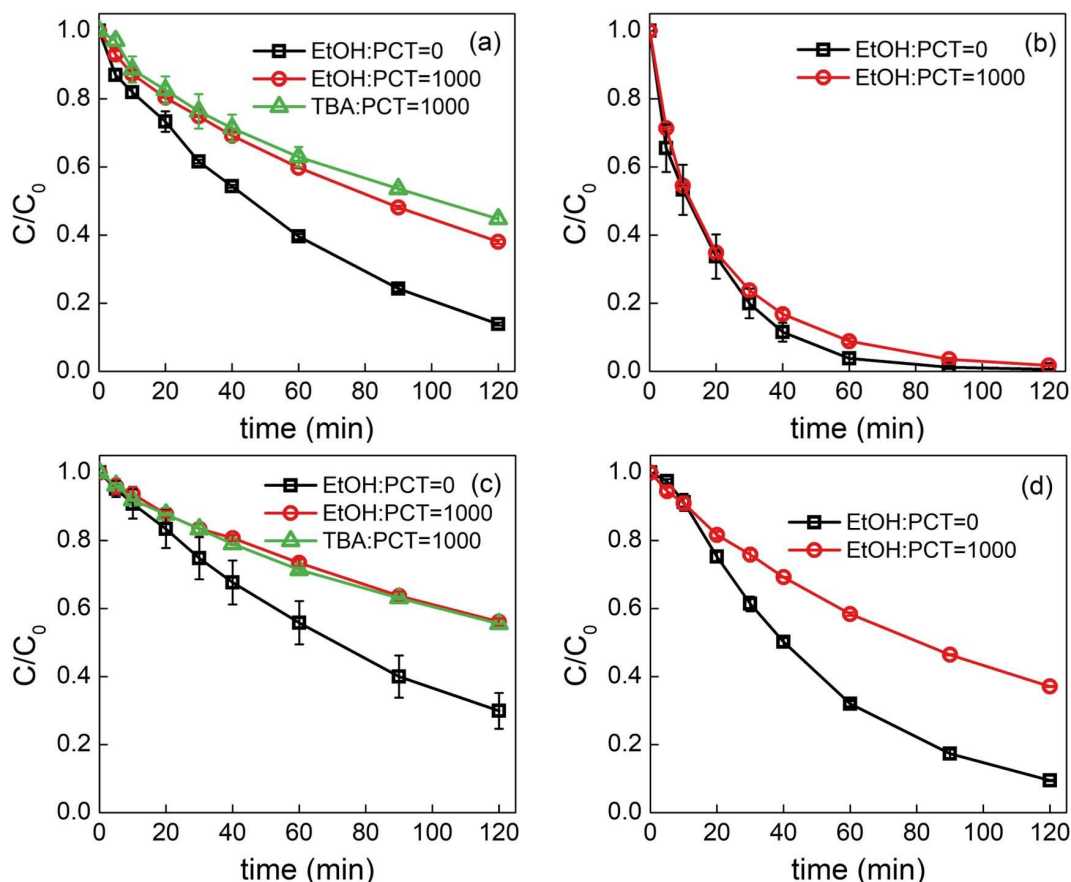


Fig. 3-17 - PCT degradation during anodic oxidation process using different anode materials in the presence and absence of EtOH and TBA: (a) foam 1, (b) foam 2, (c) Ti/TiO<sub>x</sub> plate and (d) BDD (initial  $C_{PCT} = 0.1$  mM, effective surface area = 23.6 cm<sup>2</sup>,  $S_{electrode}/V_{solution} = 7.9$  m<sup>-1</sup>, current density = 5 mA cm<sup>-2</sup>,  $mol_{EtOH/TBA}/mol_{PCT} = 1000$ )

### 3.3.4 Formation of degradation by-products

Complete mineralization of an organic compound such as PCT is a complex process involving different intermediate steps. Different primary aromatic by-products can be generated via different pathways. In this case, HQ and BQ were identified as main primary aromatic by-products. As proposed by previous studies, PCT can be firstly degraded to HQ, which is further oxidized to BQ by  $\cdot OH$  (Fig. 3-18) (Sirés et al., 2006). These two by-products were analyzed in both quenching and non-quenching experiments in order to better understand

reaction mechanisms. Fig. 3-19 depicts the evolution of HQ and BQ during 2 hours of treatment of PCT (Figs. 3-19 (a)-(d)) and the evolution of the ratio between the sum of HQ + BQ in the solution and the amount of PCT degraded (Fig. 3-19 (e)).

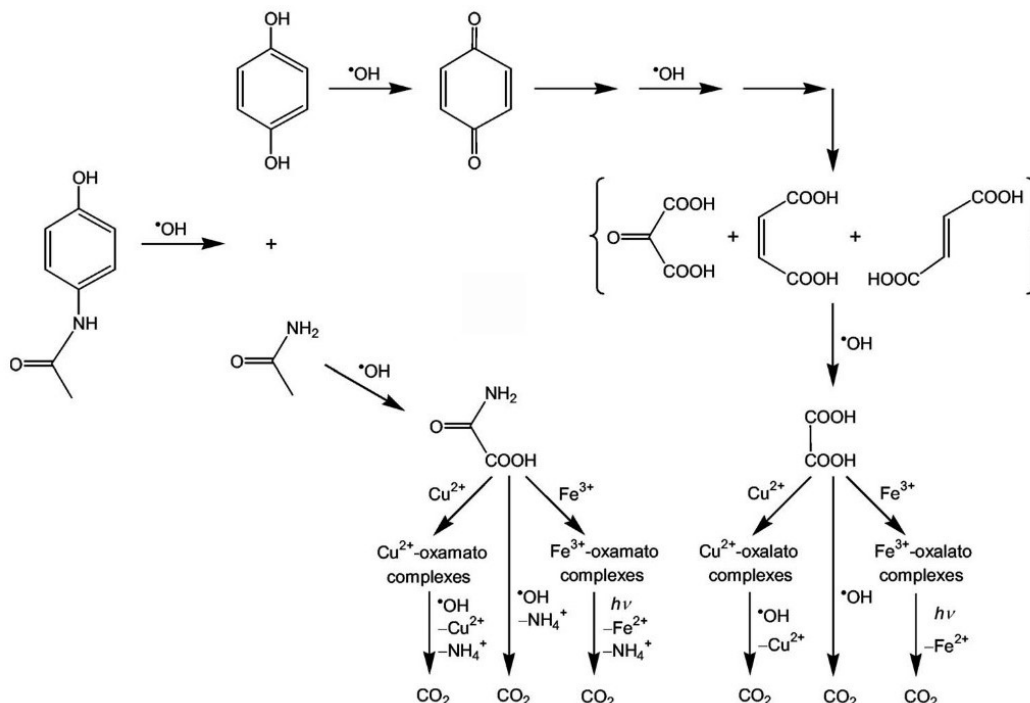


Fig. 3-18 - Paracetamol degradation mechanism proposed by Sirés et al. (Sirés et al., 2006)

It is interesting to notice that foam 1 and Ti/TiO<sub>x</sub> plate behaved similarly to BDD in absence of EtOH. Very low accumulation (<0.006 mM) of HQ and BQ was observed (Figs. 3-19 (a), (c) and (d)), suggesting comparable formation and destruction rate of these by-products. HQ and BQ initially accounted for 40-80% of degraded PCT at the beginning of electrolysis, indicating that they were the primary by-products initially generated from oxidative degradation of PCT. This fraction then rapidly decreased throughout the 2 h electrolysis until less than 7% (Fig. 3-19 (e)) suggesting the continuous destruction of these aromatic by-products to other intermediates such as carboxylic acids. For foam 2, much higher accumulation of HQ and BQ was observed during the treatment. Faster PCT degradation kinetic by foam 2 through DET (see subsection 3.3.3) initially led to a higher accumulation of HQ and BQ. Meanwhile, HQ and BQ accounted for a higher fraction of degraded PCT (Fig. 3-19 (e)) during the first hour of treatment. It indicated that further oxidation of HQ and BQ was less favored at foam 2. The possible reason



might be the lower generation rate of  $\cdot\text{OH}$  of the foam 2 and the low reactivity of BQ through DET reaction (Jing and Chaplin, 2017). It is consistent with DFT calculations from Zaky and Chaplin (2014) highlighting that BQ oxidation was primarily due to  $\cdot\text{OH}$ -mediated oxidation at the surface of Ti<sub>4</sub>O<sub>7</sub> electrode (Zaky and Chaplin, 2014).

In the presence of EtOH as quencher, significant HQ accumulation was observed for Ti/TiO<sub>x</sub> plate, foam 1 and BDD to a lesser extent. The accumulation of HQ in quenching experiment suggested that PCT can be degraded to HQ through DET but  $\cdot\text{OH}$  were required for further degradation. Moreover, BQ can also be easily reduced to HQ at cathode (Mousset et al., 2016), thus favoring the accumulation of HQ rather than BQ. Besides, the fraction of HQ + BQ (compared to the amount of PCT degraded) was much higher all along the treatment for all electrodes when adding EtOH as quencher. This result confirmed the important role of  $\cdot\text{OH}$  in further degradation of these aromatic by-products. In contrast, foam 2 led to the accumulation of BQ and HQ at relatively high concentrations. As these by-products might represent an environmental issue or a danger for human health (Bolton et al., 2000; Hamdi El Najjar et al., 2014), foam 2 did not appear as a suitable electrode material.

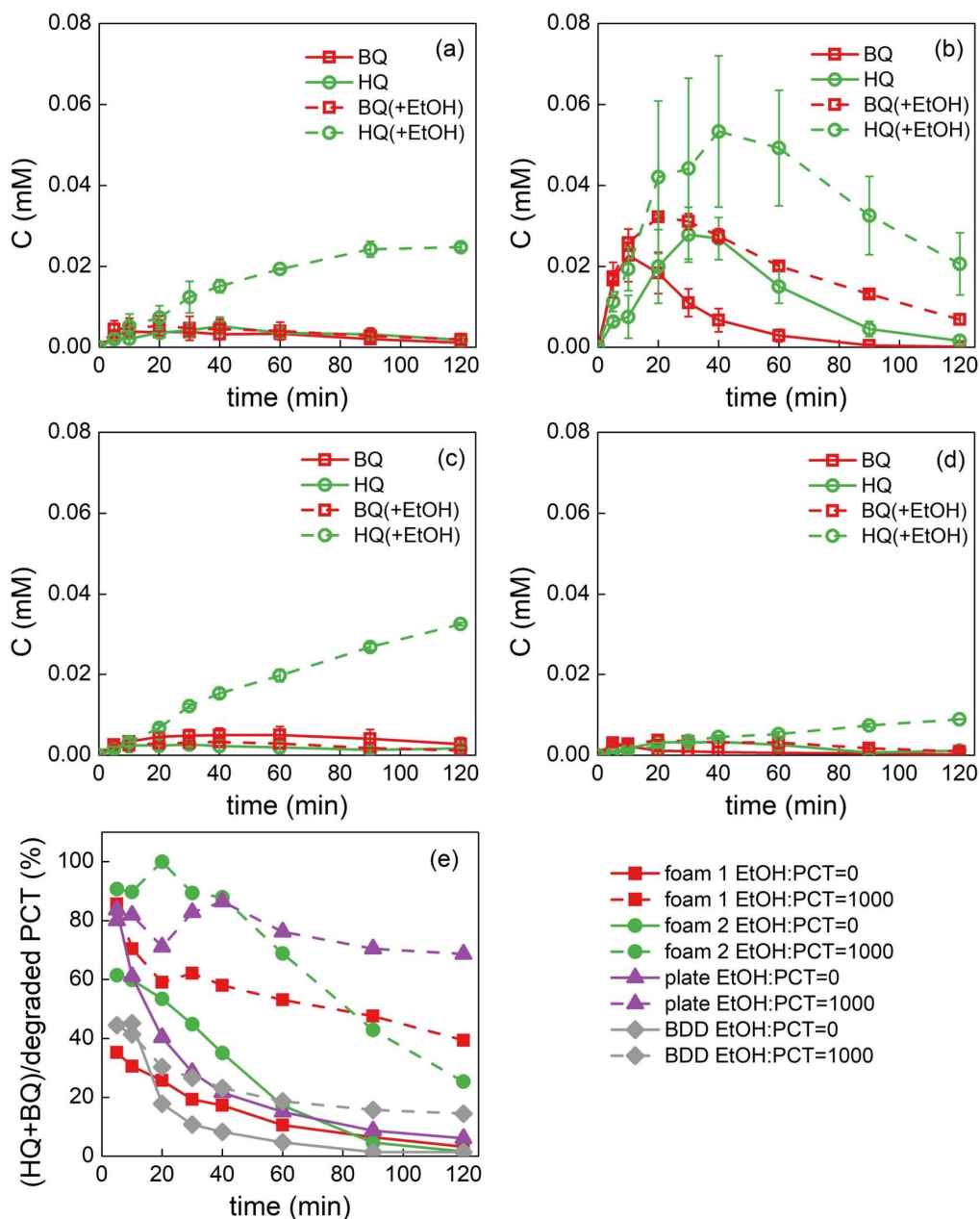


Fig. 3-19 - Evolution of by-products during PCT degradation by different materials in the absence and presence of EtOH: (a) foam 1, (b) foam 2, (c) Ti/TiO<sub>x</sub> plate and (d) BDD and (e) evolution of total concentration of (HQ + BQ) (initial CPCT = 0.1 mM, effective surface area = 23.6 cm<sup>2</sup>,  $S_{\text{electrode}}/V_{\text{solution}} = 7.9 \text{ m}^{-1}$ , current density = 5 mA cm<sup>-2</sup>,  $\text{mol}_{\text{EtOH/TBA}}/\text{mol}_{\text{PCT}} = 1000$ )

### 3.4 Application of foam 1 in flow-through configuration

Previous tests have shown the capacity of Ti/TiO<sub>x</sub> foams to improve both degradation and mineralization rates compared to Ti/TiO<sub>x</sub> plate, even in a stirred-tank configuration. An additional experiment was performed to assess the suitability of the application of foam 1 in flow-through configuration. The solution was continuously recirculated through the electrode and a similar  $S_{\text{electrode}}/V_{\text{solution}}$  ratio was used for proper comparison of results obtained in stirred-tank and flow-through configurations. The apparent rate constant increased from  $(1.48 \pm 0.04) \times 10^{-2} \text{ min}^{-1}$  in stirred-tank configuration to  $(3.77 \pm 0.16) \times 10^{-2} \text{ min}^{-1}$  in flow-through configuration. At high flow rate, the boundary diffusion film can potentially reach a value lower than the electrode pore radius. In the case of foam 1, the median pore radius (as regards to the total surface area) was 7.5  $\mu\text{m}$  (from Hg porosimetry data). Comparing this value to the diffusion layer thickness (obtained from the limiting current density technique) in stirred-tank reactor (30  $\mu\text{m}$ ) allows for highlighting the benefit of this flow-through configuration. These more favorable diffusion conditions allows for enhancing PCT degradation kinetic (Fig. 3-20) due to convective-enhanced mass transport of organic compounds from bulk to the electrode surface in flow-through configuration (Zaky and Chaplin, 2013; Trelu et al., 2018a; Liu et al., 2020).

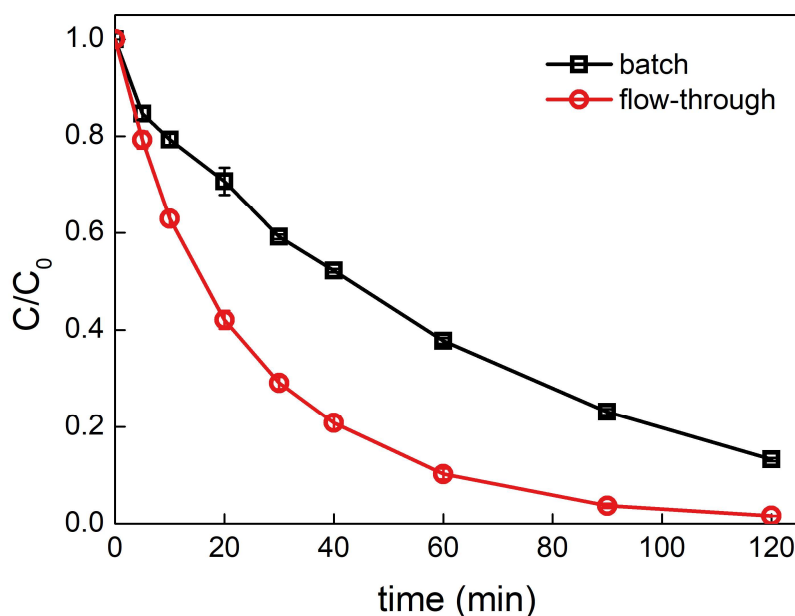


Fig. 3-20 - PCT concentration kinetic during anodic oxidation with foam 1 in batch and

flow-through mode with continuous recirculation of the solution flowing through the electrode ( $[PCT]_0 = 0.1 \text{ mM}$ , effective surface area =  $9.6 \text{ cm}^2$ ,  $S_{\text{electrode}}/V_{\text{solution}} = 7.9 \text{ m}^{-1}$ , current density =  $5 \text{ mA cm}^{-2}$ , flux =  $1200 \text{ L h}^{-1} \text{ m}^{-2}$ )

### 3.5 Electrode stability

The stability of electrodes was assessed by monitoring Ti leaching in the solution and following the degradation kinetic evolution of PCT during several successive cycles.

Ti analysis results show that Ti concentration in the solution was lower than the detection limit of  $0.05 \text{ mg L}^{-1}$ . Fig. 3-21 shows the PCT degradation kinetics by Ti/TiO<sub>x</sub> plate during different cycles. The pseudo first order rate constant ranges from  $0.008\text{-}0.011 \text{ min}^{-1}$ , suggesting the good stability of the electrode.

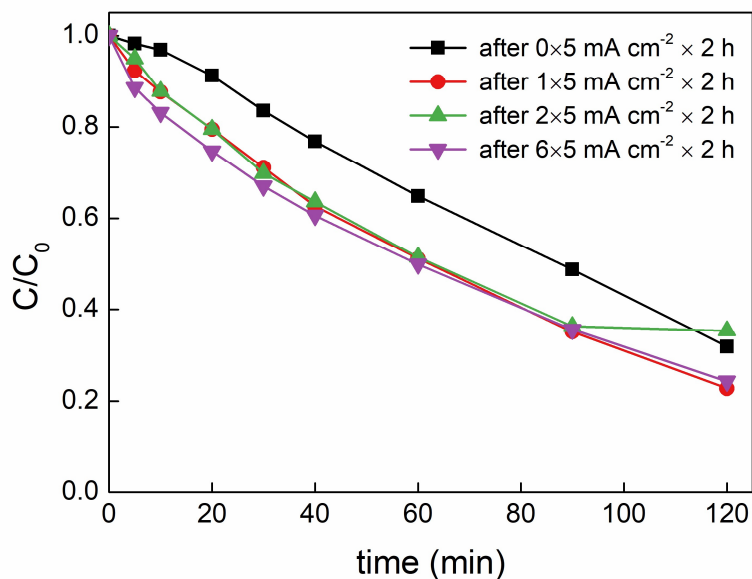


Fig. 3-21 - Evolution of the concentration of paracetamol ( $C/C_0$ ) using Ti/TiO<sub>x</sub> plate electrode at  $5 \text{ mA cm}^{-2}$ . The same electrode was used for several repetitive cycles (initial  $C_{PCT} = 0.1 \text{ mM}$ , effective surface area =  $23.6 \text{ cm}^2$ ,  $S_{\text{electrode}}/V_{\text{solution}} = 7.9 \text{ m}^{-1}$ , current density =  $5 \text{ mA cm}^{-2}$ )

## 4. Conclusions

Porous Ti/TiO<sub>x</sub> electrodes used in this study were obtained from plasma spraying technique on various Ti substrates. The morphology of foam 2 did not appear to be suitable for non-selective removal of recalcitrant compounds from water. The open porosity structure is optimal for mass transport conditions and allows faster reaction of organic compounds through DET. Unfortunately, this structure also prevents the deposition of a homogeneous TiO<sub>x</sub> layer. The presence of uncovered Ti surface that is easily accessible to the electrolyte hinders the formation of ·OH, as highlighted from experiments with probe molecules and quenchers. On the contrary, the morphology of foam 1 allowed for a homogeneous TiO<sub>x</sub> coating, thus promoting ·OH-mediated oxidation of organic compounds. This latter reaction mechanism enables to increase mineralization yields owing to non-selective oxidation of recalcitrant by-products.

In stirred-tank reactor, the degradation kinetic of PCT and TA by anodic oxidation with Ti/TiO<sub>x</sub> foam 1 was 1.5 and 2.4 times higher than the value obtained with Ti/TiO<sub>x</sub> plate, respectively. The coarse roughness of foam 1 improved mass transport conditions even in stirred-tank configuration since the characteristic scale of the roughness was larger than the thickness of the diffusion boundary layer. The calculation of the ERF value highlighted the importance of this coarse roughness. The degradation kinetic of PCT in flow-through configuration with Ti/TiO<sub>x</sub> foam 1 was 3.9 times higher than with Ti/TiO<sub>x</sub> plate in stirred-tank reactor, thanks to the convective-enhanced mass transport. It corresponds to a 1.9 times enhancement compared to BDD plate (gold standard electrode for such application). Further mass transport enhancement would be achieved in flow-through configuration by using porous materials with lower pore size in order to reduce the limitation from diffusion of pollutants within pores. However, the great advantage of such foams with larger pore size is its capacity to be used with less fouling issues and lower pressure drop for the treatment of real effluents.

## Acknowledgements

Jing Ma acknowledges China Scholarship Council for the financial support for her PhD work

(201906970041). Authors acknowledge Saint-Gobain Research Provence for providing TiO<sub>x</sub> electrodes. Authors acknowledge Chloé Fourdrin for Raman spectroscopy analyses. Jing Ma acknowledges Thibault Dubois for his help with the Python program.

## References

- Anipsitakis, G.P., Dionysiou, D.D., 2004. Radical generation by the interaction of transition metals with common oxidants. *Environ. Sci. Technol.* 38, 3705–3712. <https://doi.org/10.1021/es035121o>
- Attri, P., Kim, Y.H., Park, D.H., Park, J.H., Hong, Y.J., Uhm, H.S., Kim, K.N., Fridman, A., Choi, E.H., 2015. Generation mechanism of hydroxyl radical species and its lifetime prediction during the plasma-initiated ultraviolet (UV) photolysis. *Sci. Rep.* 5, 1–8. <https://doi.org/10.1038/srep09332>
- Bockris, J.O., Otagawa, T., 1984. The Electrocatalysis of Oxygen Evolution on Perovskites. *J. Electrochem. Soc.* 131, 290–302. <https://doi.org/10.1149/1.2115565>
- Bolton, J.L., Trush, M.A., Penning, T.M., Dryhurst, G., Monks, T.J., 2000. Role of quinones in toxicology. *Chem. Res. Toxicol.* 13, 135–160. <https://doi.org/10.1021/tx9902082>
- Buxton, G. V., Greenstock, C.L., Helman, W.P., Ross, A.B., 1988. Critical Review of rate constants for reactions of hydrated electrons, hydrogen atoms and hydroxyl radicals ( $\cdot\text{OH}$ / $\cdot\text{O}^-$  in Aqueous Solution. *J. Phys. Chem. Ref. Data* 17, 513–886. <https://doi.org/10.1063/1.555805>
- Cai, J., Zhou, M., Pan, Y., Du, X., Lu, X., 2019. Extremely efficient electrochemical degradation of organic pollutants with co-generation of hydroxyl and sulfate radicals on Blue-TiO<sub>2</sub> nanotubes anode. *Appl. Catal. B Environ.* 257, 117902. <https://doi.org/10.1016/j.apcatb.2019.117902>
- Chen, G., 2004. Electrochemical technologies in wastewater treatment. *Sep. Purif. Technol.* 38, 11–41. <https://doi.org/10.1016/j.seppur.2003.10.006>
- De Faria, L.A., Boodts, J.F.C., Trasatti, S., 1996. Electrocatalytic properties of ternary oxide mixtures of composition Ru<sub>0.3</sub>Ti<sub>(0.7-x)</sub>Ce<sub>x</sub>O<sub>2</sub>: Oxygen evolution from acidic solution. *J. Appl. Electrochem.* 26, 1195–1199. <https://doi.org/10.1007/BF00243745>
- Ganiyu, S.O., Martínez-Huitle, C.A., Oturan, M.A., 2021. Electrochemical advanced oxidation processes for wastewater treatment: Advances in formation and detection of reactive species and mechanisms. *Curr. Opin. Electrochem.* 27, 100678.

<https://doi.org/10.1016/j.coelec.2020.100678>

- Ganiyu, S.O., Oturan, N., Raffy, S., Cretin, M., Esmilaire, R., van Hullebusch, E., Esposito, G., Oturan, M.A., 2016. Sub-stoichiometric titanium oxide (Ti<sub>4</sub>O<sub>7</sub>) as a suitable ceramic anode for electrooxidation of organic pollutants: A case study of kinetics, mineralization and toxicity assessment of amoxicillin. *Water Res.* 106, 171–182. <https://doi.org/10.1016/j.watres.2016.09.056>
- Garcia-Segura, S., Ocon, J.D., Chong, M.N., 2018. Electrochemical oxidation remediation of real wastewater effluents — A review. *Process Saf. Environ. Prot.* 113, 48–67. <https://doi.org/10.1016/j.psep.2017.09.014>
- Ghanbari, F., Hassani, A., Waclawek, S., Wang, Z., Matyszczyk, G., Lin, K.Y.A., Dolatabadi, M., 2021. Insights into paracetamol degradation in aqueous solutions by ultrasound-assisted heterogeneous electro-Fenton process: Key operating parameters, mineralization and toxicity assessment. *Sep. Purif. Technol.* 266. <https://doi.org/10.1016/j.seppur.2021.118533>
- Groenen-Serrano, K., Weiss-Hortala, E., Savall, A., Spiteri, P., 2013. Role of Hydroxyl Radicals During the Competitive Electrooxidation of Organic Compounds on a Boron-Doped Diamond Anode. *Electrocatalysis* 4, 346–352. <https://doi.org/10.1007/s12678-013-0150-5>
- Guo, L., Jing, Y., Chaplin, B.P., 2016. Development and Characterization of Ultrafiltration TiO<sub>2</sub> Magnéli Phase Reactive Electrochemical Membranes. *Environ. Sci. Technol.* 50, 1428–1436. <https://doi.org/10.1021/acs.est.5b04366>
- Guo, W., Ngo, H.H., Li, J., 2012. A mini-review on membrane fouling. *Bioresour. Technol.* 122, 27–34. <https://doi.org/10.1016/j.biortech.2012.04.089>
- Hamdi El Najjar, N., Touffet, A., Deborde, M., Journel, R., Karpel Vel Leitner, N., 2014. Kinetics of paracetamol oxidation by ozone and hydroxyl radicals, formation of transformation products and toxicity. *Sep. Purif. Technol.* 136, 137–143. <https://doi.org/10.1016/j.seppur.2014.09.004>
- Hayon, E., Treinin, A., Wilf, J., 1972. Electronic Spectra, Photochemistry, and Autoxidation Mechanism of the Sulfite-Bisulfite-Pyrosulfite Systems. The SO<sub>2</sub><sup>-</sup>, SO<sub>3</sub><sup>-</sup>, SO<sub>4</sub><sup>-</sup>, and SO<sub>5</sub><sup>-</sup> Radicals. *J. Am. Chem. Soc.* 94, 47–57.



- Hinojosa Guerra, M.M., Oller Alberola, I., Malato Rodriguez, S., Agüera López, A., Acevedo Merino, A., Egea-Corbacho Lopera, A., Quiroga Alonso, J.M., 2019. Oxidation mechanisms of amoxicillin and paracetamol in the photo-Fenton solar process. *Water Res.* 156, 232–240. <https://doi.org/10.1016/j.watres.2019.02.055>
- Jia, M., Yang, Z., Xiong, W., Cao, J., Xiang, Y., Peng, H., Jing, Y., Zhang, C., Xu, H., Song, P., 2021. Magnetic heterojunction of oxygen-deficient Ti<sup>3+</sup>-TiO<sub>2</sub> and Ar-Fe<sub>2</sub>O<sub>3</sub> derived from metal-organic frameworks for efficient peroxydisulfate (PDS) photo-activation. *Appl. Catal. B Environ.* 298, 120513. <https://doi.org/10.1016/j.apcatb.2021.120513>
- Jing, Y., Chaplin, B.P., 2017. Mechanistic Study of the Validity of Using Hydroxyl Radical Probes to Characterize Electrochemical Advanced Oxidation Processes. *Environ. Sci. Technol.* 51, 2355–2365. <https://doi.org/10.1021/acs.est.6b05513>
- Kapalka, A., Fóti, G., Comninellis, C., 2009. The importance of electrode material in environmental electrochemistry. Formation and reactivity of free hydroxyl radicals on boron-doped diamond electrodes. *Electrochim. Acta* 54, 2018–2023. <https://doi.org/10.1016/j.electacta.2008.06.045>
- Kapalka, A., Fóti, G., Comninellis, C., 2008. Determination of the Tafel slope for oxygen evolution on boron-doped diamond electrodes. *Electrochem. Commun.* 10, 607–610. <https://doi.org/10.1016/j.elecom.2008.02.003>
- Konopka, S.J., McDuffie, B., 1970. Diffusion Coefficients of Ferri- and Ferrocyanide Ions in Aqueous Media, Using Twin-Electrode Thin-Layer Electrochemistry. *Anal. Chem.* 42, 1741–1746. <https://doi.org/10.1021/ac50160a042>
- Krstajic, N., Trasatti, S., 1998. Cathodic behaviour of RuO<sub>2</sub>-doped Ni/Co<sub>3</sub>O<sub>4</sub> electrodes in alkaline solutions: Hydrogen evolution. *J. Appl. Electrochem.* 28, 1291–1297. <https://doi.org/10.1023/A:1003444110172>
- Li, W., Xiao, R., Lin, H., Yang, K., He, K., Yang, L.H., Pu, M., Li, M., Lv, S., 2022. Electro-activation of peroxymonosulfate by a graphene oxide/iron oxide nanoparticle-doped Ti<sub>4</sub>O<sub>7</sub> ceramic membrane: mechanism of singlet oxygen generation in the removal of 1,4-dioxane. *J. Hazard. Mater.* 424, 127342. <https://doi.org/10.1016/j.jhazmat.2021.127342>

- Li, X., Zhu, A.L., Qu, W., Wang, H., Hui, R., Zhang, L., Zhang, J., 2010. Magnéli phase Ti<sub>4</sub>O<sub>7</sub> electrode for oxygen reduction reaction and its implication for zinc-air rechargeable batteries. *Electrochim. Acta* 55, 5891–5898. <https://doi.org/10.1016/j.electacta.2010.05.041>
- Liang, S., Lin, H., Yan, X., Huang, Q., 2018. Electro-oxidation of tetracycline by a Magnéli phase Ti<sub>4</sub>O<sub>7</sub> porous anode: Kinetics, products, and toxicity. *Chem. Eng. J.* 332, 628–636. <https://doi.org/10.1016/j.cej.2017.09.109>
- Lin, H., Niu, J., Liang, S., Wang, C., Wang, Y., Jin, F., Luo, Q., 2018. Development of macroporous Magnéli phase Ti<sub>4</sub>O<sub>7</sub> ceramic materials: As an efficient anode for mineralization of poly- and per fluoroalkyl substances 354, 1058–1067. <https://doi.org/10.1016/j.cej.2018.07.210>
- Liu, Y., Gao, G., Vecitis, C.D., 2020. Prospects of an Electroactive Carbon Nanotube Membrane toward Environmental Applications. *Acc. Chem. Res.* 53, 2892–2902. <https://doi.org/10.1021/acs.accounts.0c00544>
- Moreira, F.C., Boaventura, R.A.R., Brillas, E., Vilar, V.J.P., 2017. Electrochemical advanced oxidation processes: A review on their application to synthetic and real wastewaters. *Appl. Catal. B Environ.* 202, 217–261. <https://doi.org/10.1016/j.apcatb.2016.08.037>
- Mousset, E., 2022. Interest of micro-reactors for the implementation of advanced electrocatalytic oxidation with boron-doped diamond anode for wastewater treatment. *Curr. Opin. Electrochem.* 32, 100897. <https://doi.org/10.1016/j.coelec.2021.100897>
- Mousset, E., Frunzo, L., Esposito, G., Hullebusch, E.D. van, Oturan, N., Oturan, M.A., 2016. A complete phenol oxidation pathway obtained during electro-Fenton treatment and validated by a kinetic model study. *Appl. Catal. B Environ.* 180, 189–198. <https://doi.org/10.1016/j.apcatb.2015.06.014>
- Nayak, S., Chaplin, B.P., 2018. Fabrication and characterization of porous, conductive, monolithic Ti<sub>4</sub>O<sub>7</sub> electrodes. *Electrochim. Acta* 263, 299–310. <https://doi.org/10.1016/j.electacta.2018.01.034>
- Neta, P., Huie, R.E., Ross, A.B., 1988. Rate Constants for Reactions of Aliphatic Carbon-Centered Radicals in Aqueous Solution. *Natl. Bur. Stand. Natl. Stand. Ref. Data Ser.* 17, 1027–

1284.

- Nidheesh, P. V., Divyapriya, G., Oturan, N., Trelu, C., Oturan, M.A., 2019. Environmental Applications of Boron-Doped Diamond Electrodes: 1. Applications in Water and Wastewater Treatment. *Chem. Electro. Chem* 6, 2124–2142. <https://doi.org/10.1002/celec.201801876>
- Nidheesh, P. V., Zhou, M., Oturan, M.A., 2018. An overview on the removal of synthetic dyes from water by electrochemical advanced oxidation processes. *Chemosphere* 197, 210–227. <https://doi.org/10.1016/j.chemosphere.2017.12.195>
- Oturan, M.A., 2021. Outstanding performances of the BDD film anode in electro-Fenton process: Applications and comparative performance. *Curr. Opin. Solid State Mater. Sci.* 25, 100925. <https://doi.org/10.1016/j.cossms.2021.100925>
- Oturan, M.A., Aaron, J.J., 2014. Advanced oxidation processes in water/wastewater treatment: Principles and applications. A review. *Crit. Rev. Environ. Sci. Technol.* 44, 2577–2641. <https://doi.org/10.1080/10643389.2013.829765>
- Panizza, M., Cerisola, G., 2009. Direct And Mediated Anodic Oxidation of Organic Pollutants. *Chem. Rev.* 109, 6541–6569. <https://doi.org/10.1021/cr9001319>
- Przybyła, G.W., Szychowski, K.A., Gmiński, J., 2021. Paracetamol – An old drug with new mechanisms of action. *Clin. Exp. Pharmacol. Physiol.* 48, 3–19. <https://doi.org/10.1111/1440-1681.13392>
- Radjenovic, J., Sedlak, D.L., 2015. Challenges and Opportunities for Electrochemical Processes as Next-Generation Technologies for the Treatment of Contaminated Water. *Environ. Sci. Technol.* 49, 11292–11302. <https://doi.org/10.1021/acs.est.5b02414>
- Scialdone, O., 2009. Electrochemical oxidation of organic pollutants in water at metal oxide electrodes: A simple theoretical model including direct and indirect oxidation processes at the anodic surface. *Electrochim. Acta* 54, 6140–6147. <https://doi.org/10.1016/j.electacta.2009.05.066>
- Shih, Y.J., Huang, C.P., Chan, Y.H., Huang, Y.H., 2019. Electrochemical degradation of oxalic acid over highly reactive nano-textured  $\Gamma$ - and  $\text{A-MnO}_2$ /carbon electrode fabricated by  $\text{KMnO}_4$  reduction on loofah sponge-derived active carbon. *J. Hazard. Mater.* 379, 120759.

<https://doi.org/10.1016/j.jhazmat.2019.120759>

- Sirés, I., Brillas, E., Oturan, M.A., Rodrigo, M.A., Panizza, M., 2014. Electrochemical advanced oxidation processes: today and tomorrow. A review. *Environ. Sci. Pollut. Res.* 21, 8336–8367. <https://doi.org/10.1007/s11356-014-2783-1>
- Sirés, I., Garrido, J.A., Rodríguez, R.M., Cabot, P. I. luis, Centellas, F., Arias, C., Brillas, E., 2006. Electrochemical Degradation of Paracetamol from Water by Catalytic Action of Fe<sup>2+</sup>, Cu<sup>2+</sup>, and UVA Light on Electrogenerated Hydrogen Peroxide. *J. Electrochem. Soc.* 153, D1. <https://doi.org/10.1149/1.2130568>
- Trellu, C., Chaplin, B.P., Coetsier, C., Esmilaire, R., Cerneaux, S., Causserand, C., Cretin, M., 2018a. Electro-oxidation of organic pollutants by reactive electrochemical membranes. *Chemosphere* 208, 159–175. <https://doi.org/10.1016/j.chemosphere.2018.05.026>
- Trellu, C., Coetsier, C., Rouch, J.-C.C., Esmilaire, R., Rivallin, M., Cretin, M., Causserand, C., 2018b. Mineralization of organic pollutants by anodic oxidation using reactive electrochemical membrane synthesized from carbothermal reduction of TiO<sub>2</sub>. *Water Res.* 131, 310–319. <https://doi.org/10.1016/j.watres.2017.12.070>
- Trellu, C., Olvera Vargas, H., Mousset, E., Oturan, N., Oturan, M.A., 2021. Electrochemical technologies for the treatment of pesticides. *Curr. Opin. Electrochem.* 26, 100677. <https://doi.org/10.1016/j.coelec.2020.100677>
- Walsh, F.C., Wills, R.G.A., 2010. The continuing development of Magnéli phase titanium sub-oxides and Ebonex® electrodes. *Electrochim. Acta* 55, 6342–6351. <https://doi.org/10.1016/j.electacta.2010.05.011>
- Wang, G., Liu, Y., Ye, J., Lin, Z., Yang, X., 2020. Chemosphere li phase Ti<sub>4</sub>O<sub>7</sub> Electrochemical oxidation of methyl orange by a Magn e anode. *Chemosphere* 241, 125084. <https://doi.org/10.1016/j.chemosphere.2019.125084>
- Wang, J., Zhi, D., Zhou, H., He, X., Zhang, D., 2018. Evaluating tetracycline degradation pathway and intermediate toxicity during the electrochemical oxidation over a Ti/Ti<sub>4</sub>O<sub>7</sub> anode. *Water Res.* 137, 324–334. <https://doi.org/10.1016/j.watres.2018.03.030>
- Watanabe, M., 2009. Raman spectroscopy of charge-ordered states in Magnéli titanium oxides. *Phys. Status Solidi C Curr. Top. Solid State Phys.* 6, 260–263.

<https://doi.org/10.1002/pssc.200879898>

- Wu, X., Rigby, K., Huang, D., Hedtke, T., Wang, X., Chung, M.W., Weon, S., Stavitski, E., Kim, J.H., 2022. Single-Atom Cobalt Incorporated in a 2D Graphene Oxide Membrane for Catalytic Pollutant Degradation. *Environ. Sci. Technol.* 56, 1341–1351. <https://doi.org/10.1021/acs.est.1c06371>
- Xie, J., Ma, J., Zhang, C., Kong, X., Wang, Z., Waite, T.D., 2020. Effect of the Presence of Carbon in Ti<sub>4</sub>O<sub>7</sub> Electrodes on Anodic Oxidation of Contaminants. *Environ. Sci. Technol.* 54, 5227–5236. <https://doi.org/10.1021/acs.est.9b07398>
- Yao, S., Xue, S., Zhang, Y., Shen, X., Qian, X., Li, T., Xiao, K., Qin, S., Xiang, J., 2017. Synthesis, characterization, and electrochemical performance of spherical nanostructure of Magnéli phase Ti<sub>4</sub>O<sub>7</sub>. *J. Mater. Sci. Mater. Electron.* 28, 7264–7270. <https://doi.org/10.1007/s10854-017-6410-z>
- You, S., Liu, B., Gao, Y., Wang, Y., Tang, C.Y., Huang, Y., Ren, N., 2016. Monolithic Porous Magnéli-phase Ti<sub>4</sub>O<sub>7</sub> for Electro-oxidation Treatment of Industrial Wastewater. *Electrochim. Acta* 214, 326–335. <https://doi.org/10.1016/j.electacta.2016.08.037>
- Zaky, Amr M., Chaplin, B.P., 2014. Mechanism of p-substituted phenol oxidation at a Ti<sub>4</sub>O<sub>7</sub> reactive electrochemical membrane. *Environ. Sci. Technol.* 48, 5857–5867. <https://doi.org/10.1021/es5010472>
- Zaky, A.M., Chaplin, B.P., 2013. Porous Substoichiometric TiO<sub>2</sub> Anodes as Reactive Electrochemical Membranes for Water Treatment. <https://doi.org/10.1021/es401287e>

## **Chapter IV**

### **Porous Magnéli Phase Obtained from 3D Printing for Efficient Anodic Oxidation Process**

## Abstract

3D printing was used for the first time for synthesis of a 3D TiO<sub>x</sub> electrode applied to the removal of organic compounds from water by electrooxidation process. After characterization of the synthesized material, effectiveness and reaction mechanisms of the electrode for water treatment was assessed through (i) using probe molecules and paracetamol (PCT) as model compound (ii) monitoring the fate of degradation by-products and mineralization yields, and (iii) quenching experiments to clarify oxidation mechanism. Results emphasized that the suitable porous structure of the 3D TiO<sub>x</sub> promoted both direct electron transfer and hydroxyl radical-mediated oxidation at the electrode surface. Compared to Ti/TiO<sub>x</sub> and BDD plates anodes, 3D TiO<sub>x</sub> anode achieved faster degradation of PCT (3.3- and 1.7- times enhancement, respectively), lower accumulation of degradation by-products and higher mineralization yield (75% vs 15% and 66%, for Ti/TiO<sub>x</sub> and BDD anodes, respectively, after 2-h treatment, under similar operating conditions). This study highlights the potential of 3D printing for designing electrode materials with suitable porous structure able to favor mass transport conditions and consequently enhance the efficiency of electrochemical advanced oxidation processes.

## Keywords

3D printing; electro-oxidation; sub-stoichiometric titanium oxide; hydroxyl radical; mass transport

## 1. Introduction

Anodic oxidation (AO) (or electrooxidation) is a widely applied electrochemical advanced oxidation process (EAOP) based on *in-situ* generation of reactive species, mostly hydroxyl radicals ( $\cdot\text{OH}$ ) (Martínez-Huitle et al., 2015; You et al., 2016; Garcia-Segura and Brillas, 2017; Nidheesh et al., 2018; Fan et al., 2020; Du et al., 2021; Martínez-Huitle and Brillas, 2021; Oturan, 2021; Nienhauser et al., 2022). Formation of a large amount of  $\cdot\text{OH}$ , in cooperation with direct electron transfer (DET) and mediated oxidation (thanks to the reactive species generated from the inorganic matrix), can accomplish high efficiency in terms of degradation and mineralization rate of organic pollutants in water (Panizza et al., 2001; Brillas et al., 2009; Zaky and Chaplin, 2014; Martínez-Huitle et al., 2015, 2022; Trelu et al., 2016, 2021; Mousset et al., 2018; Brito et al., 2021; Souza et al., 2021; Hao et al., 2022).

The nature of the anode material is a crucial parameter for the AO process. Magnéli phases ( $\text{Ti}_n\text{O}_{2n-1}$ ,  $3 < n < 10$ ) have been identified as potentially favorable materials owing to their high reactivity for  $\cdot\text{OH}$  generation, good electrical conductivity and lower production cost compared to standard materials based on boron-doped diamond (BDD) anodes (Chaplin, 2018; Nayak and Chaplin, 2018; Trelu et al., 2018a, 2020). The efficiency of AO can also be limited by the transport of molecules from bulk solution to electrode surface (Trelu et al., 2021). Recent research has been focused on the development of porous  $\text{Ti}_n\text{O}_{2n-1}$  electrodes in order to improve (i) the electro-active surface area and (ii) mass transport conditions, particularly in flow-through configuration (Radjenovic et al., 2020; Mousset, 2022). Therefore, it is important to be able to control the porous structure of the material (Trelu et al., 2018a). The development of fabrication methods to customize electrodes characteristics would be noteworthy for an efficient AO process. Porous monolithic  $\text{Ti}_n\text{O}_{2n-1}$  electrodes are generally fabricated from (carbo)thermal reduction of  $\text{TiO}_2$  or anodization-cathodization method (blue  $\text{TiO}_2$ ) (Nayak and Chaplin, 2018; Trelu et al., 2018b; Cai et al., 2019; Xu et al., 2021; Zhang et al., 2021). However, the morphology (porous structure) of these electrodes is less controllable and can be greatly influenced by parameters concerning  $\text{TiO}_2$  precursor and reduction process (e.g., temperature, treatment time) (Trelu et al., 2018a). Thus, a great challenge for material synthesis is related to



the development of methods able to precisely control both chemical composition and porous structure of the material.

Three-dimensional (3D) printing (additive manufacturing) is a technique which fabricates materials by depositing layers upon layers (Ngo et al., 2018). 3D printing has been developed since 1986 and applied in several different fields (aerospace, engineering, material science, chemistry, etc.) (Ngo et al., 2018). This technique allows shaping diverse precursors into materials with specific morphology in a large range of scales (Ngo et al., 2018; Tofail et al., 2018; Browne et al., 2020). Most importantly, 3D printing makes the customization of material morphology more controllable, including shape, thickness and porous structure (Ambrosi and Pumera, 2016; Ruiz-Morales et al., 2017; Foo et al., 2018; Lu et al., 2018; Fan et al., 2020; Zhang et al., 2020). Based on the success acquired in other fields, the AO process may also benefit from 3D printing for fabrication of electrode material with suitable characteristics.

In this study, a porous Magnéli phase electrode was successfully synthesized for the first time using 3D printing technique. This electrode was then used as anode in the AO process to remove organic pollutants from water. First, the chemical composition and morphology of the synthesized electrode were characterized. Then, terephthalic acid (TA) and oxalic acid (OA) were used as probe molecules for assessing the electrochemical reactivity of this electrode. Finally, it was applied for degradation and mineralization of a model pollutant (paracetamol (PCT)). Different quenchers were used for highlighting the key reaction mechanisms. Aromatic degradation by-products formed during AO process were identified and quantified. The effectiveness of this new electrode was assessed by comparison with a Ti/TiO<sub>x</sub> plate anode for highlighting the role of the 3D structure. The comparison was also made with a boron-doped diamond (BDD) anode since it is considered as gold standard material for such applications.

## **2. Materials and methods**

### **2.1 Chemicals**

Paracetamol (98%), hydroquinone ( $\geq 99\%$ ), phosphoric acid (85-88%), formic acid ( $\geq 96\%$ ) and 2-hydroxyterephthalic acid (97%) were obtained from Sigma-Aldrich. Terephthalic acid ( $\geq 99\%$ )

was purchased from Acros Organics. Sodium hydroxide ( $\geq 98\%$ ) and oxalic acid ( $\geq 97\%$ ) were obtained from Fluka. Ethanol ( $\geq 97\%$ ) was obtained from Chimie-Plus Laboratoires. All chemicals were used as received. Ultrapure water ( $R > 18.2 \text{ M}\Omega$ , obtained from Smart2Pure, Molsheim) was used for eluents preparation of HPLC and UHPLC.

## 2.2 Electrode synthesis

The 3D printed porous electrodes (hereafter referred as 3D  $\text{TiO}_x$ ) were synthesized using an ExOne binder jetting 3D printer by Saint-Gobain Research Provence, CREE. An ExOne Innovent Enhanced Recoater was used for printing the green body from a  $\text{TiO}_x$  powder mixture (40 wt% of  $\text{Ti}_5\text{O}_9$  and 60 wt% of  $\text{Ti}_6\text{O}_{11}$ ) and aqueous binder (BA005, ExOne). The  $\text{TiO}_x$  powder contained fine and coarse particles with a ratio of 20:80. Then the green body was heated up to  $375 \text{ }^\circ\text{C}$  (at an increasing rate of  $5 \text{ }^\circ\text{C min}^{-1}$ ) and held for 1 h under air to remove the binder. After replacing the air atmosphere with argon, the body was further heated up to  $1500 \text{ }^\circ\text{C}$  (at a rate of  $5 \text{ }^\circ\text{C min}^{-1}$ ) and held for 4 h. Cooling down was performed at  $5 \text{ }^\circ\text{C min}^{-1}$ .

## 2.3 Physico-chemical characterization

Porous structure of 3D  $\text{TiO}_x$  was observed by a digital optical microscope (KEYENCE, VHX-7000) and scanning electron microscopy (SEM, TM3030 and TM-1000, HITACHI). Electrode surface roughness was also characterized by optical microscopy (KEYENCE, VHX-7000). X-Ray diffraction (XRD) (Bruker D8 ENDEAVOR, Cu  $K\alpha$  radiation source,  $\lambda = 1.5418 \text{ \AA}$  at 40 kV and 40 mA) was used to study the Magnéli phase composition of 3D  $\text{TiO}_x$ . Mercury porosimetry was performed to analyze the distribution of pores smaller than  $345 \text{ }\mu\text{m}$ . Pores with size larger than  $345 \text{ }\mu\text{m}$  were counted and presented as pores per inch (ppi). The void volume of 3D  $\text{TiO}_x$  was calculated by subtracting solid volume of the printed skeleton (using the density of  $4.33 \text{ g cm}^{-3}$  obtained by Helium pycnometry) from bulk volume of the electrode. The porosity (void fraction) was then obtained from the ratio between void volume and bulk

volume of 3D TiO<sub>x</sub>.

## 2.4 Electrochemical characterization

Linear sweep voltammetry (LSV) and cyclic voltammetry (CV) were conducted on a Metrohm Autolab PGSTAT to study oxygen evolution potential (OEP) and electroactive surface area (EASA) of 3D printed TiO<sub>x</sub>, respectively. An Ag/AgCl (3 M KCl) electrode was used as reference electrode, 100 mM NaClO<sub>4</sub> was used as supporting electrolyte and a stainless-steel electrode served as counter electrode.

LSV tests were performed from open circuit potential (OCP) to 3.0 V vs Ag/AgCl/3 M KCl at a scan rate of 0.01 V s<sup>-1</sup>. Raw data were corrected to compensate ohmic drop (Krstajic and Trasatti, 1998).

Calculation of EASA was based on the measurement of the capacitance of the material using the method described by Chaplin et al. (Nayak and Chaplin, 2018). Capacitance was measured from CV tests performed from 0.55 to 1.17 V vs Ag/AgCl (3 M KCl) at scan rates from 0.006 to 0.010 V s<sup>-1</sup>. EASA was then calculated by taking into consideration the specific capacitance of this kind of metal oxide (60 μF cm<sup>-2</sup>) (Bockris and Otagawa, 1984).

## 2.5 Experimental

Batch experiments were conducted using an undivided cell maintained under continuous agitation. 3D TiO<sub>x</sub> electrode was used as anode while carbon felt was used as cathode. Both electrodes had similar shape with an effective geometric surface area of 23.6 cm<sup>2</sup>. They were set in parallel in a solution of 300 mL. The ratio between the surface of the electrode and the volume of the solution ( $S_{\text{electrode}}/V_{\text{solution}}$ ) was 7.9 m<sup>-1</sup>. The inter-electrode gap was 2.5 cm. All experiments were conducted in galvanostatic mode at current density of 5 mA cm<sup>-2</sup>. Samples were taken at different time intervals for analysis.

PCT ( $C_0 = 0.1$  mM, initial total organic carbon (TOC) = 9.6 mg L<sup>-1</sup>) was selected as model

pollutant to study the performance of 3D TiO<sub>x</sub>. TA (C<sub>0</sub> = 0.1 mM, TOC<sub>0</sub> = 9.6 mg L<sup>-1</sup>) was chosen as a suitable probe molecule for <sup>•</sup>OH-mediated oxidation as it was reported in previous studies (Jing and Chaplin, 2017). Similarly, OA (C<sub>0</sub> = 0.4 mM, TOC<sub>0</sub> = 9.6 mg L<sup>-1</sup>) was chosen as probe molecule for DET due to its low reaction rate with <sup>•</sup>OH (Shih et al., 2019).

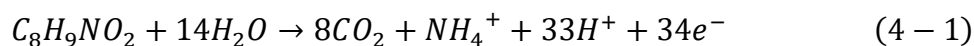
Quenching experiments were also conducted to verify the contribution of <sup>•</sup>OH-mediated oxidation and DET to PCT degradation. Ethanol (EtOH) was chosen as quencher because of its high reaction rate constant with <sup>•</sup>OH (Wu et al., 2022). EtOH was added at a concentration of 0.1 M.

## 2.6 Analytical methods

PCT and its main by-products were analyzed by a Dionex UltiMate 3000 UHPLC system with an UltiMate 3000 RS pump (at flow rate of 0.1 mL min<sup>-1</sup>), an UltiMate 3000 diode array detector (λ = 243 nm) and a Hypersil GOLD™ column (100×2.1 mm, 1.9 μm), which was set in an oven at 40 °C. A mixture of methanol (15%) and phosphate buffer (85%) (5 mM Na<sub>2</sub>HPO<sub>4</sub> and 7.5 mM H<sub>3</sub>PO<sub>4</sub>) was used as eluent. TA and its by-product, 2-hydroxyterephthalic acid (HTA), were analyzed by a HITACHI Elite LaChrom HPLC system. The HPLC system included a fluorescence detector set at Ex/Em = 315/435 nm (L-2480), an UV detector set at λ = 254 nm (L-2400), a pump with flow rate of 0.8 mL min<sup>-1</sup> and a LiChroCART Purospher® STAR RP-18e (5 μm) column set at 40 °C. The evolution of the TOC of treated solutions was measured by a TOC analyzer (SHIMADZU, TOC-L).

## 2.7 Calculation of mineralization current efficiency (MCE)

The mineralization of PCT refers to its complete conversion into carbon dioxide and the general mineralization reaction can be expressed as follow (Eq. 4-1) (Garcia-Segura and Brillas, 2011; Trellu et al., 2018b; Hien et al., 2022):



In this study, the mineralization yield of PCT was reported as TOC removal and the mineralization current efficiency can be therefore calculated using Eq. 4-2:

$$MCE (\%) = \frac{n F V (TOC_0 - TOC_t)}{12000 m I t} \times 100 \quad (4 - 2)$$

where  $n$  is the number of electrons involved in the mineralization reaction,  $F$  is Faraday constant,  $V$  is the solution volume,  $TOC_0$  is the initial TOC,  $TOC_t$  is the TOC at time  $t$ , 12000 ( $\text{mg mol}^{-1}$ ) is a conversion factor,  $m$  is the number of carbon atoms,  $I$  is the current intensity (A) and  $t$  is the reaction time (s).

### 3. Results and discussion

#### 3.1 Physicochemical characterization of 3D $\text{TiO}_x$ electrode

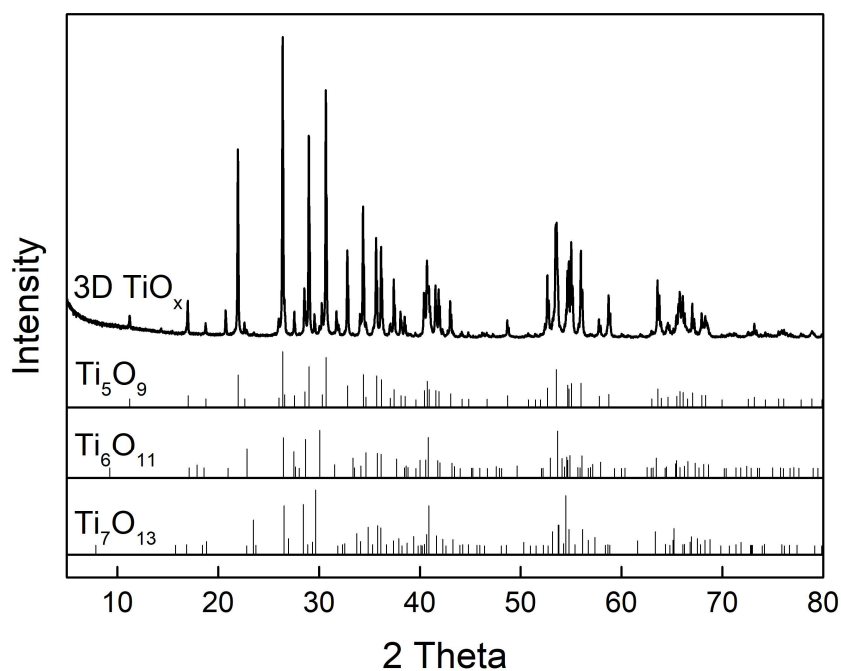


Fig. 4-1 - XRD pattern for 3D  $\text{TiO}_x$  electrode

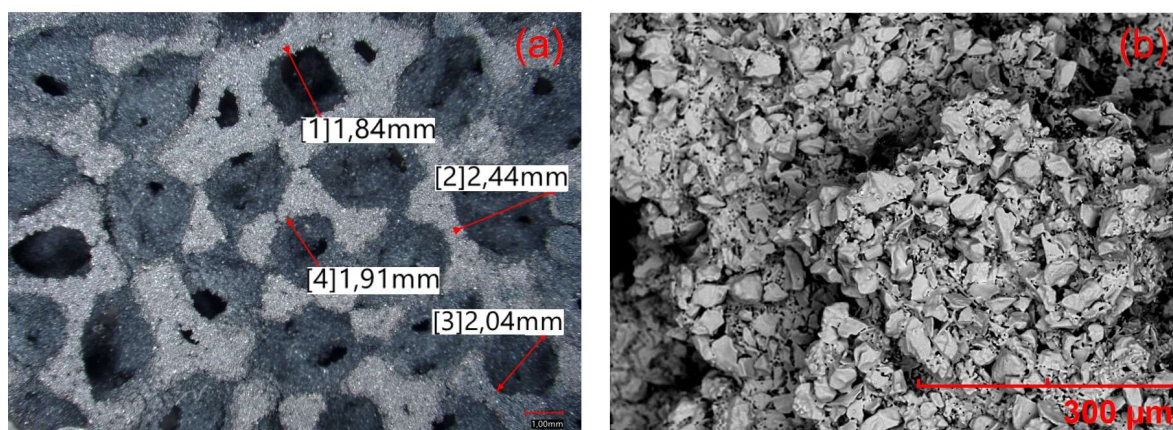


Fig. 4-2 - Porous structure and pore size of 3D  $\text{TiO}_x$  observed by microscopy (a), SEM image of 3D  $\text{TiO}_x$  (b)

Data obtained from XRD analysis of 3D  $\text{TiO}_x$  Magnéli phase are shown in Fig. 4-1. The results highlighted that 3D  $\text{TiO}_x$  contained  $\text{Ti}_5\text{O}_9$  and  $\text{Ti}_6\text{O}_{11}$  as major phases. It is consistent with the  $\text{TiO}_x$  powders used for the synthesis.  $\text{Ti}_7\text{O}_{13}$  was also observed as minor phase. It might be ascribed to a slight re-oxidation of the powders during the thermal treatment.

Fig. 4-2 shows the porous structure of 3D  $\text{TiO}_x$ . The pore size distribution smaller than  $345 \mu\text{m}$  was depicted in Table 4-1. Pore size of  $2\text{-}10 \mu\text{m}$  accounted the majority of pores smaller than  $345 \mu\text{m}$ . The total porosity of the material was calculated as 84.3%. The porous structure of 3D  $\text{TiO}_x$  is at millimeter scale. As reported in a previous study (Ma et al., 2022), the coarse roughness of electrode at millimeter scale is able to improve mass transport conditions in stirred-tank reactor. The effective roughness factor (ERF) was calculated following the methodology described by Ma et al. (2022). The ERF takes only into consideration the electrode roughness that is not averaged within the diffusion field. With a diffusion layer of  $30 \mu\text{m}$ , ERF of 3D  $\text{TiO}_x$  was 5.2; this value was 5 times greater than BDD (1.07) and  $\text{Ti}/\text{TiO}_x$  plate (1.002) thanks to its porous structure at millimeter scale.

Table 4-1 Pore size distribution of 3D TiO<sub>x</sub> electrode

Pore size	0 – 2 μm	2 – 10 μm	10 – 20 μm	20 – 100 μm	100 – 345 μm
Vol %	0.8	31.4	3.7	4.6	5.5

### 3.2 Electrochemical characterization of 3D TiO<sub>x</sub> electrode

The EASA of 3D TiO<sub>x</sub> was obtained from the measurement of the capacitance of the electrode (Fig. 4-3). The value obtained was 1452 cm<sup>2</sup>, thus corresponding to a roughness factor of 62. This roughness factor is much higher than the ERF previously calculated since it takes into consideration also the electrode roughness at micrometer scale. For comparison, the EASA of Ti/TiO<sub>x</sub> plate electrode was 2200 cm<sup>2</sup> (with roughness factor of 93). The higher EASA of the Ti/TiO<sub>x</sub> plate electrode might be ascribed to (i) the use of plasma spraying technique that promotes electrode roughness at micrometer and sub-micrometer scale, (ii) the lack of interconnectivity of some pores in the 3D TiO<sub>x</sub> electrode. The former reason might be related to the removal of the aqueous binder during the first step of thermal treatment of the 3D TiO<sub>x</sub> electrode.

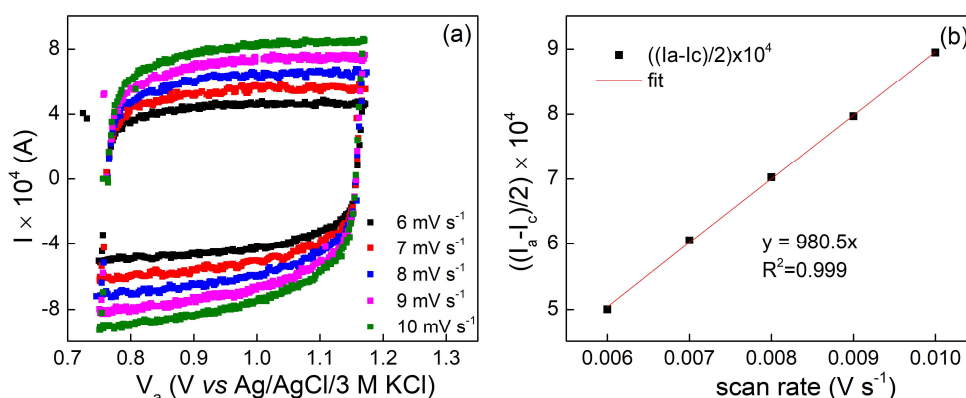


Fig. 4-3 - Measurement of double layer capacitance for 3D TiO<sub>x</sub> (reference electrode: Ag/AgCl/3 M KCl, supporting electrolyte: 100 mM NaClO<sub>4</sub>, scan rate: 0.006-0.01 V s<sup>-1</sup>)

LSV was performed in order to measure the OEP of the electrodes. Electrodes are usually divided in two classes, including (i) active electrodes with low overpotential for oxygen evolution reaction and (ii) non-active electrodes with high overpotential for oxygen evolution reaction (Panizza and Cerisola, 2009). Non-active electrodes are usually the most suitable electrodes for the formation of  $\cdot\text{OH}$ . Results from LSV are presented in Fig. 4-4. The 3D  $\text{TiO}_x$  presented an OEP of 2.75 V vs Ag/AgCl, while the OEPs of Ti/ $\text{TiO}_x$  plate and BDD were 2.78 and 2.27 V vs Ag/AgCl, respectively. The OEP of 3D  $\text{TiO}_x$  was sufficient for  $\cdot\text{OH}$  generation (2.17 V vs Ag/AgCl/3 M KCl) (Kapałka et al., 2009) and was comparable to that of Ti/ $\text{TiO}_x$  plate and typical Magnéli phase electrodes (Lin et al., 2018; Trelu et al., 2018a). This largest OEP of 3D printed  $\text{TiO}_x$  anode enables greater production of  $\cdot\text{OH}$ .

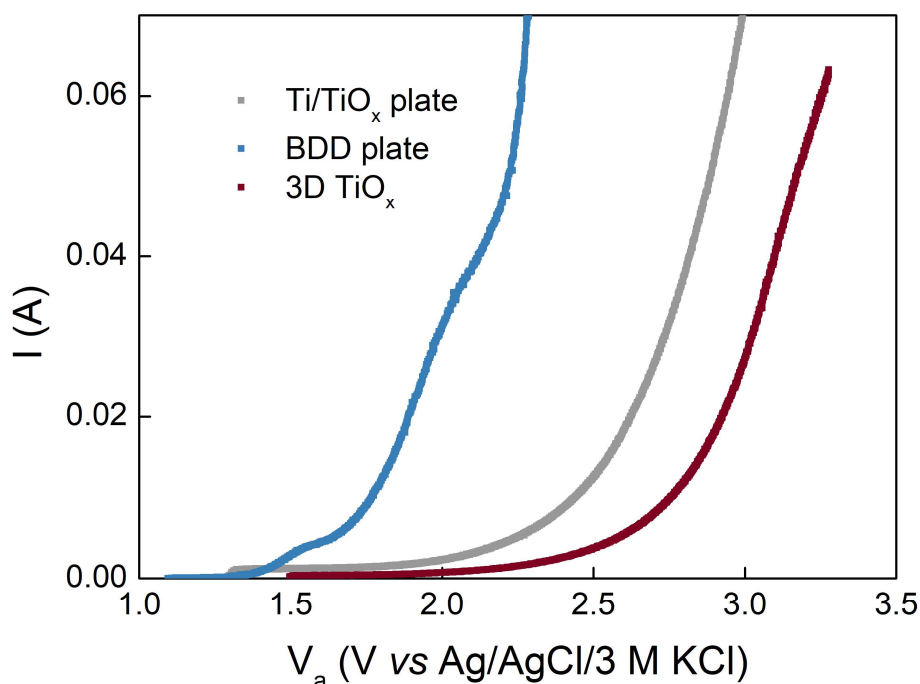


Fig. 4-4 - LSV curves obtained with 3D  $\text{TiO}_x$  anode compared to BDD and Ti/ $\text{TiO}_x$  plate anodes (reference electrode: Ag/AgCl/3 M KCl), supporting electrolyte: 100 mM  $\text{NaClO}_4$ , scan rate:  $0.01 \text{ V s}^{-1}$ )

### 3.3 Electrochemical reactivity assessment

TA and OA were used as probe molecules to assess electrochemical reactivity of 3D  $\text{TiO}_x$  for



$\cdot\text{OH}$ -mediated oxidation and DET, respectively. Fig. 4-5(a) shows the oxidative degradation of OA using 3D  $\text{TiO}_x$  anode in comparison with BDD and  $\text{Ti}/\text{TiO}_x$  plate anodes. The pseudo first order rate constants were calculated and plotted in Fig. 4-5(b). BDD and  $\text{Ti}/\text{TiO}_x$  plate achieved comparable degradation kinetic ( $0.008 \pm 0.002 \text{ min}^{-1}$  for BDD and  $0.008 \pm 0.001 \text{ min}^{-1}$  for  $\text{Ti}/\text{TiO}_x$  plate). Thus, both electrodes were able to remove OA in a similar way through DET. Removal of OA was then enhanced by using 3D  $\text{TiO}_x$  electrode. The pseudo first order rate constant was 2.8 times higher than plate electrodes. The OA removal yield was 53, 50 and 91% after 90 min of treatment by BDD plate,  $\text{Ti}/\text{TiO}_x$  plate and 3D  $\text{TiO}_x$ , respectively. The more favorable results obtained with 3D  $\text{TiO}_x$  might be mainly explained by the higher ERF of this electrode that favors mass transport of OA from the bulk to the electrode surface.

Degradation kinetics of TA are reported in Fig. 4-5(c) and 4-5(d). The generation of by-product, HTA, is presented in Fig.4-5(e). Faster degradation kinetic was obtained with BDD plate, compared to  $\text{Ti}/\text{TiO}_x$  plate. It might be ascribed to a better electrochemical behavior for production of  $\cdot\text{OH}$  at the electrode surface. The lifetime of  $\cdot\text{OH}$  is very short and results in the accumulation of  $\cdot\text{OH}$  only in a thin layer at the anode surface (in the range  $0.1 - 1 \mu\text{m}$ ) (Kapałka et al., 2009). The electrochemical behavior of BDD might promote the formation of  $\cdot\text{OH}$  (and/or hinder further evolution of  $\cdot\text{OH}$  in wasting reactions) that would increase the thickness of this reaction zone. However, 3D  $\text{TiO}_x$  electrode achieved a degradation kinetic rate of  $0.020 \pm 0.001 \text{ min}^{-1}$ , which was 2.5 times higher than that of  $\text{Ti}/\text{TiO}_x$  plate and 1.3 times higher than that of BDD plate ( $0.016 \pm 0.001 \text{ min}^{-1}$ ). After 90 min of electrolysis, 3D  $\text{TiO}_x$  reached a TA degradation rate of 88%, which was higher than both BDD (77%) and  $\text{Ti}/\text{TiO}_x$  plate (56%) electrodes. These results emphasized that the suitable porous structure of 3D  $\text{TiO}_x$  is able to strongly improve the reactivity of the electrode for  $\cdot\text{OH}$ -mediated oxidation of organics thanks to mass transport enhancement. Such optimization of the morphology of the electrode even allowed for reaching a better behavior than the BDD electrode.

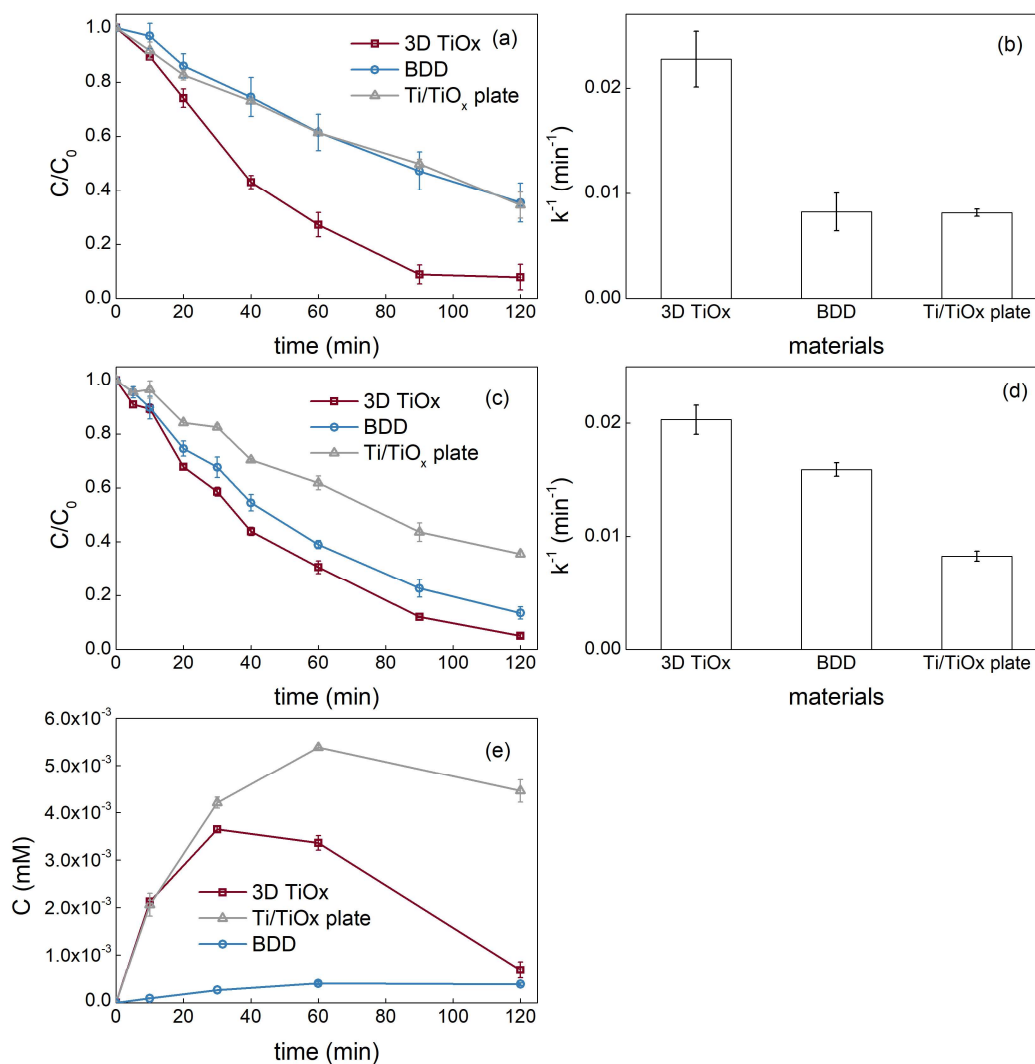


Fig. 4-5 - Degradation kinetic of OA by AO using 3D TiO<sub>x</sub> anode compared to BDD and Ti/TiO<sub>x</sub> plate anodes (a) and corresponding pseudo first order rate constants (b); degradation kinetic of TA by AO using 3D TiO<sub>x</sub> compared to BDD and Ti/TiO<sub>x</sub> plate anodes (c) and corresponding pseudo first order rate constants (d); generation of HTA during degradation of TA by 3D TiO<sub>x</sub>, BDD and Ti/TiO<sub>x</sub> plates anodes (e). Experimental conditions: initial  $C_{TA} = 0.1$  mM, initial  $C_{OA} = 0.4$  mM, effective surface area = 23.6 cm<sup>2</sup>,  $S_{\text{electrode}}/V_{\text{solution}} = 7.9$  m<sup>-1</sup>, current density = 5 mA cm<sup>-2</sup>

### 3.4 Degradation of paracetamol in the absence and presence of quenchers

Electrodes under study were then applied for the removal of PCT as model pollutant. Fig. 4-6(a) shows PCT degradation kinetic obtained with 3D TiO<sub>x</sub>, BDD plate and Ti/TiO<sub>x</sub> plate. 3D TiO<sub>x</sub>

achieved 97% of PCT degradation after 90 min of treatment, which is higher than that obtained with BDD (83%) and Ti/TiO<sub>x</sub> plate (60%). The degradation kinetic obtained with 3D TiO<sub>x</sub> was respectively 1.7 and 3.3 times higher than with the BDD plate and Ti/TiO<sub>x</sub> plate electrodes. This is consistent with the previous subsection (§ 3.3), which provides evidences that the electrochemical reactivity of 3D TiO<sub>x</sub> for both •OH-mediated oxidation and DET was greatly improved compared to the BDD and Ti/TiO<sub>x</sub> plate electrodes.

EtOH (100 mM) was then used as quencher of •OH in order to assess the degradation of PCT through DET (Fig. 4-6(a)). Compared to previous results obtained without •OH quenchers, the degradation kinetic of PCT was divided by 1.7, 2.2 and 1.9 for 3D TiO<sub>x</sub>, BDD plate and Ti/TiO<sub>x</sub> plate anodes. These results are consistent with the slower degradation kinetics obtained using OA as probe molecule for DET compared to those obtained with TA as probe molecule for •OH. The degradation kinetic through •OH-mediated oxidation was faster since the accumulation of •OH within a thin layer ( $\approx 1 \mu\text{m}$ ) at the vicinity of the anode surface increases the reaction zone compared to DET that occurs only at the anode surface.

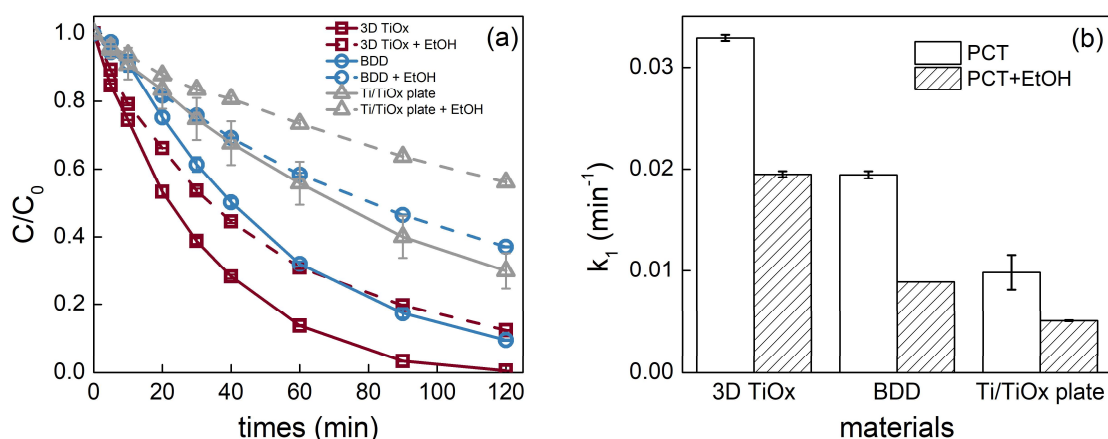


Fig. 4-6 - Degradation kinetic of PCT by 3D TiO<sub>x</sub> in comparison with BDD and Ti/TiO<sub>x</sub> plate electrodes with and without using EtOH as quencher (a) and corresponding pseudo first order rate constants (b). Experimental conditions: initial  $C_{\text{PCT}} = 0.1 \text{ mM}$ ,  $C_{\text{EtOH}}/C_{\text{PCT}} = 1000$ , effective surface area =  $23.6 \text{ cm}^2$ ,  $S_{\text{electrode}}/V_{\text{solution}} = 7.9 \text{ m}^{-1}$ , current density =  $5 \text{ mA cm}^{-2}$

### 3.5 Fate of degradation by-products

Degradation of the mother molecule might lead to the formation of toxic by-products which,

should also be removed from the solution. Therefore, the fate of primarily aromatic by-products and mineralization yields were also monitored.

Hydroquinone (HQ) and benzoquinone (BQ) were identified as the main aromatic by-products of PCT degradation in this study. It is consistent with previous studies related to the degradation pathway of PCT (Sirés et al., 2006). Fig. 4-7(a) shows the evolution of HQ and BQ during PCT degradation by AO using 3D TiO<sub>x</sub> anode. Fig. 4-7(b) shows the fraction of HQ and BQ in the solution compared to the amount of PCT degraded. In the absence of EtOH, very low accumulation of HQ and BQ was observed for both 3D TiO<sub>x</sub> and BDD, with a slight advantage for 3D TiO<sub>x</sub>. After 2 h of treatment, the sum of HQ and BQ was representing less than 1.5% of the amount of PCT degraded with 3D TiO<sub>x</sub> and BDD anodes (Fig. 4-7b). By comparison, higher concentrations of HQ and BQ were measured in the solution during the degradation of PCT by Ti/TiO<sub>x</sub> plate anode.

In the presence of EtOH, much higher concentrations of HQ were observed during the treatment. The predominance of HQ compared to BQ might be ascribed to the fast reduction of BQ to HQ at the cathode. Such higher accumulation of by-products can be explained by the recalcitrance of these compounds for further oxidation by DET. For example, BQ is well known for its recalcitrance to oxidation by DET (Jing and Chaplin, 2017). These results highlight that <sup>•</sup>OH-mediated oxidation is also a key parameter for further degradation of by-products.

Therefore, the better behavior of 3D TiO<sub>x</sub> and BDD for <sup>•</sup>OH-mediated oxidation (section 3.3) might explain the lower accumulation of aromatic by-products observed during experiments without quenchers. These results are also consistent with mineralization yields obtained after two hours of treatment (Fig. 4-8). In absence of quenchers, the effectiveness of the electrodes followed the same order as for the accumulation of aromatic by-products: 3D TiO<sub>x</sub> > BDD >> Ti/TiO<sub>x</sub> plate. 3D TiO<sub>x</sub> achieved 75% of TOC removal after 2 h of treatment (Fig. 4-8)). It corresponds to a current efficiency of 8.7%. By comparison, Ti/TiO<sub>x</sub> plate anode achieved a five times lower mineralization efficiency, corresponding to a current efficiency of only 1.6%. The mineralization yield achieved with 3D TiO<sub>x</sub> was even higher than that obtained with BDD (66%). BDD is usually considered as a gold standard for such application, particularly for achieving complete combustion of organic compounds (Brillas et al., 2005; Garcia-Segura and

Brillas, 2011; Mart et al., 2015; Martínez-Huitle et al., 2015; de Oliveira Silva et al., 2021; Oturan, 2021; Bansal et al., 2022). Therefore, the results obtained here highlight the great promises of 3D TiO<sub>x</sub> for further development in removal of organic pollutants.

It is also interesting to notice that the addition of EtOH as quencher of  $\cdot\text{OH}$  had a bigger adverse effect on the accumulation of by-products for 3D TiO<sub>x</sub> compared to BDD anode. The addition of 100 mM of EtOH might not ensure for 100% quenching of  $\cdot\text{OH}$ . Therefore, this behavior might be ascribed to the more favorable reactivity of BDD for the accumulation of a great amount of  $\cdot\text{OH}$  at the electrode surface; since it is more difficult to fully quench a higher local concentration of  $\cdot\text{OH}$ . Thus, the presence of a higher residual concentration of  $\cdot\text{OH}$  might explain the lower accumulation of aromatic by-products during quenching experiments with BDD anode. These results further highlight that the effectiveness of the 3D TiO<sub>x</sub> is tightly related to its suitable porous structure for mass transport enhancement, rather than to a superior reactivity.

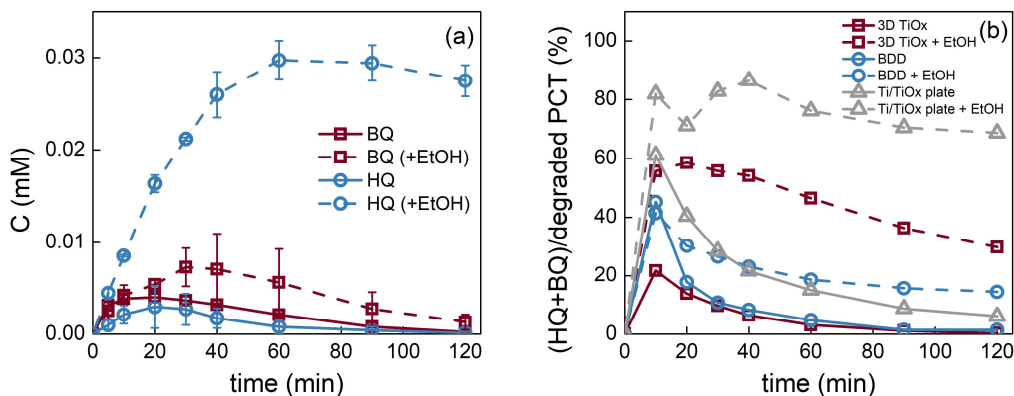


Fig. 4-7 - Evolution of HQ and BQ (a) and total amount of HQ and BQ during the PCT degradation by AO using 3D TiO<sub>x</sub> anode in comparison with BDD and Ti/TiO<sub>x</sub> plate anodes (b) in absence and presence of EtOH. Experimental conditions: initial  $C_{\text{PCT}} = 0.1$  mM,  $C_{\text{EtOH}}/C_{\text{PCT}} = 1000$ , effective surface area =  $23.6$  cm<sup>2</sup>,  $S_{\text{electrode}}/V_{\text{solution}} = 7.9$  m<sup>-1</sup>, current density =  $5$  mA cm<sup>-2</sup>

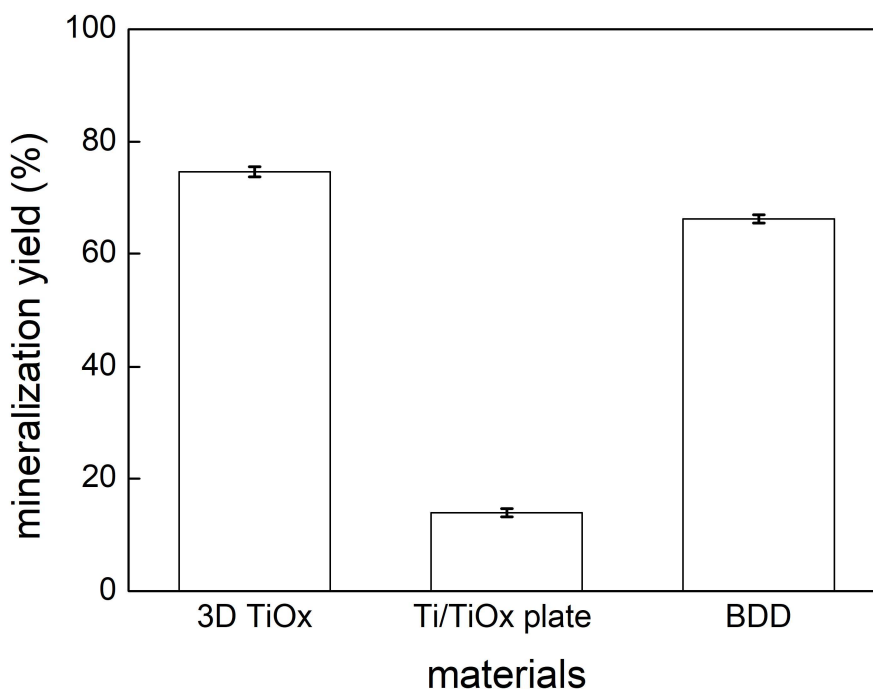


Fig. 4-8 - PCT mineralization yield after 2 h electrolysis by 3D TiO<sub>x</sub>, Ti/TiO<sub>x</sub> plate and BDD plate anodes. Experimental conditions: initial C<sub>PCT</sub> = 0.1 mM, effective surface area = 23.6 cm<sup>2</sup>,  $S_{\text{electrode}}/V_{\text{solution}} = 7.9 \text{ m}^{-1}$ , current density = 5 mA cm<sup>-2</sup>

#### 4. Conclusions

The development of 3D printing techniques offers new possibilities for the synthesis of electrode materials with suitable properties for removal of organic compounds from water by the electrooxidation process. Particularly, electrode morphology must promote mass transport enhancement of organic pollutants from bulk to the electrode surface. In this study, 3D printing enabled the synthesis of a TiO<sub>x</sub> material with an appropriate coarse roughness allowing the increase of ERF. Such morphology allowed for improving the effectiveness of the process for application in stirred-tank reactor in which mass transport is limited by the diffusion layer at the electrode surface.

Results emphasized that 3D TiO<sub>x</sub> allowed (i) 2.8 times enhancement of degradation kinetics of OA (probe molecule for DET) compared to both BDD plate and Ti/TiO<sub>x</sub> plate anodes, (ii) 2.5 and 1.3 times enhancement of degradation kinetics of TA (probe molecule for •OH-mediated

oxidation) compared to Ti/TiO<sub>x</sub> plate and BDD plate anodes, respectively, (iii) 3.3 and 1.7 times enhancement of degradation kinetics of PCT compared to Ti/TiO<sub>x</sub> plate and BDD plate anodes, respectively, (iv) lower accumulation of toxic aromatic by-products such as HQ and BQ, and, (v) higher mineralization yield than Ti/TiO<sub>x</sub> plate and BDD plate electrodes.

The suitable porous structure of 3D TiO<sub>x</sub> (with higher ERF) promotes both DET and ·OH-mediated oxidation and allows for a more efficient use of current for the removal of organic compounds by AO under mass transport limitation. Continuous development of 3D-printing technique (e.g., improvement of the resolution) might continue to offer new possibilities for development of electrode materials with precise control of the porous structure and therefore more efficient removal of organic pollutants from water/wastewater.

## **Acknowledgement**

Jing Ma acknowledges China Scholarship Council for the financial support for her PhD work (201906970041). Authors acknowledge Saint-Gobain Research Provence for providing TiO<sub>x</sub> electrodes.

## References

- Ambrosi, A., Pumera, M., 2016. 3D-printing technologies for electrochemical applications. *Chem. Soc. Rev.* 45, 2740–2755. <https://doi.org/10.1039/c5cs00714c>
- Bansal, R., Verduzco, R., Wong, M.S., Westerhoff, P., Garcia-Segura, S., 2022. Development of nano boron-doped diamond electrodes for environmental applications. *J. Electroanal. Chem.* 907, 116028. <https://doi.org/10.1016/j.jelechem.2022.116028>
- Bockris, J.O., Otagawa, T., 1984. The Electrocatalysis of Oxygen Evolution on Perovskites. *J. Electrochem. Soc.* 131, 290–302. <https://doi.org/10.1149/1.2115565>
- Brillas, E., Sirés, I., Arias, C., Cabot, P.L., Centellas, F., Rodríguez, R.M., Garrido, J.A., 2005. Mineralization of paracetamol in aqueous medium by anodic oxidation with a boron-doped diamond electrode. *Chemosphere* 58, 399–406. <https://doi.org/10.1016/j.chemosphere.2004.09.028>
- Brillas, E., Sirés, I., Oturan, M.A., 2009. Electro-fenton process and related electrochemical technologies based on fenton's reaction chemistry. *Chem. Rev.* 109, 6570–6631. <https://doi.org/10.1021/cr900136g>
- Brito, L.R.D., Ganiyu, S.O., dos Santos, E. V., Oturan, M.A., Martínez-Huitle, C.A., 2021. Removal of antibiotic rifampicin from aqueous media by advanced electrochemical oxidation: Role of electrode materials, electrolytes and real water matrices. *Electrochim. Acta* 396, 139254. <https://doi.org/10.1016/j.electacta.2021.139254>
- Browne, M.P., Redondo, E., Pumera, M., 2020. 3D Printing for Electrochemical Energy Applications. *Chem. Rev.* 120, 2783–2810. <https://doi.org/10.1021/acs.chemrev.9b00783>
- Cai, J., Zhou, M., Pan, Y., Du, X., Lu, X., 2019. Extremely efficient electrochemical degradation of organic pollutants with co-generation of hydroxyl and sulfate radicals on Blue-TiO<sub>2</sub> nanotubes anode. *Appl. Catal. B Environ.* 257, 117902. <https://doi.org/10.1016/j.apcatb.2019.117902>
- Chaplin, B.P., 2019. The Prospect of Electrochemical Technologies Advancing Worldwide Water Treatment. *Acc. Chem. Res.* 52 (2019) 596-604. <https://doi.org/10.1021/acs.accounts.8b00611>
- de Oliveira Silva, K.N., Rodrigo, M.A., dos Santos, E.V., 2021. Electrochemical treatment of soil-washing effluent with boron-doped diamond electrodes: A review. *Curr. Opin. Solid State Mater. Sci.* 25. <https://doi.org/10.1016/j.cossms.2021.100962>



- Du, X., Oturan, M.A., Zhou, M., Belkessa, N., Su, P., Cai, J., Trelu, C., Mousset, E., 2021. Nanostructured electrodes for electrocatalytic advanced oxidation processes: From materials preparation to mechanisms understanding and wastewater treatment applications. *Appl. Catal. B Environ.* 296, 120332. <https://doi.org/10.1016/j.apcatb.2021.120332>
- Fan, Z., Wei, C., Yu, L., Xia, Z., Cai, J., Tian, Z., Zou, G., Dou, S.X., Sun, J., 2020. 3D Printing of Porous Nitrogen-Doped Ti<sub>3</sub>C<sub>2</sub> MXene Scaffolds for High-Performance Sodium-Ion Hybrid Capacitors. *ACS Nano* 14, 867–876. <https://doi.org/10.1021/acsnano.9b08030>
- Foo, C.Y., Lim, H.N., Mahdi, M.A., Wahid, M.H., Huang, N.M., 2018. Three-Dimensional Printed Electrode and Its Novel Applications in Electronic Devices. *Sci. Rep.* 8, 1–11. <https://doi.org/10.1038/s41598-018-25861-3>
- Garcia-Segura, S., Brillas, E., 2017. Applied photoelectrocatalysis on the degradation of organic pollutants in wastewaters. *J. Photochem. Photobiol. C Photochem. Rev.* 31, 1–35. <https://doi.org/10.1016/j.jphotochemrev.2017.01.005>
- Garcia-Segura, S., Brillas, E., 2011. Mineralization of the recalcitrant oxalic and oxamic acids by electrochemical advanced oxidation processes using a boron-doped diamond anode. *Water Res.* 45, 2975–2984. <https://doi.org/10.1016/j.watres.2011.03.017>
- Hao, Y., Ma, H., Proietto, F., Galia, A., Scialdone, O., 2022. Electrochemical treatment of wastewater contaminated by organics and containing chlorides: Effect of operative parameters on the abatement of organics and the generation of chlorinated by-products. *Electrochim. Acta* 402, 139480. <https://doi.org/10.1016/j.electacta.2021.139480>
- Hien, S.A., Trelu, C., Oturan, N., Assémian, A.S., Briton, B.G.H., Drogui, P., Adouby, K., Oturan, M.A., 2022. Comparison of homogeneous and heterogeneous electrochemical advanced oxidation processes for treatment of textile industry wastewater. *J. Hazard. Mater.* 437. <https://doi.org/10.1016/j.jhazmat.2022.129326>
- Jing, Y., Chaplin, B.P., 2017. Mechanistic Study of the Validity of Using Hydroxyl Radical Probes to Characterize Electrochemical Advanced Oxidation Processes. *Environ. Sci. Technol.* 51, 2355–2365. <https://doi.org/10.1021/acs.est.6b05513>
- Kapalka, A., Fóti, G., Comninellis, C., 2009. The importance of electrode material in environmental electrochemistry. Formation and reactivity of free hydroxyl radicals on boron-doped diamond

- electrodes. *Electrochim. Acta* 54, 2018–2023. <https://doi.org/10.1016/j.electacta.2008.06.045>
- Krstajic, N., Trasatti, S., 1998. Cathodic behaviour of RuO<sub>2</sub>-doped Ni/Co<sub>3</sub>O<sub>4</sub> electrodes in alkaline solutions: Hydrogen evolution. *J. Appl. Electrochem.* 28, 1291–1297. <https://doi.org/10.1023/A:1003444110172>
- Lin, H., Niu, J., Liang, S., Wang, C., Wang, Y., Jin, F., Luo, Q., 2018. Development of macroporous Magnéli phase Ti<sub>4</sub>O<sub>7</sub> ceramic materials : As an efficient anode for mineralization of poly- and perfluoroalkyl substances 354, 1058–1067. <https://doi.org/10.1016/j.ccej.2018.07.210>
- Lu, X., Zhao, T., Ji, X., Hu, J., Li, T., Lin, X., Huang, W., 2018. 3D printing well organized porous iron-nickel/polyaniline nanocages multiscale supercapacitor. *J. Alloys Compd.* 760, 78–83. <https://doi.org/10.1016/j.jallcom.2018.05.165>
- Ma, J., Trellu, C., Oturan, N., Raffy, S., Oturan, M.A., 2022. Development of Ti/TiO<sub>x</sub> Foams for Removal of Organic Pollutants from Water: Influence of Porous Structure of Ti Substrate. *Appl. Catal. B: Environ.* 317 (2022) 121736. <https://doi.org/10.1016/j.apcatb.2022.121736>.
- Martínez-Huitle, C.A., Brillas, E., 2021. A critical review over the electrochemical disinfection of bacteria in synthetic and real wastewaters using a boron-doped diamond anode. *Curr. Opin. Solid State Mater. Sci.* 25, 100926. <https://doi.org/10.1016/j.cossms.2021.100926>
- Martínez-Huitle, C.A., Einaga, Y., Oturan, M.A., 2022. Conductive-synthetic diamond materials in meeting the sustainable development goals. *Curr. Opin. Solid State Mater. Sci.* 26, 101019. <https://doi.org/10.1016/j.cossms.2022.101019>
- Martínez-Huitle, C.A., Rodrigo, M.A., Sirés, I., Scialdone, O., 2015. Single and Coupled Electrochemical Processes and Reactors for the Abatement of Organic Water Pollutants: A Critical Review. *Chem. Rev.* 115, 13362–13407. <https://doi.org/10.1021/acs.chemrev.5b00361>
- Mousset, E., 2022. Interest of micro-reactors for the implementation of advanced electrocatalytic oxidation with boron-doped diamond anode for wastewater treatment. *Curr. Opin. Electrochem.* 32, 100897. <https://doi.org/10.1016/j.coelec.2021.100897>
- Mousset, E., Wang, Z., Olvera-Vargas, H., Lefebvre, O., 2018. Advanced electrocatalytic pre-treatment to improve the biodegradability of real wastewater from the electronics industry — A detailed investigation study. *J. Hazard. Mater.* 360, 552–559. <https://doi.org/10.1016/j.jhazmat.2018.08.023>
- Nayak, S., Chaplin, B.P., 2018. Fabrication and characterization of porous, conductive, monolithic Ti<sub>4</sub>O<sub>7</sub>

- electrodes. *Electrochim. Acta* 263, 299–310. <https://doi.org/10.1016/j.electacta.2018.01.034>
- Ngo, T.D., Kashani, A., Imbalzano, G., Nguyen, K.T.Q., Hui, D., 2018. Additive manufacturing (3D printing): A review of materials, methods, applications and challenges. *Compos. Part B Eng.* 143, 172–196. <https://doi.org/10.1016/j.compositesb.2018.02.012>
- Nidheesh, P. V., Zhou, M., Oturan, M.A., 2018. An overview on the removal of synthetic dyes from water by electrochemical advanced oxidation processes. *Chemosphere* 197, 210–227. <https://doi.org/10.1016/j.chemosphere.2017.12.195>
- Nienhauser, A.B., Ersan, M.S., Lin, Z., Perreault, F., Westerhoff, P., Garcia-Segura, S., 2022. Boron-doped diamond electrodes degrade short- and long-chain per- and polyfluorinated alkyl substances in real industrial wastewaters. *J. Environ. Chem. Eng.* 10, 107192. <https://doi.org/10.1016/j.jece.2022.107192>
- Oturan, M.A., 2021. Outstanding performances of the BDD film anode in electro-Fenton process: Applications and comparative performance. *Curr. Opin. Solid State Mater. Sci.* 25, 100925. <https://doi.org/10.1016/j.cossms.2021.100925>
- Panizza, M., Cerisola, G., 2009. Direct And Mediated Anodic Oxidation of Organic Pollutants. *Chem. Rev.* 109, 6541–6569. <https://doi.org/10.1021/cr9001319>
- Panizza, M., Michaud, P.A., Cerisola, G., Comninellis, C.H., 2001. Anodic oxidation of 2-naphthol at boron-doped diamond electrodes. *J. Electroanal. Chem.* 507, 206–214. [https://doi.org/10.1016/S0022-0728\(01\)00398-9](https://doi.org/10.1016/S0022-0728(01)00398-9)
- Radjenovic, J., Duinslaeger, N., Avval, S.S., Chaplin, B.P., 2020. Facing the Challenge of Poly- And Perfluoroalkyl Substances in Water: Is Electrochemical Oxidation the Answer? *Environ. Sci. Technol.* 54, 14815–14829. <https://doi.org/10.1021/acs.est.0c06212>
- Ruiz-Morales, J.C., Tarancón, A., Canales-Vázquez, J., Méndez-Ramos, J., Hernández-Afonso, L., Acosta-Mora, P., Marín Rueda, J.R., Fernández-González, R., 2017. Three dimensional printing of components and functional devices for energy and environmental applications. *Energy Environ. Sci.* 10, 846–859. <https://doi.org/10.1039/c6ee03526d>
- Shih, Y.J., Huang, C.P., Chan, Y.H., Huang, Y.H., 2019. Electrochemical degradation of oxalic acid over highly reactive nano-textured  $\Gamma$ - and  $\text{A-MnO}_2$ /carbon electrode fabricated by  $\text{KMnO}_4$  reduction on loofah sponge-derived active carbon. *J. Hazard. Mater.* 379, 120759.

- <https://doi.org/10.1016/j.jhazmat.2019.120759>
- Sirés, I., Garrido, J.A., Rodríguez, R.M., Cabot, P. I. luís, Centellas, F., Arias, C., Brillas, E., 2006. Electrochemical Degradation of Paracetamol from Water by Catalytic Action of Fe<sup>2+</sup>, Cu<sup>2+</sup>, and UVA Light on Electrogenated Hydrogen Peroxide. *J. Electrochem. Soc.* 153, D1. <https://doi.org/10.1149/1.2130568>
- Souza, F.L., Zougagh, M., Sáez, C., Cañizares, P., Ríos, A., Rodrigo, M.A., 2021. Electrochemically-based hybrid oxidative technologies for the treatment of micropollutants in drinking water. *Chem. Eng. J.* 414. <https://doi.org/10.1016/j.cej.2021.128531>
- Tofail, S.A.M., Koumoulos, E.P., Bandyopadhyay, A., Bose, S., O'Donoghue, L., Charitidis, C., 2018. Additive manufacturing: scientific and technological challenges, market uptake and opportunities. *Mater. Today* 21, 22–37. <https://doi.org/10.1016/j.mattod.2017.07.001>
- Trellu, C., Chaplin, B.P., Coetsier, C., Esmilaire, R., Cerneaux, S., Causserand, C., Cretin, M., 2018a. Electro-oxidation of organic pollutants by reactive electrochemical membranes. *Chemosphere* 208, 159–175. <https://doi.org/10.1016/j.chemosphere.2018.05.026>
- Trellu, C., Coetsier, C., Rouch, J.-C.C., Esmilaire, R., Rivallin, M., Cretin, M., Causserand, C., 2018b. Mineralization of organic pollutants by anodic oxidation using reactive electrochemical membrane synthesized from carbothermal reduction of TiO<sub>2</sub>. *Water Res.* 131, 310–319. <https://doi.org/10.1016/j.watres.2017.12.070>
- Trellu, C., Olvera Vargas, H., Mousset, E., Oturan, N., Oturan, M.A., 2021. Electrochemical technologies for the treatment of pesticides. *Curr. Opin. Electrochem.* 26, 100677. <https://doi.org/10.1016/j.coelec.2020.100677>
- Trellu, C., Péchaud, Y., Oturan, N., Mousset, E., Huguenot, D., van Hullebusch, E.D., Esposito, G., Oturan, M.A., 2016. Comparative study on the removal of humic acids from drinking water by anodic oxidation and electro-Fenton processes: Mineralization efficiency and modelling. *Appl. Catal. B Environ.* 194, 32–41. <https://doi.org/10.1016/j.apcatb.2016.04.039>
- Trellu, C., Rivallin, M., Cerneaux, S., Coetsier, C., Causserand, C., Oturan, M.A., Cretin, M., 2020. Integration of sub-stoichiometric titanium oxide reactive electrochemical membrane as anode in the electro-Fenton process. *Chem. Eng. J.* 400, 125936. <https://doi.org/10.1016/j.cej.2020.125936>
- Wu, X., Rigby, K., Huang, D., Hedtke, T., Wang, X., Chung, M.W., Weon, S., Stavitski, E., Kim, J.H., 2022.

- Single-Atom Cobalt Incorporated in a 2D Graphene Oxide Membrane for Catalytic Pollutant Degradation. *Environ. Sci. Technol.* 56, 1341–1351. <https://doi.org/10.1021/acs.est.1c06371>
- Xu, L., Niu, J., Xie, H., Ma, X., Zhu, Y., Crittenden, J., 2021. Effective degradation of aqueous carbamazepine on a novel blue-colored TiO<sub>2</sub> nanotube arrays membrane filter anode. *J. Hazard. Mater.* 402, 123530. <https://doi.org/10.1016/j.jhazmat.2020.123530>
- You, S., Liu, B., Gao, Y., Wang, Y., Tang, C.Y., Huang, Y., Ren, N., 2016. Monolithic Porous Magnéli-phase Ti<sub>4</sub>O<sub>7</sub> for Electro-oxidation Treatment of Industrial Wastewater. *Electrochim. Acta* 214, 326–335. <https://doi.org/10.1016/j.electacta.2016.08.037>
- Zaky, Amr M., Chaplin, B.P., 2014. Mechanism of p-substituted phenol oxidation at a Ti<sub>4</sub>O<sub>7</sub> reactive electrochemical membrane. *Environ. Sci. Technol.* 48, 5857–5867. <https://doi.org/10.1021/es5010472>
- Zhang, M., Mei, H., Chang, P., Cheng, L., 2020. 3D printing of structured electrodes for rechargeable batteries. *J. Mater. Chem. A* 8, 10670–10694. <https://doi.org/10.1039/d0ta02099k>
- Zhang, Y., Xu, X., Cai, J., Pan, Y., Zhou, M., 2021. Degradation of 2,4-dichlorophenoxyacetic acid by a novel photoelectrocatalysis/photoelectro-Fenton process using Blue-TiO<sub>2</sub> nanotube arrays as the anode. *Chemosphere* 266, 129063. <https://doi.org/10.1016/j.chemosphere.2020.129063>

## **Chapter V**

### **Development of 100% TiO<sub>x</sub> Electrodes for Removal of Organic Compounds in Flow-Through Configuration: The Key Role of Material Pore Size**

## Abstract

Two new 100% TiO<sub>x</sub> porous electrodes were synthesized and applied in different configurations. Similar chemical composition was obtained (Ti<sub>4</sub>O<sub>7</sub>/Ti<sub>5</sub>O<sub>9</sub>), while different porous structure (small vs large pore size) allowed investigation of the influence of porous structure on degradation rate of target organic compounds. In stirred-tank reactor, lower reaction rates were obtained using electrode with small pore size ( $\approx 2.2 \mu\text{m}$ ). However, the same electrode allowed obtaining optimal mass transport enhancement for flow-through application. Reaction rate for oxidative degradation of terephthalic acid (as probe molecule for  $\cdot\text{OH}$ -mediated oxidation) was 48 times higher compared to stirred-tank reactor when the optimal filtration flux of  $J = 1600 \text{ L h}^{-1} \text{ m}^{-2}$  was used. At higher flux, reaction rate decreased because of kinetic limitation and promotion of the competition with O<sub>2</sub> evolution. Foams with larger pore size ( $\approx 100 \mu\text{m}$ ) might provide a solution for reducing pressure drop and fouling issues in real wastewater treatment. However, reaction rates were still limited from diffusion within pores, even at low filtration flux ( $J = 600 \text{ L h}^{-1} \text{ m}^{-2}$ ). Such behavior would reduce current efficiency for the treatment of effluents with low concentration of pollutants. Therefore, this study highlights the key role of porous structure of electrodes for flow-through application, which should be optimized depending on the target application.

**Keywords:** TiO<sub>x</sub> electrode, Porous structure, Flow-through, Hydroxyl radicals

## 1. Introduction

With the development of electrochemical technologies and applications in water treatment, many studies have been dedicated to promote the efficiency of anodic oxidation process for the removal of organic compounds (Panizza and Cerisola, 2009; Chaplin, 2014; Sirés et al., 2014; Radjenovic and Sedlak, 2015; Hu et al., 2021; Oturan, 2021). Electrode material and reactor design have attracted most attention, due to their crucial impact on the two most important factors of anodic oxidation (AO) process: formation of reactive species and mass transfer conditions.

Dimensionally stable anodes (DSA), carbonaceous materials, metal oxides (e.g., PbO<sub>2</sub> and SnO<sub>2</sub>), Pt and boron-doped diamond (BDD) have all been studied as anode material but they suffer from one or more drawbacks, including relatively low reactivity, low chemical resistance to corrosion, possible leak of toxic metal ions or high cost (Marselli et al., 2003; Martínez-Huitle and Ferro, 2006; Panizza and Cerisola, 2009; Li et al., 2011; Rueffer et al., 2011; Brillas and Martínez-Huitle, 2015; Sopaj et al., 2016; Nidheesh et al., 2018; Hu et al., 2021; Oturan et al., 2021). In terms of reactivity, BDD is an ideal anode for the generation of physisorbed hydroxyl radicals (<sup>•</sup>OH) and subsequent non-selective removal of organic compounds (Oturan, 2021). However, some studies have shown that materials based on Magnéli phases (particularly Ti<sub>4</sub>O<sub>7</sub> and Ti<sub>5</sub>O<sub>9</sub>) might be a promising alternative to BDD due to: (i) their high conductivity and suitable electrochemical reactivity for <sup>•</sup>OH generation and (ii) their low cost since Ti is an abundant element on Earth (Padilha et al., 2014; Liang et al., 2018; Liu et al., 2022). Therefore, TiO<sub>x</sub> electrodes are currently the focus of several studies on removal of different organic pollutants and decontamination of real wastewaters (Aust and Kirste, 2014; Ganiyu et al., 2016; You et al., 2016; Lin et al., 2018; Wang et al., 2021).

Reactor design and optimization of operating conditions is also catching much attention for improving mass transfer conditions of organic pollutants from bulk to electrode surface. Flow-by reactors using plate electrodes aim at improving process efficiency by convection-enhanced mass transport that reduces the thickness of the diffusion layer at electrode/solution interface (Reis et al., 2013; Urtiaga et al., 2014; Wachter et al., 2019; Li et



al., 2022). More recently, further improvement has been obtained by the combination of filtration and anodic oxidation using flow-through reactor. In fact, the time scale of diffusion can be strongly reduced thanks to fast radial diffusion within small pores. However, small pores might also represent a drawback as regards to the pressure drop required to reach sufficiently high fluxes. Moreover, fouling might also become an issue. Therefore, the development of porous electrodes with suitable porous structure is currently an important challenge (Trellu et al., 2018; C. Li et al., 2022; W. Li et al., 2022).

Different TiO<sub>x</sub> materials have been synthesized and their effectiveness has been reported in literature. These TiO<sub>x</sub> electrodes include dense and porous materials presenting different characteristics in terms of (i) nature of Magnéli phases obtained and (ii) porous structure/surface roughness. However, it is still difficult to draw a clear conclusion on the role of porous structure in TiO<sub>x</sub> electrodes in application to the removal of organic compounds from water. Therefore, the objective of this study is to present the characteristics and reactivity of two new 100% TiO<sub>x</sub> materials with different porous structure. They were obtained from either carbothermal reduction of TiO<sub>2</sub> (small pores) or foaming process of TiO<sub>x</sub> suspension (large pores). Another electrode obtained from plasma spraying coating of TiO<sub>x</sub> on a porous Ti substrate was used to compare with the two 100% TiO<sub>x</sub> porous electrodes. The investigation focused on: (i) the electrochemical reactivity for removal of organic compounds using probe molecules, (ii) the influence of reactor configuration, including stirred-tank and flow-through configurations, (iii) the correlation between material characteristics and process effectiveness and (iv) the identification of limiting phenomena among diffusion, convection and reaction, according to material characteristics and operating conditions. This study provides new insights into the role of porous structure of TiO<sub>x</sub> materials in application for water treatment by electrooxidation process.

## 2. Materials and methods

### 2.1 Chemicals

Terephthalic acid ( $\geq 99\%$ ) was obtained from Acros Organics. Oxalic acid ( $\geq 97\%$ ), sodium hydroxide ( $\geq 98\%$ ) and sodium sulfate ( $\geq 99\%$ ) were obtained from Fluka. Formic acid ( $\geq 96\%$ ) was obtained from Sigma-Aldrich. Methanol (HPLC grade,  $\geq 99.9\%$ ) was obtained from Honeywell Riedel-de-Haën. All chemicals were used as received without any purification. Ultrapure water ( $R > 18.2 \text{ M}\Omega$ ) obtained from a Smart2Pure device (Thermo Scientific, France) was used for eluents preparation for HPLC and ion chromatography.

### 2.2 Material synthesis

All the 100% TiO<sub>x</sub> electrodes (100% TiO<sub>x</sub> foam and 100% TiO<sub>x</sub> REM) and Ti/TiO<sub>x</sub> foam were provided by Saint-Gobain Research Provence, CREE.

100% TiO<sub>x</sub> foam was synthesized according to the patent WO2006018537. A TiO<sub>x</sub> suspension in water was mixed, sheared and then dried to get a preform. Afterwards, discs were obtained using a slip casting method. Discs were then dried and sintered at 1450 °C under Ar (20 L h<sup>-1</sup>) atmosphere for 2 h.

For 100% TiO<sub>x</sub> REM, electrodes were obtained from uniaxial pressing of a mixture of 96.6 wt% TiO<sub>2</sub> Anatase (ALTI-CHEM) and 3.4 wt% Carbon Black Thermax 990 (CANCARB) to form a cylinder of 60 mm of diameter and 30 mm of height. Then, the cylinder was sintered at 1300 °C under Ar (20 L h<sup>-1</sup>) atmosphere for 2 h. This step allowed for carbothermal reduction of TiO<sub>2</sub> to obtain TiO<sub>x</sub> phase and generate porosity within the material. A diamond wheel was used to cut porous disks with a thickness of 4 mm. Unfortunately, the synthesis method of 100% TiO<sub>x</sub> REM is not yet protected by Saint-Gobain patents. Therefore, no further details for the synthesis are currently available.

The results obtained with 100% TiO<sub>x</sub> electrodes were compared with a Ti/TiO<sub>x</sub> foam electrode (synthesized as presented in Chapter III).

### 2.3 Material characterization

Porosity, pore size distribution and specific surface area were analyzed by mercury intrusion porosimetry. The analysis was conducted on a Micromeritics porosimeter (AutoPore IV 9500 V1.06) with Hg contact angle of 140.9 degrees and Hg surface tension of 485 dynes cm<sup>-1</sup>. The Hg intrusion pressure was set from 0.1 to 60000 psia. The chemical composition of 100% TiO<sub>x</sub> electrodes was characterized by X-Ray diffraction (XRD). The analysis was conducted on a Bruker D8 ENDEAVOR diffractometer (Cu K $\alpha$  radiation,  $\lambda=1.5418$  Å) at 40 kV and 40 mA. Database of PDF2-2004 (ICDD) was used for identification of TiO<sub>x</sub> phases. Morphology and porous structure of 100% TiO<sub>x</sub> electrodes were observed by a field emission electron probe microanalyzer (JEOL FEG JXA-8530F) and a KEYENCE digital microscope (VHX-7000). Raman analysis was performed on a Renishaw inVia Raman microscope with solid-state green laser (Nd: YAG) at 532 nm with laser energy filter of 5%.

### 2.4 Electrochemical characterization

All electrochemical characterization were performed on a Metrohm Autolab PGSTAT with a three electrodes system including a working electrode (100% TiO<sub>x</sub> and Ti/TiO<sub>x</sub> electrodes), a stainless steel as counter electrode and an Ag/AgCl/3 M KCl electrode as reference. Experiments were performed in 300 mL of 0.1 M NaClO<sub>4</sub> as supporting electrolyte.

Linear sweep voltammetry (LSV) tests were carried out from open circuit potential (OCP) to 3.8 V vs Ag/AgCl/3 M KCl at 0.01 V s<sup>-1</sup> in order to study electrode behavior for oxygen evolution reaction. Raw LSV data were corrected according to the uncompensated resistance of the electrochemical system (Faria, 1996; Kapalka et al., 2008; Krstajic and Trasatti, 1998). Further details were provided in Chapter III.

A method based on the measurement of double layer capacitance was used to calculate the electro-active surface area (EASA) (Nayak and Chaplin, 2018). Cyclic voltammetry (CV)

tests were carried out at scan rate from 6-10 mV s<sup>-1</sup> to calculate the double layer capacitance (as detailed in Chapter III). Then a specific capacitance of 60 μF cm<sup>-2</sup> (typical for such material) was taken into consideration to calculate EASA (Bockris and Otagawa, 1984; Nayak and Chaplin, 2018).

## 2.5 Experimental configurations for stirred-tank and flow-through reactors

A 400 mL cylindrical undivided stirred-tank reactor was operated in batch mode at a constant current density of 5 mA cm<sup>-2</sup>. Ti/TiO<sub>x</sub> foam and 100% TiO<sub>x</sub> electrodes were used as anode. Carbon felt was used as cathode. Anode and cathode were placed face to face in the solution with an inter-electrode distance of 2.5 cm. The ratio between the geometric surface area of electrodes immersed in the solution and the volume of the solution was maintained constant at  $S_{\text{electrode}}/V_{\text{solution}} = 7.9 \text{ m}^{-1}$ . The solution was stirred using a magnetic bar at a constant rate of 750 rpm. Samples were taken from the reactor at different time interval for analysis.

Flow-through experiments were performed in a glass reactor with  $S_{\text{electrode}} = 12.6 \text{ cm}^2$ . Porous 100% TiO<sub>x</sub> electrode was put at the bottom of the reactor as anode and a BDD grid was put at the top of the reactor as cathode. The solution was pumped from the feedwater reservoir through the reactor in dead-end filtration mode. Flow-through experiments were operated at constant current density of 5 mA cm<sup>-2</sup> in continuous mode (single pass, 0% recirculation).

## 2.6 Electrode reactivity assessment using probe molecules

As detailed in Chapter III, oxalic acid (OA) and terephthalic acid (TA) were used as probe molecules for direct electron transfer (DET) and •OH-mediated oxidation, respectively. 0.4 mM OA and 0.1 mM TA were used to have the same initial total organic carbon (TOC) (9.6 mg L<sup>-1</sup>). 50 mM Na<sub>2</sub>SO<sub>4</sub> was used as supporting electrolyte. Reactivity tests were performed in both stirred-tank and flow-through reactors. In the flow-through reactor, degradation rate of probe molecules was studied according to the flow rate through the electrode.

## 2.7 Analytical methods

Mineralization degree of OA and TA solutions was assessed by a SHIMADZU TOC analyzer (TOC-L). Concentration of TA and its degradation by-product HTA (2-hydroxyterephthalic acid) were analyzed by an Elite LaChrom HPLC system (HITACHI) coupled with a L-2400 UV detector ( $\lambda = 254$  nm), a L-2480 fluorescence detector (Ex/Em=315/435 nm), a L-2130 pump (with a flow rate of 0.8 mL min<sup>-1</sup>) and a LiChroCART Purospher ® STAR RP-18e (5  $\mu$ m) column set in the oven at 40 °C. The eluent was a mixture of methanol (40%) and 0.1% formic acid in water (60%).

## 2.8 Calculation of mineralization current efficiency (MCE)

MCE of OA and TA by different electrodes was calculated as detailed in Chapter IV.

# 3. Results and discussions

## 3.1 Material characterization

### 3.1.1 Pore size distribution

Results obtained from Hg porosimetry showed that 100% TiO<sub>x</sub> foam has a median pore size of 127.2  $\mu$ m as regards to pore volume (Fig. 5-1 (a)) and 2.3  $\mu$ m as regards to pore surface area. The porosity and specific surface area of 100% TiO<sub>x</sub> foam were determined as 69% and 0.104 m<sup>2</sup> g<sup>-1</sup>, respectively (Table 5-1). On the other hand, REM has median pore size of 2.2  $\mu$ m as regards to pore volume (Fig. 5-1 (b)) and 1.9  $\mu$ m as regards to pore surface area. REM has a porosity of 29% and specific surface area of 0.202 m<sup>2</sup> g<sup>-1</sup> (Table 5-1). Summary of Hg porosimetry analysis of different TiO<sub>x</sub> electrodes are presented in Table 5-1.

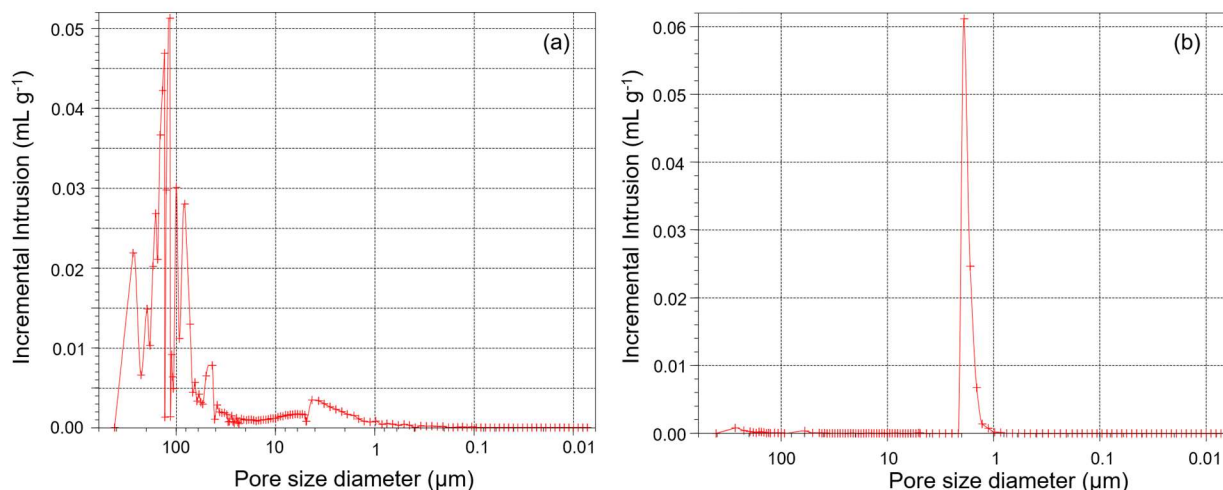


Fig. 5-1 - Incremental intrusion volume of Hg according to pore diameter: 100% TiO<sub>x</sub> foam (a) and 100% TiO<sub>x</sub> REM (b)

Table 5-1 Hg porosimetry analysis of different TiO<sub>x</sub> electrodes

Electrode	Porosity	Specific	Median pore	Median pore
		surface area	size (volume)	size (area)
		(m <sup>2</sup> g <sup>-1</sup> )	(μm)	(μm)
Ti/TiO <sub>x</sub> foam	35%	0.013	88.0	15.2
100% TiO <sub>x</sub> foam	69%	0.104	127.2	2.3
100% TiO <sub>x</sub> REM	29%	0.202	2.2	1.9

### 3.1.2 Porous structure

The porous structure of 100% TiO<sub>x</sub> foam and REM was observed by a field emission electron probe microanalyzer (Figs. 5-2(a) and 5-2(b) for 100% TiO<sub>x</sub> foam and REM, respectively) and a digital microscope (Figs. 5-2(c) and 5-2(d) for 100% TiO<sub>x</sub> foam and REM, respectively). 100% TiO<sub>x</sub> REM presents a homogeneously interconnected and open porous structure with much smaller pore size compared to 100% TiO<sub>x</sub> foam. As regards to 100% TiO<sub>x</sub> foam, the open porous structure is mainly ascribed to large pores (which represent the main fraction of

porous volume) while small pores are ascribed to small defects within the porous structure. These small pores will participate to a little extent in water permeation. Therefore, median pore size calculated as regards to pore volume seems to be more appropriate for characterizing the effect of porous structure on process effectiveness in flow-through configuration.

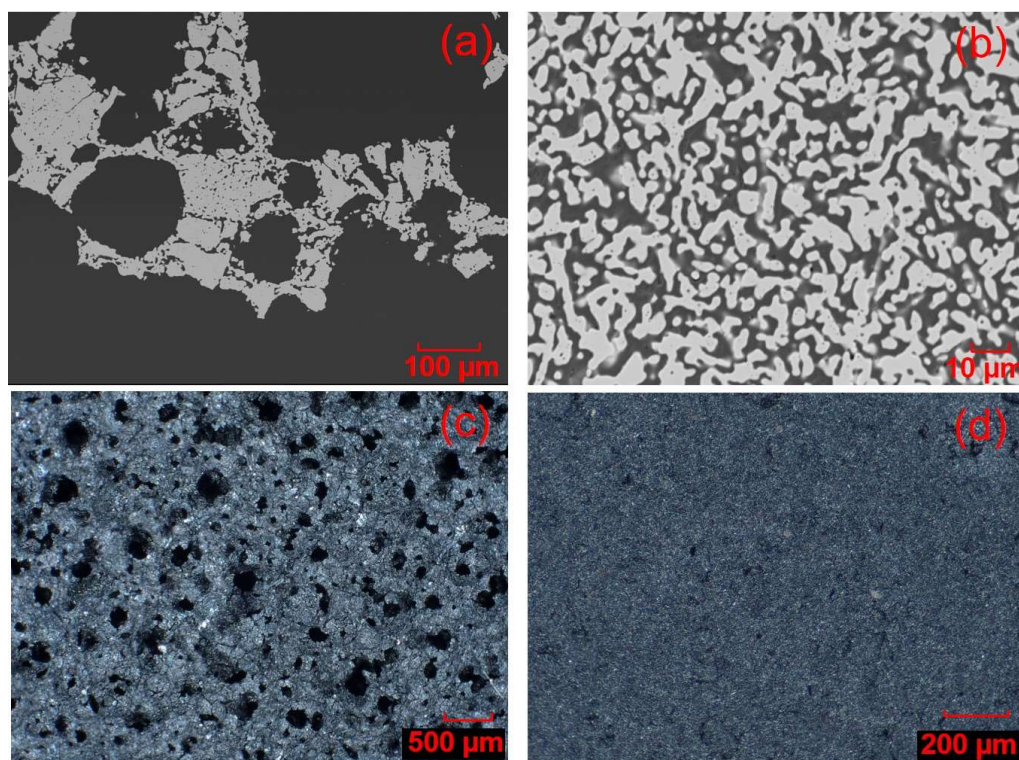


Fig. 5-2 - Porous structure observed by a field emission electron probe microanalyzer for 100% TiO<sub>x</sub> foam (a) and REM (b) and by a digital microscope for 100% TiO<sub>x</sub> foam (c) and REM (d)

### 3.1.4 X-ray diffraction and Raman spectra

Chemical composition of 100% TiO<sub>x</sub> electrodes was then assessed by XRD (Fig. 5-3). For both 100% TiO<sub>x</sub> foam (Fig. 5-3 (a)) and REM (Fig. 5-3 (b)), the results indicate that the major phases were Ti<sub>4</sub>O<sub>7</sub> and Ti<sub>5</sub>O<sub>9</sub>. Ti<sub>6</sub>O<sub>11</sub> was also detected as minor phase for 100% TiO<sub>x</sub> REM. Different synthesis methods may lead to different stoichiometry of these Magnéli phases;

however, very similar chemical composition was obtained in this study. Ti<sub>4</sub>O<sub>7</sub> and Ti<sub>5</sub>O<sub>9</sub> are the most conductive Magnéli phases and the most suitable phases for application in the anodic oxidation process (Zhao et al., 2022). Raman spectra (Fig. 5-4) was performed for further confirmation of chemical composition. The absence of well-defined peaks at low laser energy is typical for TiO<sub>x</sub> phases, while the presence of well-defined peaks at high laser energy highlights the re-oxidation of the material to TiO<sub>2</sub> under high laser irradiation (Chapter III).

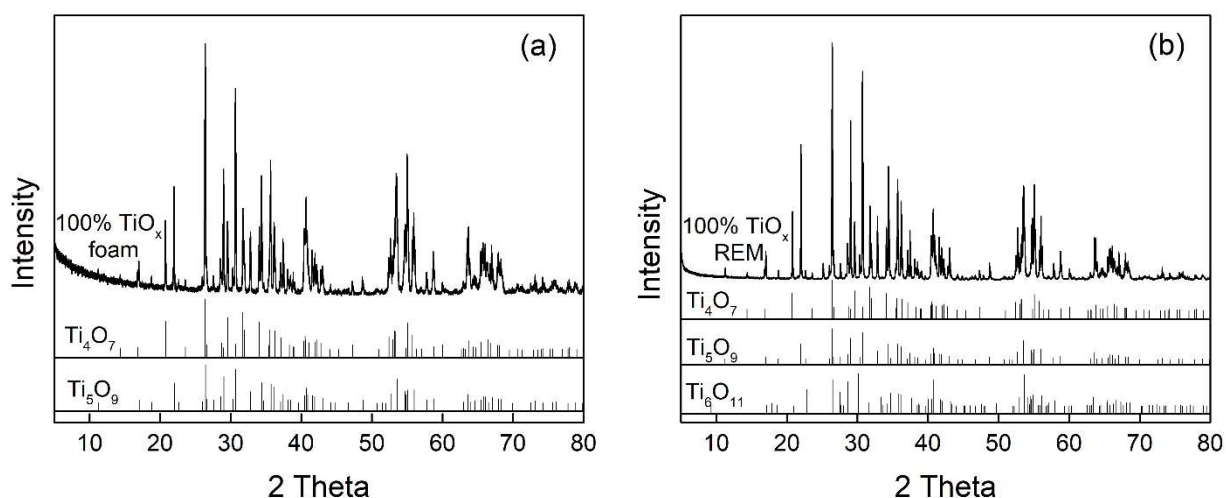


Fig. 5-3 – XRD patterns for 100% TiO<sub>x</sub> foam (a) and REM (b) electrodes (database: PDF2-2004)

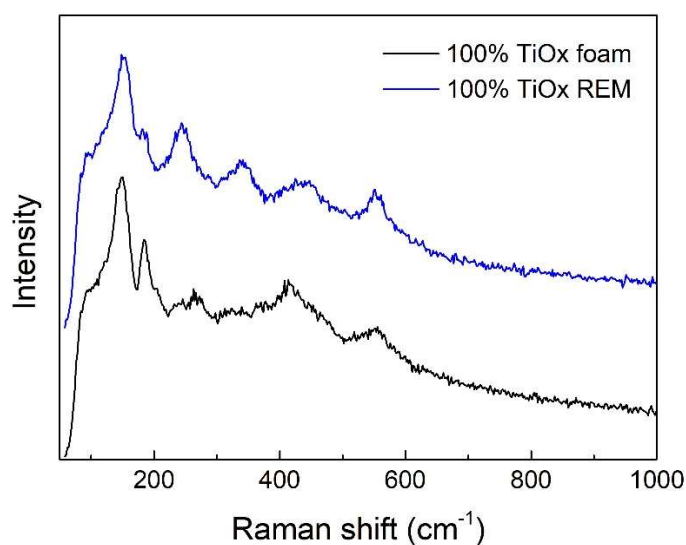


Fig. 5-4 – Raman spectra of 100% TiO<sub>x</sub> foam and REM



### 3.1.5 Electrochemical characteristics

Fig. 5-5 presents the overpotential for oxygen evolution reaction (OER) of 100% TiO<sub>x</sub> foam and REM. 100% TiO<sub>x</sub> foam has an oxygen evolution potential (OEP) of 2.85 V vs Ag/AgCl/3 M KCl, which is comparable to that of Ti/TiO<sub>x</sub> foam (2.82 V vs Ag/AgCl/3 M KCl) (Table 5-2), probably due to their similar pore size and porous structure. However, 100% TiO<sub>x</sub> REM has lower OEP of 2.29 V vs Ag/AgCl/3 M KCl. The determined EASA of 100% TiO<sub>x</sub> foam and REM are 1096 and 7411 cm<sup>2</sup>, corresponding to roughness factor of 46 and 416, respectively (Table 5-2).

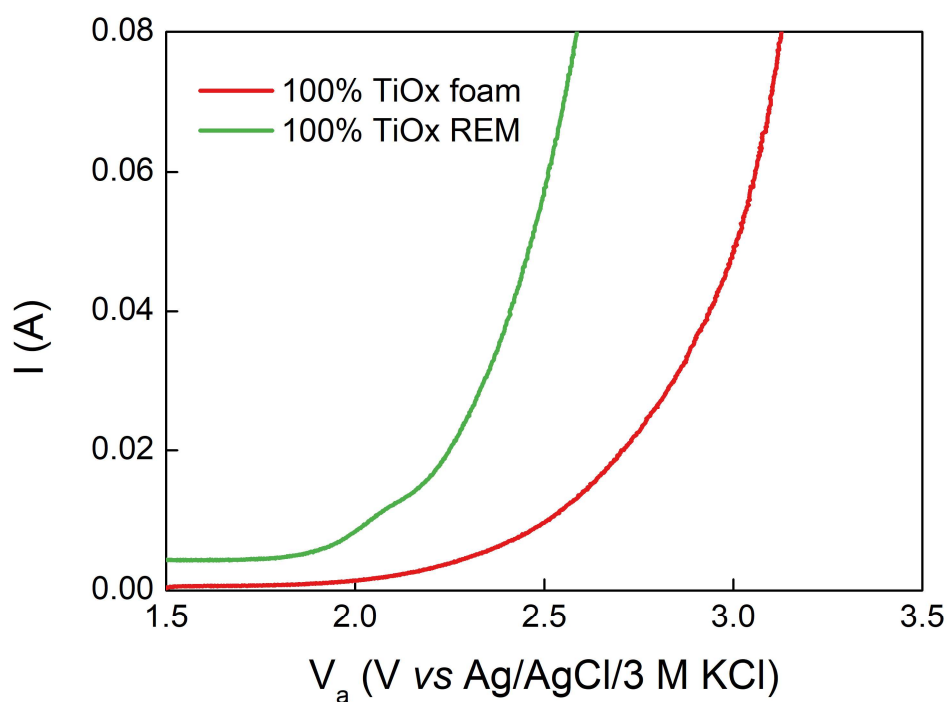


Fig. 5-5 - LSV curves of 100% TiO<sub>x</sub> foam and REM (reference electrode: Ag/AgCl/3 M KCl, supporting electrolyte: 100 mM NaClO<sub>4</sub>, scan rate: 0.01 V s<sup>-1</sup>)

Table 5-2 Electrochemical characteristics of TiO<sub>x</sub> electrodes

	OEP (V vs Ag/AgCl/3 M KCl)	EASA (cm <sup>2</sup> )	Geometric surface area (cm <sup>2</sup> )	Roughness factor
<b>Ti/TiO<sub>x</sub> foam</b>	2.82	1620	23.6	69
<b>100% TiO<sub>x</sub> foam</b>	2.85	1096	23.6	46
<b>100% TiO<sub>x</sub> REM</b>	2.29	7411	17.8	416

### 3.2 Reactivity of TiO<sub>x</sub> electrodes in stirred-tank reactor

During AO process, organics can be degraded through both DET and •OH-mediated oxidation. Fig. 5-6 (a) shows the degradation kinetic of OA, which is related to the reactivity of different TiO<sub>x</sub> electrodes for DET. Similar performance was obtained for 100% TiO<sub>x</sub> REM and Ti/TiO<sub>x</sub> foam, while the fastest kinetic was obtained with 100% TiO<sub>x</sub> foam (2.5-times higher degradation rate constant than that of Ti/TiO<sub>x</sub> foam and REM). Low mineralization current efficiency values were obtained for all electrodes, i.e., 1.9%, 2.7% and 1.8% for Ti/TiO<sub>x</sub> foam, 100% TiO<sub>x</sub> foam and 100% TiO<sub>x</sub> REM. It was mainly ascribed to a strong mass transport limitation. Previous results showed that the porous structure of electrodes has a great impact on the effectiveness of the process, even in stirred-tank reactor (Chapter III). In this configuration, a thick diffusion layer forms at the electrode/solution interface. Therefore, it was highlighted that coarse roughness surface (i.e., large pores) with characteristic scale larger than the diffusion boundary layer is actually more suitable for mass transport enhancement in stirred-tank reactor. In fact, fine roughness surface (i.e., small pores) is averaged within the diffusion field and does not provide additional electrode surface for mass transport enhancement of organic compounds from the bulk to the electrode surface. The comparison of results obtained with 100% TiO<sub>x</sub> foam (large pore size) and REM (small pore size) confirms that this advantage comes from the presence of a coarse roughness for mass transport enhancement in stirred-tank reactor. Besides, 100% TiO<sub>x</sub> foam has similar porous

structure to that of Ti/TiO<sub>x</sub> foam (median pore size of 127 μm and 88 μm for 100% TiO<sub>x</sub> and Ti/TiO<sub>x</sub> foams, respectively). Thus, the lower performance of Ti/TiO<sub>x</sub> foam might be ascribed to a different chemical composition and reactivity, instead of different mass transport conditions. The 100% TiO<sub>x</sub> foam contains only Ti<sub>4</sub>O<sub>7</sub> and Ti<sub>5</sub>O<sub>9</sub>, which have the highest conductivity among Magnéli phases, while the Ti/TiO<sub>x</sub> (Ti coated by TiO<sub>x</sub>) foam also contains more oxidized Magnéli phases (Table 5-3) that might impact its conductivity and affect the electron transfer kinetic at the electrode.

Table 5-3 Chemical composition of TiO<sub>x</sub> electrodes

	Major phases	Minor phases
<b>Ti/TiO<sub>x</sub> foam</b>	Ti <sub>4</sub> O <sub>7</sub>	Ti <sub>6</sub> O <sub>11</sub> , Ti <sub>8</sub> O <sub>15</sub> , TiO <sub>2</sub>
<b>100% TiO<sub>x</sub> foam</b>	Ti <sub>4</sub> O <sub>7</sub> , Ti <sub>5</sub> O <sub>9</sub>	---
<b>100% TiO<sub>x</sub> REM</b>	Ti <sub>4</sub> O <sub>7</sub> , Ti <sub>5</sub> O <sub>9</sub>	Ti <sub>6</sub> O <sub>11</sub>

Degradation kinetics of TA were then investigated to assess the reactivity of electrodes for •OH-mediated oxidation. A different trend was observed. Fast and similar degradation kinetics were obtained with the two foams, while the slowest kinetic was obtained with 100% TiO<sub>x</sub> REM. First, these results confirm again the more favorable mass transport conditions when using electrodes with large pore size (coarse roughness) in stirred-tank reactor. Besides, the results suggest that the different chemical composition of the TiO<sub>x</sub> coating compared to the 100% TiO<sub>x</sub> foam (Table 5-3) did not significantly affect its capacity to remove TA through •OH mediated oxidation.

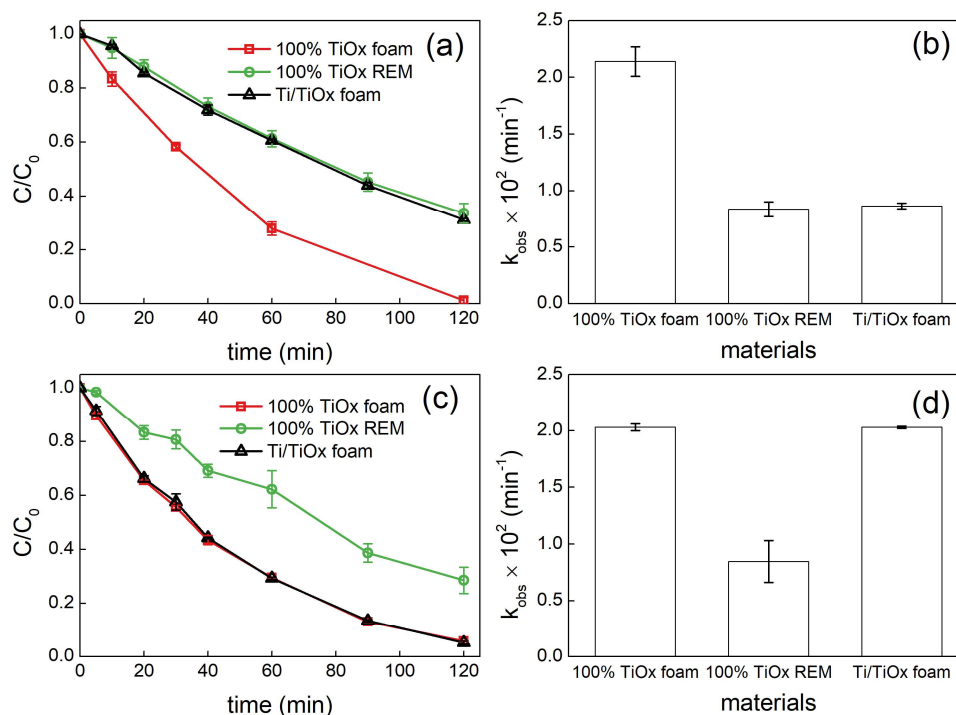


Fig. 5-6 - Degradation kinetics of OA (a) with the pseudo first order rate constants (b) and degradation kinetics of TA (c) with the pseudo first order rate constants (d) by anodic oxidation with 100% TiO<sub>x</sub> anodes in the stirred-tank reactor (compared with Ti/TiO<sub>x</sub> foam) (initial C<sub>TA</sub> = 0.1 mM, initial C<sub>OA</sub> = 0.4 mM, S<sub>electrode</sub>/V<sub>solution</sub> = 7.9 m<sup>-1</sup>, current density = 5 mA cm<sup>-2</sup>)

The mineralization yield of TA solution after 2 h of electrolysis is depicted in Fig. 5-7. 100% TiO<sub>x</sub> foam achieved 15% more mineralization yield than Ti/TiO<sub>x</sub> foam. It corresponds to a higher mineralization current efficiency (8.2%, 4.3% and 6.6% for 100% TiO<sub>x</sub> foam, 100% TiO<sub>x</sub> REM and Ti/TiO<sub>x</sub> foam, respectively). As observed above, the two foams performed similarly with TA degradation as probe molecule for •OH-mediated oxidation. Therefore, the better behavior of 100% TiO<sub>x</sub> foam for TA mineralization might be ascribed to its faster reactivity for DET, as observed previously for OA (Fig. 5-6 (a)). Both DET and •OH-mediated oxidation contribute to the mineralization of the parent compound and intermediate products to CO<sub>2</sub> since short-chain carboxylic acids (such as OA) are important intermediates of the oxidative degradation pathway (Chen et al., 2020). The lowest mineralization yield was obtained with 100% TiO<sub>x</sub> REM (42%). It is consistent with previous results highlighting its

lower effectiveness for the removal of both probe molecules.

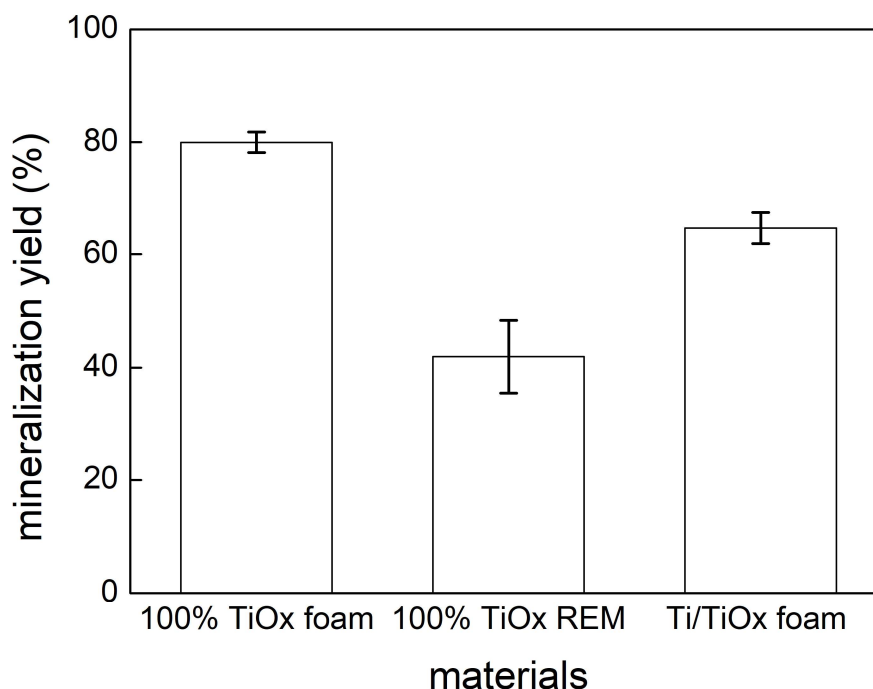


Fig. 5-7 - Mineralization yield of 0.1 mM TA solution by anodic oxidation with 100% TiO<sub>x</sub> anodes after 2 h of electrolysis in the stirred-tank reactor (compared with Ti/TiO<sub>x</sub> foam)

( $S_{\text{electrode}}/V_{\text{solution}} = 7.9 \text{ m}^{-1}$ , current density =  $5 \text{ mA cm}^{-2}$ )

### 3.3 Reactivity of electrodes in flow-through reactor

As discussed in sub-section 3.2, the stirred-tank reactor could not take full advantage of these porous materials. Therefore, in this sub-section, the porous electrodes under study were investigated in flow-through configuration and very different trends were obtained.

Fig. 5-8 and Fig. 5-9 show the degradation efficiency of OA and TA (in terms of g of compounds removed per hour and per square meter of membrane) as regards to the volumetric filtration flux through the different porous TiO<sub>x</sub> electrodes. Dash lines represent the effectiveness achieved in stirred-tank reactor.

As compared to results obtained in the stirred-tank reactor, both OA and TA degradation rate was greatly enhanced for all electrodes in flow-through reactor. At optimum flux, OA degradation rate by 100% TiO<sub>x</sub> foam, Ti/TiO<sub>x</sub> foam and REM was enhanced by 2.6, 8.9 and

32 times, respectively, while TA degradation rate was enhanced by 3.8, 1.9, and 48 times, respectively. These results highlight that application in flow-through configurations is the key point for taking advantage of the internal porosity and electro-active surface area of porous electrodes.

Increasing the filtration flux allowed for improving OA reaction rate due to an increase of the convective mass transfer. Such behavior indicates that convection might be the limiting phenomenon at low flux. However, much higher reaction rate enhancement was obtained with 100% TiO<sub>x</sub> REM compared to the two foams. For example, the maximum OA removal rate obtained with 100% TiO<sub>x</sub> REM was 4.0 and 4.8 times higher than that obtained with 100% TiO<sub>x</sub> foam and Ti/TiO<sub>x</sub> foam, respectively. In terms of mineralization current efficiency, it corresponds to a decrease from 53.1% (for 100% TiO<sub>x</sub> REM) to 11.7% and 10.5 % for 100% TiO<sub>x</sub> foam and Ti/TiO<sub>x</sub> foam, respectively. This lower efficiency might be ascribed to a limitation from diffusion within pores due to larger pore size of two foams. In fact, diffusion limitation might occur when the time scale of diffusion ( $t_D$ , Eq. 5-1) exceeds the time scale of convection ( $t_C$ , Eq. 5-2), i.e., when the time required for target compounds to diffuse from inside of the pores to pore surface becomes longer than the residence time of target compounds within the electro-active volume of the electrode. For example, by taking into consideration the median pore radius (according to pore volume) of 100% TiO<sub>x</sub> foam and  $l = 1$  mm,  $t_D > t_C$  would be reached at  $J = 615 \text{ L h}^{-1} \text{ m}^{-2}$  (i.e., at the beginning of the range of the flux tested in this study). By comparison, with the 100% TiO<sub>x</sub> REM, the lower pore size involves that  $t_D > t_C$  would be reached only at  $J = 8.63 \times 10^5 \text{ L h}^{-1} \text{ m}^{-2}$ , a value much higher than the range of tested operating conditions.

$$t_D = r_p^2 / D \quad (5 - 1)$$

$$t_C = l / v \quad (5 - 2)$$

where  $r_p$  is the average pore radius (m),  $D$  is the diffusion coefficient of the target compounds ( $\text{m}^2 \text{ s}^{-1}$ ) ( $1.0 \times 10^{-9} \text{ m}^2 \text{ s}^{-1}$  for oxalic acid (Šljukić et al., 2007)),  $l$  is the electro-active layer thickness (m) and  $v$  is the average pore velocity ( $\text{m s}^{-1}$ ).

These results highlight that using foams with large pore size for the treatment of low

concentration of organic compounds might still result in a strong mass transfer limitation related to the radial diffusion within pores, even in flow-through configuration. On the contrary, using 100% TiO<sub>x</sub> REM with low pore size, mass transfer rate was simply improved by increasing convection rate (without significant limitation from diffusion). However, the OA reaction rate reached a plateau at fluxes above 1900 L h<sup>-1</sup> m<sup>-2</sup>. Two phenomena might explain such behavior. First, lower residence time within the electro-active volume of the electrode might lead to a kinetic limitation for reaction at electrode surface. Moreover, it was reported that high fluxes through porous electrodes increase the current for oxygen evolution by sweeping gas bubbles from the electrode surface (Guo et al., 2016). Thus, promoting the competition with oxygen evolution reaction probably limited the OA reaction rate.

In the case of <sup>•</sup>OH-mediated oxidation, the evolution of TA reaction rate according to flow rate and electrode materials followed similar trends. When increasing convection through the electrodes, the highest enhancement of TA reaction rate was obtained with 100% TiO<sub>x</sub> REM. The maximum TA degradation rate obtained with 100% TiO<sub>x</sub> REM was 2.8 and 6.2 times higher than with 100% TiO<sub>x</sub> foam and Ti/TiO<sub>x</sub> foam, respectively. As detailed previously for OA reaction rate, it might be mainly ascribed to the absence of a diffusion limitation in this range of filtration flux, while the larger pores of the two foams involved a limitation from the diffusion within pores.

It is interesting to notice that lower enhancement of TA reaction rate (compared to stirred-tank configuration) was observed with Ti/TiO<sub>x</sub> foam. A 8.9 times enhancement of OA reaction rate was obtained, but this value decreased to 1.9 for TA reaction rate. It might be ascribed to the specific morphology of the Ti/TiO<sub>x</sub> foam, for which only the top of the electrode was coated. While both Ti substrate and TiO<sub>x</sub> coating could participate in the removal of OA through DET, only TiO<sub>x</sub> coating is able to generate physisorbed <sup>•</sup>OH. Thus, the electro-active thickness for <sup>•</sup>OH formation might be considered to reach a value of only few hundreds of μm, according to images obtained from scanning electron microscopy (Chapter III). Therefore, the time scale for convection within this smaller electro-active thickness might be strongly reduced. Such phenomenon would result in further mass transfer limitation and lower reaction rate compared, for example, to the 100% TiO<sub>x</sub> electrodes presenting similar pore size.

A slight decrease of TA reaction rate was also obtained at high filtration flux. A kinetic limitation for  $\cdot\text{OH}$ -mediated oxidation of TA might occur when the residence time within the electro-active volume decreases, as for OA oxidation. Moreover, formation of  $\cdot\text{OH}$  is an intermediate step of the global oxygen evolution reaction. Therefore, sweeping gas bubbles from the electrode surface might promote further oxidation of  $\cdot\text{OH}$  to O<sub>2</sub>.

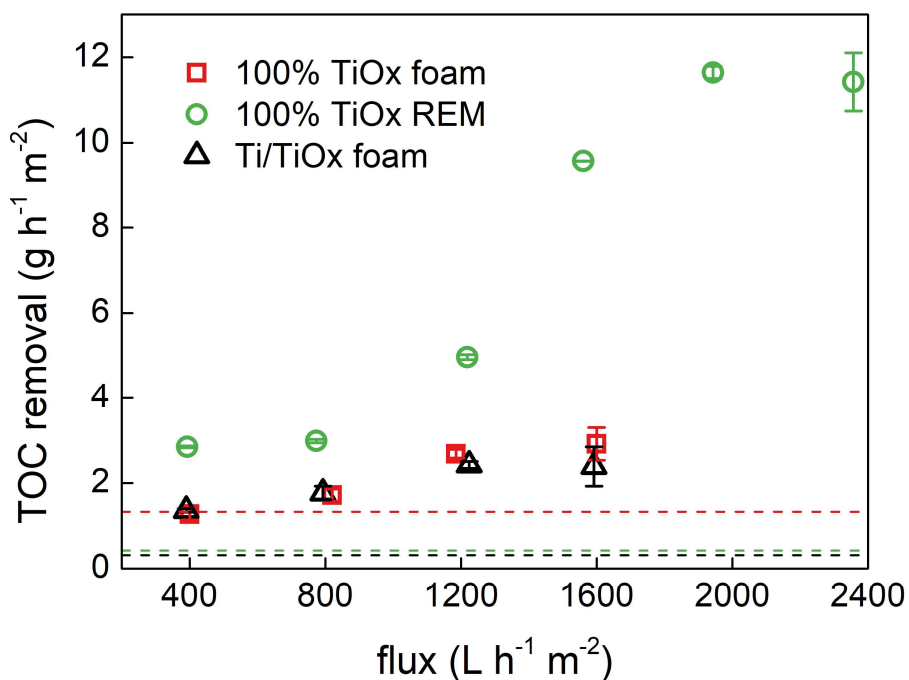


Fig. 5-8 - OA mineralization yield by 100% TiO<sub>x</sub> foam, REM and Ti/TiO<sub>x</sub> foam in flow-through configuration and the comparison with the mineralization yield (dash lines) obtained in stirred-tank reactor (with same electric charge passed) (initial C<sub>OA</sub> = 0.4 mM, effective surface area = 12.56 cm<sup>2</sup>, current density = 5 mA cm<sup>-2</sup>)



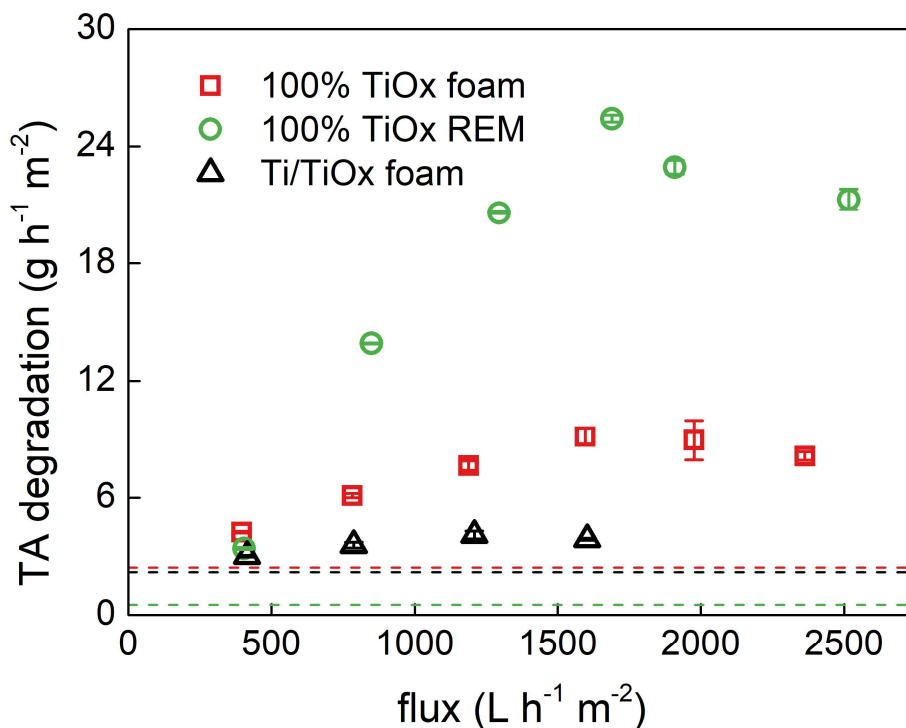


Fig. 5-9 - TA degradation efficiency by 100% TiO<sub>x</sub> foam, REM and Ti/TiO<sub>x</sub> foam during anodic oxidation in flow-through configuration comparing to the efficiency (dash lines) in stirred-tank reactor with same electric charge (initial C<sub>TA</sub> = 0.1 mM, effective surface area = 12.56 cm<sup>2</sup>, current density = 5 mA cm<sup>-2</sup>)

#### 4. Conclusions

Both 100% TiO<sub>x</sub> electrodes presented very similar chemical composition, including the most conductive Magnéli phases, Ti<sub>4</sub>O<sub>7</sub> and Ti<sub>5</sub>O<sub>9</sub>, as main phases. However, their very different pore size distribution highlighted the role of porous structure of these materials as anode in electrooxidation process.

In stirred-tank reactor, coarse roughness (i.e., large pores) was more favorable for improving mass transport conditions since fine roughness surface was averaged within the diffusion field.

In flow-through reactor, convection through the porous electrode allowed for taking advantage of the internal EASA, while fast radial diffusion within pores strongly reduced

diffusion limitation. For example, TA reaction rate was multiplied by 48 times when using 100% TiO<sub>x</sub> REM (small pore size) under optimal volumetric filtration flux compared to the reaction rate obtained in stirred-tank reactor. At low filtration flux, convection through the electrode was the main limitation. However, using electrodes with large pore size (foam) rapidly led to a limitation from diffusion within pores since the time scale for diffusion was higher than the time scale for convection even at low filtration flux (e.g.,  $J > 615 \text{ L h}^{-1} \text{ m}^{-2}$  for 100% TiO<sub>x</sub> foam). This limitation was further enhanced when using Ti/TiO<sub>x</sub> foam for TA oxidation since residence time within the active zone for  $\cdot\text{OH}$ -mediated oxidation was reduced to the superficial TiO<sub>x</sub>-coated layer of the electrode. Diffusion limitation did not occur in this range of filtration flux when using 100% TiO<sub>x</sub> REM due to smaller pore size. However, degradation rate of target compounds decreased or reached a plateau at high flux because of (i) a kinetic limitation related to the shorter residence time within the electrode and (ii) a strong competition with O<sub>2</sub> evolution rate which is enhanced at high filtration flux.

These results highlight advantages and drawbacks related to the different porous structure of electrodes and emphasize the key role of the reactor configuration. Electrodes with low pore size are the most suitable to apply in flow-through configurations for mass transport enhancement and efficient removal of low concentration of organic pollutants. However, electrodes with large pore size might still provide a solution for avoiding high-pressure drop and fouling issues.

## References

- Aust, N., Kirste, A., 2014. Paired Electrosynthesis, in: Kreysa, G., Ota, K., Savinell, R.F. (Eds.), *Encyclopedia of Applied Electrochemistry*. Springer New York, New York, NY, pp. 1505–1510. [https://doi.org/10.1007/978-1-4419-6996-5\\_370](https://doi.org/10.1007/978-1-4419-6996-5_370)
- Bockris, J.O., Otagawa, T., 1984. The Electrocatalysis of Oxygen Evolution on Perovskites. *J. Electrochem. Soc.* 131, 290–302. <https://doi.org/10.1149/1.2115565>
- Brillas, E., Martínez-Huitle, C.A., 2015. Decontamination of wastewaters containing synthetic organic dyes by electrochemical methods. An updated review. *Appl. Catal. B Environ.* 166–167, 603–643. <https://doi.org/10.1016/j.apcatb.2014.11.016>
- Chaplin, B.P., 2014. Critical review of electrochemical advanced oxidation processes for water treatment applications. *Env. Sci Process. Impacts* 16, 1182–1203. <https://doi.org/10.1039/C3EM00679D>
- Chen, X., Huang, Z.-H., Ji, Z.-Y., Guo, X.-F., Zhao, L.-M., Yuan, J.-S., 2020. Efficient treatment of pure terephthalic acid wastewater with Na<sub>2</sub>S<sub>2</sub>O<sub>8</sub> based on thermal activation. *Environ. Technol. Innov.* 19, 100897. <https://doi.org/10.1016/j.eti.2020.100897>
- Faria, L.A.D., 1996. Electrocatalytic properties of ternary oxide mixtures of composition Ru<sub>0.3</sub>Ti<sub>(0.7-x)</sub>Ce<sub>x</sub>O<sub>z</sub>: oxygen evolution from acidic solution. *J. Appl. Electrochem.* 26, 1195–1199. <https://doi.org/10.1007/BF00243745>
- Ganiyu, S.O., Oturan, N., Raffy, S., Cretin, M., Esmilaire, R., van Hullebusch, E., Esposito, G., Oturan, M.A., 2016. Sub-stoichiometric titanium oxide (Ti<sub>4</sub>O<sub>7</sub>) as a suitable ceramic anode for electrooxidation of organic pollutants: A case study of kinetics, mineralization and toxicity assessment of amoxicillin. *Water Res.* 106, 171–182. <https://doi.org/10.1016/j.watres.2016.09.056>
- Guo, L., Jing, Y., Chaplin, B.P., 2016. Development and Characterization of Ultrafiltration TiO<sub>2</sub> Magnéli Phase Reactive Electrochemical Membranes. *Environ. Sci. Technol.* 50, 1428–1436. <https://doi.org/10.1021/acs.est.5b04366>
- Hu, Z., Cai, J., Song, G., Tian, Y., Zhou, M., 2021. Anodic oxidation of organic pollutants: Anode fabrication, process hybrid and environmental applications. *Curr. Opin. Electrochem.* 26, 100659. <https://doi.org/10.1016/j.coelec.2020.100659>
- Kapalka, A., Fóti, G., Comninellis, C., 2008. Determination of the Tafel slope for oxygen evolution on boron-doped diamond electrodes. *Electrochem. Commun.* 10, 607–610.

<https://doi.org/10.1016/j.elecom.2008.02.003>

- Krstajic, N., Trasatti, S., 1998. Cathodic behaviour of RuO<sub>2</sub>-doped Ni/Co<sub>3</sub>O<sub>4</sub> electrodes in alkaline solutions: hydrogen evolution. *J. Appl. Electrochem.* 28, 1291–1297. <https://doi.org/10.1023/A:1003444110172>
- Li, C., Zhu, J., Zhao, Z., Wang, J., Yang, Q., Sun, H., Jiang, B., 2022. An efficient and robust flow-through electrochemical Ti<sub>4</sub>O<sub>7</sub> membrane system for simultaneous Cr(VI) reduction and Cr immobilization with membrane cleaning by a periodic polarity reversal strategy. *Sep. Purif. Technol.* 297, 121424. <https://doi.org/10.1016/j.seppur.2022.121424>
- Li, W., Xiao, R., Lin, H., Yang, K., Li, W., He, K., Yang, L.-H., Pu, M., Li, M., Lv, S., 2022. Electro-activation of peroxymonosulfate by a graphene oxide/iron oxide nanoparticle-doped Ti<sub>4</sub>O<sub>7</sub> ceramic membrane: mechanism of singlet oxygen generation in the removal of 1,4-dioxane. *J. Hazard. Mater.* 424, 127342. <https://doi.org/10.1016/j.jhazmat.2021.127342>
- Li, X., Pletcher, D., Walsh, F.C., 2011. Electrodeposited lead dioxide coatings. *Chem. Soc. Rev.* 40, 3879. <https://doi.org/10.1039/c0cs00213e>
- Liang, S., Lin, H., Yan, X., Huang, Q., 2018. Electro-oxidation of tetracycline by a Magnéli phase Ti<sub>4</sub>O<sub>7</sub> porous anode: Kinetics, products, and toxicity. *Chem. Eng. J.* 332, 628–636. <https://doi.org/10.1016/j.cej.2017.09.109>
- Lin, H., Niu, J., Liang, S., Wang, C., Wang, Y., Jin, F., Luo, Q., Huang, Q., 2018. Development of macroporous Magnéli phase Ti<sub>4</sub>O<sub>7</sub> ceramic materials: As an efficient anode for mineralization of poly- and perfluoroalkyl substances. *Chem. Eng. J.* 354, 1058–1067. <https://doi.org/10.1016/j.cej.2018.07.210>
- Liu, H.J., Luo, M.Q., Yang, L.X., Zeng, C.L., Fu, C., 2022. A high strength and conductivity bulk Magnéli phase Ti<sub>4</sub>O<sub>7</sub> with superior electrochemical performance. *Ceram. Int.* 48, 25538–25546. <https://doi.org/10.1016/j.ceramint.2022.05.233>
- Marselli, B., Garcia-Gomez, J., Michaud, P.-A., Rodrigo, M.A., Comninellis, Ch., 2003. Electrogeneration of Hydroxyl Radicals on Boron-Doped Diamond Electrodes. *J. Electrochem. Soc.* 150, D79. <https://doi.org/10.1149/1.1553790>
- Martínez-Huitle, C.A., Ferro, S., 2006. Electrochemical oxidation of organic pollutants for the wastewater treatment: direct and indirect processes. *Chem. Soc. Rev.* 35, 1324–1340.

<https://doi.org/10.1039/B517632H>

- Nayak, S., Chaplin, B.P., 2018. Fabrication and characterization of porous, conductive, monolithic Ti4O7 electrodes. *Electrochim. Acta* 263, 299–310. <https://doi.org/10.1016/j.electacta.2018.01.034>
- Nidheesh, P.V., Zhou, M., Oturan, M.A., 2018. An overview on the removal of synthetic dyes from water by electrochemical advanced oxidation processes. *Chemosphere* 197, 210–227. <https://doi.org/10.1016/j.chemosphere.2017.12.195>
- Oturan, M.A., 2021. Outstanding performances of the BDD film anode in electro-Fenton process: Applications and comparative performance. *Curr. Opin. Solid State Mater. Sci.* 25, 100925. <https://doi.org/10.1016/j.cossms.2021.100925>
- Oturan, N., Bo, J., Trellu, C., Oturan, M.A., 2021. Comparative Performance of Ten Electrodes in Electro-Fenton Process for Removal of Organic Pollutants from Water. *Chem. Electro. Chem.* 8, 3294–3303. <https://doi.org/10.1002/celec.202100588>
- Padilha, A.C.M., Osorio-Guillén, J.M., Rocha, A.R., Dalpian, G.M., 2014. Ti<sub>n</sub>O<sub>2n-1</sub> Magnéli phases studied using density functional theory. *Phys. Rev. B* 90, 035213. <https://doi.org/10.1103/PhysRevB.90.035213>
- Panizza, M., Cerisola, G., 2009. Direct And Mediated Anodic Oxidation of Organic Pollutants. *Chem. Rev.* 109, 6541–6569. <https://doi.org/10.1021/cr9001319>
- Radjenovic, J., Sedlak, D.L., 2015. Challenges and Opportunities for Electrochemical Processes as Next-Generation Technologies for the Treatment of Contaminated Water. *Environ. Sci. Technol.* 49, 11292–11302. <https://doi.org/10.1021/acs.est.5b02414>
- Reis, R.M., Baio, J.A.F., Migliorini, F.L., Rocha, R. da S., Baldan, M.R., Ferreira, N.G., Lanza, M.R. de V., 2013. Degradation of dipyrone in an electrochemical flow-by reactor using anodes of boron-doped diamond (BDD) supported on titanium. *J. Electroanal. Chem.* 690, 89–95. <https://doi.org/10.1016/j.jelechem.2012.12.003>
- Rueffer, M., Bejan, D., Bunce, N.J., 2011. Graphite: An active or an inactive anode? *Electrochim. Acta* 56, 2246–2253. <https://doi.org/10.1016/j.electacta.2010.11.071>
- Sirés, I., Brillas, E., Oturan, M.A., Rodrigo, M.A., Panizza, M., 2014. Electrochemical advanced oxidation processes: today and tomorrow. A review. *Environ. Sci. Pollut. Res.* 21, 8336–8367. <https://doi.org/10.1007/s11356-014-2783-1>

- Šljukić, B., Baron, R., Compton, R.G., 2007. Electrochemical Determination of Oxalate at Pyrolytic Graphite Electrodes. *Electroanalysis* 19, 918–922. <https://doi.org/10.1002/elan.200703852>
- Sopaj, F., Oturan, N., Pinson, J., Podvorica, F., Oturan, M.A., 2016. Effect of the anode materials on the efficiency of the electro-Fenton process for the mineralization of the antibiotic sulfamethazine. *Appl. Catal. B Environ.* 199, 331–341. <https://doi.org/10.1016/j.apcatb.2016.06.035>
- Trellu, C., Coetsier, C., Rouch, J.-C., Esmilaire, R., Rivallin, M., Cretin, M., Causserand, C., 2018. Mineralization of organic pollutants by anodic oxidation using reactive electrochemical membrane synthesized from carbothermal reduction of TiO<sub>2</sub>. *Water Res.* 131, 310–319. <https://doi.org/10.1016/j.watres.2017.12.070>
- Urtiaga, A., Fernandez-Castro, P., Gómez, P., Ortiz, I., 2014. Remediation of wastewaters containing tetrahydrofuran. Study of the electrochemical mineralization on BDD electrodes. *Chem. Eng. J.* 239, 341–350. <https://doi.org/10.1016/j.cej.2013.11.028>
- Wachter, N., Aquino, J.M., Denadai, M., Barreiro, J.C., Silva, A.J., Cass, Q.B., Bocchi, N., Rocha-Filho, R.C., 2019. Electrochemical degradation of the antibiotic ciprofloxacin in a flow reactor using distinct BDD anodes: Reaction kinetics, identification and toxicity of the degradation products. *Chemosphere* 234, 461–470. <https://doi.org/10.1016/j.chemosphere.2019.06.053>
- Wang, L., Nickelsen, M., Chiang, S.-Y. (Dora), Woodard, S., Wang, Y., Liang, S., Mora, R., Fontanez, R., Anderson, H., Huang, Q., 2021. Treatment of perfluoroalkyl acids in concentrated wastes from regeneration of spent ion exchange resin by electrochemical oxidation using Magnéli phase Ti<sub>4</sub>O<sub>7</sub> anode. *Chem. Eng. J. Adv.* 5, 100078. <https://doi.org/10.1016/j.cej.2020.100078>
- You, S., Liu, B., Gao, Y., Wang, Y., Tang, C.Y., Huang, Y., Ren, N., 2016. Monolithic Porous Magnéli-phase Ti<sub>4</sub>O<sub>7</sub> for Electro-oxidation Treatment of Industrial Wastewater. *Electrochim. Acta* 214, 326–335. <https://doi.org/10.1016/j.electacta.2016.08.037>
- Zhao, Z., Zhang, J., Yao, J., You, S., 2022. Electrochemical removal of 4-chlorophenol in water using a porous Magnéli-phase (Ti<sub>4</sub>O<sub>7</sub>) electrode. *Environ. Res.* 210, 113004. <https://doi.org/10.1016/j.envres.2022.113004>



## **Chapter VI**

### **Chloride Oxidation on $\text{TiO}_x$ Electrodes: Influence of Porous Structure and Reactor Configuration**



## Abstract

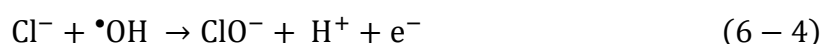
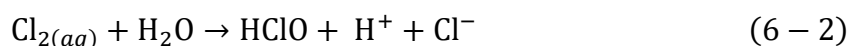
New porous  $\text{TiO}_x$  electrodes were investigated for promoting active chlorine mediated anodic oxidation. The influence of porous structure and configuration was studied. Formation and evolution of toxic by-products were followed to learn the feasibility of future application. These electrodes were also tested for treatment of a textile effluent. Active chlorine generation was favored by  $\text{TiO}_x$  electrodes with larger pore size in stirred-tank reactor and hydroxyl radicals played a dominated role in active chlorine formation on these electrodes. In flow-through configuration, formation of active chlorine increased with flow rate and less by-products were observed compared to stirred-tank reactor. Moreover, faster discoloration and mineralization rates of textile effluent were also obtained in flow-through configuration. However, formation of AOX were noted in all cases. To conclude, these new porous  $\text{TiO}_x$  electrodes with suitable porous structure and applied configuration can be promising for Cl<sup>-</sup>-containing effluent treatment only if the accumulation of toxic by-products can be solved by further improvement of material or other processes.

**Keywords:** Anodic oxidation,  $\text{TiO}_x$  electrode, Active chlorine, Porous structure, Flow-through, By-products

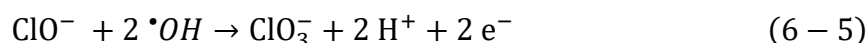
## 1. Introduction

Development of the anodic oxidation (AO) process requires further taking into consideration the inorganic matrix of real wastewaters. Particularly, the presence of chloride ions is of great importance. Electrode materials such as dimensionally stable anodes (DSA), Pt, boron-doped diamond (BDD), graphite or PbO<sub>2</sub> are able to promote formation of active chlorine (Cl<sub>2</sub>, HOCl, ClO<sup>-</sup>) species from oxidation of chloride ions present in the medium. Active chlorine might be beneficial for (i) reaction with organic compounds, (ii) reaction with ammonium and (iii) disinfection (Brito et al., 2015; Bruguera-Casamada et al., 2017; García-Espinoza et al., 2018; Perea et al., 2019; Rahmani et al., 2019; Ferreira de Melo et al., 2020; Mandal et al., 2020). However, formation of organo-chlorinated compounds and further oxidation of active chlorine to toxic by-products (chlorate and perchlorate) represents a major drawback. The nature of the electrode material as well as reactor configuration must participate to address these issues (Bergmann et al., 2009; Jung et al., 2010).

Several steps are involved in chloride oxidation during the AO process. First, chloride ions can react at anode surface through direct electron transfer (DET) for formation of Cl<sub>2,aq</sub> (Eq. 6-1) (Martínez-Huitle et al., 2015). Hydrolysis of Cl<sub>2,aq</sub> (Eq. 2) then leads to the formation of other forms of free active chlorine according to the acid-base equilibrium between HOCl and ClO<sup>-</sup> (Eq. 3) (Martínez-Huitle et al., 2015). Reaction with hydroxyl radicals (<sup>•</sup>OH) might also promote the formation of active chlorine (Eq. 4) (Brito et al., 2015). Active chlorine is a well-known remanent oxidant with long lifetime that can be accumulated in bulk solution.



An undesired reaction is then related to the oxidation of active chlorine to chlorate through <sup>•</sup>OH-mediated oxidation (Eq. 6-5) (Brito et al., 2015; Martínez-Huitle et al., 2015).



Direct oxidation of ClO<sub>3</sub><sup>-</sup> by <sup>•</sup>OH was reported to be below the quantification limit of the spin trap method (i.e., < 1 × 10<sup>6</sup> M<sup>-1</sup> s<sup>-1</sup>) (Buxton et al., 1988). However, further oxidation of chlorate might also occur. It is the rate-determining step for formation of perchlorate. The first step involves the formation of chlorate radicals by DET at electrode surface (Eq. 6-6). Then, subsequent reaction at electrode vicinity with <sup>•</sup>OH has been determined as the main pathway for formation of ClO<sub>4</sub><sup>-</sup> (Eq. 6-7) (Azizi et al., 2011).



Formation rate of ClO<sub>4</sub><sup>-</sup> from ClO<sub>3</sub><sup>-</sup> was reported to be significantly slower than the mass transfer rate. Therefore, ClO<sub>3</sub><sup>-</sup> might accumulate at electrode surface where they are produced from Eq. 6-5 (Chaplin, 2014). Both chlorate and perchlorate are persistent compounds that are also able to accumulate in the solution, thus causing a major drawback for the quality of the treated water (Chaplin, 2014).

The formation and accumulation of <sup>•</sup>OH at vicinity of electrode is an important factor which influences the formation of ClO<sub>3</sub><sup>-</sup> and ClO<sub>4</sub><sup>-</sup> (Brito et al., 2015). The formation rate of ClO<sub>4</sub><sup>-</sup> is also strongly influenced by the nature and amount of surface groups of electrode. Previous investigations have highlighted the key role of functional surface sites that could stabilize chlorate radicals (i.e., increase their lifetime) and promote reaction with <sup>•</sup>OH for the formation of ClO<sub>4</sub><sup>-</sup> (Chaplin, 2014; Hubler et al., 2014). For example, very different formation rate of ClO<sub>4</sub><sup>-</sup> was observed at BDD anodes with different sp<sup>3</sup>/sp<sup>2</sup> ratios. Adsorption of chlorine species on sp<sup>2</sup> carbon facilitated the formation of chlorate and perchlorate (Brito et al., 2015). Interestingly, density functional theory (DFT) modeling also indicated that adsorption of chlorate radicals at ≡C<sup>•</sup> sites and subsequent reaction with <sup>•</sup>OH might form ClO<sub>3</sub><sup>-</sup> and an oxidized surface sites ≡C-O<sup>•</sup>. Such catalytic pathway might explain the slower formation of ClO<sub>4</sub><sup>-</sup> compared to other oxychlorine species (Azizi et al., 2011).

It is a crucial challenge for electrochemical engineering to discover solutions for avoiding the formation of these compounds. For example, Isidro et al. (2020) emphasized that short contact time between the treated water and BDD surface might be a solution for lowering the

formation of ClO<sub>3</sub><sup>-</sup> and ClO<sub>4</sub><sup>-</sup> since <sup>•</sup>OH are only accumulated within a thin layer (<1 μm) close to the anode surface (Isidro et al., 2020). Donaghue and Chaplin (2013) also showed that operating AO under kinetic limitation for organic compounds removal might inhibit perchlorate formation at BDD anode owing to <sup>•</sup>OH scavenging by the reaction with organic compounds (Donaghue and Chaplin, 2013).

The main novelty of this study is to investigate how the porous structure of different TiO<sub>x</sub> materials as well as reactor configurations (stirred-tank vs flow-through) might influence the evolution of active chlorine and other oxychlorine species. In fact, these two parameters might strongly influence local hydrodynamic conditions at electrode surface as well as contact time between <sup>•</sup>OH and active chlorine / oxychlorine species.

Moreover, the influence of the presence of organic compounds was also assessed during the treatment of an effluent from textile industry containing high concentration of chloride as well as dyes as organic compounds. Such application requires taking into consideration the issue related to the detection of halogenated-organic compounds (HOCs), which come from the reaction of organic compounds with active chlorine species, chlorine radicals and oxychlorine radicals (Bagastyo et al., 2012; Chaplin, 2014; Radjenovic and Sedlak, 2015). However, it is currently very difficult to highlight structure-function relationships related to this issue.

## 2. Materials and methods

### 2.1 Chemicals

Potassium iodate (>99.5%), potassium iodide (>99%), sulfuric acid (95-97%), sodium sulfite (98%) and N,N-Diethyl-p-phenylenediamine sulfate salt (≥98%) were purchased from Sigma-Aldrich. Disodium phosphate (99.9%) and sodium carbonate (≥99.8%) were purchased from VWR Prolabo. Monopotassium phosphate and tert-Butanol (99.5%) were obtained from Acros Organics. Ethylenediaminetetraacetic acid (99%) was obtained from Alfa Aesar. Sodium bicarbonate (≥99.7%) and sodium hydroxide (≥98%) were purchased from Fluka.

Sodium chloride ( $\geq 99.5\%$ ) was purchased from Fisher Scientific. All chemicals were used as received without any purification. Ultrapure water ( $R > 18.2 \text{ M}\Omega$ ) used for active chlorine analysis and all eluents for HPLC and ion chromatography was obtained from a Smart2Pure device (Thermo Scientific, France).

## 2.2 Electrode materials

Several different TiO<sub>x</sub> materials were used in this Chapter, including (i) Ti/TiO<sub>x</sub> plate presented in Chapter III, (ii) Ti/TiO<sub>x</sub> foam described as the most relevant Ti/TiO<sub>x</sub> foam material in Chapter III (foam 1), (iii) 100% TiO<sub>x</sub> foam tested in Chapter V and (iv) 100% TiO<sub>x</sub> REM tested in Chapter V. These electrodes have been characterized previously in terms of porous structure, chemical composition, electrochemical characteristics and reactivity for oxidation of organics in each respective chapter. [Table 6-1](#) provides a brief overview of the most important characteristics of each material.

The reactivity of these electrodes for chlorine evolution was compared with the results obtained with a BDD electrode (Condias, Germany) and a DSA (IrO<sub>2</sub>/RuO<sub>2</sub>) acquired from Baoji Xinyu GuangJiDian Limited Liability Company (China). DSA is a kind of well-known gold-standard electrode for active chlorine generation. Meanwhile, BDD, as non-active electrode, has also been demonstrated as an effective electrode for active chlorine generation. However, its high efficiency is accompanied by noticeable formation of chlorate and perchlorate, which represents one of the main drawbacks for application of this gold-standard electrode for  $\cdot\text{OH}$  generation.

Table 6-1 Summary of characteristics of TiO<sub>x</sub> electrodes

Electrodes	Ti/TiO <sub>x</sub> plate	Ti/TiO <sub>x</sub> foam	100% TiO <sub>x</sub> foam	100% TiO <sub>x</sub> REM
<b>Synthesis method</b>	plasma spraying	plasma spraying	foaming	carbothermal reduction of TiO <sub>2</sub>
<b>Major phase</b>	Ti <sub>4</sub> O <sub>7</sub>	Ti <sub>4</sub> O <sub>7</sub>	Ti <sub>4</sub> O <sub>7</sub> , Ti <sub>5</sub> O <sub>9</sub>	Ti <sub>4</sub> O <sub>7</sub> , Ti <sub>5</sub> O <sub>9</sub>
<b>Porosity</b>	---	35%	69%	29%
<b>Median pore size (volume) (μm)</b>	---	88.0	127.2	2.2
<b>OEP (V vs Ag/AgCl/3 M KCl)</b>	2.78	2.82	2.85	2.29
<b>Roughness factor</b>	93	69	46	416

### 2.3 Treatment of synthetic solutions in stirred-tank and flow-through reactors

Experiments were first conducted in both stirred-tank and flow-through reactors with a synthetic solution containing 12 mM NaCl (same concentration as in the real effluent). Formation of active chlorine, ClO<sub>3</sub><sup>-</sup> and ClO<sub>4</sub><sup>-</sup> at different electrode materials was compared. Another set of experiments was performed with addition of 0.12 M of tert-Butyl alcohol (TBA) as quencher to assess the role of ·OH on chlorine evolution (Buxton et al., 1988; Neta et al., 1988; Anipsitakis and Dionysiou, 2004; Li et al., 2022).

A cylindrical undivided stirred-tank reactor was operated in batch mode at a constant current density of 5 mA cm<sup>-2</sup>. All of the different TiO<sub>x</sub> electrodes were used successively as anode. Carbon felt (CF) or stainless steel (SS) was used as cathode. Anode and cathode were placed face to face in the solution with an inter-electrode distance of 2.5 cm. The ratio between the immersed geometric surface area of electrodes and the volume of solution was maintained constant at  $S_{\text{electrode}}/V_{\text{solution}} = 7.9 \text{ m}^{-1}$ . The solution was stirred at a constant rate of 750 rpm

using a magnetic bar. Samples were taken from the reactor at different time intervals for analysis.

Flow-through experiments were performed in a glass reactor with effective surface area of 12.6 cm<sup>2</sup>. Porous 100% TiO<sub>x</sub> electrode was placed at the bottom of the reactor as anode and a BDD grid was put at the top of the reactor as cathode. The solution was pumped from the feed water reservoir through the reactor in dead-end filtration mode. Flow-through experiments were operated at constant current density of 5 mA cm<sup>-2</sup> in either batch (100% recirculation of the solution from the top of the reactor to the feed water reservoir) or continuous (0% recirculation) mode. In continuous mode, chlorine evolution was studied according to the flow rate ( $J$ , in L h<sup>-1</sup> m<sup>-2</sup>). In batch mode, experiments were performed with a ratio  $S_{\text{electrode}}/V_{\text{solution}} = 3.6 \text{ m}^{-1}$ .

#### **2.4 Treatment of a real effluent in stirred-tank and flow-through reactors**

The effluent used in this study was obtained from a textile industry in Ivory Coast. The effluent was first filtered using filter paper and diluted to reach an initial total organic carbon (TOC) of 9.6 mg L<sup>-1</sup> (same as studies with probe molecules in previous chapters). Characteristics of the effluent used for the experiments are provided in [Table 6-2](#). The effluent was then treated without adding electrolyte. The effluent was treated in batch reactor and flow-through reactor under batch mode (100% recirculation). For both configurations, the ratio  $S_{\text{electrode}}/V_{\text{solution}}$  (3.6 m<sup>-1</sup>) and the current density (5 mA cm<sup>-2</sup>) were maintained constant. A BDD grid and a BDD plate were used as cathode in flow-through and stirred-tank configurations, respectively.

Table 6-2 Main characteristics of the effluent used for experiments

Parameters	Value
pH	13.1
Cl <sup>-</sup> concentration (mM)	12
TOC (mg L <sup>-1</sup> )	9.1
Color (Abs <sub>668</sub> )	Blue (0.0766)

## 2.5 Analytical methods

Active chlorine was analyzed by colorimetric method using DPD (N,N,-diethyl-p-phenylenediamine). Measurements were performed using a UV spectrophotometer (UV-1800, SHIMADZU) at a wavelength of 510 nm.

Formation of chlorate and perchlorate was monitored using a Dionex ICS-1000 ion chromatography equipped with a 25 µL injection loop, a DS6 conductivity detector, an ASRS 300 suppressor and an AS4A-SC anionic column (4 mm×250 mm). The eluent was a mixture of 4.49 mM Na<sub>2</sub>CO<sub>3</sub> and 1.42 mM NaHCO<sub>3</sub>.

Concentration of chloride was determined using the same ion chromatography. However, co-elution of active chlorine and chloride might interfere the quantification of chloride. Therefore, 352 mM Na<sub>2</sub>SO<sub>3</sub> was used as a trap for active chlorine to convert it to chloride. Then the chloride concentration measured from ion chromatography was the sum of chloride and active chlorine. The real chloride concentration can be obtained by subtracting active chlorine concentration determined by DPD colorimetric method.

Mineralization of organic compounds in the real effluent was analyzed using a SHIMADZU TOC analyzer (TOC-L). Discoloration was followed using the same UV spectrophotometer (UV-1800, SHIMADZU) at  $\lambda = 668$  nm (corresponding to the maximum of absorbance of the initial effluent).



Concentrations of adsorbable organic halides (AOX) (specifically AOCl, AOBr and AOI) were followed. Briefly, 100 mL of diluted samples were acidified by NaNO<sub>3</sub>-HNO<sub>3</sub> solution and then passed through an activated carbon cartridge (TXA-04 AOX adsorption unit). NaNO<sub>3</sub>-HNO<sub>3</sub> washing solution was used to wash away inorganic halides. Combustion of the cartridge and gas adsorption were then performed using an AQF-2100H automatic quick furnace at 1000 °C and a GA-210 gas adsorption unit (Mitsubishi Chemical Analytech), respectively. At last, AOX was analyzed by a thermo DiONEX Integrion HPIC system.

## 2.6 Calculation of accumulation rate of different chlorine species

The evolution of different chlorinated species was followed according to treatment time (in batch configuration) or flow rate (in continuous flow-through configuration). The accumulation rate of each species ( $r_i$ , in mmol h<sup>-1</sup> m<sup>-2</sup>) was calculated in stirred-tank reactor or flow-through configuration working under batch mode (with 100% recirculation) as Eq. 6-8:

$$r_i = \frac{(C_{i,t+\Delta t} - C_{i,t}) * V}{S_{electrode} * \Delta t} \quad (6 - 8)$$

where  $C_{i,t+\Delta t}$  and  $C_{i,t}$  (mmol L<sup>-1</sup>) are the concentrations of the compound  $i$  after  $t + \Delta t$  and  $t$  (h) of treatment, respectively,  $V$  is the volume of solution and  $S_{electrode}$  is the effective geometric surface area of electrode.

The accumulation rate of each species in flow-through configuration (working under continuous mode with 0% recirculation) was calculated as Eq. 6-9:

$$r_i = (C_{i,out} - C_{i,f}) * J \quad (6 - 9)$$

where  $C_{i,out}$  and  $C_{i,f}$  (mmol L<sup>-1</sup>) are the concentrations of the compound  $i$  at the outlet of the flow-through reactor and in the feed water, respectively,  $J$  is the applied flux.

### 3. Results and discussions

#### 3.1 Chloride oxidation in synthetic solution

##### 3.1.1 Comparison of anode materials in stirred-tank reactor

In this study, active chlorine, chlorate and perchlorate were identified as main oxidation products of chloride. Fig. 6-1 shows an example of mass balance calculation with 100% TiO<sub>x</sub> foam as anode and CF as cathode. The mass balance ranged from 0.96 – 0.98, suggesting there might be slight loss of gaseous Cl<sub>2</sub>, Cl<sub>2</sub>O or ClO<sub>2</sub> due to the acidic local pH near anode surface. However, these concentrations were not significant compared to the other species analyzed.

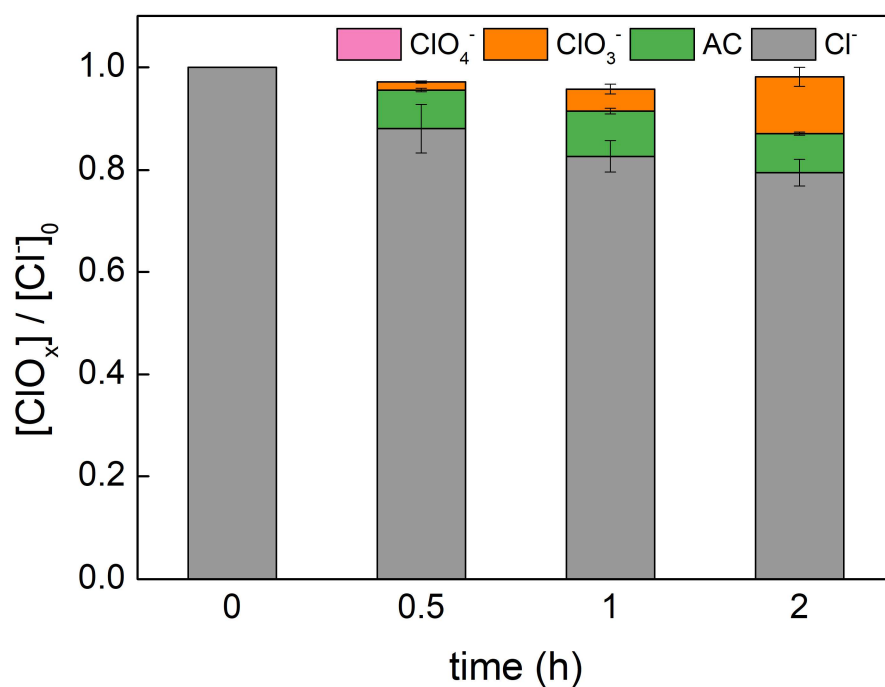
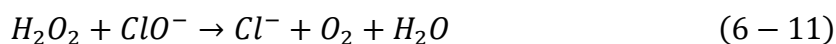
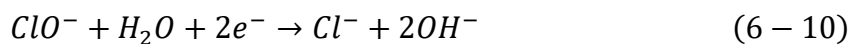


Fig. 6-1 - Mass balance of chloride and different oxidation species (anode: 100% TiO<sub>x</sub> foam, cathode: CF, initial  $[NaCl]_0 = 12$  mM, pH<sub>0h</sub>: 5.7-5.9, pH<sub>2h</sub>: 7.1-7.8,  $S_{electrode}/V_{solution} = 7.9$  m<sup>-1</sup>, current density = 5 mA cm<sup>-2</sup>)

Fig. 6-2 presents the evolution of active chlorine using different anode materials. For all electrodes, a rapid increase of active chlorine concentration was observed during the first 30

min of treatment. Then, a plateau was reached after 1 h of treatment. This plateau might be explained by the equilibrium between the formation rate at anode and the destruction rate at cathode. Given the alkaline local pH and possible H<sub>2</sub>O<sub>2</sub> production at the cathode, Eqs. 6 - 10 and 6 - 11 might be the main pathways for active chlorine destruction.



The fastest accumulation of active chlorine was obtained by two foams with a rate of 299 and 210 mM of active chlorine (AC) h<sup>-1</sup> m<sup>-2</sup> (during first 30 min of treatment) for 100% TiO<sub>x</sub> foam and Ti/TiO<sub>x</sub> foam, respectively. Meanwhile, no significant difference was obtained using Ti/TiO<sub>x</sub> plate, 100% TiO<sub>x</sub> REM and BDD (active chlorine formation rates were in the range 88 – 122 mM (AC) h<sup>-1</sup> m<sup>-2</sup> during first 30 min of treatment). As explained in Chapter V, 100% TiO<sub>x</sub> REM might behave as dense electrode since its fine roughness (small pore size) might be averaged within the thick diffusion layer at electrode surface. Small differences in terms of chemical composition were reported (particularly, TiO<sub>x</sub> coating of Ti/TiO<sub>x</sub> electrodes presents more oxidized Magnéli phases than 100% TiO<sub>x</sub> electrodes), however, it is interesting to highlight that the porous structures of foams appeared to be the key parameter for promoting active chlorine generation. It is particularly emphasized when comparing Ti/TiO<sub>x</sub> plate and Ti/TiO<sub>x</sub> foam which present similar coating.

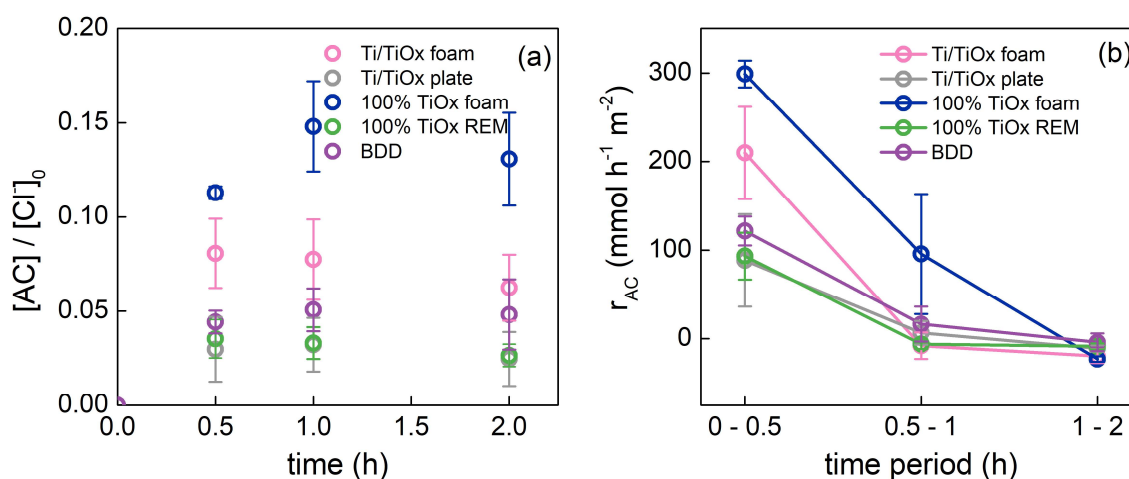


Fig. 6-2 - Generation of active chlorine (a) and accumulation rate evolution of active chlorine (b) by different anodes in stirred-tank reactor (initial [NaCl]<sub>0</sub> = 12 mM, pH<sub>0h</sub>: 5.6-6.5, pH<sub>2h</sub>:

6.0-7.8, cathode: CF,  $S_{\text{electrode}}/V_{\text{solution}} = 7.9 \text{ m}^{-1}$ , current density =  $5 \text{ mA cm}^{-2}$ ). Results of active chlorine generation are presented as a molar ratio between active chlorine (AC) and initial concentration of chloride ions

Then, for further understanding the behavior of electrodes, it was required to follow the evolution of other oxychlorinated species, including chlorate and perchlorate (Fig. 6-3). For perchlorate, the trend was the opposite of active chlorine. The formation of perchlorate was below the detection limit ( $10 \mu\text{M}$ ) for both foams, while higher concentrations were obtained for other electrodes. The increase of perchlorate concentration with BDD, Ti/TiO<sub>x</sub> plate and 100% TiO<sub>x</sub> REM followed a linear rise with time since (i) perchlorate could not be reduced at cathode and (ii) perchlorate formation was not limited by mass transport or the decrease of Cl<sup>-</sup> concentration in the solution (because of high Cl<sup>-</sup> concentration). It is also the reason why the accumulation rate of ClO<sub>4</sub><sup>-</sup> was constant or even increasing during the treatment. For example, the average perchlorate accumulation rate at the BDD anode was  $13.0 \pm 1.1 \text{ mmol (ClO}_4^-) \text{ h}^{-1} \text{ m}^{-2}$ . By comparison, perchlorate formation at foams was below  $0.64 \text{ mmol (ClO}_4^-) \text{ h}^{-1} \text{ m}^{-2}$  during 2 h electrolysis, taking into consideration the detection limit ( $10 \mu\text{M}$ ). The highest formation rate of perchlorate was obtained for Ti/TiO<sub>x</sub> plate ( $50.9 \pm 3.3 \text{ mmol (ClO}_4^-) \text{ h}^{-1} \text{ m}^{-2}$ ). It could not be ascribed to more formation of <sup>•</sup>OH (which would promote perchlorate formation through Eq. 6-7) since BDD is a well-known gold standard for formation of <sup>•</sup>OH. It might be more likely ascribed to the presence of surface functional groups stabilizing chlorate radicals and promoting their reaction with <sup>•</sup>OH (Chaplin, 2014).

As regards to the formation of chlorates, a significant increase of the concentration was also obtained. Lower formation rate of ClO<sub>3</sub><sup>-</sup> was obtained using Ti/TiO<sub>x</sub> plate. It might be due to the favorable conditions for further oxidation to ClO<sub>4</sub><sup>-</sup>, as explained previously. Then, once more, the two foams behaved similarly and obtained lower accumulation rate of ClO<sub>3</sub><sup>-</sup> ( $71.7 \pm 22.4$  and  $77.4 \pm 16.1 \text{ mmol (ClO}_3^-) \text{ h}^{-1} \text{ m}^{-2}$  for 100% TiO<sub>x</sub> foam and Ti/TiO<sub>x</sub> foam, respectively) compared to BDD or 100% TiO<sub>x</sub> REM. For all electrodes, the accumulation rate of ClO<sub>3</sub><sup>-</sup> increased with time. These results indicated that the formation of ClO<sub>3</sub><sup>-</sup> was promoted by the accumulation of active chlorine in the solution.

Fig. 6-4 shows the current efficiency ascribed to the evolution of active chlorine, chlorate and perchlorate for the different anodes during electrolysis. The two foams presented similar global current efficiency for chloride oxidation (taking into consideration all species), while Ti/TiO<sub>x</sub> plate, 100% TiO<sub>x</sub> REM and BDD presented higher global current efficiency. Since experiments were performed with high concentration of chloride, chloride oxidation was not limited by mass transport of chloride ions from bulk solution to electrode surface. Different current efficiencies might indicate different competition with oxygen evolution reaction (OER). Ti/TiO<sub>x</sub> plate, 100% TiO<sub>x</sub> REM and BDD also showed higher current efficiency for chlorate/perchlorate evolution than the foams, suggesting more suitable local conditions for the reaction between active chlorine/chlorate radicals and  $\cdot\text{OH}$ .

These results indicated that the higher formation rate of active chlorine by foams might be significantly ascribed to the slower oxidation of active chlorine towards chlorate or perchlorate. Further oxidation of active chlorine highly depends on the contact time between active chlorine (for chlorate) or chlorate radical (for perchlorate) and the electrode surface where  $\cdot\text{OH}$  are accumulated within a thin layer. Higher local concentrations of active chlorine and chlorate radicals are expected in the vicinity of anode where it is generated. The higher the accumulation rate of these species at electrode surface, the higher the formation of chlorate and perchlorate might be expected. Therefore, more favorable results obtained with foams might be ascribed to their porous structure that modifies local hydrodynamic conditions at electrode surface and reduces contact time between these species and  $\cdot\text{OH}$ . Again, the key role of the porous structure is particularly emphasized when comparing the results obtained with Ti/TiO<sub>x</sub> plate and Ti/TiO<sub>x</sub> foam.

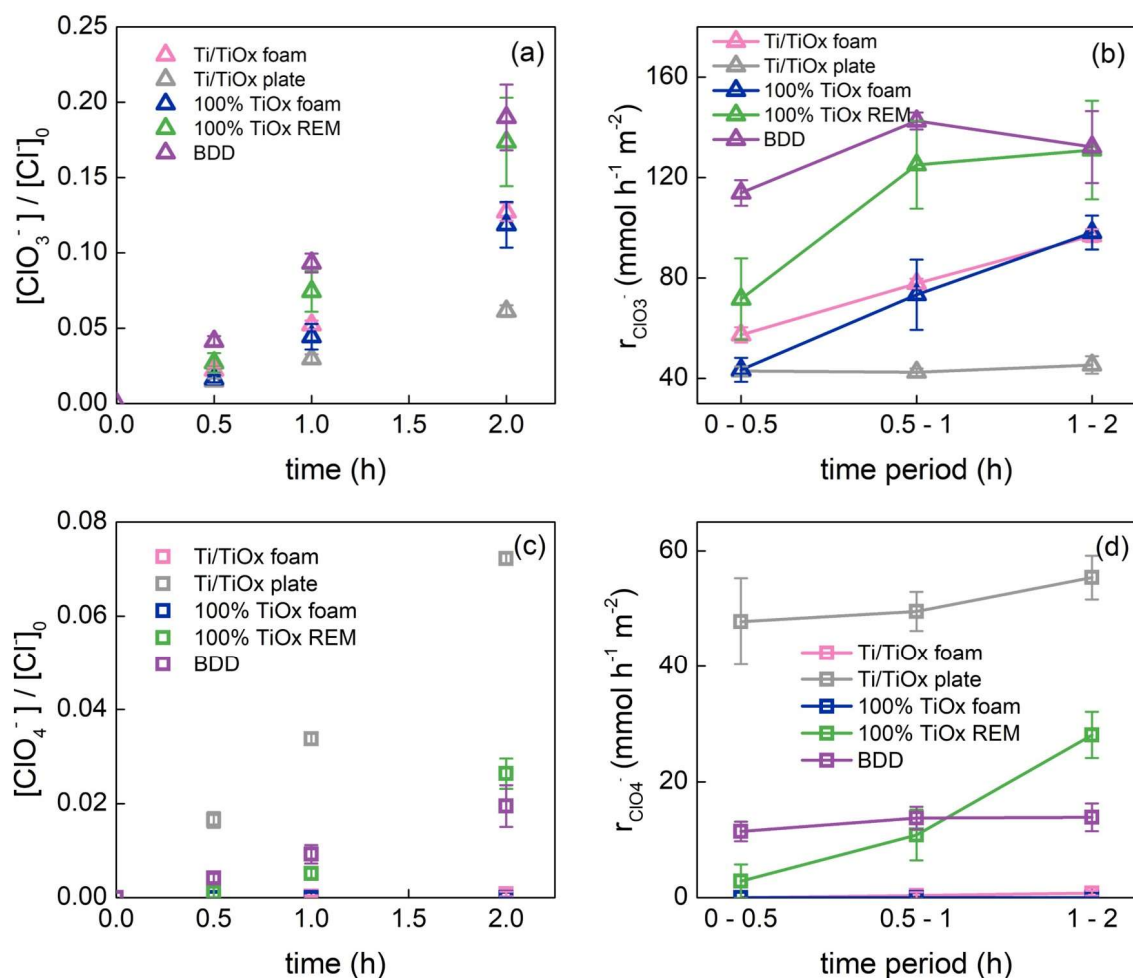


Fig. 6-3 - Evolution of chlorate (a), perchlorate (c) and accumulation rate of chlorate (b), perchlorate (d) during 2 h electrolysis by different anodes in stirred-tank reactor; ( $[\text{NaCl}]_0 = 12 \text{ mM}$ , cathode: CF,  $S_{\text{electrode}}/V_{\text{solution}} = 7.9 \text{ m}^{-1}$ , current density =  $5 \text{ mA cm}^{-2}$ ). Evolution of chlorate and perchlorate formation are presented as a molar ratio between the target oxychlorinated compound and the initial concentration of chloride ions

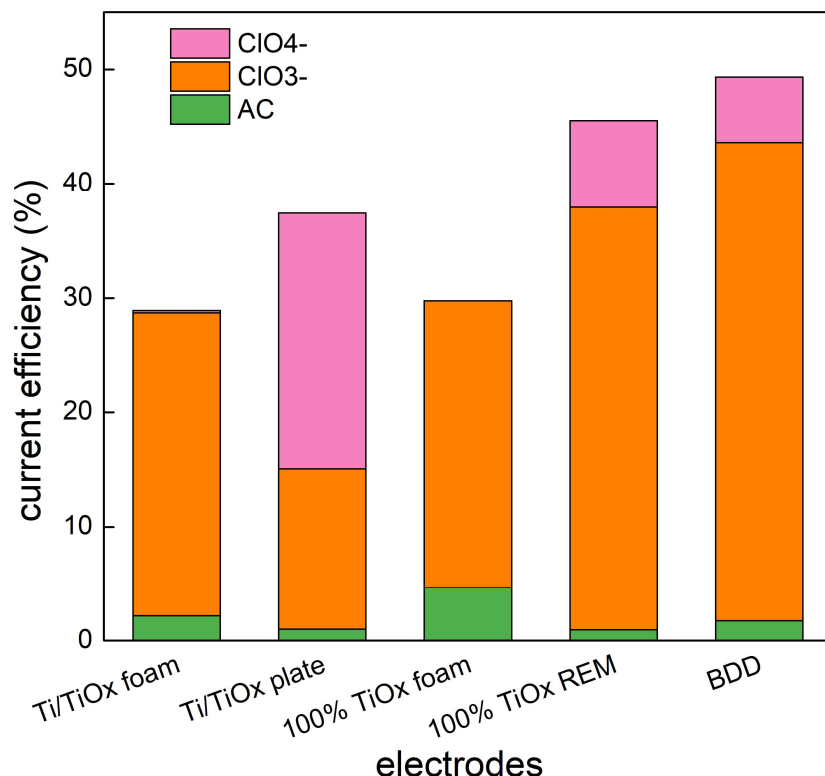


Fig. 6-4 - Calculation of current efficiency for chloride oxidation during 2 h electrolysis by different anodes in stirred-tank reactor ( $[\text{NaCl}]_0 = 12 \text{ mM}$ , cathode: CF,  $S_{\text{electrode}}/V_{\text{solution}} = 7.9 \text{ m}^{-1}$ , current density =  $5 \text{ mA cm}^{-2}$ )

### 3.1.2 Influence of cathode material in stirred-tank reactor

The influence of cathode material on active chlorine evolution was investigated using CF or SS material as cathode, while 100% TiO<sub>x</sub> and Ti/TiO<sub>x</sub> foams were used as anode (Fig. 6-5). Compared to CF, when SS was used as cathode, active chlorine accumulation rate during the first 30 min of treatment was multiplied by 3.5 and 2.6 times for 100% TiO<sub>x</sub> foam and Ti/TiO<sub>x</sub> foam, respectively. The concentration plateau of active chlorine accumulated in the solution also reached a much higher value. As explained previously, the accumulation of active chlorine comes from the difference between the formation rate at anode and the destruction rate at cathode and from reaction with H<sub>2</sub>O<sub>2</sub>. Therefore, the slower accumulation of active chlorine when using CF cathode might be related to (i) higher electro-active surface area of CF, a porous material, which may promote reduction of active chlorine at cathode (Eq. 10), (ii)

the well-known promotion of H<sub>2</sub>O<sub>2</sub> formation from O<sub>2</sub> reduction at such carbonaceous material (Petrucci et al., 2016).

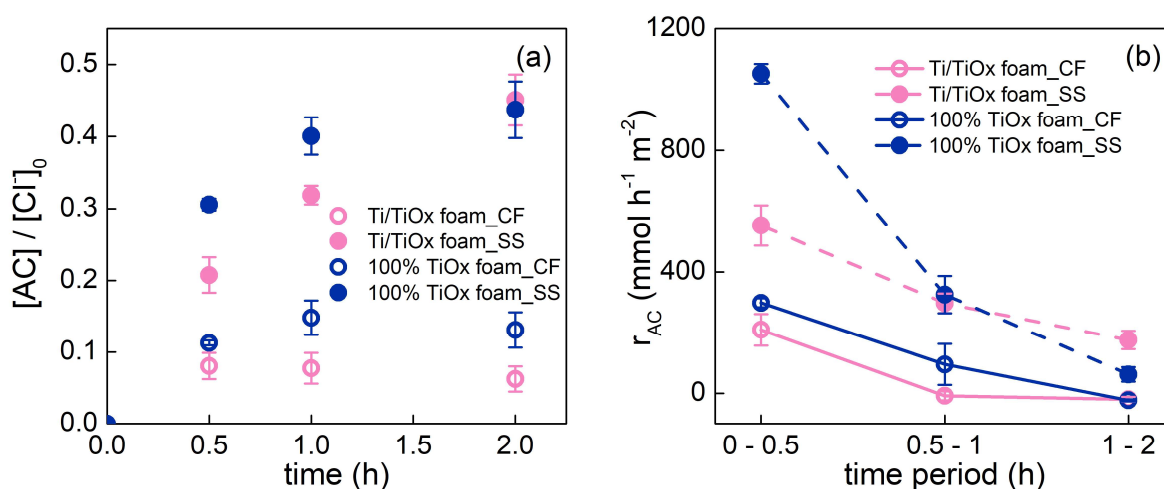


Fig. 6-5 - Generation of active chlorine (a) and its accumulation rate (b) by 100% TiO<sub>x</sub> and Ti/TiO<sub>x</sub> foams using different cathodes ( $[NaCl]_0 = 12$  mM,  $S_{electrode}/V_{solution} = 7.9$  m<sup>-1</sup>, current density = 5 mA cm<sup>-2</sup>). Active chlorine generation are presented as a molar ratio between active chlorine (AC) and the initial concentration of chloride ions

### 3.1.3 Reaction mechanism for active chlorine generation on TiO<sub>x</sub> electrodes

Formation of active chlorine might come from both DET and <sup>•</sup>OH-mediated oxidation (Eq. 6-1 and 6-4). For example, DSA electrodes are well-known for formation of active chlorine by DET, while they are active electrodes for OER with low accumulation of <sup>•</sup>OH at their surface. On the contrary, as it has been proved in previous chapters, TiO<sub>x</sub> materials perform well for <sup>•</sup>OH generation. The objective was therefore to assess whether chlorine evolution at TiO<sub>x</sub> electrodes may involve <sup>•</sup>OH. TBA was used as <sup>•</sup>OH quencher to study the role of <sup>•</sup>OH. Similar test was performed with a DSA electrode for comparison.

As can be seen on Fig. 6-6, comparable active chlorine accumulation rates were obtained during the first 30 min of treatment for DSA (707 mmol (AC) h<sup>-1</sup> m<sup>-2</sup>) and Ti/TiO<sub>x</sub> foam (554 mmol (AC) h<sup>-1</sup> m<sup>-2</sup>) without quencher, while 100% TiO<sub>x</sub> foam accumulated even higher concentration of active chlorine than DSA (1052 mmol (AC) h<sup>-1</sup> m<sup>-2</sup>). When TBA was added



as  $\cdot\text{OH}$  quencher, DSA produced similar amount of active chlorine, which was expected because it can produce a small amount of physisorbed  $\cdot\text{OH}$  available for reaction at electrode surface. On the contrary, accumulation of active chlorine by 100% TiO<sub>x</sub> and Ti/TiO<sub>x</sub> foams drastically decreased close to zero mmol h<sup>-1</sup> m<sup>-2</sup> with TBA as  $\cdot\text{OH}$  quencher. These results indicate that  $\cdot\text{OH}$  is decisive for active chlorine generation in the case of TiO<sub>x</sub> foams.

Overall, it is interesting to highlight that TiO<sub>x</sub> materials were as efficient as DSA for active chlorine accumulation, while  $\cdot\text{OH}$ -mediated chloride oxidation played a significant role. Therefore,  $\cdot\text{OH}$  scavenging and competition phenomena might play a key role in reaction rates.

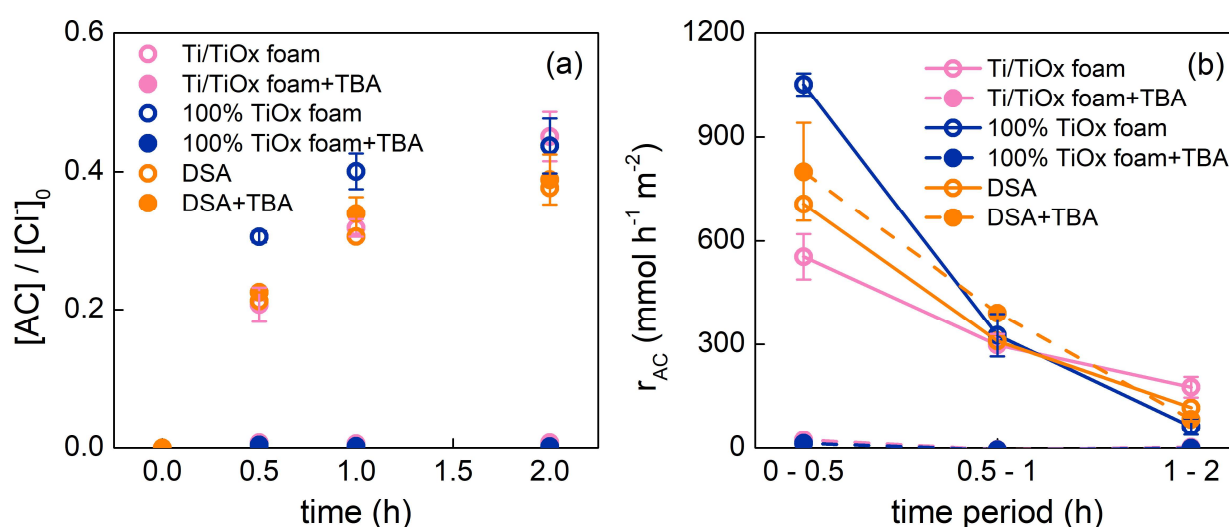


Fig. 6-6 - Generation of active chlorine (a) and its accumulation rate (b) by 100% TiO<sub>x</sub>, Ti/TiO<sub>x</sub> foams and DSA with/without using TBA as  $\cdot\text{OH}$  quencher (stirred-tank reactor, initial  $[\text{NaCl}]_0 = 12 \text{ mM}$ , cathode: SS,  $S_{\text{electrode}}/V_{\text{solution}} = 7.9 \text{ m}^{-1}$ , current density =  $5 \text{ mA cm}^{-2}$ ). Generation of active chlorine are presented as a molar ratio between active chlorine (AC) and the initial concentration of chloride ions

### 3.1.4 Chloride oxidation in flow-through reactor

Porous TiO<sub>x</sub> electrodes were then applied in flow-through configuration and chlorine evolution was monitored according to flow rate (with a single pass through the electrode). The

results are depicted in Fig. 6-7 in which the standard deviation at each flux was obtained from 3 samples at different sampling times in one experiment. Experiments were also performed with 100% recirculation of solution (under batch condition) for comparison with the stirred-tank reactor operated in batch condition.

First, it is interesting to notice that the accumulation rate of active chlorine increased with flow rate. For example, it was multiplied by 1.4 times when comparing data obtained at 380 and 1580 L h<sup>-1</sup> m<sup>-2</sup> with the 100% TiO<sub>x</sub> foam. As chlorine evolution was not mass transport limited (due to the high concentration of chloride), these results might not be explained by a convection-enhanced mass transport of chlorides from the bulk to the electrode surface. It is also the reason why 100% TiO<sub>x</sub> REM did not result in higher efficiency despite its more favorable porous structure for mass transport enhancement in flow-through configuration (small pore size) (Chapter V). As detailed previously, it is important to take into consideration that the accumulation of active chlorine is a result of both formation and destruction rates. Thus, lower accumulation rate of ClO<sub>3</sub><sup>-</sup> (Fig. 6-7) at high flow rate contributed to the higher accumulation rate of active chlorine. However, the decrease of chlorate accumulation rate did not completely compensate the increase of active chlorine accumulation rate. The global current efficiency for chloride oxidation (taking into account all Cl<sup>-</sup> containing species) increased from 53% at 380 L h<sup>-1</sup> m<sup>-2</sup> to 66% at 1580 L h<sup>-1</sup> m<sup>-2</sup>. Therefore, it is also necessary to take into consideration other competition phenomena. Previous studies have highlighted that increasing flow rate promotes oxygen evolution reaction by sweeping O<sub>2</sub> gas bubbles from the electrode surface (Guo et al., 2016). Such phenomenon should reinforce the competition between OER and chlorine evolution resulting in lower active chlorine accumulation rate. However, similar phenomena might also compensate this adverse effect. First, active chlorine formation might also be promoted by Cl<sub>2</sub> gas bubbles sweeping from the electrode surface (bubbles formed if the local Cl<sub>2</sub> concentration reaches the solubility limit) (Martínez-Huitle et al., 2015). At the cathode, hydrogen evolution reaction (HER) might also be promoted at high flow rate by sweeping H<sub>2</sub> gas bubbles. Thus, active chlorine reduction at cathode would decrease at high flow rate by enhanced competition with HER. As regards to the comparison with stirred-tank reactor, it is complicated to conclude on the beneficial or

adverse effect of the reactor configuration on active chlorine accumulation since experiments were not performed with the same cathode material.

As regards to the formation of chlorate, comparison with stirred tank reactor was possible since low reduction rate of chlorate at cathode is expected. The minimum accumulation rate of chlorate was 31.9, 19.9 and 60.7 mmol h<sup>-1</sup> m<sup>-2</sup> when using 100% TiO<sub>x</sub> foam, 100% TiO<sub>x</sub> REM and Ti/TiO<sub>x</sub> foam at around  $J = 1580 \text{ L h}^{-1} \text{ m}^{-2}$  (maximum flux). These accumulation rates were consistent with the values obtained at 0.5 h in flow-through condition with 100 % recirculation of the solution (Fig. 6-8). For a given electrical charge ( $q = 0.20 \text{ A h L}^{-1}$ ) the chlorate accumulation rate was 1.04 and 1.3 times higher in stirred-tank reactor compared to flow-through configuration (100% recirculation), for 100% TiO<sub>x</sub> foam and 100% TiO<sub>x</sub> REM, respectively. As detailed previously, it might also be explained by the decrease of the contact time between active chlorine and <sup>•</sup>OH in flow-through conditions. It is also interesting to notice that the accumulation rate of ClO<sub>3</sub><sup>-</sup> decreased with the increase of flow rate. It can be ascribed to (i) the decrease of contact time between active chlorine and <sup>•</sup>OH and (ii) increase of the competition with OER at high flow rate. For the industrial application, it is interesting to highlight that increasing flow rates allowed for increasing the ratio between accumulation rate of active chlorine and chlorate, which increased, for example, from 18.1 at 380 L h<sup>-1</sup> m<sup>-2</sup> to 32.5 at 1580 L h<sup>-1</sup> m<sup>-2</sup> for 100% TiO<sub>x</sub> foam.

Application in flow-through configuration was also beneficial for lowering perchlorate formation. While perchlorate concentration was already below the detection limit for 100% TiO<sub>x</sub> foam in stirred-tank reactor, the perchlorate formation rate decreased from 17.5 mmol h<sup>-1</sup> m<sup>-2</sup> in stirred-tank reactor for the 100% TiO<sub>x</sub> REM to lower than detection limit in flow-through configuration (i.e., < 3.8 mmol h<sup>-1</sup> m<sup>-2</sup> at 380 L h<sup>-1</sup> m<sup>-2</sup>). Once more, it might be ascribed to the lower contact time between chlorate radicals and <sup>•</sup>OH owing to the convection-enhanced renewal of solution in the vicinity of electrode surface.

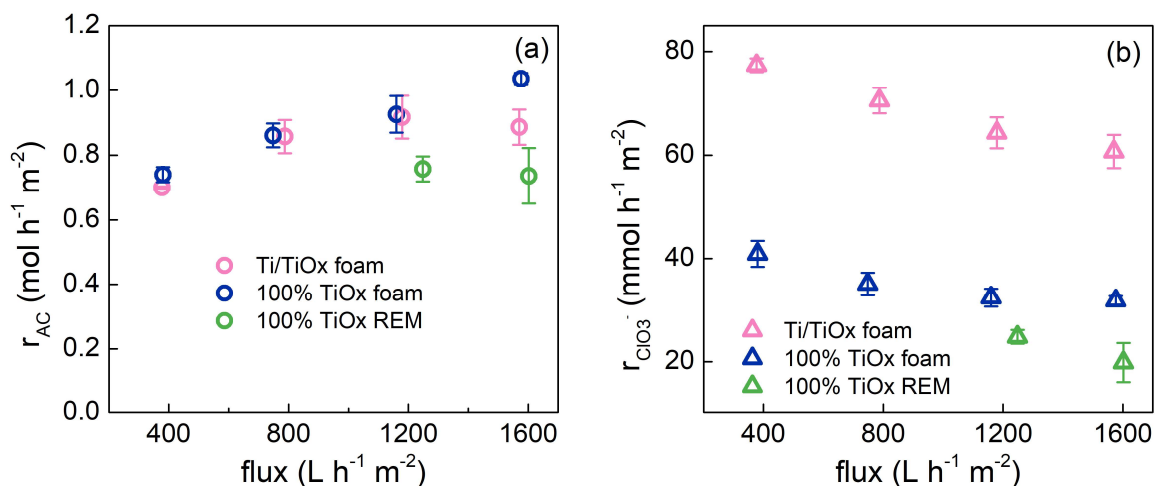


Fig. 6-7 - Evolution of active chlorine (a) and chlorate (b) by 100% TiO<sub>x</sub> foam, REM and Ti/TiO<sub>x</sub> foam regarding flux in flow-through configuration with 0% recirculation of the solution (initial  $[\text{NaCl}]_0 = 12 \text{ mM}$ , current density =  $5 \text{ mA cm}^{-2}$ , BDD grid as cathode)

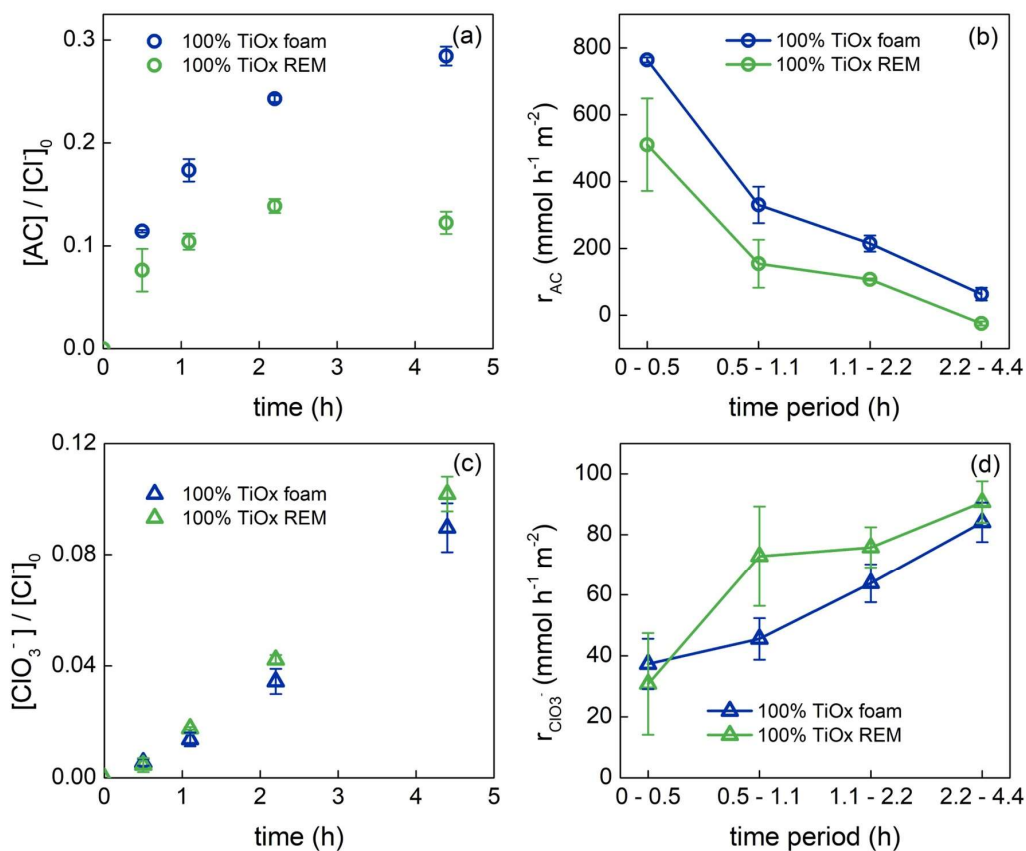


Fig. 6-8 - Evolution of active chlorine (a), chlorate (c) and their accumulation rates ((b) for active chlorine and (d) for chlorate) during 4.4 h electrolysis by 100% TiO<sub>x</sub> foam and REM in

flow-through reactor with continuous recirculation of the solution (batch mode) ( $[\text{NaCl}]_0 = 12$  mM,  $S_{\text{electrode}}/V_{\text{solution}} = 3.6 \text{ m}^{-1}$ , current density =  $5 \text{ mA cm}^{-2}$ , BDD grid as cathode,  $J = 1590 \text{ L h}^{-1} \text{ m}^{-2}$ )

### **3.2 Application of 100% TiO<sub>x</sub> electrodes for a complex effluent treatment and the role of organic pollutants**

The next objective was to assess the potential of TiO<sub>x</sub> electrodes for the removal of organic compounds in a chloride-containing effluent. It represents currently an important challenge for electrochemical engineering because of the potential production of toxic by-products, including chlorate, perchlorate and HOCs.

100% TiO<sub>x</sub> foam was applied in flow-through condition (with 100% recirculation of the feed water) at flow rate of  $1590 \text{ L h}^{-1} \text{ m}^{-2}$  since it represents the optimal conditions for (i) removal of organic compounds through hydroxyl radical mediated oxidation (Chapter V), (ii) minimizing chlorate and perchlorate formation (subsection 3.1.4). This electrode was selected as the most suitable material to avoid high pressure drop and fouling issues. It was also applied in stirred-tank configuration under the same conditions. Comparison was made with standard DSA and BDD plates anodes.

#### **3.2.1 Discoloration and TOC removal during the treatment**

UV absorption at 668 nm was measured to follow the discoloration of the effluent during the treatment of a real dye effluent. More than 95% discoloration was obtained for all electrodes in both reactors after 2.2 h of treatment (Fig. 6-9 (a)). However, different discoloration kinetics were obtained. Slower discoloration was obtained with DSA plate. Compared to TiO<sub>x</sub> and BDD, DSA does not generate large amounts of  $\cdot\text{OH}$ , therefore, these results indicate that DET and/or active chlorine participated in the degradation of dyes but  $\cdot\text{OH}$  also played a significant role. The most efficient discoloration was obtained by 100% TiO<sub>x</sub> foam in

flow-through configuration. It might be directly ascribed to the convection-enhanced mass transport of dyes for reaction in flow-through conditions.

As regards to TOC removal (Fig. 6-9 (b)), better results were obtained with BDD compared to DSA, indicating that  $\cdot\text{OH}$ -mediated oxidation also played a major role in mineralization effectiveness. However, higher mineralization yield was obtained after 4.4 h of treatment using 100% TiO<sub>x</sub> foam in flow-through condition, compared to BDD plate, which can be attributed to the convection-enhanced mass transport of organic pollutants to the electrode surface. These results indicate that mass transport enhancement in flow-through conditions was still a key factor for the removal of organic compounds, despite the strong competition between chlorine evolution and water oxidation at anode surface.

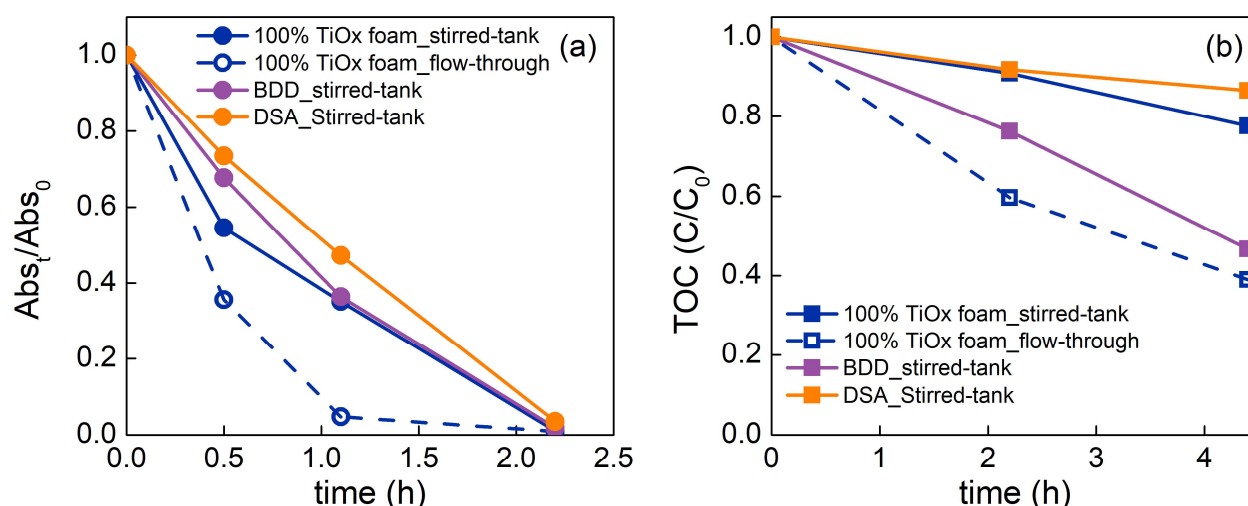


Fig. 6-9 - Discoloration (a) and TOC removal (b) during 4.4 h treatment of the dye effluent by 100% TiO<sub>x</sub> foam in both stirred-tank and flow-through reactors (batch mode) and compared with BDD and DSA in stirred-tank reactor ( $[\text{NaCl}]_0 = 12 \text{ mM}$ , initial TOC =  $9.6 \text{ mg L}^{-1}$ , cathode: BDD grid,  $S_{\text{electrode}}/V_{\text{solution}} = 3.6 \text{ m}^{-1}$ , current density =  $5 \text{ mA cm}^{-2}$ ,  $J = 1590 \text{ L h}^{-1} \text{ m}^{-2}$ )

### 3.2.2 Chloride oxidation during the treatment

Figs. 6-10 (a), (c) and (e) show the evolution of active chlorine, chlorate and perchlorate

during the treatment of the real effluent. In stirred-tank reactor, higher accumulation of active chlorine was obtained using 100% TiO<sub>x</sub> foam compared to BDD plate. Meanwhile, lower accumulation of chlorate and perchlorate was obtained. Perchlorate concentration was even below the detection limit in the case of 100% TiO<sub>x</sub> foam. These results are consistent with previous observations obtained from experiments in synthetic effluent (sub-section 3.1.1). It is interesting to notice that DSA did not promote formation of chlorate and perchlorate (below the detection limit); however, as discussed above, DSA presented also a limitation in terms of organic compounds removal.

For 100% TiO<sub>x</sub> foam in stirred-tank reactor, the accumulation rate of active chlorine (179 mmol h<sup>-1</sup> m<sup>-2</sup> during the first 2.2 h of treatment) was significantly lower than that obtained in similar conditions using synthetic solution without organic compounds (376 ± 35 mmol h<sup>-1</sup> m<sup>-2</sup> during the first 2 h of treatment), indicating that organic compounds have reacted with active chlorine and participated to decrease the accumulation of active chlorine in the medium. The application of 100% TiO<sub>x</sub> foam in flow-through configuration also led to the decrease of the accumulation rate of active chlorine (49 mmol h<sup>-1</sup> m<sup>-2</sup> during the first 2.2 h of treatment). It might be explained by further promotion of the reaction of organic compounds with •OH (owing to mass transport enhancement) instead of chlorine evolution. Similarly, the average chlorate accumulation rate strongly decreased from 77 mmol h<sup>-1</sup> m<sup>-2</sup> in stirred-tank reactor to 29 mmol h<sup>-1</sup> m<sup>-2</sup> in flow-through conditions. It might also be related to the promotion of the competition of •OH-mediated oxidation of organic compounds instead of •OH-mediated oxidation of active chlorine to chlorate.

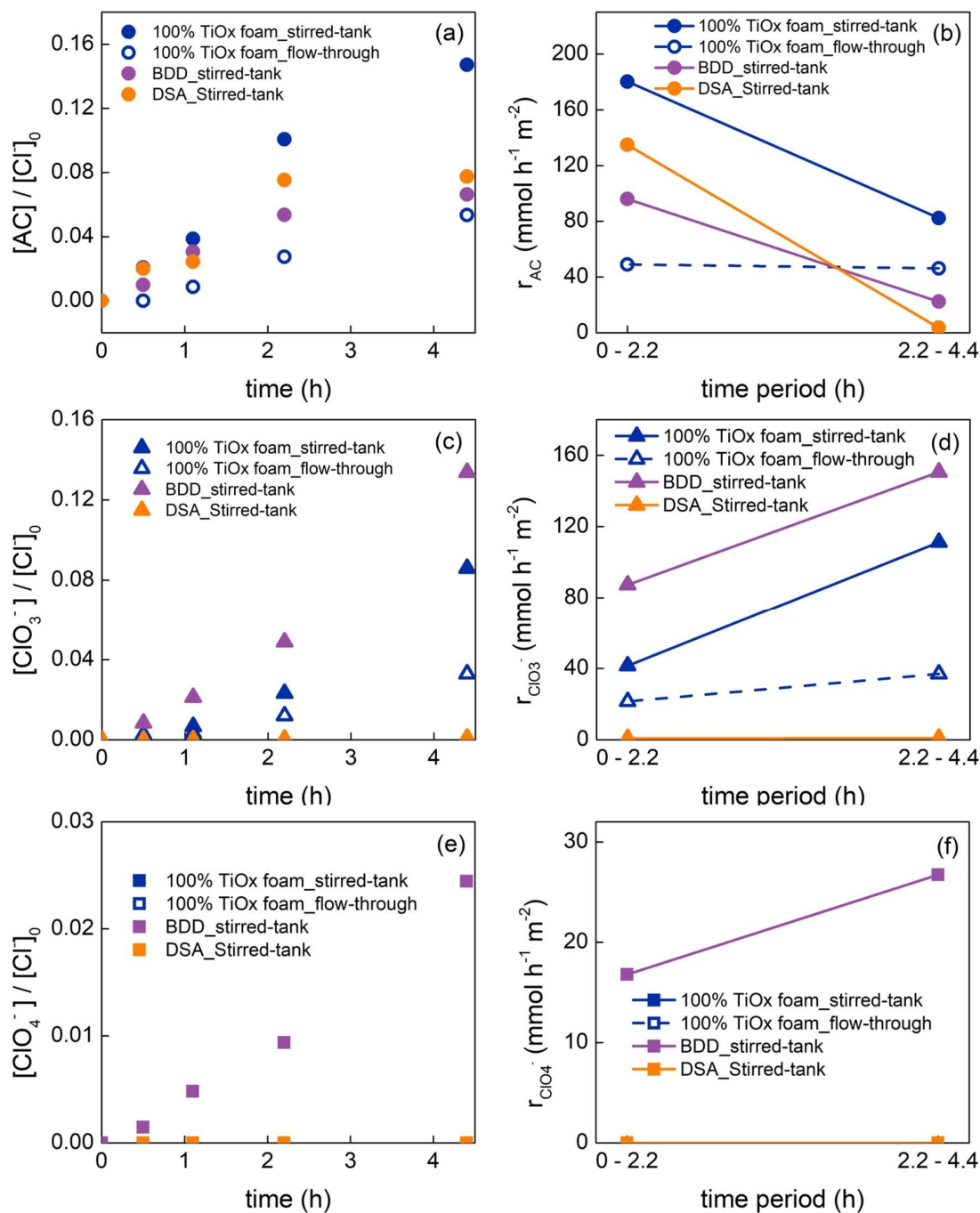


Fig. 6-10 - Evolution and accumulation rates of active chlorine ((a) and (b)), chlorate ((c) and (d)) and perchlorate ((e) and (f)) during 4.4 h treatment by anodic oxidation using 100% TiO<sub>x</sub> foam as anode in stirred-tank and flow-through reactors ( $J = 1590 \text{ L h}^{-1} \text{ m}^{-2}$ ; batch mode with 100% recirculation). Results are compared with BDD and DSA plates applied in stirred-tank reactor ( $[\text{NaCl}]_0 = 12 \text{ mM}$ , initial TOC =  $9.6 \text{ mg L}^{-1}$ ,  $S_{\text{electrode}}/V_{\text{solution}} = 3.6 \text{ m}^{-1}$ , current density =  $5 \text{ mA cm}^{-2}$ )



### 3.2.3 Formation of halogenated organic compounds

Adsorbable organic chloride (AOCl) was the only class of AOX quantified in original and treated samples. The concentrations of adsorbable organic bromide and iodide (AOBr and AOI) were below the detection limit (10 ppb). Therefore, AOX corresponds to only AOCl in this study. As shown in Fig. 6-11, the amount of AOX generated at the beginning of the treatment in stirred-tank reactor ( $t = 0.6$  h) was qualitatively correlated to the capacity of the different electrodes to generate active chlorine in synthetic solutions. It means that the higher the rate of active chlorine accumulation was (DSA and 100% TiO<sub>x</sub> foam), the higher the formation of AOX was observed during the treatment in stirred-tank reactor. It is also interesting to observe that the formation of AOX was 1.6 times higher in stirred-tank reactor compared to flow-through reactor for 100% TiO<sub>x</sub> foam in the first 0.6 h. It might be attributed to the promotion of the degradation of organic precursors through  $\cdot\text{OH}$ -mediated oxidation (owing to enhanced mass transport to the electrode surface in flow-through configuration) instead of homogeneous reaction with active chlorine in the bulk solution.

At longer treatment time ( $t = 4.4$  h), the accumulation of AOX in the treated solution increased for all electrodes and configurations. It is difficult to compare the evolution of AOX for different electrodes. In fact, the nature of organic precursors (i.e., presence/absence of AOX precursors) was modified because of different electro-oxidation mechanisms ( $\cdot\text{OH}$  or active chlorine mediated oxidation, DET) that lead to the presence of different degradation by-products in the solution depending on the electrode used. However, it can still be noticed that the concentration of AOX was 1.4 times higher in stirred-tank reactor compared to flow-through configuration for 100% TiO<sub>x</sub> foam. It is also important to highlight that 4.4 h of treatment (corresponding to an electrical charge of  $0.79 \text{ A h L}^{-1}$ ) was not sufficient for the removal of AOX from the solution. Longer treatment times would be required to achieve higher mineralization yield and subsequent decrease of AOX.

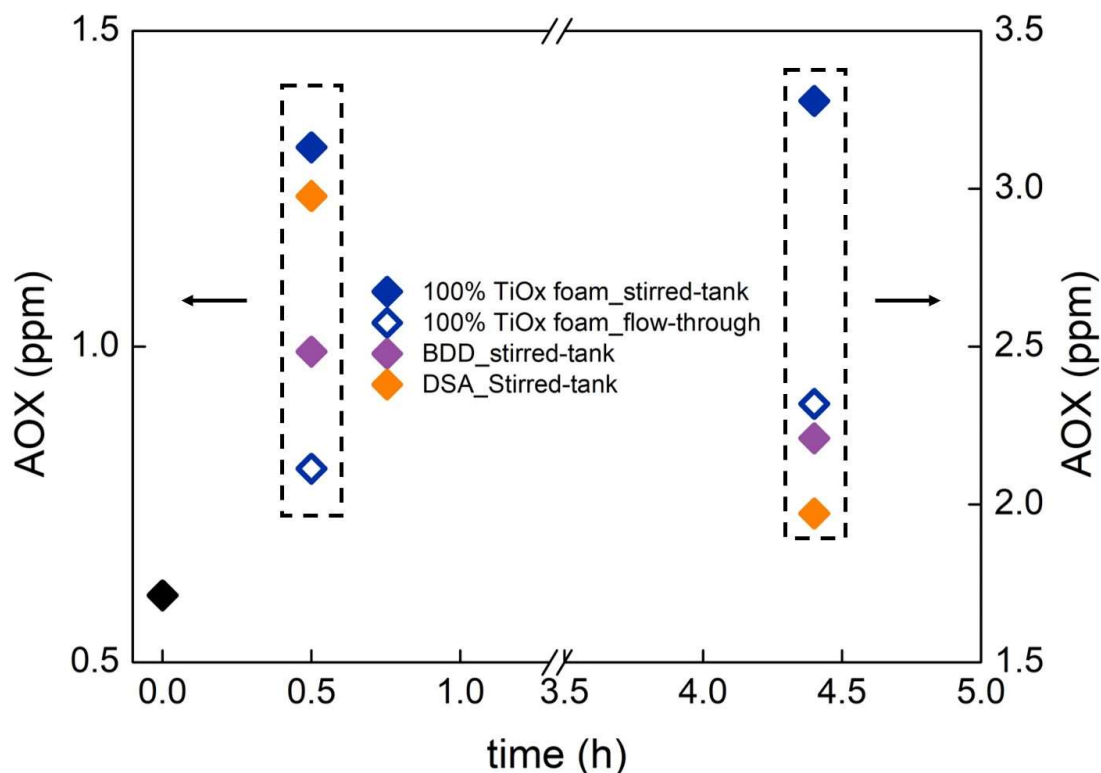


Fig. 6-11 - Evolution of AOX during anodic oxidation with different anodes in stirred-tank and flow-through reactors (batch mode with 100% recirculation) ( $J = 1590 \text{ L h}^{-1} \text{ m}^{-2}$ ; initial  $\text{TOC} = 9.6 \text{ mg L}^{-1}$ ,  $S_{\text{electrode}}/V_{\text{solution}} = 3.6 \text{ m}^{-1}$ , current density =  $5 \text{ mA cm}^{-2}$ )

#### 4. Conclusions

The results obtained in this study provide new insights in the role of porous structure and reactor configuration for chlorine evolution. Application of TiO<sub>x</sub> foams in stirred-tank reactor allowed for an increase of active chlorine formation, resulting in lesser formation of other oxychlorinated species ( $\text{ClO}_3^-$  and  $\text{ClO}_4^-$ ). The accumulation rate of active chlorine reached similar value when using standard DSA electrode. However, quenching experiments highlighted that  $\cdot\text{OH}$ -mediated oxidation was the key mechanism for chloride oxidation to active chlorine at TiO<sub>x</sub> electrodes on the contrary to DSA electrode for which DET was the predominant mechanism. Reactions at cathode should also be taken into consideration if the objective is to maximize the accumulation rate of active chlorine. In fact, accumulation of active chlorine was highly depending on the capacity of cathode material to promote/avoid

reduction of active chlorine.

In flow-through conditions, active chlorine accumulation rate increased with flow rate. Further investigations are required to clearly highlight the underlying mechanisms, which seem to be related to the promotion of chlorine evolution at anode and/or stronger competition of HER for active chlorine reduction at cathode. On the contrary, formation of chlorate decreased with flow rate and formation of perchlorate at 100% TiO<sub>x</sub> REM also decreased below the detection limit by switching from stirred-tank to flow-through configuration. Based on the current state of knowledge, less formation of chlorate and perchlorate at TiO<sub>x</sub> foams as well as in flow-through conditions might be most probably ascribed to the decrease of the contact time between active chlorine (for ClO<sub>3</sub><sup>-</sup> formation)/chlorate radicals (for ClO<sub>4</sub><sup>-</sup> formation) and •OH re accumulated in the vicinity of anode surface.

During the application of the anodic oxidation process for treatment of a real effluent containing organic dyes and high concentration of chloride, less accumulation of AOX in the solution was observed in flow-through conditions. The most probable reason was that dyes degradation was more favored through •OH-mediated oxidation at electrode surface than through active chlorine-mediated oxidation in bulk solution. However, 4.4 h of treatment ( $q = 0.79 \text{ A h L}^{-1}$ , corresponding to a TOC removal yield of 61%) was not sufficient to avoid accumulation of AOX in the treated solution. Longer treatment time would be required to eliminate AOX. The toxicity of AOX compounds should be therefore carefully studied. Moreover, despite positive results for reducing the concentrations of chlorate and perchlorate, their presence might still make important the implementation of a post-treatment step. Another strategy would be the development of electrode materials with very low electrocatalytic activity for chlorine evolution but also high electrocatalytic activity for removal of organic compounds. For example, DSA electrode allowed for less ClO<sub>3</sub><sup>-</sup> and ClO<sub>4</sub><sup>-</sup> formation but degradation and mineralization rates of organic compounds were also limited. Studies on graphene-based sponges have recently highlighted promising results in this area (Baptista-Pires et al., 2021).

## References

- Anipsitakis, G.P., Dionysiou, D.D., 2004. Radical generation by the interaction of transition metals with common oxidants. *Environ. Sci. Technol.* 38, 3705–3712. <https://doi.org/10.1021/es035121o>
- Azizi, O., Hubler, D., Schrader, G., Farrell, J., Chaplin, B.P., 2011. Mechanism of perchlorate formation on boron-doped diamond film anodes. *Environ. Sci. Technol.* 45, 10582–10590. <https://doi.org/10.1021/es202534w>
- Bagastyo, A.Y., Batstone, D.J., Kristiana, I., Gernjak, W., Joll, C., Radjenovic, J., 2012. Electrochemical oxidation of reverse osmosis concentrate on boron-doped diamond anodes at circumneutral and acidic pH. *Water Res.* 46, 6104–6112. <https://doi.org/10.1016/j.watres.2012.08.038>
- Baptista-Pires, L., Norra, G.F., Radjenovic, J., 2021. Graphene-based sponges for electrochemical degradation of persistent organic contaminants. *Water Res.* 203, 117492. <https://doi.org/10.1016/j.watres.2021.117492>
- Bergmann, M.E.H., Rollin, J., Iourtchouk, T., 2009. The occurrence of perchlorate during drinking water electrolysis using BDD anodes. *Electrochim. Acta* 54, 2102–2107. <https://doi.org/10.1016/j.electacta.2008.09.040>
- Brito, C. do N., de Araújo, D.M., Martínez-Huitle, C.A., Rodrigo, M.A., 2015. Understanding active chlorine species production using boron doped diamond films with lower and higher sp<sup>3</sup>/sp<sup>2</sup> ratio. *Electrochem. Commun.* 55, 34–38. <https://doi.org/10.1016/j.elecom.2015.03.013>
- Bruguera-Casamada, C., Sirés, I., Brillas, E., Araujo, R.M., 2017. Effect of electrogenerated hydroxyl radicals, active chlorine and organic matter on the electrochemical inactivation of *Pseudomonas aeruginosa* using BDD and dimensionally stable anodes. *Sep. Purif. Technol.* 178, 224–231. <https://doi.org/10.1016/j.seppur.2017.01.042>
- Buxton, G.V., Greenstock, C.L., Helman, W.P., Ross, A.B., 1988. Critical review of rate constants for reactions of hydrated electrons, hydrogen atoms and hydroxyl radicals ( $\cdot\text{OH}/\cdot\text{O}^-$ ) in aqueous solution. *J. Phys. Chem. Ref. Data* 17, 513–886. <https://doi.org/10.1063/1.555805>
- Chaplin, B.P., 2014. Critical review of electrochemical advanced oxidation processes for water treatment applications. *Env. Sci. Process. Impacts* 16, 1182–1203. <https://doi.org/10.1039/C3EM00679D>
- Donaghue, A., Chaplin, B.P., 2013. Effect of select organic compounds on perchlorate formation at boron-doped diamond film anodes. *Environ. Sci. Technol.* 47, 12391–12399.

<https://doi.org/10.1021/es4031672>

- Ferreira de Melo, J., Medeiros de Araújo, D., Ribeiro da Silva, D., Martinez Huitle, C.A., Villegas-Guzman, P., 2020. Applicability of electrochemical technology for treating a real petrochemical effluent by electro-generated active chlorine species. *Int. J. Electrochem. Sci.* 15, 10262–10275. <https://doi.org/10.20964/2020.10.66>
- García-Espinoza, J.D., Mijaylova-Nacheva, P., Avilés-Flores, M., 2018. Electrochemical carbamazepine degradation: Effect of the generated active chlorine, transformation pathways and toxicity. *Chemosphere* 192, 142–151. <https://doi.org/10.1016/j.chemosphere.2017.10.147>
- Guo, L., Jing, Y., Chaplin, B.P., 2016. Development and characterization of ultrafiltration TiO<sub>2</sub> Magnéli phase reactive electrochemical membranes. *Environ. Sci. Technol.* 50, 1428–1436. <https://doi.org/10.1021/acs.est.5b04366>
- Hubler, D.K., Baygents, J.C., Chaplin, B.P., Farrell, J., 2014. Understanding chlorite, chlorate and perchlorate formation when generating hypochlorite using boron doped diamond film electrodes. *ECS Trans.* 58, 21–32. <https://doi.org/10.1149/05835.0021ecst>
- Isidro, J., Brackemeyer, D., Sáez, C., Llanos, J., Lobato, J., Cañizares, P., Matthée, T., Rodrigo, M.A., 2020. How to avoid the formation of hazardous chlorates and perchlorates during electro-disinfection with diamond anodes? *J. Environ. Manage.* 265, 110566. <https://doi.org/10.1016/j.jenvman.2020.110566>
- Jung, Y.J., Baek, K.W., Oh, B.S., Kang, J.W., 2010. An investigation of the formation of chlorate and perchlorate during electrolysis using Pt/Ti electrodes: The effects of pH and reactive oxygen species and the results of kinetic studies. *Water Res.* 44, 5345–5355. <https://doi.org/10.1016/j.watres.2010.06.029>
- Li, W., Xiao, R., Lin, H., Yang, K., Li, W., He, K., Yang, L.H., Pu, M., Li, M., Lv, S., 2022. Electro-activation of peroxymonosulfate by a graphene oxide/iron oxide nanoparticle-doped Ti<sub>4</sub>O<sub>7</sub> ceramic membrane: Mechanism of singlet oxygen generation in the removal of 1,4-dioxane. *J. Hazard. Mater.* 424, 127342. <https://doi.org/10.1016/j.jhazmat.2021.127342>
- Mandal, P., Yadav, M.K., Gupta, A.K., Dubey, B.K., 2020. Chlorine mediated indirect electro-oxidation of ammonia using non-active PbO<sub>2</sub> anode: Influencing parameters and mechanism identification. *Sep. Purif. Technol.* 247, 116910. <https://doi.org/10.1016/j.seppur.2020.116910>

- Martínez-Huitle, C.A., Rodrigo, M.A., Sirés, I., Scialdone, O., 2015. Single and coupled electrochemical processes and reactors for the abatement of organic water pollutants: A critical review. *Chem. Rev.* 115, 13362–13407. <https://doi.org/10.1021/acs.chemrev.5b00361>
- Neta, P., Huie, R.E., Ross, A.B., 1988. Rate constants for reactions of inorganic radicals in aqueous solution. *J. Phys. Chem. Ref. Data* 17, 1027. <https://doi.org/10.1063/1.555808>
- Perea, L.A., Palma-Goyes, R.E., Vazquez-Arenas, J., Romero-Ibarra, I., Ostos, C., Torres-Palma, R.A., 2019. Efficient cephalexin degradation using active chlorine produced on ruthenium and iridium oxide anodes: Role of bath composition, analysis of degradation pathways and degradation extent. *Sci. Total Environ.* 648, 377–387. <https://doi.org/10.1016/j.scitotenv.2018.08.148>
- Petrucci, E., Da Pozzo, A., Di Palma, L., 2016. On the ability to electrogenerate hydrogen peroxide and to regenerate ferrous ions of three selected carbon-based cathodes for electro-Fenton processes. *Chem. Eng. J.* 283, 750–758. <https://doi.org/10.1016/j.cej.2015.08.030>
- Radjenovic, J., Sedlak, D.L., 2015. Challenges and opportunities for electrochemical processes as next-generation technologies for the treatment of contaminated water. *Environ. Sci. Technol.* 49, 11292–11302. <https://doi.org/10.1021/acs.est.5b02414>
- Rahmani, A.R., Samarghandi, M.R., Nematollahi, D., Zamani, F., 2019. A comprehensive study of electrochemical disinfection of water using direct and indirect oxidation processes. *J. Environ. Chem. Eng.* 7, 102785. <https://doi.org/10.1016/j.jece.2018.11.030>



## **Chapter VII**

### **Conclusions and Perspectives**



## 1. General conclusions

This thesis work focused on the development of new porous  $\text{TiO}_x$  electrodes and their application in anodic oxidation for water treatment. Porous electrodes have been successfully synthesized by our industrial partner (Saint Gobain Research Provence) using different techniques:  $\text{TiO}_x$  coated on different Ti substrates by plasma spraying, 3D printing, foaming process and carbothermal reduction. These electrodes present very different porous structures. They were characterized and their electrochemical behaviors were studied. It can be concluded that porous structure of electrode plays a key role in their performance for application in the removal of organic compounds from water.

Porous Ti/ $\text{TiO}_x$  electrodes were fabricated using plasma spraying technique, in which  $\text{TiO}_x$  particles were coated on Ti substrates. The porous structure of these Ti substrates greatly affected the distribution and homogeneity of  $\text{TiO}_x$  coating. The more open porous structure of Ti/ $\text{TiO}_x$  foam 2 favored mass transport conditions in stirred-tank reactors but also hindered hydroxyl radical mediated oxidation by affecting the homogeneity of  $\text{TiO}_x$  coating. On the contrary, Ti/ $\text{TiO}_x$  foam 1 had more suitable porous structure thanks to the possibility to obtain a more homogeneous  $\text{TiO}_x$  coating for the promotion of hydroxyl radical mediated oxidation of organic compounds. Improvement of mass transport conditions in stirred-tank reactor using porous Ti substrate was interpreted in terms of effective roughness factor, which takes into consideration that fine roughness is averaged within the diffusion field. Coarse roughness appeared as a more suitable feature for improvement of mass transfer conditions in the stirred-tank reactor.

Based on these results, it appeared relevant to synthesize a 100%  $\text{TiO}_x$  electrode using 3D printing technique. This technique allowed for controlling the electrode porous structure and a higher effective roughness factor was obtained for enhancing mass transport conditions in stirred-tank reactor. Therefore, the 3D printed 100%  $\text{TiO}_x$  electrode achieved higher reaction rates for both direct electron transfer (DET) and hydroxyl radical mediated oxidation than Ti/ $\text{TiO}_x$  plate or even boron-doped diamond (BDD) electrode. When paracetamol was used as model pollutant, a higher mineralization yield with low accumulation of toxic degradation

by-products was also observed using 3D printed 100% TiO<sub>x</sub> electrode.

Two other porous 100% TiO<sub>x</sub> electrodes (100% TiO<sub>x</sub> foam and 100% TiO<sub>x</sub> REM) were also synthesized from a foaming process and carbothermal reduction. As observed with Ti/TiO<sub>x</sub> electrodes, the coarse roughness of 100% TiO<sub>x</sub> foam (large pore size with a median of 127.2 μm) also favored reaction rates in stirred-tank reactor. On the opposite, the fine roughness of 100% TiO<sub>x</sub> REM (low pore size with a median of 2.2 μm) did not improve reaction rates in stirred-tank reactor, despite a larger electro-active surface area. However, much better results were obtained with 100% TiO<sub>x</sub> REM in flow-through reactor, which can take better advantage of internal surface area of porous electrodes and minimize diffusion limitation owing to fast radial diffusion within small pores. For example, the degradation rate of 0.1 mM of terephthalic acid was enhanced 48 times compared to the application in stirred-tank reactor. This great enhancement was obtained by the convection-enhanced mass transport of organic pollutants.

Porous TiO<sub>x</sub> electrodes could also promote efficient active chlorine generation, during which electrode structure and applied configuration played important roles. For example, porous TiO<sub>x</sub> electrodes promoted comparable active chlorine generation than dimensionally stable anodes (DSA) in stirred-tank reactor. However, different reaction mechanisms were highlighted. Generation of active chlorine on DSA was mostly related to DET while hydroxyl radical mediated oxidation played the dominant role in the case of porous TiO<sub>x</sub> electrodes. Efficient active chlorine generation by TiO<sub>x</sub> electrodes was also achieved in flow-through reactor. Therefore, 100% TiO<sub>x</sub> foam was used for treatment of a chloride-containing textile effluent. The result showed that the most effective discoloration and mineralization rates were obtained in flow-through configuration, thanks to the combination of hydroxyl radical mediated oxidation at electrode surface and active chlorine mediated oxidation in the bulk. However, toxic by-products including chlorate, perchlorate and adsorbable organic halides (AOX) were also observed during the treatment. Results obtained in this study indicated that the porous structure of TiO<sub>x</sub> electrodes might contribute to the decrease of the formation of chlorate and perchlorate. However, a great attention should be given on this issue for application to the treatment of chloride-containing effluents.

The results obtained in this thesis highlight that the choice of the most suitable electrode would depend on the nature of the effluent to be treated. For the treatment of low concentrations of pollutants, the use of the 100% TiO<sub>x</sub> REM (small pore size) in flow-through configuration appeared as the most suitable option for minimizing mass transport limitations. However, such application might also raise other issues related to fouling and pressure drop under filtration conditions.

The use of foams might be suitable for the treatment of more concentrated effluents (e.g., in the range of few mg L<sup>-1</sup> - dozens of mg L<sup>-1</sup>). Larger pore size might reduce fouling and pressure drop in filtration conditions. For such application, diffusion limitations might still occur within large pore size. The flow-through configuration would improve mass transport conditions when pore size is not too large. Besides, application in flow-by or stirred-tank reactor would benefit from a coarse roughness for improving the effective roughness factor.

In the case of highly concentrated effluents and absence of mass transport limitation, the use of porous electrodes might not be relevant.

## 2. Perspectives and future work

Further development of such electrochemical advanced oxidation process requires the implementation of pilot-scale reactors or full-scale demonstrators. Several technological challenges are still related to the design of suitable reactors at large scale. However, in this thesis work, the choice was made to focus on another crucial issue. As detailed in Chapter III to Chapter VI, TiO<sub>x</sub> electrodes studied in this thesis work showed promising features for application in water treatment. However, there are still important questions related to the lifetime of such electrodes. Before further industrial development of a novel electrode, it is necessary to assess its stability and the potential service time. There is always a lack of information in the scientific literature on the lifetime of different kinds of novel electrode materials. Most of the time, it is assessed by the repetition of the same experiment for comparison of the electrode effectiveness among different cycles (Geng et al., 2015; Meng et al., 2022). However, such tests give information only on the stability of the electrode during few hours, which corresponds to the time scale of laboratory tests. Long-term lifetime assessment could be a challenge for lab-scale study because it can be time consuming. The most common method for lifetime assessment is accelerated lifetime tests, which is conducted under more aggressive conditions than the common application condition (Chen et al., 2011; Palma-Goyes et al., 2016; Guo et al., 2021; Lin et al., 2021; Wang et al., 2022).

During this thesis study, some preliminary experiments have been performed regarding electrode stability and lifetime assessment. The obtained results raise different questions for the future.

### 2.1 How is the stability of TiO<sub>x</sub> electrodes?

Fig. 7-1 shows the degradation of paracetamol (PCT) using Ti/TiO<sub>x</sub> foam electrode for 7 cycles. The effectiveness was improved slightly for the first 4 cycles, probably due to the removal of impurities from the pristine electrode during electrolysis. Then the effectiveness was more or less stable with  $C/C_0$  reaching similar values from 0.08 to 0.14 after 2 h of

electrolysis. This result suggests that Ti/TiO<sub>x</sub> foam has good stability for application in the time scale of laboratory tests performed during this thesis. The stability of Ti/TiO<sub>x</sub> plate was also proved by similar experiments (Chapter III, Fig. 3-21), suggesting the general short-term stability of TiO<sub>x</sub> electrodes regardless of their different structures. No Ti leaching in the solution was observed in all cases (detection limit: 0.05 mg L<sup>-1</sup>) (Chapter III). However, repetition of the same experiment is time consuming and do not allow for assessment of the service time at the time scale that is interesting for industrial application. Therefore, accelerated lifetime tests have been conducted to study electrode's service time.

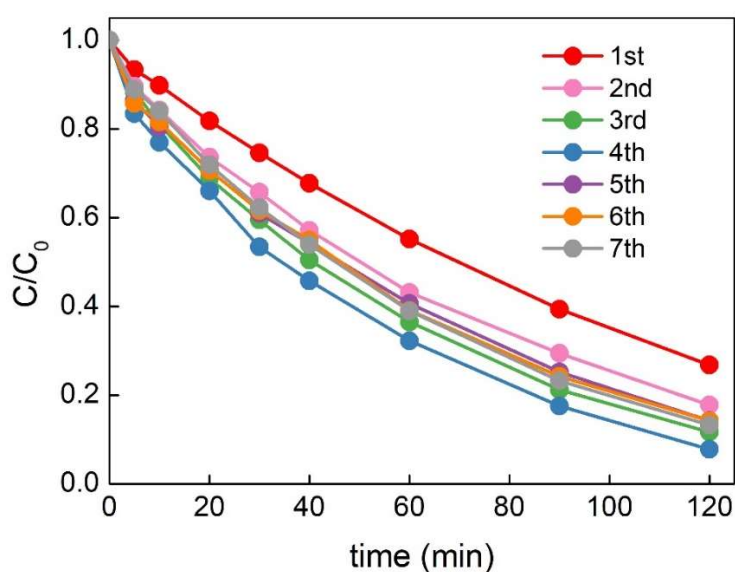


Fig. 7-1 - Effectiveness of Ti/TiO<sub>x</sub> foam anode during seven consecutive experiments for degradation of paracetamol ( $C/C_0$ ) under same experimental conditions (cathode: carbon felt, initial  $C_{PCT} = 0.1$  mM, effective surface area =  $23.6$  cm<sup>2</sup>,  $S_{electrode}/V_{solution} = 7.9$  m<sup>-1</sup>, current density =  $5$  mA cm<sup>-2</sup>, electrolyte:  $50$  mM Na<sub>2</sub>SO<sub>4</sub>)

## 2.2 How the increase of the anodic potential allows for prediction of the lifetime of TiO<sub>x</sub> electrodes?

Following the increase of the anodic potential during experiments performed at high current density (and in acidic conditions) is the most widely used method for accelerated lifetime tests. However, these data are not often provided in the literature and operating conditions differ

from one study to another.

In this study, the accelerated lifetime test was performed using Ti/TiO<sub>x</sub> plate at current density of 75 mA cm<sup>-2</sup> (in 50 mM Na<sub>2</sub>SO<sub>4</sub> medium) to predict the lifetime of the electrode (Fig. 7-2) and anodic potential was monitored during the ageing process. Stable anodic potential was observed during the first 8 h, and then it started to increase. When the anodic potential reached a value 1.5 V higher than the initial stable anodic potential, the corresponding time is considered as electrode failure time (16 h at 75 mA cm<sup>-2</sup> for Ti/TiO<sub>x</sub> plate electrode). Then the failure time of the electrode at other applied current densities could be extrapolated using Eq. 7-1, according to the literature (Chen et al., 2011; Lin et al., 2021).

$$t_{app} = t_{ac} \left( \frac{i_{ac}}{i_{app}} \right)^n \quad (7 - 1)$$

where  $t_{ac}$  (h) and  $i_{ac}$  (mA cm<sup>-2</sup>) are failure time and applied current density in accelerated lifetime test, respectively,  $i_{app}$  (mA cm<sup>-2</sup>) and  $t_{app}$  (h) are applied current density and predicted failure time,  $n$  ranges from 1.4 to 2.0 and was assumed 1.7 (Lin et al., 2021).

The corresponding failure times of TiO<sub>x</sub> electrode at different applied current density obtained from this correlation are reported in Table 7-1. Applying low current density can significantly increase service time of the electrode. Reasonable results were, for example, obtained at 5 mA cm<sup>-2</sup> for which the predicted service time was 66 days. However, the selection of the  $n$  value might be a topic for future investigations.

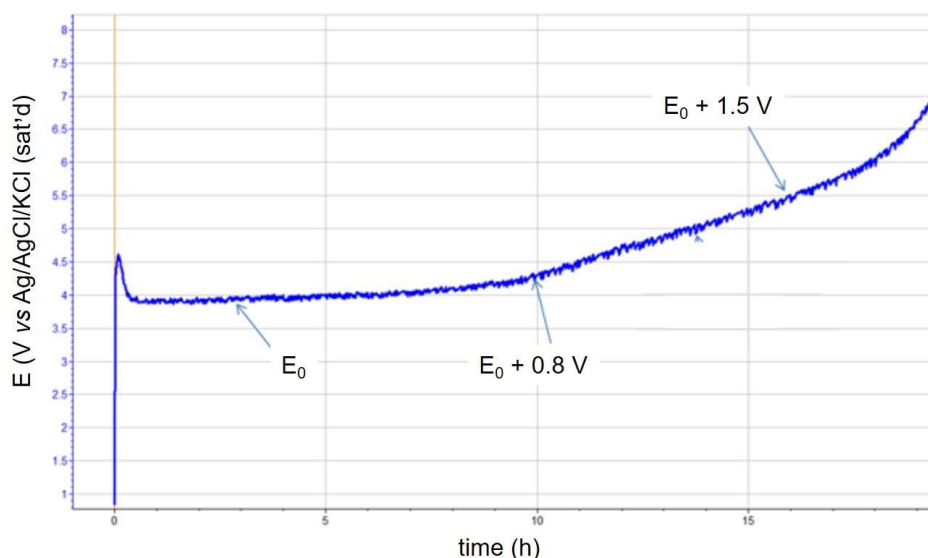


Fig. 7-2 - Evolution of anodic potential during the accelerated lifetime test of Ti/TiO<sub>x</sub> plate electrode (30°C, current density = 75 mA cm<sup>-2</sup>, electrolyte: 1 M Na<sub>2</sub>SO<sub>4</sub>)

Table 7-1 Prediction of TiO<sub>x</sub> electrode failure time at different current density

$i_{app}$ (mA cm <sup>-2</sup> )	5	10	50	100
$t_{app}$ (h)	1597.6	491.7	31.9	9.8

### 2.3 Is the increase of anodic potential suitable for representing the real reactivity loss of TiO<sub>x</sub> electrodes for removal of organic compounds?

Accelerated lifetime test is the most widely used method for service time prediction, which assumes that the electrode effectiveness would remain sufficient during this service time. However, to the best of our knowledge, there is a lack of studies on the evolution of the electrode reactivity in the literature, by considering the objective of organic compounds removal. Therefore, the evolution of electrode reactivity (regarding hydroxyl radical mediated oxidation) during ageing process at 50 mA cm<sup>-2</sup> was studied and the results are shown in Fig. 7-3. As predicted before, at 50 mA cm<sup>-2</sup>, Ti/TiO<sub>x</sub> plate can serve 31.9 h, corresponding to an electrical charge of 37.6 A h. According to Fig. 7-3, Ti/TiO<sub>x</sub> plate lost already 20% of its

reactivity after 1.77 A h electrical charge passed. Further tests at higher electric charge would be required for proper comparison with previous results. However, these results may indicate that electrode might lose significantly its reactivity for hydroxyl radical mediated oxidation before the predicted failure time. These preliminary tests raise several questions:

- How to correlate the results obtained from the evolution of the anodic potential to the loss of reactivity regarding hydroxyl radical mediated oxidation?
- What is the most appropriate methodology to obtain relevant data for industrial applications?
- Which operating conditions should be selected for designing the most relevant tests?

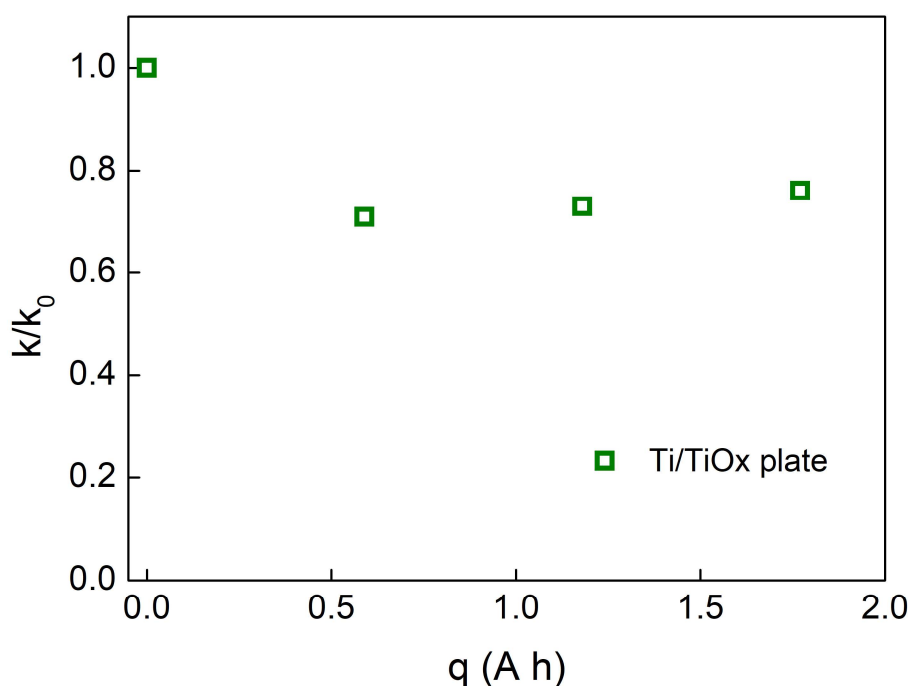


Fig. 7-3 - Evolution of apparent rate constant for terephthalic acid degradation by Ti/TiO<sub>x</sub> plate during the accelerated lifetime tests under following operating conditions: current density = 50 mA cm<sup>-2</sup>, electrolyte: 50 mM Na<sub>2</sub>SO<sub>4</sub>, cathode: stainless steel; terephthalic acid degradation conditions: cathode: carbon felt, initial C<sub>TA</sub> = 0.1 mM, effective surface area = 23.6 cm<sup>2</sup>, S<sub>electrode</sub>/V<sub>solution</sub> = 7.9 m<sup>-1</sup>, current density = 5 mA cm<sup>-2</sup>, electrolyte: 50 mM Na<sub>2</sub>SO<sub>4</sub>



## 2.4 What is the cause for the reactivity loss of TiO<sub>x</sub> electrodes?

Significant reactivity loss was observed during ageing process. Understanding the mechanism of this reactivity loss might be useful for enhancing the service time from material fabrication and choosing the most relevant operating conditions. Different characterization techniques were used to reveal the evolution of material characteristics during electrode ageing. Oxidation of TiO<sub>x</sub> material and subsequent decrease of electrode conductivity might be the most plausible explanation (Jing et al., 2018). The different materials tested during this thesis work were analyzed after ageing at 50 mA cm<sup>-2</sup> for an electrical charge of 1.77 A h. From the preliminary results obtained, it seems that the most relevant technique for assessment of surface oxidation of TiO<sub>x</sub> electrode might be X-ray photoelectron spectroscopy (XPS) analysis. For example, Fig. 7-4 shows XPS results obtained for the 100% TiO<sub>x</sub> foam. Table 7-2 shows the contents of Ti (III) and Ti (IV) obtained from XPS analysis before and after ageing. The increase of Ti (IV) content suggests the oxidation of electrode surface. Such trend was obtained for all materials.

Other analysis could also highlight the oxidation of the TiO<sub>x</sub> material for some electrodes, particularly for 100% TiO<sub>x</sub> foam. Analysis by microprobe (Fig. 7-5) shows that Ti content did not change much while an obvious increase of oxygen content was observed. A change in the X-ray diffraction (XRD) spectra was also observed (Fig. 7-6), indicating the presence of more oxidized Magnéli phases. However, a significant evolution of material characteristics was not always obtained from these analyses, depending on electrode materials. It might be ascribed to the fact that electrode ageing might be mostly ascribed to oxidation of the electrode material at the very near surface, for which XPS analysis is the most relevant technique.

Previous results obtained from Jing et al. (2018) showed that the formation of TiOSO<sub>4</sub> surface species might also contribute to electrode passivation. However, it was not observed during these tests, most probably because of the use of a lower concentration of electrolyte (0.05 M Na<sub>2</sub>SO<sub>4</sub>) instead of 1 M H<sub>2</sub>SO<sub>4</sub> used in the work of Jing et al. (2018). These results also raise the question related to the selection of operating conditions for

performing relevant ageing tests. Interestingly, the study of Jing et al. (2018) also observed surface reoxidation of Magnéli phases and highlighted that this process was reversible during cathodic polarization. These results were not confirmed by reactivity tests, but it paves the way for further investigation of the effect of polarization inversion for improving the lifetime of these electrodes for water treatment.

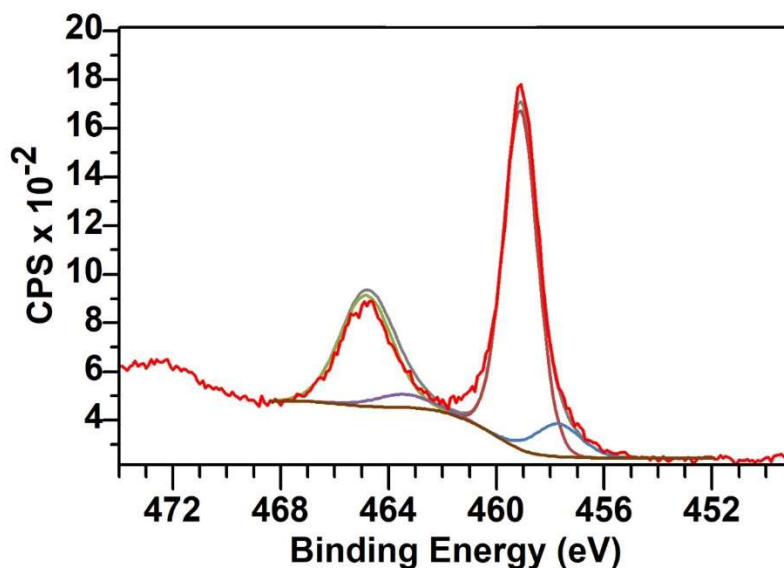


Fig. 7-4 - XPS spectra for 100% TiO<sub>x</sub> foam before ageing

Table 7-2 Ti (III) and Ti (IV) contents of 100% TiO<sub>x</sub> foam before and after ageing

state	Ti (III)	Ti (IV)	Ti (III) / (Ti (III)+Ti (IV))
before ageing	1.6	12.5	0.11
after ageing	0.8	16.4	0.05

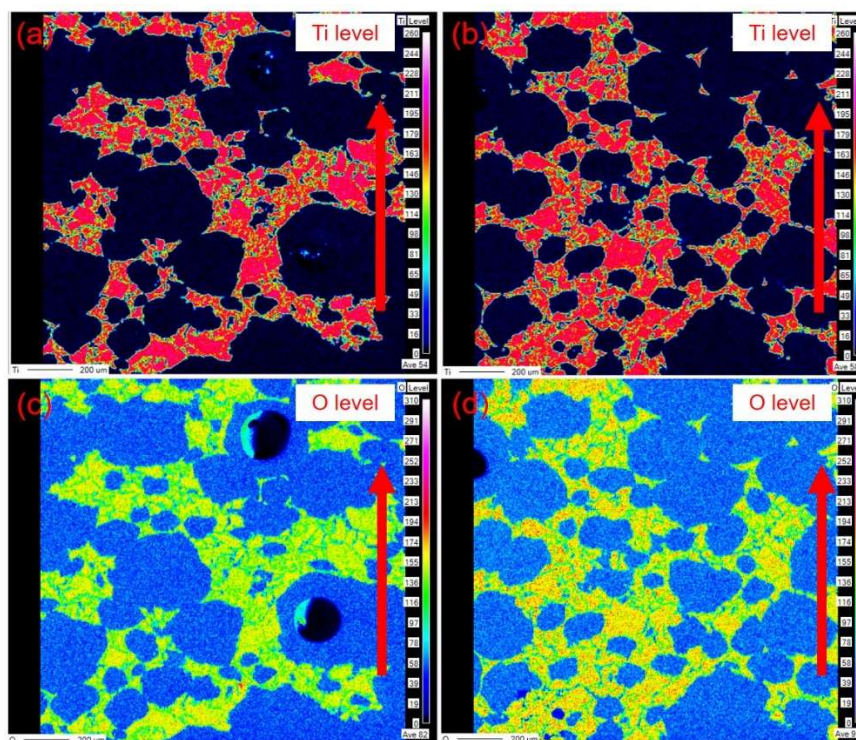


Fig. 7-5 - Elemental mapping of Ti for 100%  $\text{TiO}_x$  foam before ageing (a) and 100%  $\text{TiO}_x$  foam after ageing (b) and of O for 100%  $\text{TiO}_x$  foam before ageing (c) and 100%  $\text{TiO}_x$  foam after ageing (d). Accelerated lifetime test conditions: current density =  $50 \text{ mA cm}^{-2}$ , electrolyte: 50 mM  $\text{Na}_2\text{SO}_4$ , cathode: stainless steel; microprobe analysis: using a field emission electron probe microanalyzer (JEOL FEG JXA-8530F microscope coupled with wavelength dispersive spectrometer (WDS) and energy dispersive spectrometer (EDS) at 12 kV with current 34 nA

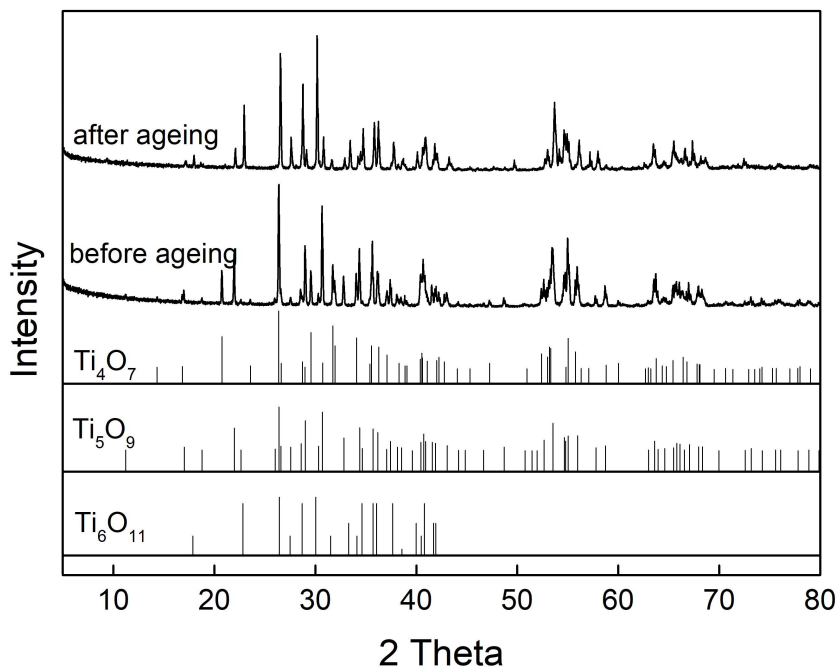


Fig. 7-6 - XRD patterns for 100% TiO<sub>x</sub> foam before and after accelerated lifetime test (using database PDF2-2004). Accelerated lifetime test conditions: current density = 50 mA cm<sup>-2</sup>, electrolyte: 50 mM Na<sub>2</sub>SO<sub>4</sub>, cathode: stainless steel; XRD analysis conditions: Bruker D8 ENDEAVOR, Cu K $\alpha$  radiation ( $\lambda=1.5418$  Å), at 40 kV and 40 mA

Taking into consideration the detailed studies depicted in Chapter III – VI as well as the preliminary tests given above, it can be concluded that the TiO<sub>x</sub> electrodes used in this study might have suitable structures for application in water treatment. However, lifetime issues still need to be examined before further development at industrial scale. Therefore, future study concerning these TiO<sub>x</sub> electrodes should focus on the following aspects:

- Based on preliminary results obtained in this thesis study, the evolution of electrode reactivity during ageing should be performed at larger time scale in order to study the correlation between predicted service time obtained from the evolution of the anodic potential and the evolution of electrode reactivity for hydroxyl radical mediated oxidation. If more comprehensive data can be obtained for the evolution of electrode reactivity, it might be possible to predict electrode lifetime based on the real electrode reactivity evolution.

- Overall, the development of suitable methodologies for assessment of electrode stability also remains an important question. Particularly, the choice of operating conditions might strongly affect the obtained results.
- With the knowledge of reactivity evolution and surface state evolution during electrode ageing, further studies should be performed on the development of a proper methodology to effectively prolong electrode service time, such as the inversion of polarization.
- Another challenge might be also related to electrode passivation depending on the characteristics of the treated water. For example, formation of a passivation film from electro-polymerization of phenolic compounds is sometimes reported during the application of electro-oxidation processes.

## References

- Chen, S., Zheng, Y., Wang, S., Chen, X., 2011. Ti/RuO<sub>2</sub>-Sb<sub>2</sub>O<sub>5</sub>-SnO<sub>2</sub> electrodes for chlorine evolution from seawater. *Chem. Eng. J.* 172, 47–51. <https://doi.org/10.1016/j.cej.2011.05.059>
- Geng, P., Su, J., Miles, C., Comninellis, C., Chen, G., 2015. Highly-Ordered Magnéli Ti<sub>4</sub>O<sub>7</sub> Nanotube Arrays as Effective Anodic Material for Electro-oxidation. *Electrochim. Acta* 153, 316–324. <https://doi.org/10.1016/j.electacta.2014.11.178>
- Guo, H., Xu, Z., Qiao, D., Wang, L., Xu, H., Yan, W., 2021. Fabrication and characterization of titanium-based lead dioxide electrode by electrochemical deposition with Ti<sub>4</sub>O<sub>7</sub> particles. *Water Environ. Res.* 93, 42–50. <https://doi.org/10.1002/wer.1339>
- Jing, Y., Almassi, S., Mehraeen, S., LeSuer, R.J., Chaplin, B.P., 2018. The roles of oxygen vacancies, electrolyte composition, lattice structure, and doping density on the electrochemical reactivity of Magnéli phase TiO<sub>2</sub> anodes. *J. Mater. Chem. A* 6, 23828–23839. <https://doi.org/10.1039/C8TA03719A>
- Lin, H., Xiao, R., Xie, R., Yang, L., Tang, C., Wang, R., Chen, J., Lv, S., Huang, Q., 2021. Defect Engineering on a Ti<sub>4</sub>O<sub>7</sub> Electrode by Ce<sup>3+</sup> Doping for the Efficient Electrooxidation of Perfluorooctanesulfonate. *Environ. Sci. Technol.* 55, 2597–2607. <https://doi.org/10.1021/acs.est.0c06881>
- Meng, C., Zhuo, Q., Wang, A., Liu, J., Yang, Z., Niu, J., 2022. Efficient electrochemical oxidation of COVID-19 treatment drugs favipiravir by a novel flow-through Ti/TiO<sub>2</sub>-NTA/Ti<sub>4</sub>O<sub>7</sub> anode. *Electrochim. Acta* 430, 141055. <https://doi.org/10.1016/j.electacta.2022.141055>
- Palma-Goyes, R.E., Vazquez-Arenas, J., Ostos, C., Torres-Palma, R.A., González, I., 2016. The Effects of ZrO<sub>2</sub> on the Electrocatalysis to Yield Active Chlorine Species on Sb<sub>2</sub>O<sub>5</sub> -Doped Ti/RuO<sub>2</sub> Anodes. *J. Electrochem. Soc.* 163, H818–H825. <https://doi.org/10.1149/2.0891609jes>
- Wang, Y., Li, L., Huang, Q., 2022. Electrooxidation of per- and polyfluoroalkyl substances in chloride-containing water on surface-fluorinated Ti<sub>4</sub>O<sub>7</sub> anodes: Mitigation and elimination of chlorate and perchlorate formation. *Chemosphere* 307, 135877. <https://doi.org/10.1016/j.chemosphere.2022.135877>



## Curriculum Vitae

**Jing Ma**

(+33) 786207747; jing.ma@univ-eiffel.fr

### Education

Ph.D. in Environmental Science and Techniques

Université Gustave Eiffel - Marne-la-Vallée, France

December 2019 - December 2022 (Expected)

Master in Environmental Engineering

Northwest University – Xi'an, China

August 2016 - June 2019

Bachelor in Environmental Science

Northwest University – Xi'an, China

September 2011 - July 2015

---

### Publications

- **Ma, J.**, Trelu, C., Oturan, N., Raffy, S., Oturan, M.A., 2022. Development of Ti/TiO<sub>x</sub> Foams for Removal of Organic Pollutants from Water: Influence of Porous Structure of Ti Substrate. *Appl. Catal. B: Environ.* 317 (2022) 121736. <https://doi.org/10.1016/j.apcatb.2022.121736>
- **Ma J.**, Trelu C., Skolotneva E., Oturan N., Oturan M.A., Mareev M. Investigating the reactivity of TiO<sub>x</sub> and BDD anodes for electro-oxidation of organic pollutants by experimental and modeling approaches. *Electrochim. Acta* 141513. <https://doi.org/10.1016/j.electacta.2022.141513>
- **Ma, J.**, Trelu, C., Oturan, N., Raffy, S., Oturan, M.A., Porous Magnéli phase obtained from 3D printing for efficient anodic oxidation process. *Chem. Eng. J.* 456, 141047. <https://doi.org/10.1016/j.cej.2022.141047>
- Development of 100% TiO<sub>x</sub> electrodes for removal of organic compounds in flow-through configuration: The key role of material pore size. To be submitted
- Chloride oxidation on TiO<sub>x</sub> electrodes: Influence of porous structure and reactor configuration. To be submitted



## Conferences

- Oral presentation: **Jing Ma**, Clément Trelu, Nihal Oturan, Mehmet A. Oturan, Porous Sub-stoichiometric Titanium Oxide for Removal of Organic Pollutants: Effectiveness, Mechanisms and Lifetime, 29th Topical Meeting of the International Society of Electrochemistry, April 2021, Mikulov, Czech Republic.
- Oral presentation: **Jing Ma**, Clément Trelu, Nihal Oturan, Stéphane Raffy, Mehmet A. Oturan, Novel porous TiO<sub>x</sub> anode materials for the removal of organic pollutants from water. 12th European Symposium on Electrochemical Engineering, June 2021, Leeuwarden, The Netherlands.
- Oral presentation: **Jing Ma**, Clément Trelu, Nihal Oturan, Stéphane Raffy, Mehmet A. Oturan, Porous TiO<sub>x</sub> electrodes for water treatment: application in flow-through mode and lifetime test. Journées d'électrochimie, July 2022, Mons, Belgium.